Computational and Experimental Investigation of Chamber Design and Combustion Process Interaction in a Spark Ignition Engine

H. J. van der Westhuizen

Thesis presented in partial fulfilment of the requirements for
The Degree of Master in Science in Engineering at
Stellenbosch University

Supervisor: Dr. T. M. Harms

Co-Supervisor: Dr. A. B. Taylor

December 2003

DEPARTMENT MECHANICAL ENGINEERING
UNIVERSITY OF STELLENBOSCH

Stellenbosch University http://scholar.sun.ac.za

Declaration

I, the undersigned, hereby declare that the work contained in this thesis is my own original work and that I have not previously in its entirety or in part submitted it at any university for a degree.

Stellenbosch University http://scholar.sun.ac.za

SUMMARY

The automotive industry in South Africa is expanding as a result of pressure on the world economy that forces vehicle manufacturers to outsource work to developing countries. In order to add value to automotive engine development, the capability to perform state-of-the-art engineering must be developed in this country. Three-dimensional fluid flow simulation is one such area and is being developed in this study in order to enhance the ability to develop combustion systems. Another capability being developed at the University of Stellenbosch is the simulation of valve train dynamics.

It was realised that there is a lack of research results of in-cylinder flow characteristics and how they influence combustion chamber processes. This project focuses on the investigation of two different combustion chamber geometries and how they influence the flow and combustion processes in two different combustion chambers. The aim is to gain a better understanding of combustion chamber flow as an indirect result from comparing the flow in two fundamentally different engines under similar operating conditions. The difference in the engines is that one was developed for reduced exhaust gas emissions while the other was developed to achieve high performance. The numerical simulation capability is developed in the process of achieving this goal.

To achieve the above-mentioned aim, a literature study was performed on the different combustion chamber flow characteristics and how they are influenced by different configurations. An experimental method of measuring combustion characteristics is studied in order to establish the ability to perform the latter. Theory of numerical flow simulation is also studied with this same goal in mind. Experimental testing is performed and combustion analysis is done on the results. In conjunction to the experimental work, numerical flow simulations are performed on the two different combustion chambers.

The results from experimental testing and numerical simulations have shown that obstructions in the flow into the combustion chamber, together with a port configuration that cause flow around the longitudinal axis of the cylinder, increases the rate at which fuel burns in the combustion chamber and thereby reduce the production of toxic emissions from the engine. The study also proved that reducing resistance to flow

Stellenbosch University http://scholar.sun.ac.za

increases the amount of air that is breathed by the engine and thereby results in increased torque generation.

Through this study, opportunities for further research are identified. The results of the study can be used when new combustion systems are developed, especially in the light of ongoing tightening of emission regulations. The contribution to numerical flow simulation capabilities developed in this study add value to the ability to develop new combustion systems in the future, especially when complimented by some of the further research topics identified.

Stellenbosch University http://scholar.sun.ac.za

OPSOMMING

Die motorbedryf in Suid-Afrika is besig om vinnig te ontwikkel as direkte gevolg van druk op die wêreldekonomie wat internasionale motorvervaardigers forseer om werk na ontwikkelende lande uit te kontrakteer. Hoogs gesofistikeerde ingenieurstegnieke moet ontwikkel word in Suid-Afrika met die doel om waarde toe te voeg aan enjin ontwikkeling. Drie-dimensionele vloei simulasie is een van hierdie vermoëns en word tydens hierdie studie ontwikkel om die verbrandingstelsel ontwikkelings-vaardighede te bevorder. Nog 'n vaardigheid wat tans ontwikkel word aan die Universiteit van Stellenbosch is die vermoë om nok-en-klepstelsel dinamika te simuleer.

Daar bestaan egter 'n leemte in navorsingsresultate van vloei eienskappe binne in die verbrandingsruim en hoe dit verbrandingsruim prosesse beïnvloed. Die projek fokus dus op 'n ondersoek van twee verskillende geometriese konfigurasies van die verbrandingsruim en hoe dit die vloei- en verbrandingsprosesse in die twee konfigurasies beïnvloed. Die doel is om 'n beter begrip te ontwikkel van verbrandingsruim prosesse as 'n indirekte gevolg van die vergelyking tussen twee fundamenteel verskillende enjins onder eenderse bedryfstoestande. Die verkil tussen die twee enjins is dat een ontwikkel is met die doel op verlaagde uitlaatgas emmissies en die ander ontwikkel is om verbeterde werkverrigting. Die numeriese simulasie vermoë is ontwikkel in die proses om die doel te bereik.

Om bogenoemde doel te bereik is 'n literatuurstudie gedoen wat verskillende vloei-eienskappe in die verbrandingsruim ondersoek, asook hoe dit deur verskillende konfigurasies beïnvloed word. 'n Eksperimentele metode in die bepaling van verbrandingseienskappe is ook bestudeer met die doel om laasgenoemde uit te voer. Teorie aangaande numeriese vloei simulasie is ook bestudeer met bogenoemde doel. Eksperimentele toetse is gedoen en verbrandingsanalise uitgevoer op die resultate. In kombinasie met die eksperimentale werk is numeriese simulasies van die prosesse in die twee verbrandingsruim konfigurasies uitgevoer.

Die resultate van die eksperimentele toetse en numeriese simulasies toon dat obstruksies in die vloei na die verbrandingsruim, gesamentlik met die poort konfigurasie wat veroorsaak dat lug om die longitudinale as van die silinder vloei, die tempo waarteen die

Stellenbosch University http://scholar.sun.ac.za

lug-brandstof mengsel verbrand verhoog en sodoende die vrystelling van skadelike uitlaatgasse na die atmosfeer verminder. Die studie het ook getoon dat die vermindering van weerstand teen vloei, die hoeveelheid lug wat in die verbrandingsruim invloei vermeerder en sodoende die wringkrag wat deur die enjin gelewer word verhoog.

Deur die studie is verdere navorsingsgeleenthede uitgewys. Die resultate van die studie kan gebruik word in die ontwikkeling van nuwe verbrandingstelsels, veral in die lig van verstrengende regulasies rakende uitlaatgas emmissies. Die bydrae tot numeriese vloei simulasie vermoëns ontwikkel in hierdie studie voeg waarde toe tot die vermoë om nuwe verbrandingstelsels te ontwikkel, veral wanneer dit gekomplimenteer word met van die verdere navorsingsonderwerpe wat geïdentifiseer is.

Stellenbosch University http://scholar.sun.ac.za

ACKNOWLEDGEMENTS

I would like to thank the following persons who inspired me to undertake and complete this study:

- My mother and farther Ina and Gert van der Westhuizen for creating a study-friendly environment at home and their financial assistance which made this study possible

- My wife, Mari van der Westhuizen for her patience and encouragement that carried me through

- My promoter, Dr. T.M. Harms, for his guidance and insight that helped me to organise my thoughts in a meaningful manner in order to achieve the objectives

- My co-promoter, Dr A.B. Taylor and Stellenbosch Automotive Engineering for providing me with a work space, intellectual property and experimental testing facilities

- The Stellenbosch Automotive Engineering research group leader, A.J. Bell for sharing his knowledge of combustion systems and assistance in interpretation of experimental results

- Stellenbosch Automotive Engineering engine test technician, Z. Mgogodlo, for his assistance with the experimental work that ensured all the testing could be performed smoothly

- Above all I would like to thank the heavenly Farther who gave me the talent and opportunities to undertake and complete this study

Stellenbosch University http://scholar.sun.ac.za

TABLE OF CONTENTS

Stellenbosch University http://scholar.sun.ac.za

Stellenbosch University http://scholar.sun.ac.za

Stellenbosch University http://scholar.sun.ac.za

Stellenbosch University http://scholar.sun.ac.za

Stellenbosch University http://scholar.sun.ac.za

LIST OF SYMBOLS

Symbols

A	Area	$[m^2]$
B	Cylinder bore	[m]
b	Normalised fuel mass fraction	
COV_{imep}	Coefficient of variance of imep	
C_V	Specific heat at constant volume	[J/(kg·K)]
F	Fuel/air ratio	
H	Total enthalpy	[J/kg]
h_c	Heat transfer coefficient	$[W/(m^2 \cdot ^oC)]$
k	Turbulent kinetic energy	$[m^2/s^2]$
m	Mass	[kg]
$\dot{m}$	Mass flow rate	[kg/s]
N	Engine rotational speed	$[s^{-1}]$
P	Pressure	[Pa]
Q_{ch}	Fuel chemical energy release	[W]
Q_{ht}	Heat transfer	[W]
Q_{HV}	Fuel heating value	[J]
R	Gas constant	[J/(kg·K)]
S	Piston stroke	[m]
S_L	Laminar flame speed	[m/s]
T	Temperature	[K]
t	Time	[s]
U	Internal energy	[J]
u	Velocity	[m/s]
u^+	Non-dimensional velocity near wall	

Stellenbosch University http://scholar.sun.ac.za

V	Cylinder volume	[m^3]
W	Relative gas velocity	[m/s]
X	Source term	
y^+	Non-dimensional distance from wall	
γ	Specific heat ratio	
ε	Turbulence dissipation rate	[$N/(s \cdot m^2)$]
Ξ	Flame wrinkling factor	
η	Efficiency	
θ	Angle	[deg]
μ	Dynamic viscosity coefficient	[$N \cdot s/m^2$]
ν	Kinematic viscosity	[m^2/s]
ρ	Density	[kg/m^3]
τ	Shear stress	[N/m^2]
Φ	Fuel/air equivalence ratio	

Subscripts

0	Reference value
c	Combustion
d	Displacement
f	Firing
f	Fuel
i	Species i
m	Motoring
P	Products
R	Reactants
s	Isentropic
s	Stoichiometric
u	Unburned

Stellenbosch University http://scholar.sun.ac.za

w	Wall

Abbreviations

BDC	Bottom dead centre
BMEP	Brake mean effective pressure
BTDC	Before top dead centre
CAD	Computer aided design
CFD	Computational fluid dynamics
ECU	Engine control unit
ETA	Engine test automation
FEM	Finite element modelling
IC	Internal combustion
IMEP	Indicated mean effective pressure
MAP	Manifold absolute pressure
PMEP	Pumping mean effective pressure
SFC	Specific fuel consumption
TDC	Top dead centre
WOT	Wide open throttle

Stellenbosch University http://scholar.sun.ac.za

LIST OF FIGURES

Stellenbosch University http://scholar.sun.ac.za

Stellenbosch University http://scholar.sun.ac.za

Stellenbosch University http://scholar.sun.ac.za

Stellenbosch University http://scholar.sun.ac.za

Stellenbosch University http://scholar.sun.ac.za

LIST OF TABLES

Stellenbosch University http://scholar.sun.ac.za

1 INTRODUCTION

Flow inside the combustion chamber of an internal combustion engine is complex, three-dimensional, and transient and involves chemical reaction of fuel and air, with heat transfer to the combustion chamber walls. A thorough understanding of combustion chamber flow is necessary when developing an engine combustion system in order to meet continuously tightening emissions regulations and increasing power requirements. Three-dimensional numerical simulations are performed of flow through the combustion chambers of two fundamentally different engines. One of these engines was optimised for reduced emissions and the other for increased power output. The numerical simulation provides graphical information enabling visualisation of the flow field, as well as quantifiable properties that are not easily measured by experimental methods. The difference in combustion properties of the two engines is determined by experimental testing and combustion analysis. The objective of this study is to investigate the effect of combustion chamber geometry on combustion chamber processes by comparison of the two engines. A secondary objective is to develop the capability to perform three-dimensional numerical simulation of combustion chamber processes.

Stellenbosch University http://scholar.sun.ac.za

2 PRELIMINARY WORK

Before commencement of the combustion chamber work, some background of the engine airflow system is provided. The use of one-dimensional fluid flow simulation software and comparison to experimental results on one of the engines under consideration is discussed. The software used for flow simulation is a commercial package developed by Ricardo, namely Ricardo Wave (2000).

2.1 Engine Components

Air flows through a series of components in the engine, all influencing the volumetric efficiency. A general layout of the engine air inducing and exhaust system is shown in Figure 2-1. The system consists of the intake, combustion chamber and exhaust systems.

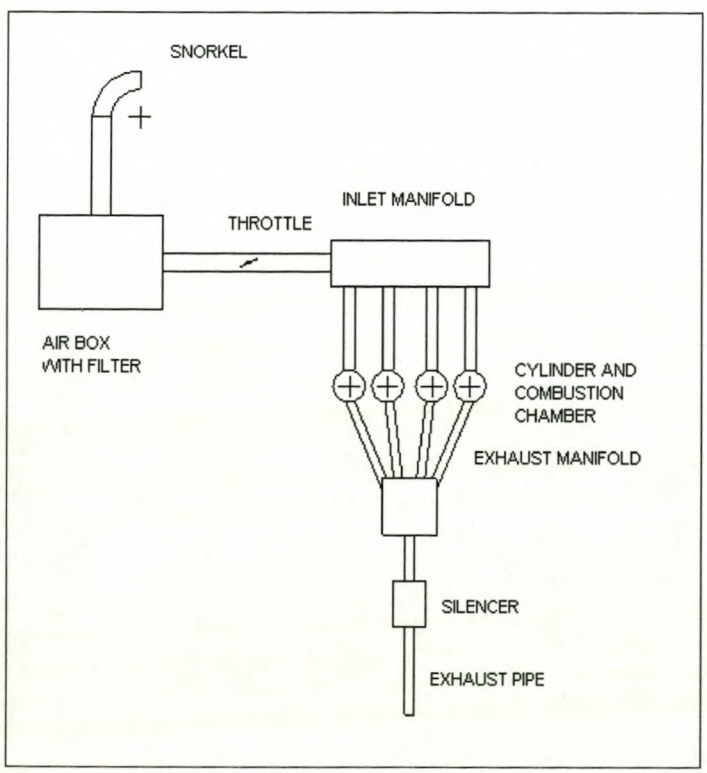

Figure 2-1: Components of airflow system in naturally aspirated engine

Stellenbosch University http://scholar.sun.ac.za

2.2 Intake System

The intake system of an engine collects a controlled amount of air from the atmosphere, removes unwanted material from it and transports it to the combustion chamber. The air must be clean, cool and at a high as possible pressure when entering the combustion chamber. Parts of the intake system are now listed with their functions explained accordingly.

2.2.1 Snorkel

Air flows through the radiator of the car into the under-bonnet area and heats up considerably. The density decrease of air with increasing temperature reduces the mass of air flowing through the engine, thereby causing poor volumetric efficiency. The snorkel must therefore collect air from a cool location and deliver it to the air box with a low as possible pressure drop, also preventing rain or splash water from entering the intake system. All the parts in the breathing system also perform an acoustic function, which is not considered in this project and will generally be neglected henceforward. Possible optimisation would be to lower pressure drop and change the intake position of the snorkel.

2.2.2 Air box

The air box receives air from the snorkel and diffuses it to the air filter. Its function is therefore to spread airflow over the filter area as effectively as possible in order to reduce pressure drop over the filter by making use of the entire filter area. Improvements that decrease pressure drop would require good aerodynamic design implying prevention of turbulent flow, breakaway of the boundary layer and reduction in flow obstructions, i.e. maximising the flow area. Heat transfer from the surrounding air must also be minimised. Figure 2-2 illustrates the effect on engine torque produced by decreasing the pressure drop over the air intake system from the snorkel up to the throttle body.

2.2.3 Air filter

The air filter is a trap to any solid materials induced by the snorkel. It typically consists of porous material, only letting particles smaller than a certain diameter through. To be efficient, the air filter must induce the smallest possible pressure drop on the airflow

Stellenbosch University http://scholar.sun.ac.za

while trapping any material that could shorten engine life or service intervals.

2.2.4 Clean air box

The clean air box receives air from the air filter and serves the inverse function of the air box. The two are usually made up of one box with the two volumes separated by the air filter. A decrease in pressure losses and lower heat transfer would be volumetric efficiency enhancing changes.

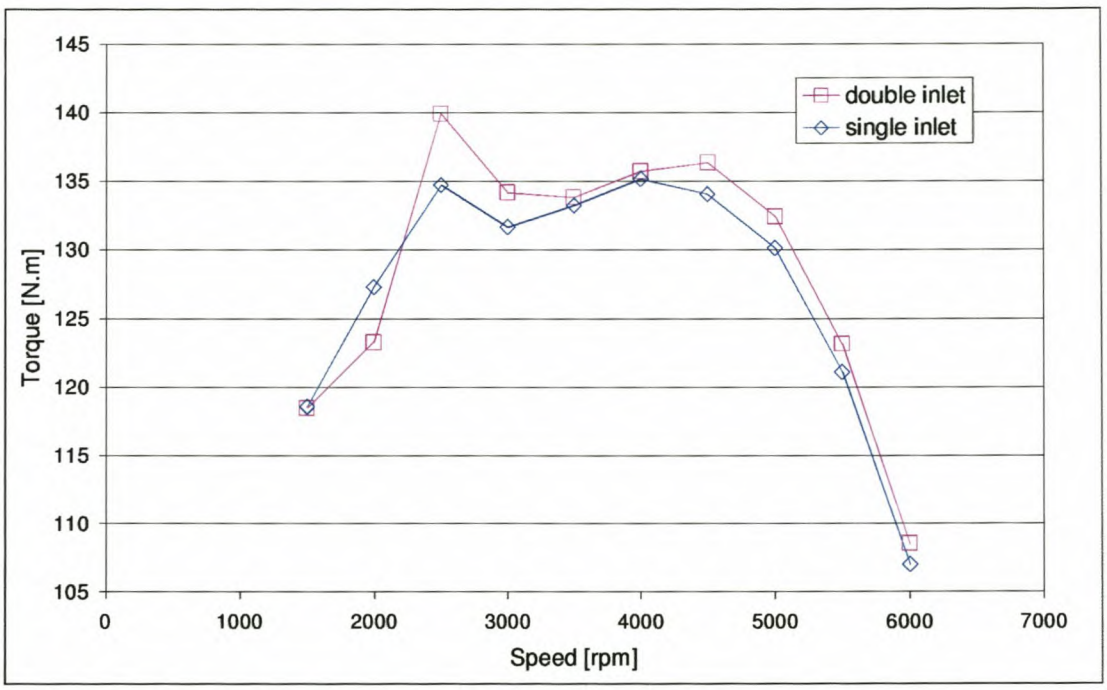

Figure 2-2: Effect of decreasing pressure drop over an air intake system on engine torque produced by doubling the flow area (courtesy of CAE)

2.2.5 Clean air pipe

The clean air pipe connects the air box to the throttle. It is once again mentioned that the heat transfer and pressure loss are major factors in the efficiency of this part. The clean air pipe must be as smooth and straight as possible, reducing pressure loss, and the cross sectional area must be sufficiently large for the required mass flow of air.

Stellenbosch University http://scholar.sun.ac.za

2.2.6 Throttle body

The throttle controls the mass flow of air into the engine by controlling the flow area through it according to the demands of the driver. The conventional way to accomplish this is by using a butterfly valve that rotates around an axis through the centre of a duct. An efficient throttle must incur the lowest possible pressure drop at the wide-open setting.

2.2.7 Intake manifold

The intake manifold hosts fuel injectors and distributes air to each of the four cylinders in the engine. The flow becomes significantly more complex from this point onward. The high-pressure effects in the combustion chamber are transferred to the intake manifold when intake valves open.

Due to the presence of pressure waves in the compressible flow region, pipe lengths play an important role in manifold design. Flow reversal occurs at pipe ends allowing for the possibility of pressure recovery in these regions. The volume of air in the manifold plays a role in the performance and driveability of an engine. A small volume gives quick response while higher volumes result in better ramming of air into the cylinders, increasing volumetric efficiency. The complexity of airflow in the manifold provides numerous optimisation opportunities.

2.2.8 Intake port and valve

The intake port relays the air-fuel mixture to the combustion chamber. It hosts the intake valve. The intake valve controls when and how long air flows into the combustion chamber. Modern engines now makes use of variable valve lift, controlling the amount of airflow into the cylinder, replacing the need for a throttle body.

Flow in the intake port must enhance mixing and evaporation of the fuel in the mixture. The airflow field past the intake valve should be optimised for maximum discharge coefficient versus maximum intake swirl and turbulence.

Stellenbosch University http://scholar.sun.ac.za

2.3 Combustion Chamber

The combustion chamber resembles the core of an IC engine where chemical fuel energy is converted to mechanical pressure energy. The cylinder head and piston crown make up the top and bottom faces of the combustion chamber while the cylinder liner surrounds it.

Air and fuel is induced into the combustion chamber during the intake stroke. During the compression stroke, the air-fuel mixture is compressed and mixed prior to combustion. Heat released from combustion then causes an expansion of the gas, making up the expansion stroke. The burned gas is then exhausted through the exhaust stroke, thereby completing the four-stroke cycle. This process is illustrated in Figure 2-3.

The purpose of combustion chamber design is to accomplish quick and clean fuel burning in a controlled fashion inside the combustion chamber.

2.4 Exhaust System

The exhaust system consists of the exhaust valve, exhaust port and exhaust manifold followed by an arrangement of ducts and junctions, catalytic converter and silencers. The configuration of these items varies for different IC powered vehicles, but Figure 2-1 illustrates a general layout. Exhaust systems influence flow through the exhaust port significantly to impact on engine performance, and also assist in protection of the valves against extreme temperatures. Exhaust systems also play an important acoustic role. These functions are both widely studied and developed in engine optimisation.

Stellenbosch University http://scholar.sun.ac.za

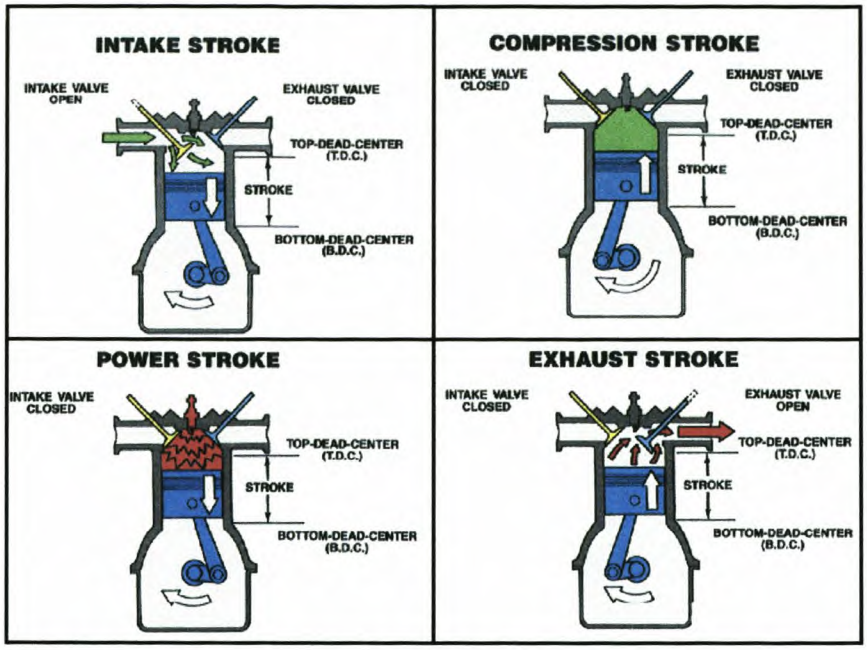

Figure 2-3: Internal combustion engine cycle (http://www.personal.wccnet.org/~eileen/Four_Stroke.html)

2.5 One-Dimensional Engine Simulation

Gas flow through most ducts in the internal combustion engine can be assumed to be one-dimensional and can thus be numerically simulated with a one-dimensional flow simulation. Most sections can be modelled as equivalent round ducts with one-dimensional flow and therefore geometric detail of cross sections is unnecessary. Ricardo Wave (2000) has been designed to perform one-dimensional modelling of this kind and is used here to perform engine simulations. The software makes use of general models to simulate what happens in the more complicated flow areas in and around the combustion chamber. These models were used by CAE to perform some preliminary performance enhancing improvements on a 1.6L litre engine.

A sample of a Ricardo Wave model graphical representation of an internal combustion engine is illustrated in Figure 2-4. The figure illustrates the ducts and junctions used to model the flow path. The top left is the intake system, where in this case a twin-intake was modelled to investigate the influence of reduced pressure drop in the inlet on engine performance.

Stellenbosch University http://scholar.sun.ac.za

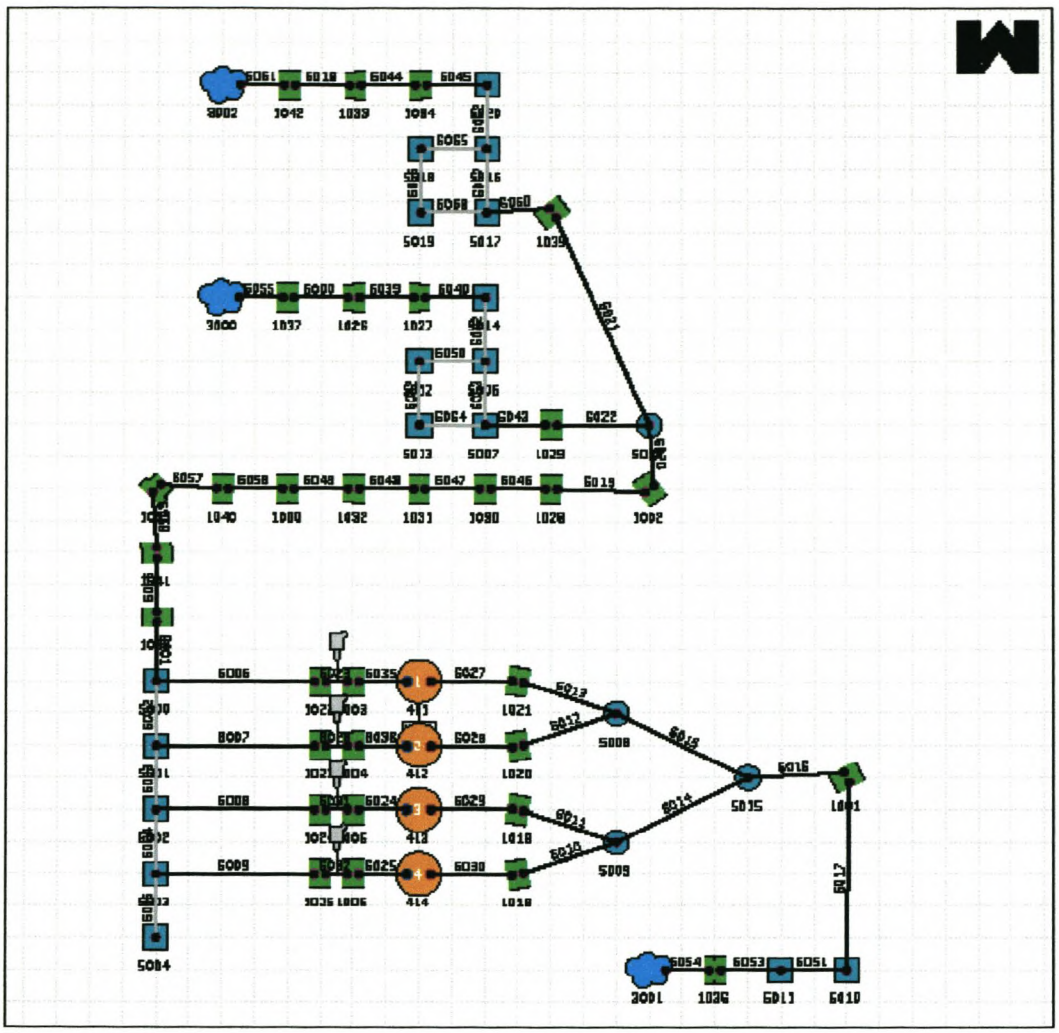

Figure 2-4: Ricardo Wave model of 1.6L litre engine (Courtesy of CAE)

Stellenbosch University http://scholar.sun.ac.za

3 ENGINE AND COMBUSTION THEORY

3.1 Combustion

The speed at which heat is released in the combustion chamber plays a significant role in the efficiency of an IC engine. Faster heat release approaches the ideal Otto cycle and results in higher thermal efficiency. Heat released before TDC increases compression work and heat released after TDC is less efficient due to the expanding volume. The objective is therefore to generate as much heat as possible in as short a time as possible near to TDC. Useful energy available to perform work on the piston surface is the chemical energy of combustion minus the heat transferred to combustion chamber walls minus energy lost through mass transfer. In order to increase the heat release rate, fuel must be burned as fast as possible and the energy contained in the gas by reducing heat transfer to the combustion chamber walls to the minimum.

The combustion process can be characterised by either a mass fraction burned or a chemical energy released curve, both plotted versus crank angle degrees. Figure 3-1 illustrates a cumulative heat released curve, with the burn rate obtained from differentiation of the cumulative heat released curve. The curves describing these processes are both S-shaped, indication of slow heat release rates at the start and end of combustion and fast burning in between. Dividing either curve into regions defined by percentage burned or percentage energy released identifies two stages of the combustion process as illustrated in Figure 3-2.

Stellenbosch University http://scholar.sun.ac.za

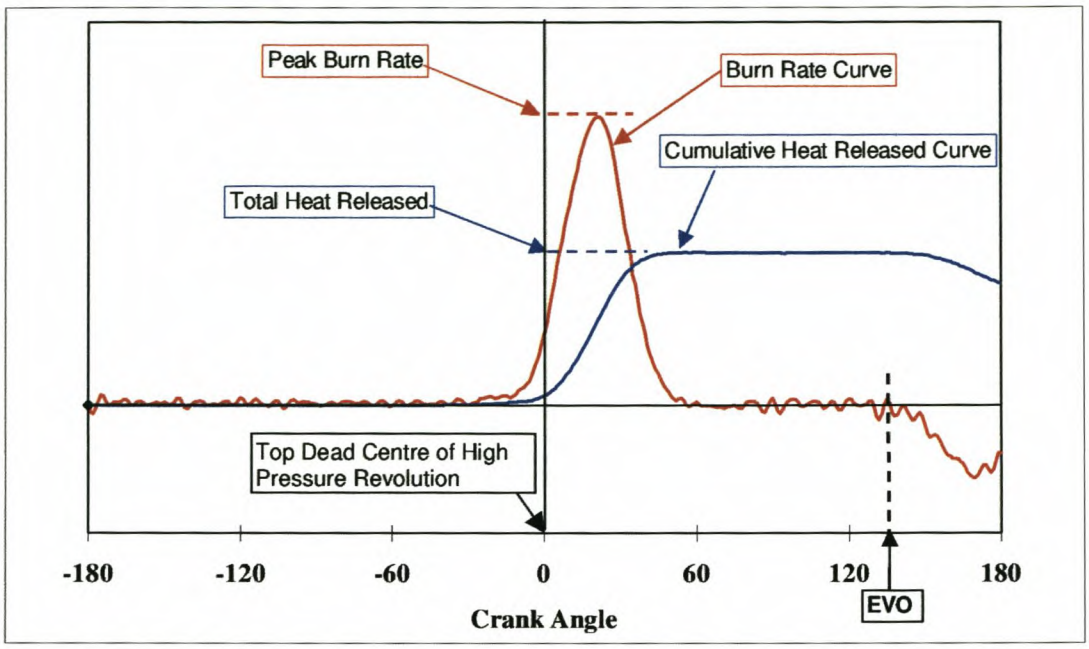

Figure 3-1: Typical burn rate and cumulative heat released curves from combustion analysis of in-cylinder pressure data (Bell, 2003)

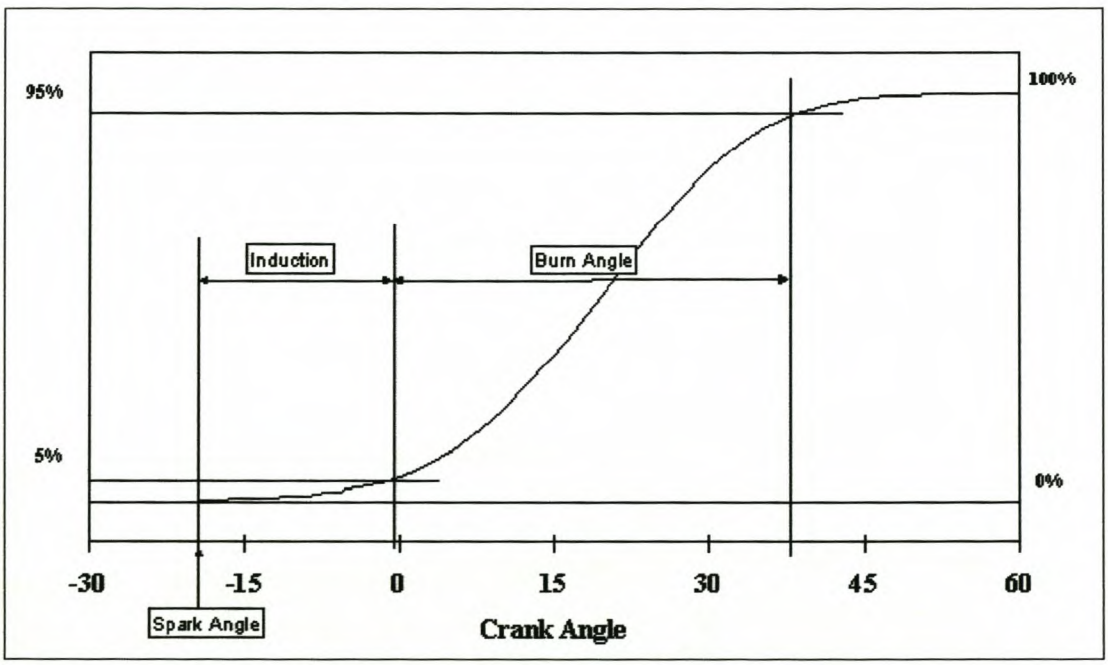

Figure 3-2: Definitions of induction period and burn angle (Bell, 2003)

These regions are called, respectively, the induction period and combustion duration angle. Ferguson (1986) defines induction period as degrees of crank angle between spark and 10% mass fraction burned and combustion duration as degrees from 10% to

Stellenbosch University http://scholar.sun.ac.za

90% burned mass fraction. Similar definitions can be made for 2 to 98% and 5 to 95% mass fraction burned, depending on the specific need. According to Ferguson (1986) the induction period is influenced by both laminar flame speed and turbulence intensity.

Engine speed and volumetric efficiency influence combustion duration quite strongly while spark timing, residual fraction and equivalence ratio also play a role. Turbulence intensity, influenced heavily by combustion chamber geometry, is a dominant factor in induction period and combustion duration (Ferguson, 1986).

3.2 Laminar Flame Speed

The flame propagates in two different modes namely by laminar and turbulent flame spreading. Laminar flame speed is defined as the one-dimensional speed at which a flame propagates into quiescent premixed unburned gas under adiabatic conditions. The laminar flame propagation rate is a function of:

Temperature - Increasing temperature increases laminar flame speed (Heywood, 1988). Higher pre-flame combustion chamber temperature in an IC engine can be achieved by an increase in compression ratio and by exhaust gas re-circulation. The effect of exhaust gas re-circulation is counteracted by the dilution of oxygen and increase in mass of the cylinder charge and should be optimised to achieve optimum flame speed. Increasing the compression ratio is limited by the occurrence of auto-ignition or knock. This is the spontaneous combustion of the mixture under extreme pressure and temperature. NO_x formation is another barrier with strict emission standards already in place. Increased temperature during combustion causes a reaction between oxygen and nitrogen resulting in the emission of hazardous gasses in the form of NO_x.

Pressure: A weak decrease in flame speed occurs with increasing pressure (Ferguson, 1986). Figure 3-3 by Metghalchi and Keck (1982) displays the effect of temperature and pressure on burning velocity.

Type of fuel: Different fuels burn at different speeds according to their chemical properties. Methanol is for instance a faster burning fuel while iso-octane burns slowly.

Stellenbosch University http://scholar.sun.ac.za

Figure 3-4 by Metghalchi and Keck (1982) illustrates the effect of fuel on laminar flame speed.

Equivalence ratio (ER): This is the ratio of the actual fuel to air divided by the stoichiometric fuel to air ratio (Ferguson, 1986). Figure 3-4 illustrates that maximum burning velocity is achieved at an equivalence ratio of about 1.1 and halves at an ER of about 0.8().

Typically for a spark ignition engine the equivalence ratio is optimised for maximum performance at WOT and maximum fuel efficiency at part throttle and the laminar flame speed can be increased only by optimising compression ratio.

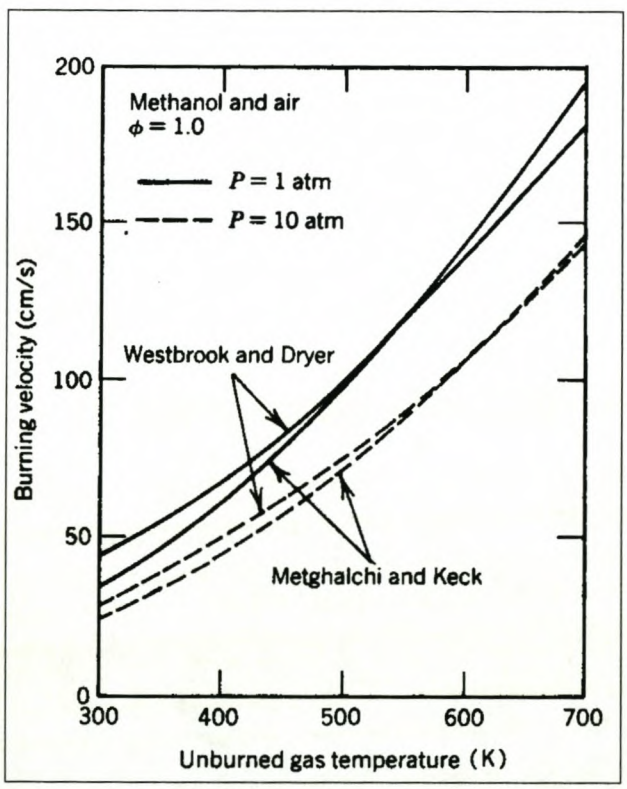

Figure 3-3: Burning velocity as a function of temperature and pressure (Ferguson, 1986)

Stellenbosch University http://scholar.sun.ac.za

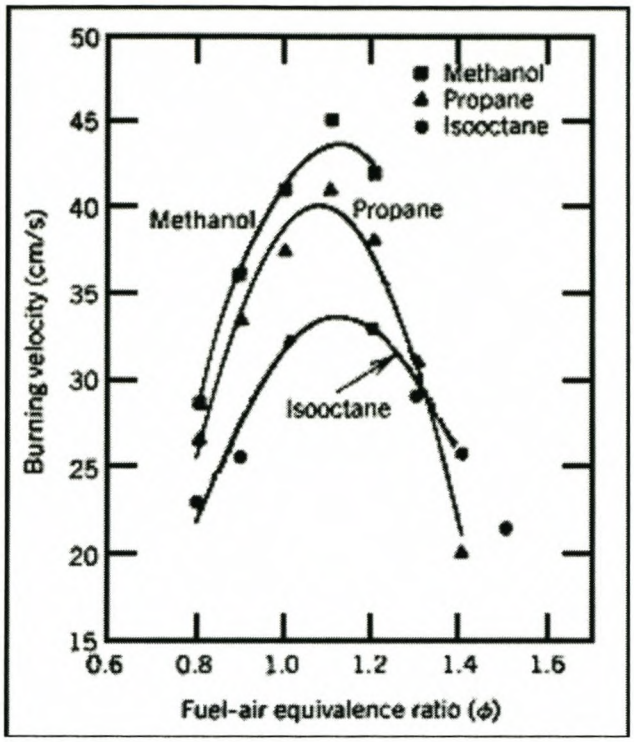

Figure 3-4: Laminar flame speed for different fuel types by Metghalchi and Keck (1982)

Heywood (1988) suggests the following relations for calculating laminar flame speed and the effects of temperature, pressure, equivalence ratio and type of fuel used:

$$S_L = S_{L,0} \cdot \left(\frac{T_u}{T_0}\right)^{\alpha} \cdot \left(\frac{p}{p_0}\right)^{\beta} \tag{3-1}$$

For propane, isooctane and methanol the constants are:

$$\begin{aligned} \alpha &= 2.18 - 0.8 \cdot (\phi - 1) \\ \beta &= -0.16 + 0.22 \cdot (\phi - 1) \\ S_{L,0} &= B_M + B_\phi \cdot (\phi - \phi_M)^2 \end{aligned} \tag{3-2}$$

With ϕ the fuel equivalence ratio and B_m, B_ϕ and ϕ_m fuel properties given by Heywood (1988) as listed in Table 3-1.

Stellenbosch University http://scholar.sun.ac.za

Table 3-1: Parameters for B_m, B_ϕ and ϕ_m for equation 3.2. Reproduced from Heywood (1988)

Fuel	ϕ_m	B_m, cm/s	B_ϕ, cm/s
Methanol	1.11	36.9	-140.5
Propane	1.08	34.2	-138.7
Isooctane	1.13	26.3	-84.7
Gasoline	1.21	30.5	-54.9

3.3 Turbulent Flame Spreading

According to Heywood (1988) the second mode of flame propagation is through movement of air on the edges of turbulent vortices. The rotation of vortices containing the burning gas spreads the flame to neighbouring gasses. An increase in turbulence at the time of combustion will therefore increase flame propagation rate. The increase of turbulence with increasing engine speed causes faster flame propagation. Therefore the burn angle stays almost constant with increasing engine speed. There is a limit to the amount of turbulence that acts favourably as very high turbulence will tend to quench flames and increase heat loss. For production vehicles with relatively low engine speeds and therefore lower turbulence this is usually not a limiting factor (Heywood, 1988).

3.4 Turbulent Gas Motion

Turbulent charge motion in the combustion chamber can be formed by disrupting flow into the cylinder and by squish, breaking large scale tumbling flow into small vortices during compression. When fluid is forced out of the region between the piston surface

Stellenbosch University http://scholar.sun.ac.za

and the cylinder head into the combustion chamber it is termed squish. These small vortices with the flame front on their perimeters lead to fast spreading of the flame front. The tumbling motion can be obtained by directing the valves in order to cause flow to rotate as it enters the combustion chamber during the intake stroke. Due to the decreasing height of the combustion chamber during compression, tumble is broken down into turbulence in this stage.

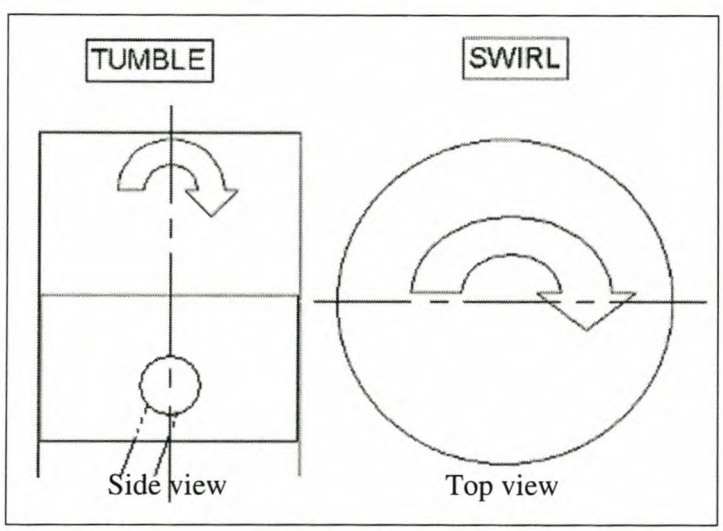

Figure 3-5: Tumble and swirl in the combustion chamber

Another mode of flow in the combustion chamber is swirl. Swirl is the angular motion of air around the longitudinal axis of the cylinder. As the flow area does not change with compression, swirl motion does not break down significantly during compression. Swirl motion, as illustrated in Figure 3-5, mixes air and fuel and is therefore very important in direct injection engines as opposed to indirect injection engines (Ferguson, 1986).

The combustion chamber and intake valve configuration should be designed to provide the maximum turbulence at the right time. The small volume in the combustion chamber at TDC cause quick decay of turbulence and the only way to regain turbulence is by use of the energy of the burning gasses. The air-fuel mixture must therefore be ignited at the moment when turbulence in that region is a maximum in order to benefit

Stellenbosch University http://scholar.sun.ac.za

from maximum turbulence effects and to induce further turbulence. Spark timing and combustion chamber design play major roles in optimisation of turbulence effects in the combustion chamber (Ferguson, 1986).

3.5 Heat Transfer

A typical spark ignition engine looses between 17 and 26% of the chemical energy released by the fuel to the cooling system and between 34 and 45% leaves the cylinder through the exhaust port at maximum power (Heywood, 1988). Spark ignition combustion chambers lose most of the heat through forced convective heat transfer which is a function of temperature difference, heat transfer coefficient and area. Heat transfer can therefore be minimised by looking at each of these factors individually.

Temperature difference and area between the gas and walls influence heat transfer linearly. The ratio of combustion chamber volume to surface area is a measure that should be maximised in order to achieve minimum heat transfer. The temperature difference can be lowered by concentrating hot gas in the centre of the combustion chamber. Figure 3-6 shows the heat flux versus crank angle as measured by Alkidas and Meyers (1986).

Stellenbosch University http://scholar.sun.ac.za

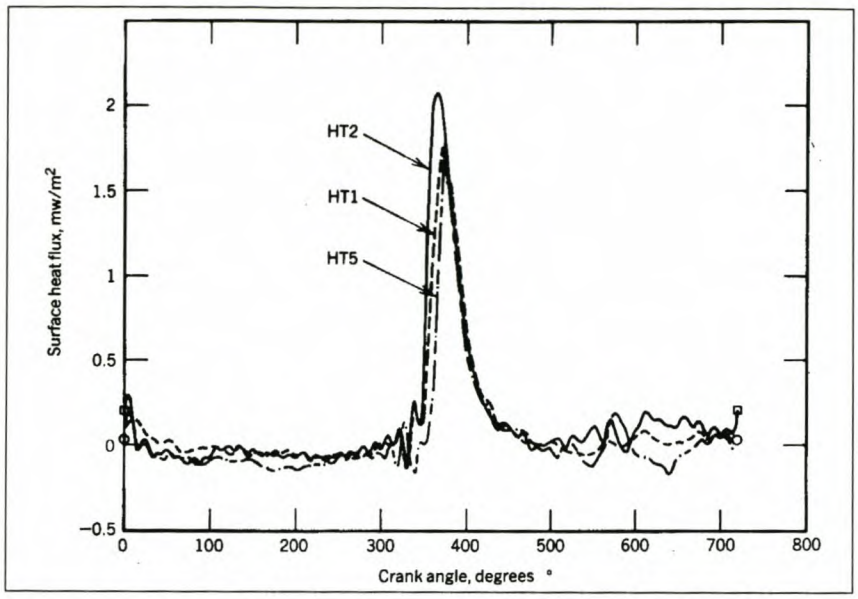

Figure 3-6: Surface heat flux versus Crank angle (Ferguson, 1986)

As expected heat flux reaches a maximum just after TDC when pressure and temperature reaches its maximum level.

3.6 Combustion Chamber and Port Geometry

Poulos and Heywood (1983) studied the effect of combustion chamber geometry and spark plug placement on spark ignition combustion. Their study was on several fundamentally different combustion chamber shapes as illustrated in Figure 3-7. Their study also covered the effect of increasing turbulence as a means of decreasing burn duration.

The rate of heat release is not only a function of laminar flame speed and turbulence in the combustion chamber. The flame front is the area where gas is ignited and heat released. Spark placement and combustion chamber geometry determines the freedom of propagation of the flame front. A spark plug located on the side of the combustion chamber effectively provides half the flame area of a central plug due to the barrier of the sidewall. Heat transfer to the wall will also increase greatly when the gasses near the wall are burned prior to the gas in the centre. A combustion chamber shape with a big volume to surface ratio will lose less heat to the walls than its counterpart. Poulos and

Stellenbosch University http://scholar.sun.ac.za

Heywood (1983) tested the simple combustion chamber geometries shown and compared in Figure 3-7. Poulos and Heywood (1983) found that the chamber geometry had a relatively small effect on thermal efficiency as opposed to turbulence and spark plug placement.

Witze (1982) shows photographs of the effect of swirl and spark placement in a round cylinder (Figure 3-8). The top three rows illustrate the effect of swirl with a side-mounted spark plug. The fourth row illustrates a centrally located spark plug while the bottom row is a twin spark plug set-up.

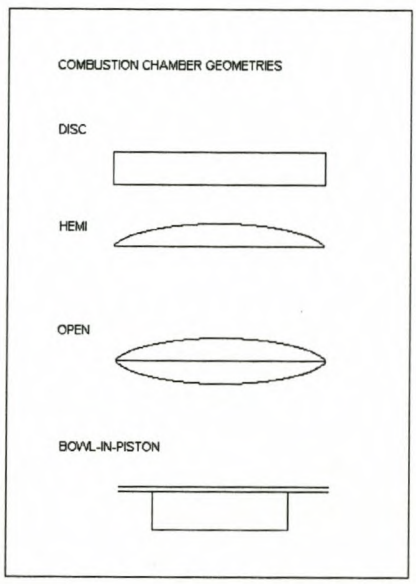

SHAPE: s: side plug, c: centre	BURN ANGLE [ratio]
disc-s	1
disc-c	0.708
hemi-s	0.922
hemi-c	0.715
bowl-s	0.890
bowl-c	0.644
open-s	0.884
open-c	0.639

Figure 3-7: Combustion chamber shapes tested by Poulos and Heywood (1983)

Stellenbosch University http://scholar.sun.ac.za

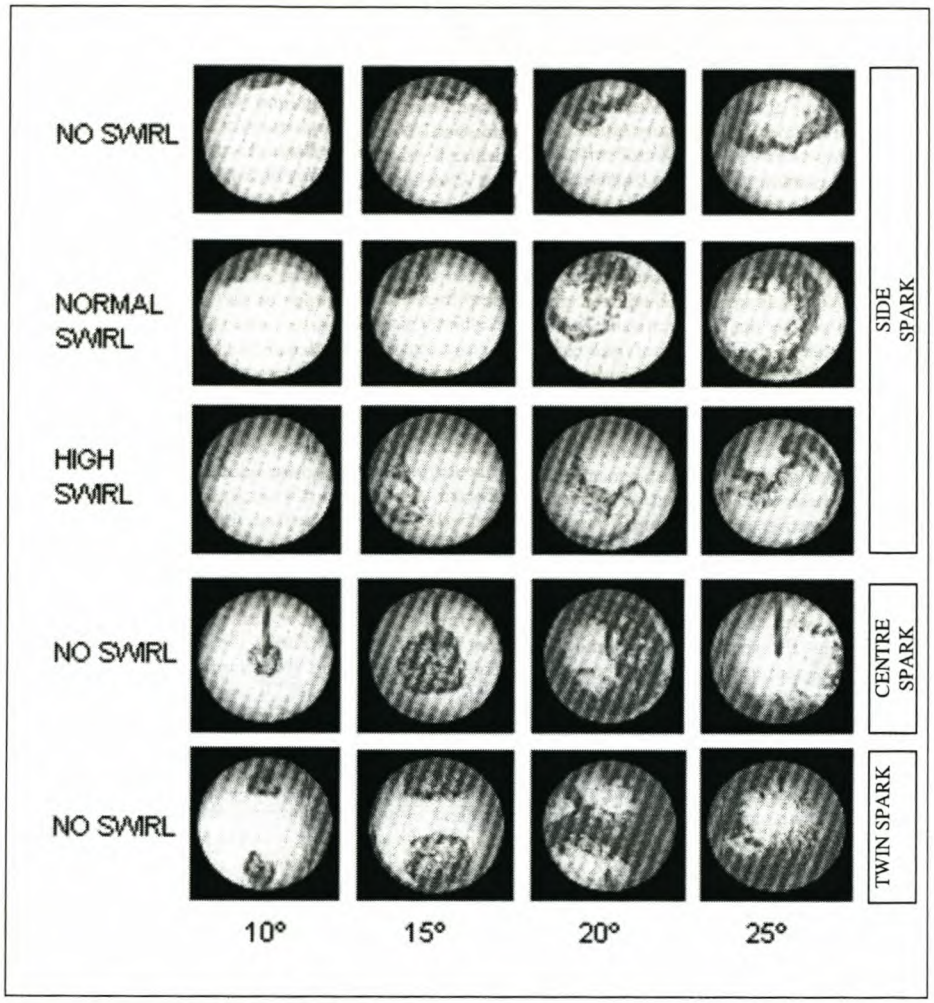

Figure 3-8: Effect of spark plug placement and swirl on combustion (Witze, 1982)

Combustion chamber shape and port geometry also play major roles in the flow properties in the chamber. Intake ports can be shaped to cause high swirl in the chamber, resulting in good mixing and high turbulence that shortens burn angles. Another method of achieving high turbulence levels is by squish. These turbulence enhancing methods do have the negative effect of increasing flow resistance causing more fluid frictional losses while the more vigorous charge motion also increase heat loss to the chamber walls (Poulos and Heywood, 1983).

Poulos and Heywood (1983) found that a significant increase in turbulence intensity is required to match the lower burn duration achieved through spark plug relocation. High turbulence was found to be the most effective in reducing ignition delay, while spark plug location proved most effective on reducing burn angles.

Stellenbosch University http://scholar.sun.ac.za

Wolfe et al. (1999) compared various configurations of the combustion system of an engine on an experimental basis. The database created from these tests was used to increase the number of options available when deciding on a final engine configuration. Three intake ports known for good volumetric efficiency characteristics were designed for comparison. The three ports represent a conventional axial flow model, a moderate swirl model and a moderate tumble model respectively. The port designs are shown in Figure 3-9.

The geometry of the cylinder head can also be used to influence airflow into the cylinder. As in Figure 3-10, a 'nose' between the intake and exhaust port directs the inflow in a circumpherential manner and results in high swirl. Also shown in Figure 3-10 is the 'masking' of the intake and exhaust ports. Masking is the term used to indicate that material is placed around the port, thereby masking it from the rest of the chamber. Tests were done on six different masking configurations, starting with masking of both intake and exhaust ports as the first variant and ending with completely de-masked ports as the sixth variant. Figure 3-10 shows the combustion chamber geometries used. Firstly the intake port was de-masked, then the exhaust port, then the nose reduced after which the intake port was de-masked further and finally all masking removed for the sixth model.

Stellenbosch University http://scholar.sun.ac.za

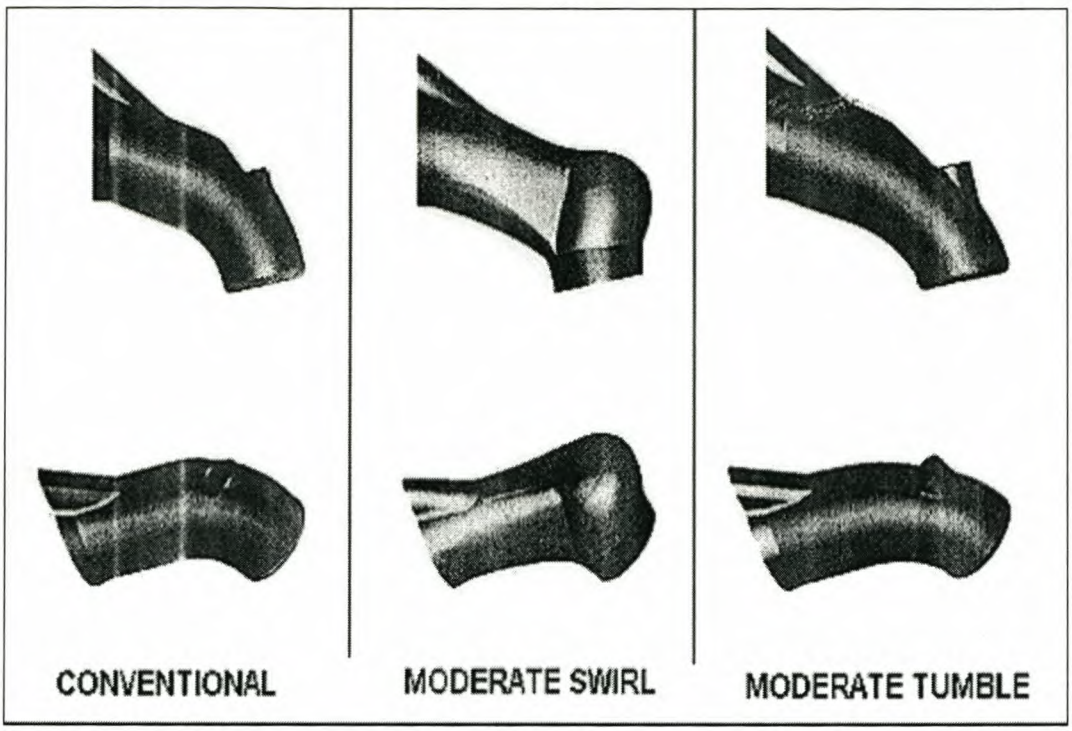

Figure 3-9: Intake port geometries (Wolfe et al. 1999)

Masking of the intake port results in higher charge motion and therefore better combustion, but the lower flow coefficient results in a loss in volumetric efficiency and therefore power. The flow coefficient is a measure of the pressure loss through the port with a known mass flow rate through it. The flow coefficient and swirl for variant 1 is used as a reference and results from other variants are displayed as a percentage of that of variant 1. As expected the flow coefficient increases from variant 1 to variant 6 (see Figure 3-11). Figure 3-12 clearly shows the effect of masking the combustion chamber on swirl and tumble.

The effects of combustion chamber shape on volumetric efficiency, combustion velocity, torque and power is shown in Figure 3-13. Clearly the increase in volumetric efficiency more than overcomes the effect of slower combustion in variant six, which achieve the highest maximum power. Evidently the maximum torque, which is achieved at lower engine speed, is almost constant for all cases showing that the decrease in volumetric efficiency of variant six is compensated for by the faster more efficient combustion of variant one.

Stellenbosch University http://scholar.sun.ac.za

The effect of tumble and swirl due to port design is shown in Figure 3-14. Evidently the decrease in volumetric efficiency due to tumble and swirl ports far exceeds the effect of faster burning, resulting in a reduced maximum power output.

The data collected during these tests prove that combustion chamber geometry and its effect on volumetric efficiency plays a larger role than port configuration in the maximum power of the engine. It must be mentioned that the emissions of the better performing engine are poorer due to the less efficient combustion.

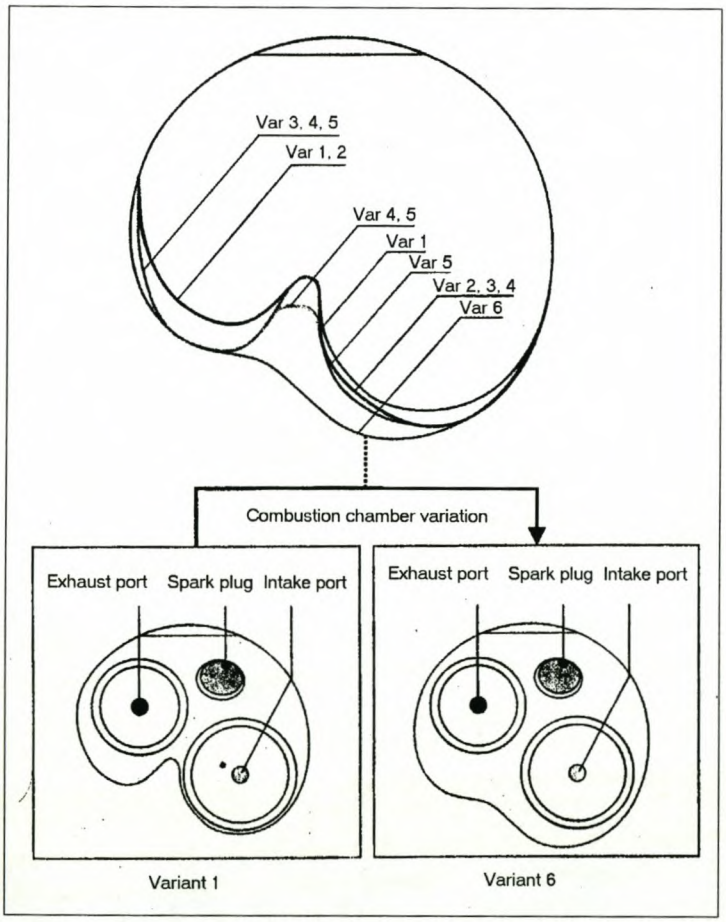

Figure 3-10: Combustion chamber variants. Reproduced from Wolfe et al. (1999)

Stellenbosch University http://scholar.sun.ac.za

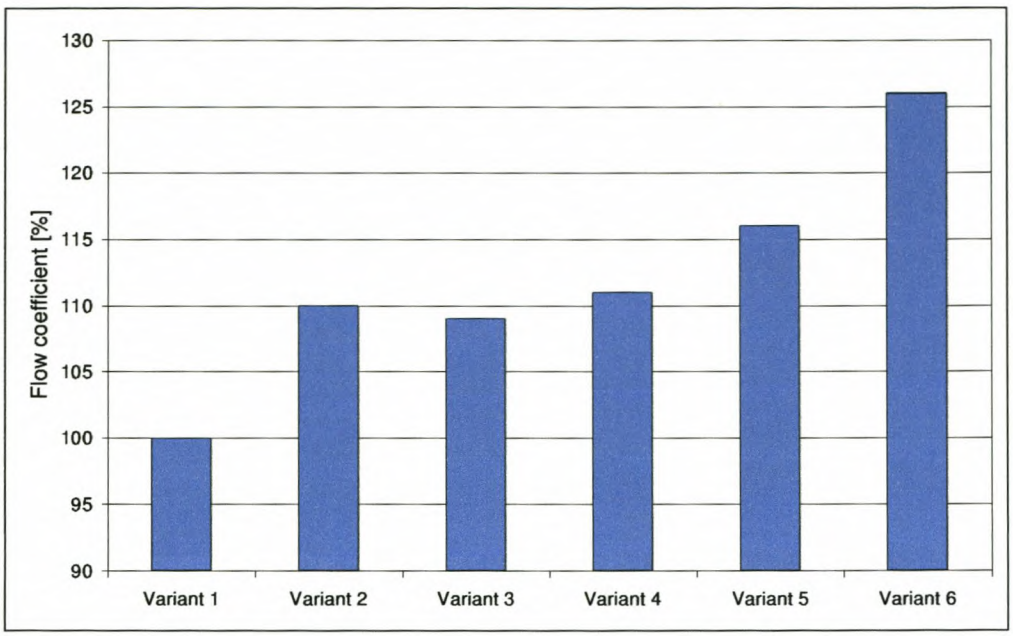

Figure 3-11: Flow coefficient for different combustion chamber shapes with a conventional intake port. Reproduced from Wolfe et al. (1999)

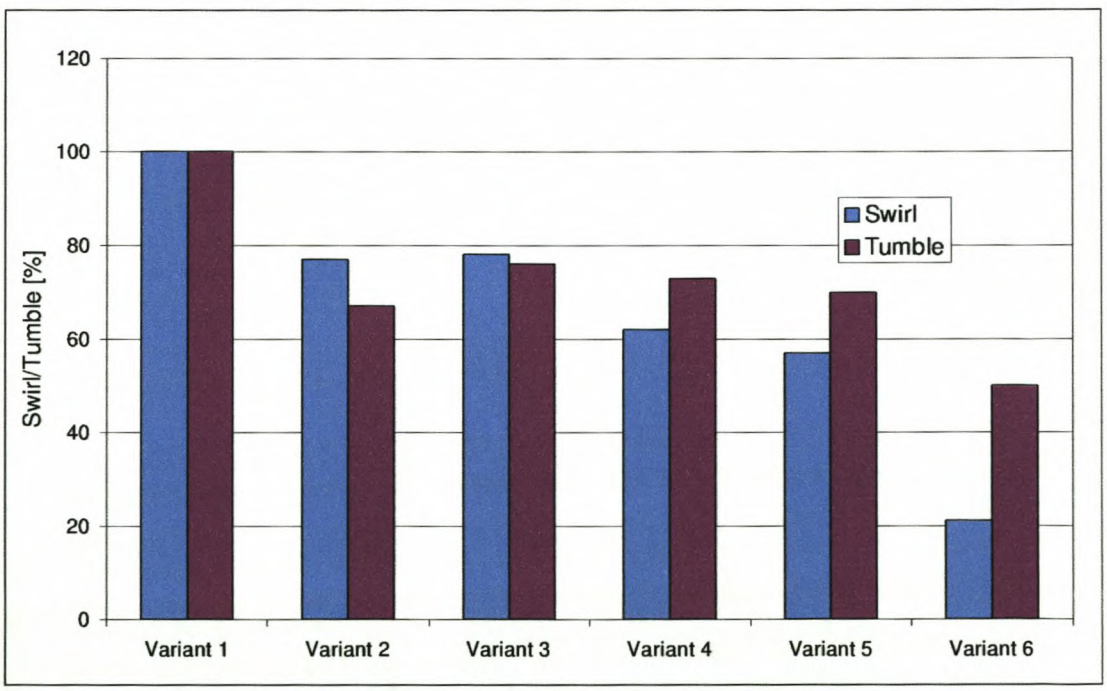

Figure 3-12: Charge motion for different combustion chambers with the conventional intake port. Reproduced from Wolfe et al. (1999)

Stellenbosch University http://scholar.sun.ac.za

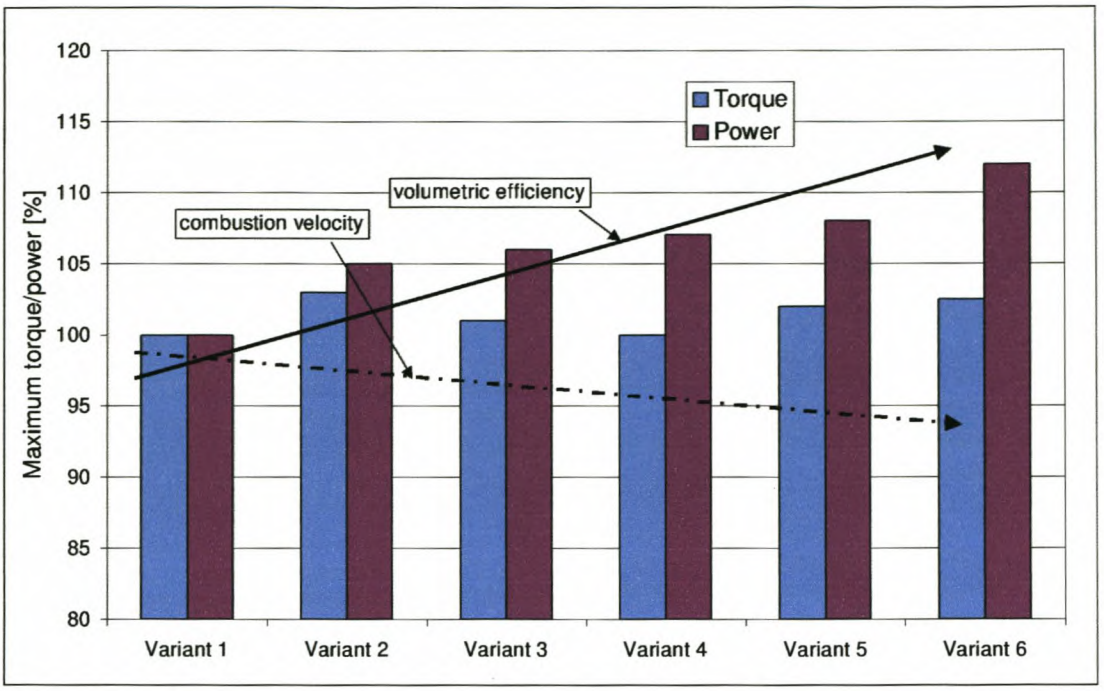

Figure 3-13: Full load data for different combustion chambers. Reproduced from Wolfe et al. (1999)

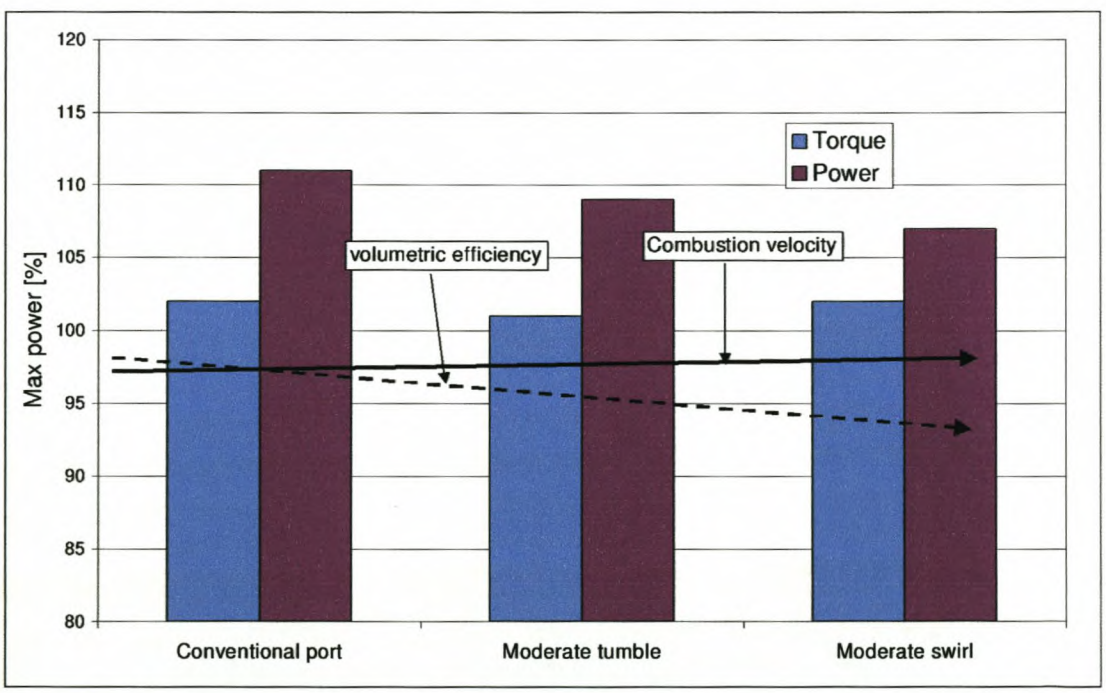

Figure 3-14: Full load data of different intake ports with a fully de-masked combustion chamber. Reproduced from Wolfe et al. (1999)

Stellenbosch University http://scholar.sun.ac.za

3.7 Temperature and Compression Ratio

Compression ratio is the ratio between the entrapped volume in the combustion chamber when the piston is at top dead centre (TDC) and the volume when the piston is at bottom dead centre (BDC). Higher compression ratios result in higher temperatures during the combustion stage as reflected by the ideal gas law, PV=mRT. Higher compression could also increase the charge motion due to higher squish in certain designs.

The effect of compression ratio on performance and efficiency at different engine speeds is illustrated by Roensch (1949) in Figure 3-15. It is evident that the coolant load drops with increasing compression ratio because the increased burning rate results in lower temperatures in the latter part of the expansion stroke thereby reducing the heat loss (Ferguson, 1986). Caris and Nelson (1959) managed to test at compression ratios of up to 20, avoiding knock with the use of specialised fuel and additives. The results are illustrated in Figure 3-16. The effects of increasing the compression ratio cause higher heat transfer and frictional losses that start to overcome the positive effects of short burn rates at very high compression ratio. Ferguson (1986) states that optimum compression ratio ranges from 12 to 18, but spark-ignition engines are usually limited to lower compression ratio due to knock.

Stellenbosch University http://scholar.sun.ac.za

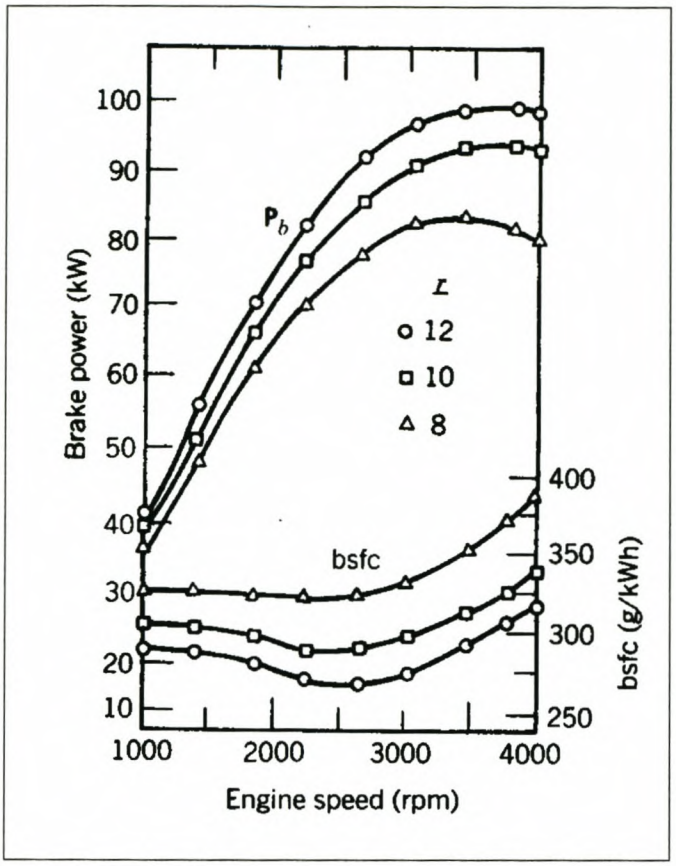

Figure 3-15: Effect of compression ratio on performance and efficiency of a spark ignition engine (Roensch, 1949)

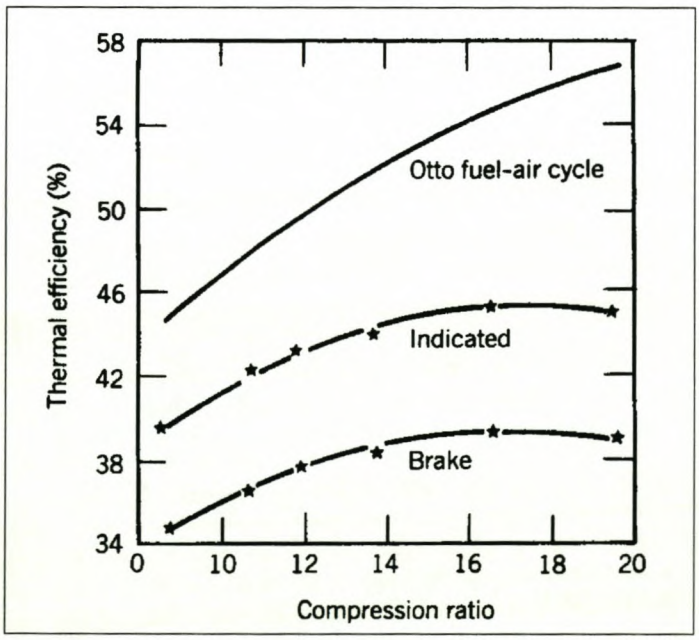

Figure 3-16: Effect of compression ratio on thermal efficiency as determined by Caris and Nelson (1959).

Stellenbosch University http://scholar.sun.ac.za

3.8 Fuel-Air Equivalence Ratio

A stoichiometric fuel-air ratio is defined such that the only products of its combustion would be carbon dioxide and water with no excess oxygen. For iso-octane this reaction is chemically described by:

$$C_8H_{18} + 59.5 \cdot (0.21 \cdot O_2 + 0.79 \cdot N_2) \rightarrow 8 \cdot CO_2 + 9 \cdot H_2O + 47.02 \cdot N_2 \quad (3\text{-}3)$$

The above-mentioned formula does not take into account the effect of nitrogen-oxygen reaction at high temperatures. Fuel-air equivalence ratio (ϕ) is defined as the actual fuel-air ratio divided by the stoichiometric fuel-air ratio:

$$\phi = F / F_s \quad (3\text{-}4)$$

With F the actual fuel-air ratio and F_s the stoichiometric fuel-air ratio given by Ferguson (1986) in Table 3-2 for different fuels.

Another term frequently used by automotive engineers is lambda. Lambda is the inverse of equivalence ratio.

Table 3-2: Stoichiometric fuel-air ratios (Ferguson, 1986)

Fuel	F_s
C_2N_2	0.1894
H_2	0.0293
NH_3	0.1653
CH_4	0.0584
C_3H_8	0.0642
C_8H_{18}	0.0665
$C_{15}H_{32}$	0.0672

Stellenbosch University http://scholar.sun.ac.za

Fuel	F_s
$C_{20}H_{40}$	0.0681
C_2H_2	0.0758
$C_{10}H_8$	0.0777
CH_4O	0.1555
C_2H_6O	0.1118
CH_3NO_2	0.5924

In practice, the exhaust gas of an internal combustion engine contains incomplete combustion products (e.g. CO, H_2, unburned hydrocarbons). Under lean ($\phi<1$) operating conditions the amounts of incomplete combustion products are small. Under fuel-rich ($\phi>1$) conditions these amounts become substantial since there is insufficient oxygen to complete combustion. Combustion efficiency is defined as the fraction of the fuel energy released divided by the fuel energy supplied to the combustion process (Heywood, 1988).

$$\eta_c = \frac{\dot{m}_P \cdot h_R - \dot{m}_P \cdot h_P}{\dot{m}_f \cdot Q_{HV}} \tag{3-5}$$

With h_R and h_P the enthalpy of reactants and products respectively and $\dot{m}$ mass flow rate. Q_{HV} is the heating value of the fuel. These quantities should all be considered at ambient temperature and pressure. Heywood (1988) illustrates the effect of fuel-air equivalence ratio on combustion efficiency in Figure 3-17. According to Heywood (1988), combustion efficiency is usually in the range of 95 to 98% for lean equivalence ratios. For rich mixtures the combustion efficiency steadily decreases as the mixture becomes richer, due to oxygen starvation.

Stellenbosch University http://scholar.sun.ac.za

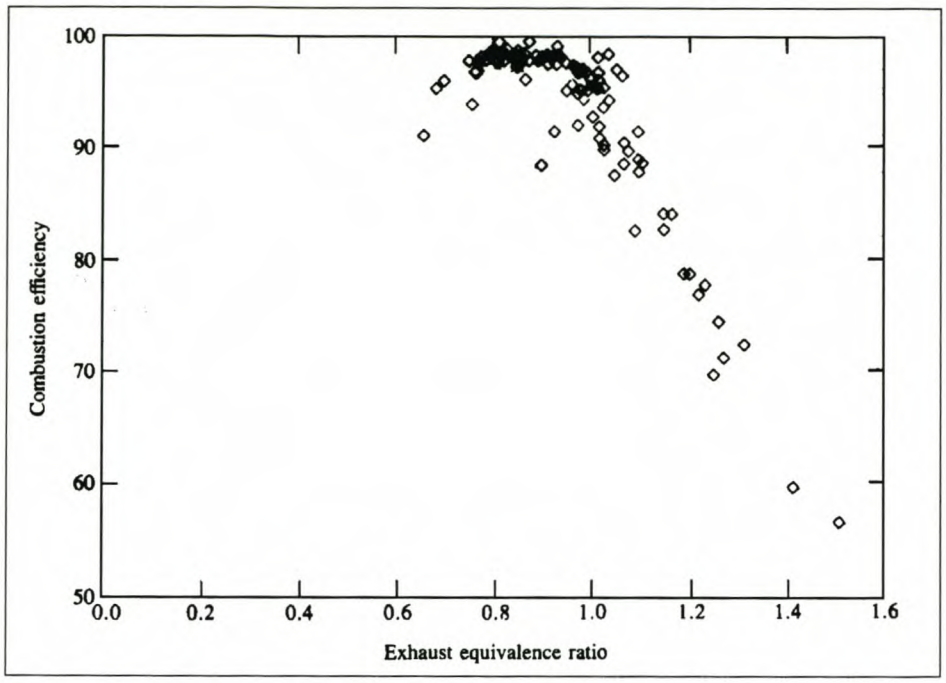

Figure 3-17: Variation of engine combustion efficiency with equivalence ratio (Heywood, 1988)

3.9 Volumetric Efficiency

Volumetric efficiency is a measure of the amount of air that the engine pumps through it versus the capacity of the engine. This is a measure of how well air flows through an engine. An increase in volumetric efficiency will therefore effectively increase the capacity of an engine and thereby increase the amount of torque that can be delivered. Optimising an engine for increased power therefore focuses highly on volumetric efficiency enhancement. Volumetric efficiency can be enhanced in several ways of which a few are listed here.

Optimising pipe lengths involves tuning the lengths of intake and exhaust manifold and exhaust pipes to achieve maximum volumetric efficiency at a given speed. Modern engines employ manifold switching and variable valve timing to increase the band of optimal performance. Volumetric efficiency is also influenced by the shape of the intake port and combustion chamber. Ports that induce swirl and tumble usually compromise volumetric efficiency, but may still be beneficial due to combustion effects.

Stellenbosch University http://scholar.sun.ac.za

3.10 Discussion of Literature Review

This section investigated some of the key factors that play a role in combustion chamber design. It was determined that optimising combustion involves shortening burn angles and decreasing heat loss to the combustion chamber walls. Burn angle can be shortened by increasing turbulent flow during the early stages of combustion, and also by introducing swirl to assist in flame spreading. Tumble is a useful way of achieving high turbulent flow, and therefore reduce induction period. Amongst the methods of minimising heat transfer to the combustion chamber walls is the reduction of the area of the chamber walls, shortening burn angle and therefore extracting more energy from the gasses. Combustion chamber and port geometry affect heat transfer and flow characteristics in the combustion chamber. Increased temperature and compression ratio reduce burn angle, as it tends to increase laminar flame speed. Increased volumetric efficiency usually results in higher power output, but compromises the generation of swirl, tumble and turbulence. This means that an increase in volumetric efficiency is usually accompanied by less efficient combustion.

Stellenbosch University http://scholar.sun.ac.za

4 INTRODUCTION TO COMBUSTION ANALYSIS

The experimental determination of combustion efficiency involves the measurement of the rate of heat release in the combustion chamber. The geometry of the combustion chamber and intake port plays a major role in the properties of flow during the process of combustion. The rate of heat release is strongly dependant on flow properties such as temperature, turbulence, swirl and tumble. The energy release rate can thus be seen as a measure of, amongst other parameters, the flow properties through the port and combustion chamber.

Cylinder pressure measurement is the most practical way of obtaining engine combustion results. Pressure in the combustion chamber is influenced by combustion, changes in the volume of the combustion chamber, heat transfer to chamber walls and mass leakage. The examination of the burning process therefore necessitates the isolation of the effect of combustion from that of volume change, heat transfer and mass loss (Gatowski et al., 1984). Performing the above mentioned is known as "heat release analysis of engine pressure data". The primary output of this type of analysis include burn rate, burn angle and heat transfer rate. These terms are defined in section 4.2. For the purpose of this investigation a simple one-zone heat release model was used. Two zone models can be more accurate as the gas in the combustion chamber is assumed to be either burned or un-burned, and gas properties are calculated independently for each zone. The one zone model is much simpler, faster and easier to configure and is sufficient for this comparative study.

4.1 Thermodynamic Analysis of Combustion Chamber Processes

The thermodynamic model of Gatowski et al. (1984) performs a simple energy balance to separate the effects of fuel-air mixture combustion, combustion chamber volume change due to piston movement, heat transfer to combustion chamber walls and mass transfer into and from crevice volume and blow-by.

Stellenbosch University http://scholar.sun.ac.za

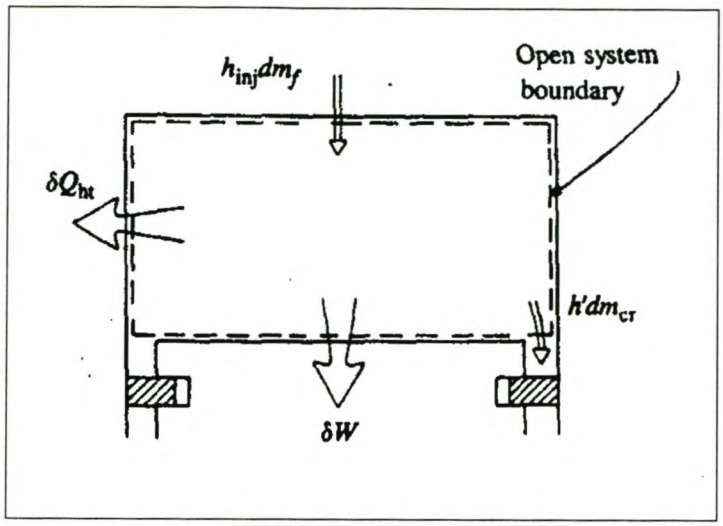

Figure 4-1: Control volume for heat transfer model (Heywood, 1988)

From a First Law energy balance the following conservation equation can be deduced (Gatowski et al., 1984):

$$\delta Q_{ch} = dU_s + \delta W + \sum h_i dm + \delta Q_{ht} \tag{4-1}$$

In this equation:

δQ_{ch} = Chemical energy released by combustion
dU_s = Change in sensible energy of the gas system
δW = Work done on the piston
$\sum h_i dm$ = Enthalpy flux across the system boundary
δQ_{ht} = Heat transfer to the chamber walls

The first two terms on the right of equation 4.1 can be resolved as follows (Gatowski et al., 1984):

$$dU_s = m \cdot c_v(T) \cdot T$$
$$\delta W = p \cdot dV \tag{4-2}$$

Stellenbosch University http://scholar.sun.ac.za

With T calculated from the ideal gas law: $T = \frac{P \cdot V}{m \cdot R}$. It should be noted that although this method of calculating dU is not exact, the mean temperature found from the ideal gas law is close to the mass averaged cylinder temperature since the molecular weights of the reactants and products are nearly identical (Gatowski et al., 1984).

Woschni's (1967) heat transfer model is used to determine instantaneous heat transfer to the combustion chamber walls. The model calculates heat transfer as a function of Reynolds number through the equation:

$$\frac{dQ_{ht}}{dt} = A \cdot h_c \cdot (T - T_w) \tag{4-3}$$

And the heat transfer coefficient is determined as:

$$h_c = 3.26 \cdot c_1 \cdot B^{m-1} \cdot p^m \cdot T^{0.75-1.62 \cdot m} \cdot w^m \tag{4-4}$$

Where:

m = Reynolds number exponent in the heat transfer correlation
A = Heat transfer area
B = Bore
p = Cylinder pressure
T = Mean cylinder charge temperature
T_W = Combustion chamber wall temperature
c_1 = Calibration constant
w = Characteristic charge velocity due to piston movement, swirl and combustion

The characteristic charge velocity by Woshni (1967) is:

Stellenbosch University http://scholar.sun.ac.za

$$w = 2.28 \cdot \left(\overline{s_p} + u_{swirl} \right) + 3.24 \cdot 10^{-3} \cdot c_2 \cdot T_{ivc} \cdot \left(\frac{V_d}{V_{ivc}} \right) \cdot \left(\frac{p_f - p_m}{p_{ivc}} \right) \quad (4\text{-}5)$$

Where

$\overline{s_p}$ = Mean piston speed
u_{swirl} = In - cylinder charge swirl velocity
V_d = Displaced volume
c_2 = Calibration constant
p_f = Firing pressure
p_m = Motoring pressure

And subscripts "ivc" indicates to the conditions at the time when the intake valve closes. The swirl velocity is obtained from the ratio between the equivalent solid body angular velocity of the rotating flow and the crankshaft angular rotation speed as:

$$u_{swirl} = \pi \cdot N \cdot B \cdot R_{swirl} \quad (4\text{-}6)$$

With N the engine rotational speed in rev/sec and R_{SWIRL} the swirl coefficient, a measure of how much swirl is produced in relation to flow into the combustion chamber.

The first term on the right of equation 4.5 is always present and describes the fluid motion induced by the moving piston and is a function of engine speed and geometry. The second term only applies after ignition occurs. This term describes fluid motion induced by combustion.

Mass flow in and out of the system could be through one of the following occurrences:

- Flow in and out of valves during valve-open periods

Stellenbosch University http://scholar.sun.ac.za

- Fuel injection directly into the system

- Flows into and out of the crevice regions including flow past rings

The valve flow will not be considered here as the combustion analysis deals with processes taking place while valves are completely closed. The engines under consideration in this project are of the indirect fuel injection type and will not necessitate consideration of direct fuel injection. Gatowski et al. (1984) developed a crevice volume consideration method. The crevices consist of the region above the top ring between the cylinder and the piston, the region around the spark plug and in the head gasket region. Because is it very difficult to measure the crevice volume it is estimated as a percentage of the clearance volume which, according to Gatowski et al. (1984) usually is in the range of 1 to 2% but depends on the engine geometry and thermal condition. These crevices are modelled as a single volume of gas at the same pressure as the cylinder pressure, but at a different temperature. As heat transfer in these crevices is very high, the crevice gas is assumed to be at the chamber wall temperature. When the chamber pressure is increasing, flow at chamber conditions is considered to be into the crevice volume, and when chamber pressure decreases, flow at crevice conditions is from the crevice volume into the chamber volume.

The final equation for the rate of chemical energy released, taking the above mentioned energy changes into account amounts to (Gatowski et al., 1984):

$$\frac{dQ_{ch}}{d\theta} = \frac{\gamma}{\gamma-1}\cdot p\cdot\frac{dV}{d\theta} + \frac{1}{\gamma-1}\cdot V\cdot\frac{dp}{d\theta} + V_{cr}\cdot\left(\frac{T'}{T_w} + \frac{T}{T_w\cdot(\gamma-1)} + \frac{1}{b\cdot T_w}\cdot\ln\left(\frac{\gamma-1}{\gamma'-1}\right)\right)\cdot\frac{dp}{d\theta} + \frac{dQ_{ht}}{d\theta} \tag{4-7}$$

Where

Stellenbosch University http://scholar.sun.ac.za

Q_{ch} = Combustion energy release
V_{cr} = Crevice volume
T' = Cylinder gas temperature when flow is into the crevice, and combustion chamber wall temperature when flow is out of the crevice
T_w = Wall temperature
γ = Ratio of specific heats for cylinder gas
γ' = Ratio of specific heats for crevice gas
Q_{ht} = Heat transfer to combustion chamber walls
b = Coefficient in the equation for gamma determination

Analysis of combustion chamber processes using the above methodology allows for a number of combustion parameters to be determined, illustrating the advantage in the Gatowski et al. (1984) method. Figure 4-2 illustrate the effects of heat transfer, crevices and combustion inefficiency on a typical set of heat-release analysis data.

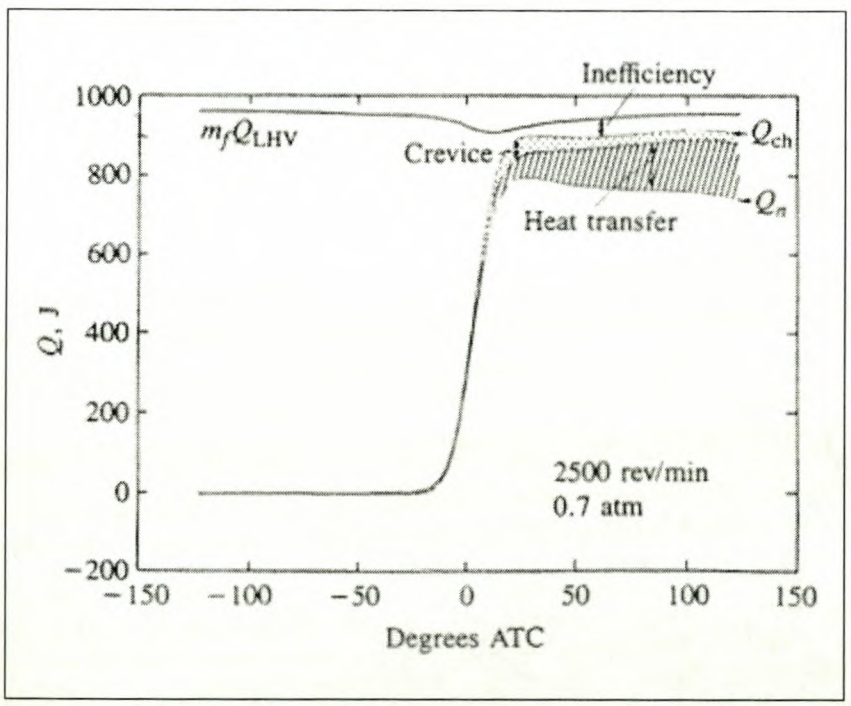

Figure 4-2: Typical influence of different factors on heat transfer model (Heywood, 1988)

Stellenbosch University http://scholar.sun.ac.za

4.2 Combustion Process Characterisation

Figure 4-3 (repeat of Figure 3-1) illustrates graphical results from a typical burn rate calculation. The S-shaped curve is the cumulative heat released while the dome shaped curve is the burn rate.

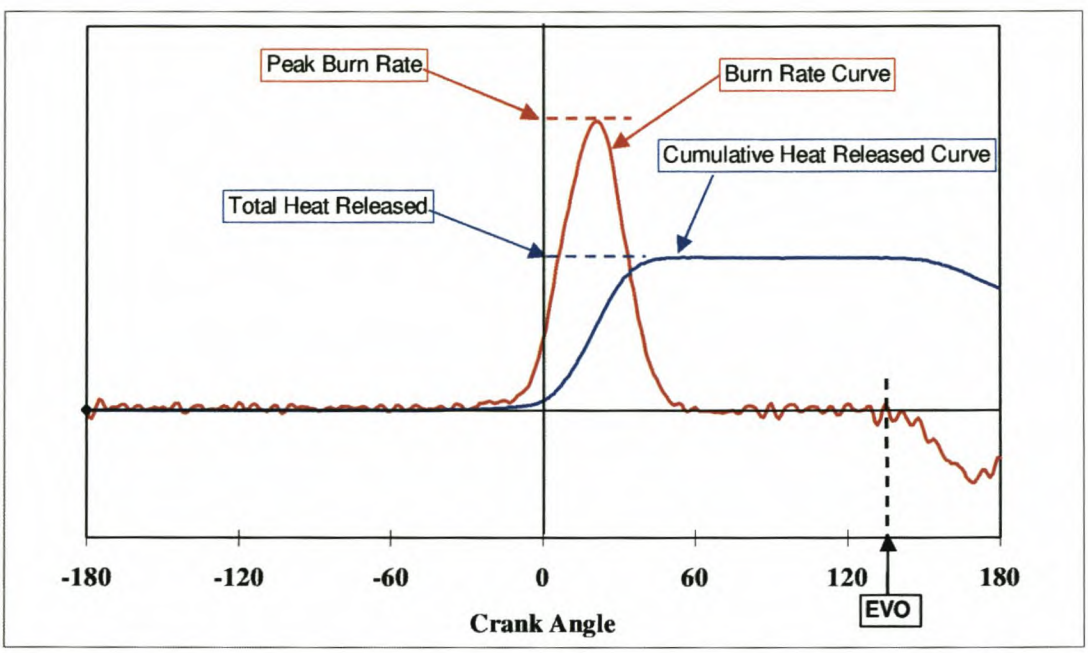

Figure 4-3: Typical burn rate and cumulative heat released curves from combustion analysis of in-cylinder pressure data (Bell, 2003)

The rate at which the fuel-air mixture burns increases from zero just before spark up to a maximum value about halfway through the burn process and then declines to zero when combustion ends. The mass fractions burned through different stages of the combustion process are now used to characterise the combustion data as seen in Figure 3-2 (Heywood, 1988).

4.2.1 Cyclic variability

Cyclic variability is a measure of the stability of combustion and is known as the "roughness" of an engine. One important measure of cyclic variability, derived from pressure data, is the coefficient of variation in indicated mean effective pressure (imep).

Stellenbosch University http://scholar.sun.ac.za

It is the standard deviation in imep divided by the average imep in percentage (Heywood, 1988):

$$COV_{imep} = \frac{\sigma_{imep}}{imep} \cdot 100 \qquad (4\text{-}8)$$

4.2.2 Induction period

The time between spark ignition and when heat release is first detected is not easily definable as the gradient of the heat release rate is very low in the initial stages of combustion. In order to achieve higher repeatability, a point where a specified amount of heat has been released is chosen to determine induction period. Typical definitions include 2, 5 and 10% of total heat released. The induction period is then defined as the crank angle between spark ignition and the angle where the specified percentage of heat has been released.

4.2.3 Maximum heat release rate

The peak value of the rate of heat release curve that is determined from the combustion analysis is the maximum heat release rate.

4.2.4 Burn angle

The burn angle is measured from the crank angle where a certain percentage of the heat of combustion has been released up to the crank angle where 100 minus that percentage of energy has been released, for example the angle between 5 and 95% energy release is known as the 5 to 95% burn angle. Other generally used burn angles are the 2 to 98% and the 10 to 90% burn angles.

4.2.5 Total heat released

The total amount of energy released during combustion is determined by integration of the heat release equation over the period of combustion. The total energy released is the sensible energy at the end of combustion minus the sensible energy at the beginning of combustion plus energy lost through heat and mass transfer.

Stellenbosch University http://scholar.sun.ac.za

4.3 Pressure Measurement

The piezoelectric effect is a property of certain crystals to produce an electrical charge under mechanical loading. The electrical charge produced by these crystals is for all practical reasons linearly related to the mechanical load. With the use of the charge amplifier principle patented by W.P. Kistler in 1950 it became possible to obtain useful pressure measurements from the piezoelectric effect. The piezoelectric crystal produces an electrical charge only when subjected to a change in pressure. The finite electrical impedance of the insulation of the measurement system makes piezoelectric transducers preferentially applicable to dynamic pressure measurement. The vast majority of pressure transducers used to measure cylinder pressures, utilize quartz crystals as the sensing element.

The advantage of piezoelectric transducers over other systems is that, because of the high stiffness and mechanical strength of the transducer element, practically no deformation occurs. Further advantages are (Ruckenbauer, 1999):

- Almost perfect linear and stable behaviour
- Small sensitivity changes with temperature
- High signal to noise ratio

Ruckenbauer (1999) lists four factors that can cause measurement error and must be considered when accurate measurement is required, especially in the determination of indicated mean effective pressure. These are:

- Transducer hysteresis
- Thermal strain
- Phase shifting of the pressure signal due to the finite time required for the gas pressure to reach the diaphragm
- Non-uniform pressure distribution due to high gas velocities

Stellenbosch University http://scholar.sun.ac.za

According to Ruckenbauer (1999) hysteresis of piezoelectric transducers lies below 0.1% and can therefore be neglected. Modern transducers are flush mounted with the combustion chamber i.e. phase shifting is only a problem for transducers with long passages. Together with these long passages occurs resonance of gas inside the passages, causing measurement fluctuations. If the pressure transducer is mounted in the squish gap, where very high gas velocities occur, inaccurate measurements will also be obtained. Spark plug mounted transducers normally have a passage and care must be taken when results are analysed to ensure that a resonant frequency does not occur.

Modern water-cooled pressure transducers are much less susceptible to thermal strain than traditional ones, although their installation is often quite challenging for small spark ignition engines. Another type of pressure transducer that is incorporated into the spark plug is available. These transducers are not water-cooled and are therefore not as accurate as their cooled counterparts. A spark plug mounted pressure transducer is used in this project and thermal strain is investigated in more detail here to achieve a better understanding of its impact on results.

4.3.1 Thermal effects

The rapid temperature change in the combustion chamber causes, through conduction and radiation, a rise in the diaphragm temperature. Thermal expansion of the diaphragm causes it to bow away from the quartz element, relieving the pressure on the element and reducing the magnitude of the pressure signal (Rosseel et al., 1999).

Thermal strain cause a cyclical reduction in the net force exerted on the quartz crystal, resulting in a cyclical error in the measured pressure (Stein et al., 1987). Stein et al. (1987) show the effect of thermal strain on an uncoated transducer vs. that in a coated transducer. Coating the diaphragm of the pressure transducer minimizes thermal strain; therefore the effect of thermal strain is evident in these graphs (Figure 4-4).

Stellenbosch University http://scholar.sun.ac.za

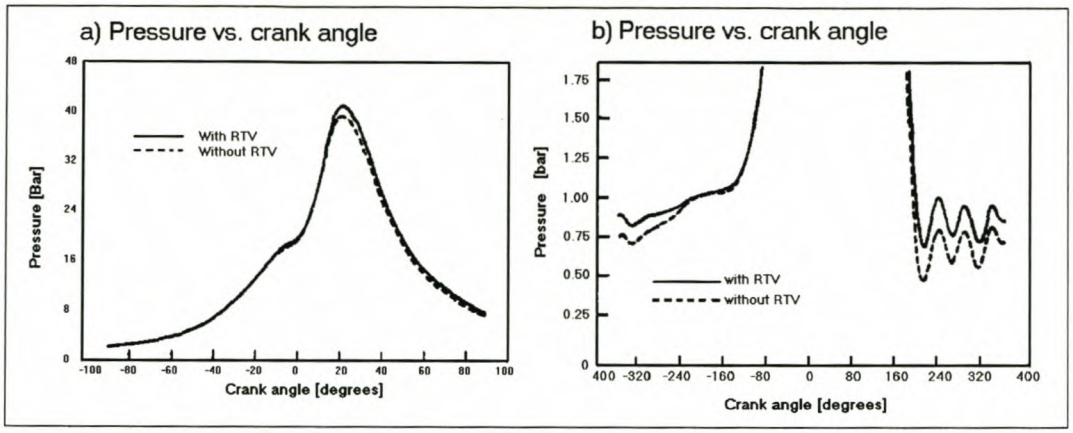

Figure 4-4: Comparison between coated and uncoated pressure transducer measurements. Reproduced from Stein, et al. (1987)

Figure 4-4a is an overlay of the measurements between the coated and uncoated transducers during the compression, combustion and expansion phases. Figure 4-4b is the same plot, focussed on the intake and exhaust phases.

Figure 4-5 is a plot of the difference between the measurements of the coated and the uncoated transducers over the entire cycle.

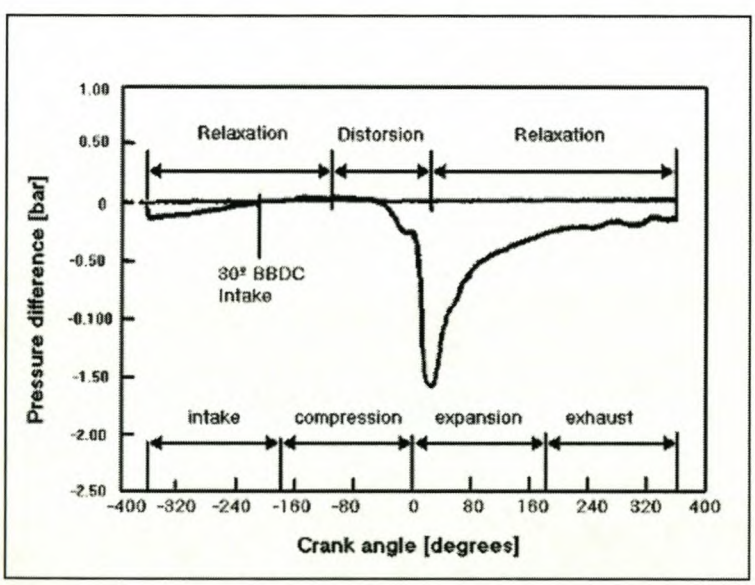

Figure 4-5: Difference between coated and uncoated pressure measurements during different stages of the engine cycle. Reproduced from Stein, et al. (1987)

Stellenbosch University http://scholar.sun.ac.za

It is apparent from the graphs of Stein et al. (1987), that the diaphragm is heated during compression and combustion, causing the measured pressure to decrease with respect to the actual pressure. This phase is called distortion. During expansion, exhaust, intake and the first part of compression the diaphragm is cooled and the measured pressure increases relatively to the actual pressure. This is called relaxation of the diaphragm.

Stein et al. (1987) also show the effect of thermal strain on the measured indicated mean effective pressure (imep) and pumping mean effective pressure (pmep) for the same set of data (Figure 4-6).

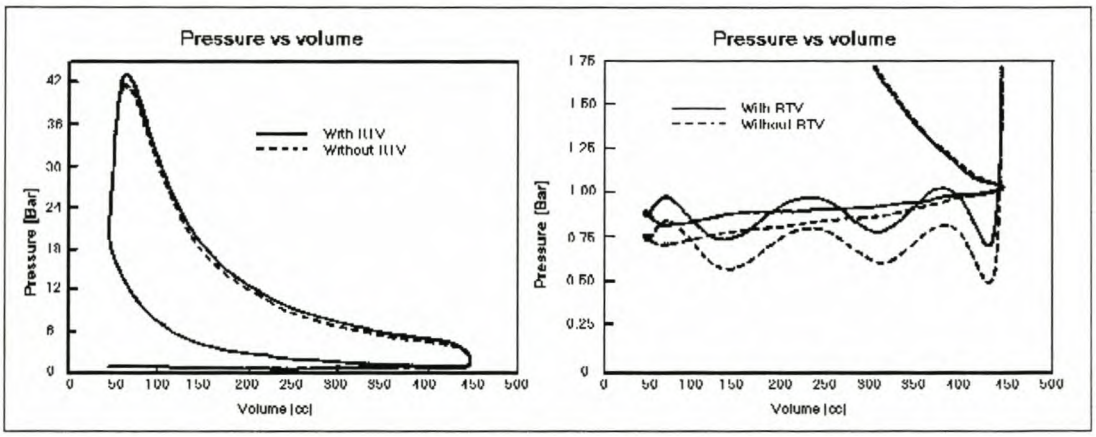

Figure 4-6: Comparison between coated and uncoated pressure vs. volume data illustrating the effect of thermal strain on measurements. Reproduced from Stein, et al. (1987)

The decrease in measured pressure caused by distortion in the compression and expansion stages results in a decrease in the value of imep due to thermal strain. The effect of distortion is still very much apparent during the exhaust stroke, thereby decreasing the apparent pumping work during exhaust, but due to relaxation of the diaphragm, the effect of thermal strain during the intake loop is not as severe, causing the intake stroke work to be more representative of the actual values. As pumping work is caused by the difference in the intake and exhaust integrated pressures, the effect of decreasing the exhaust work with a minimal effect on intake work, causes a reduction in the measured pumping work done by the engine. Rai et al. (1999) developed a numerical method for reducing the imep errors due to thermal strain. They performed

Stellenbosch University http://scholar.sun.ac.za

tests on various different types of transducers, with sensitivity to thermal strain defined by the difference in maximum observed pressure between the tested transducer and a reference transducer. The reference transducer is one that is known to have high resistance to thermal strain. Rai et al. (1999) determined that the main influencing parameters on thermal strain were transducer sensitivity, maximum cycle pressure and engine speed. The correction for imep was determined to be:

$$IMEP_{corr} = IMEP_{meas} + \left(C \cdot F \cdot P_{\max}\right) + 0.016 \cdot C \cdot \left(\frac{rpm}{1000}\right) \tag{4-9}$$

With:

$$F = 0.000133 \cdot \left(\frac{rpm}{1000}\right)^2 - 0.002 \cdot \left(\frac{rpm}{1000}\right) + 0.0105$$

And:

$$C = -1 \cdot \Delta P_{\max}(\%)$$

With $\Delta P_{\max}(\%)$ the sensitivity of the transducer defined as the difference between the maximum measured pressure by the transducer and the maximum measured pressure of the reference transducer as a percentage of the maximum pressure. Unfortunately, the correlation was not extended to the pumping loop i.e. this correction is only applicable to gross imep.

According to Stein et al. (1987), thermal strain of the transducer diaphragm during combustion, cause a decrease in measured pressure vs. actual pressure and hence also a decrease in the measured pressure rise due to combustion. By the method of Rassweiler (1938), burn angle is determined from the point of a percentage of fuel burned to another percentage of fuel burned, for example from 5 to 95% fuel burned. As thermal strain

Stellenbosch University http://scholar.sun.ac.za

will reduce the overall pressure increase due to combustion, normalizing any error in the estimation, the calculated burn rate does not differ significantly with the actual burn rate due to thermal strain. This is evident from Table 4-1 by Stein et al. (1987).

Table 4-1: Comparison of parameters calculated from cylinder pressure acquired from firing data with and without thermal coating (Stein, et al.1987)

TABLE 1 - COMPARISON OF PARAMETERS CALCULATED FROM CYLINDER PRESSURE FOR FIRING DATA ACQUIRED WITH AND WITHOUT A COATING OF RTV

1500 RPM WOT

	Gamma		Peak Pressure	IMEP	PMEP	Burn Times (°CA)		
	Comp.	Exp.	(Bar)	(Bar)	(Bar)	0-10%	10-90%	0-90%
With RTV	1.33	1.31	41.5	10.45	0.03	14	21	35
Without RTV	1.32	1.34	40.0	9.77	0.14	14	22	36
Difference			-1.5	-.68	+0.11	0	+1	+1

1500 RPM 2.6 BAR BMEP

	Gamma		Peak Pressure	IMEP	PMEP	Burn Times (°CA)		
	Comp.	Exp.	(Bar)	(Bar)	(Bar)	0-10%	10-90%	0-90%
With RTV	1.33	1.34	22.5	4.12	-0.51	22	27	49
Without RTV	1.29	1.38	22.0	3.77	-0.44	22	26	48
Difference			-0.5	-.35	+0.07	0	-1	-1

Motored data is engine data measured when the engine is motored i.e. no combustion takes place. Fired data is data measured with combustion taking place. Thermal strain can be detected by comparison of fired and motored data as the lower temperature in the motored cycle does not cause thermal strain effects of the same order as with the fired data. Stein et al. (1987) show the effect of thermal strain on the pressure vs. volume graph.

Figure 4-7 indicates the comparison between motored and fired data for a thermally coated (Figure 4-7a) and an uncoated pressure transducer (Figure 4-7b). The most obvious distinction is the slope of the exhaust phase that differs from that of the motored data when thermal strain occurs.

Stellenbosch University http://scholar.sun.ac.za

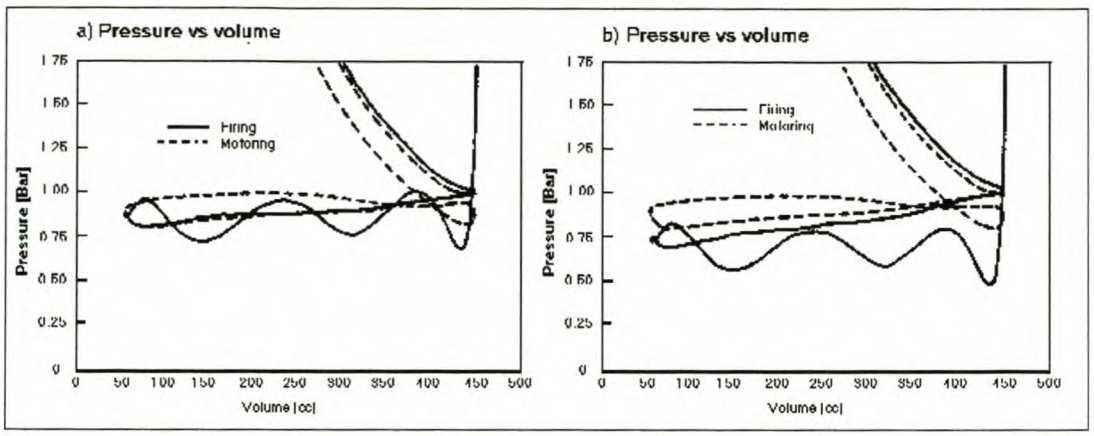

Figure 4-7: Comparison between motored and fired data for a (a) coated and a (b) uncoated transducer during the pumping loop. Reproduced from Stein et al. (1987)

4.3.2 Pressure referencing

In applications such as the measurement of engine cylinder pressure, pressure is measured over an extended time period and as the piezoelectric transducer only measures dynamic pressure differences, absolute pressures cannot be measured. Therefore, for each cycle, the pressure data is shifted so that the pressure at a certain reference point is equal to a known quantity. The pressure at or just before bottom dead centre is usually estimated to be the same as the manifold pressure and is regularly used as reference point, depending on preference.

The point of 30 deg before BDC was chosen as pressure data proved to be very constant in this region of the cycle, whereas large variation in pressure at the reference angle would cause inaccurate referencing. This point is also a point where the intake valves are still very close to fully open with the piston starting to slow down, i.e. the air is not accelerating and pressure drop across the port and valves is minimal.

4.3.3 Drift

When a constant pressure is applied to the quartz crystals and the output of the charge amplifier drifts rapidly, it is a sign of charge leakage in the system. The leakage can be either due to dirty connectors or faulty insulators, but is also influenced by the finite impedance of the charge amplifier. The time constant of leakage is influenced by the charge amplifier time constant. Increasing the charge-amp time constant can cause problems with signal drift (Lancaster, 1975). Lancaster (1975) recommends a charge

Stellenbosch University http://scholar.sun.ac.za

amplifier time constant of ≥ 1s for accurate engine pressure measurement.

4.4 Cycle Averaging

The variance in combustion in the IC engine cause high cycle-to-cycle variation in cylinder pressure data. By averaging cylinder pressure over large samples, a more repeatable result is obtained from combustion analysis. This is clear from the study by Lancaster (1975) showing how variance in combustion results decrease with the sample size (Figure 4-8).

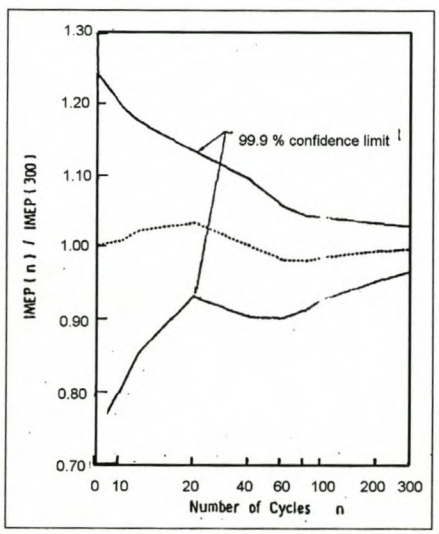

Figure 4-8: Normalised averaged imep vs. number of cycles for an unstable case

Lancaster (1975) determined that on an unstable engine, accurate results could be obtained by a sample size of 300 cycles while a stable engine only necessitates about 40 cycles for a 99.9% confidence limit. After cycle averaging the data, a Kaiser smoother is applied to achieve a more numerically stable result. The Kaiser smoother weightings were determined by the developers of Racer (Moran, 1997).

Stellenbosch University http://scholar.sun.ac.za

5 INTRODUCTION TO FLOW PROCESS MODELLING

Although analytical solutions for a wide variety of flow problems are available, no general solution is available for fluid flow problems. One way of obtaining a solution for complex flow problems is by discretising the flow domain into finite volumes or cells, and applying the basic fluid flow equations to each cell. The interfaces between cells are used to communicate properties, thereby relating the fluid flow equations of each cell to every other cell. The result is a number of simultaneous fluid flow governing equations that can be solved by iterative methods. The solution of fluid flow problems by the above mentioned method is referred to as computational fluid dynamics (CFD) by finite volume discretisation.

Flow process modelling involves definition of geometry, fluid property functions, flow properties and boundary conditions specification followed by discretisation and simultaneous solution of the governing equations. Geometry definition, fluid property functions, flow properties and boundary conditions are briefly discussed in the following sections in order to create some appreciation of the modelling task required. These are not comprehensive discussions as each could be the topic of a study on its own.

5.1 Geometry Definition and Finite Volume Discretisation

The physical geometry of the flow domain i.e. its size and shape is defined by its physical surfaces and is created either by the pre-processor of a commercial CFD package or, in the case of complex geometry, by the use of a computer aided design (CAD) package. When using the finite volume approach, the geometry should then be discretised into a number of finite volume cells to represent the flow domain. The collection of finite volume cells that describe the flow domain is called the computational mesh. Two properties of a mesh namely mesh density and mesh distortion are important and influence the accuracy, stability and computational cost of the solution to the flow problem.

Mesh density refers to the number of cells used to describe the physical geometry. The density of the mesh is primarily determined by accuracy and computational cost

Stellenbosch University http://scholar.sun.ac.za

considerations. A high density mesh (small cell size) usually produces better accuracy than a low density (large cell size) mesh, but at the cost of more computational time.

Mesh distortion is measured in terms of aspect ratio, internal angle and warp angle as shown in Figure 5-1 (StarCD user guide, 2002).

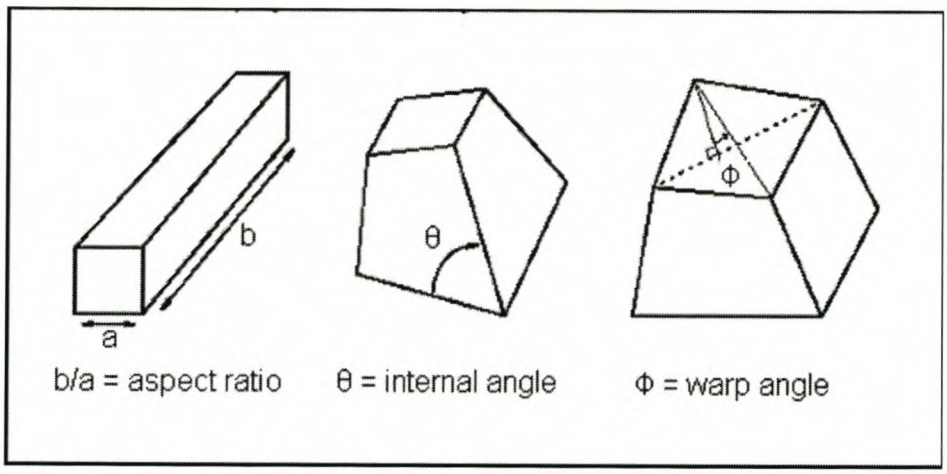

Figure 5-1: Cell distortion modes (StarCD user guide, 2002)

The user guide gives the following guidelines for limits:

- Aspect ratio: 0.1 to 10
- Internal angle: 45° to 135°
- Warp angle: -45° to 45°

These different mesh distortion modes also have a combined effect i.e. if all three of them are present in a single cell then the above mentioned limits may not be stringent enough. In regions where flow is complex, these parameters should also be kept to a minimum. The term complex flow refers to flow in regions with amongst others high pressure and velocity gradients, high temperature gradients, high concentration gradients, etc.

Stellenbosch University http://scholar.sun.ac.za

According to the StarCD user guide the numerical discretisation errors are functions of the mesh density and time step size. As high mesh densities needs high amount of storage and computational cost, the mesh should only be dense in regions where this is needed i.e. in regions with complex flow.

Both these factors play a significant role on computational cost (StarCD user guide, 2002). The main aim in the finite volume discretisation should therefore be to employ the minimum number of cells with the most undistorted (square) shape.

5.1.1 Parametric and arbitrary geometry

The simplest type of geometry is a region bounded by simple surfaces such as flat or cylindrical surfaces (see Figure 5-2). These shapes are called parametric shapes as their edges can be described by simple mathematical equations. Modern finite volume discretisation or meshing tools are very powerful and can usually perform meshing of such shapes, allowing the user to control mesh properties with very little effort. These properties include the number and distribution of cells along the edge of a surface.

Arbitrary geometry refers to geometry with edges that are not easily described by mathematical equations. It is more difficult to perform finite volume discretisation on this type of geometry than for parametric shapes. Figure 5-3 illustrates an example of an arbitrary shape. This shape necessitates more advanced meshing techniques.

Stellenbosch University http://scholar.sun.ac.za

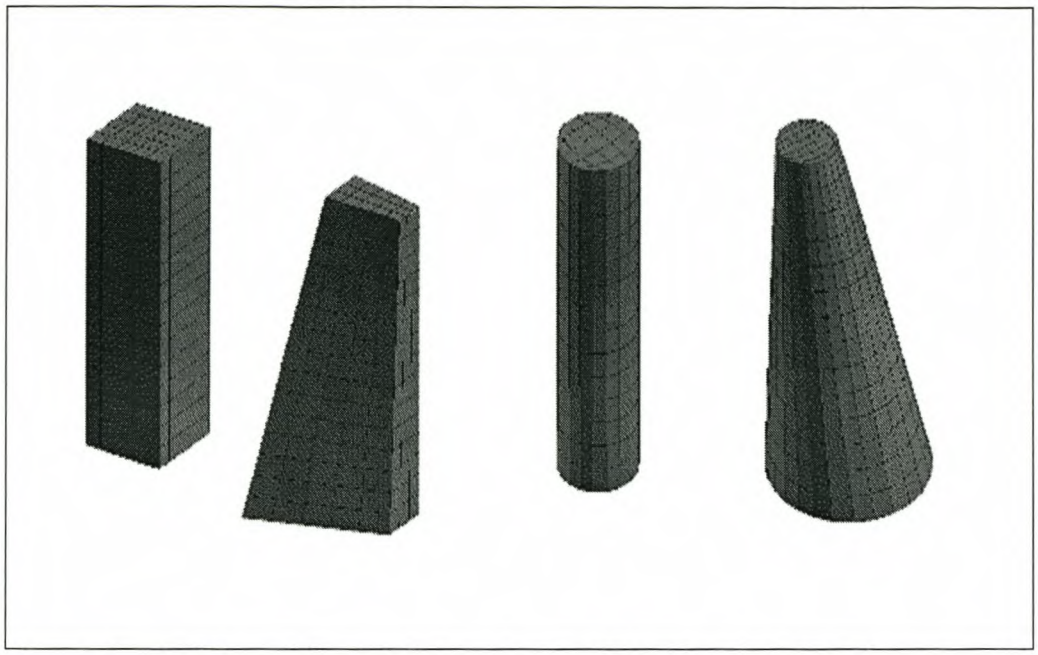

Figure 5-2: Simple shapes meshed automatically with user-defined parameters defining mesh configuration (Mesh created in Patran, 2001)

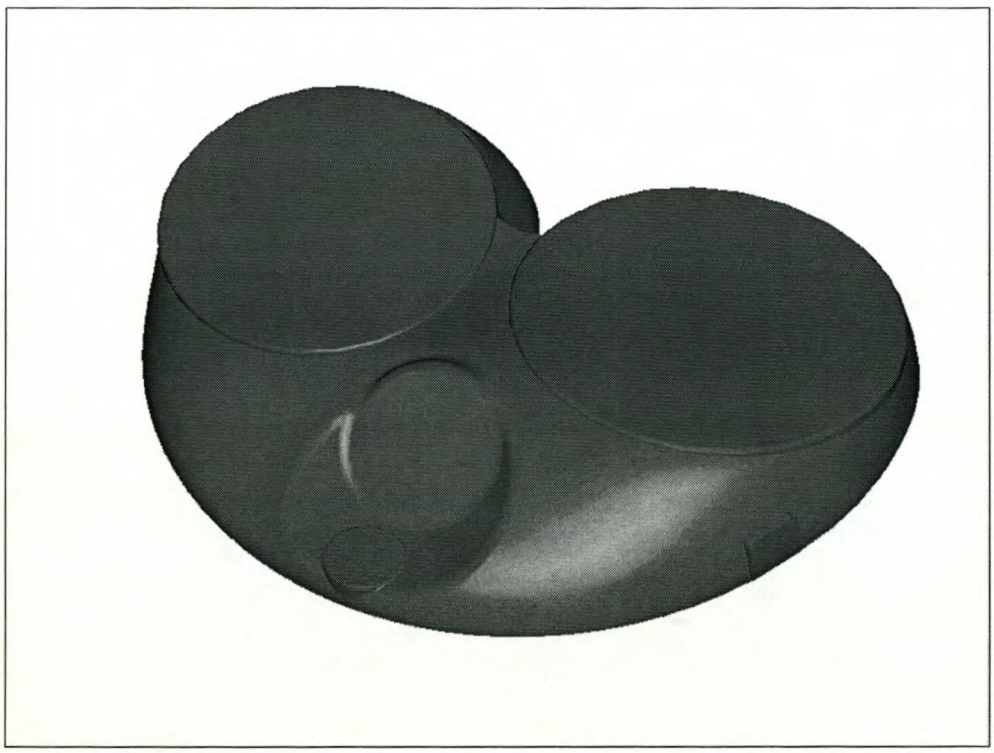

Figure 5-3: Arbitrary geometry that cannot be meshed by simple methods (Geometry created in ProEngineer)

Stellenbosch University http://scholar.sun.ac.za

5.1.2 Block structured mesh

Some geometries cannot be meshed as simple parametric parts but can be decomposed into parametric parts or blocks. This type of mesh is called a block structured mesh, consisting of different parametric blocks. The blocks are built individually, each can have it's own coordinate system, and then connected with a certain coupling tool, depending on the problem at hand. StarCD can handle any type of coupling ranging from simple meshes that fall right on top of each other to connections between two complete different meshes. Figure 5-5 illustrates different types of mesh connectivities possible in StarCD.

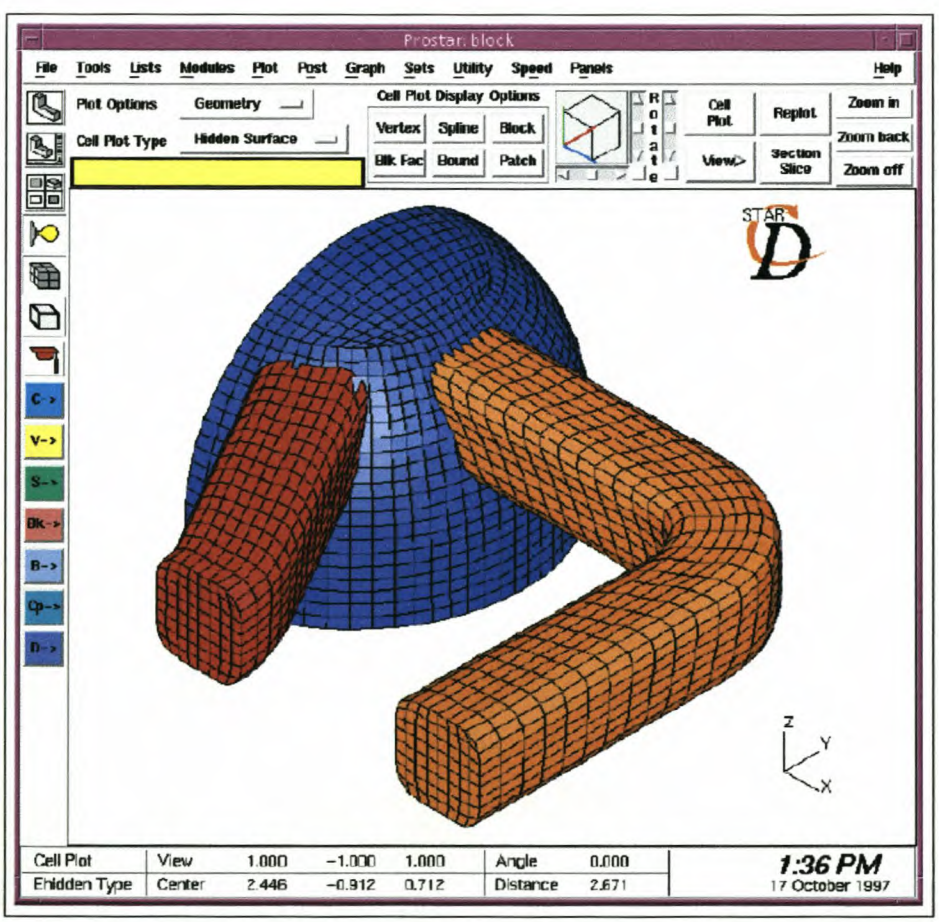

Figure 5-4: Block structured mesh consisting of three parametric blocks (StarCD user guide, 2002)

The meshes between different regions in Figure 5-4 have been connected by arbitrary couples, i.e. no similarity exists between them except that they share the same curvature

Stellenbosch University http://scholar.sun.ac.za

at their interface.

5.1.3 Unstructured mesh

Regions bounded by complex geometries that cannot be easily decomposed into parametric regions require other discretisation techniques. The method employed in this project is automatic tetrahedral meshing of solids. Tetrahedral cells are four-sided solid cells, defined by four triangular surfaces and four corner vertices. The main advantage of a tetrahedral mesh is its ability to describe complex geometries accurately and more easily than a hexahedral mesh.

Due to StarCD's ability to handle arbitrary interfaces the different mesh blocks can be mixed enabling the use of a combination of hexahedral and tetrahedral meshes.

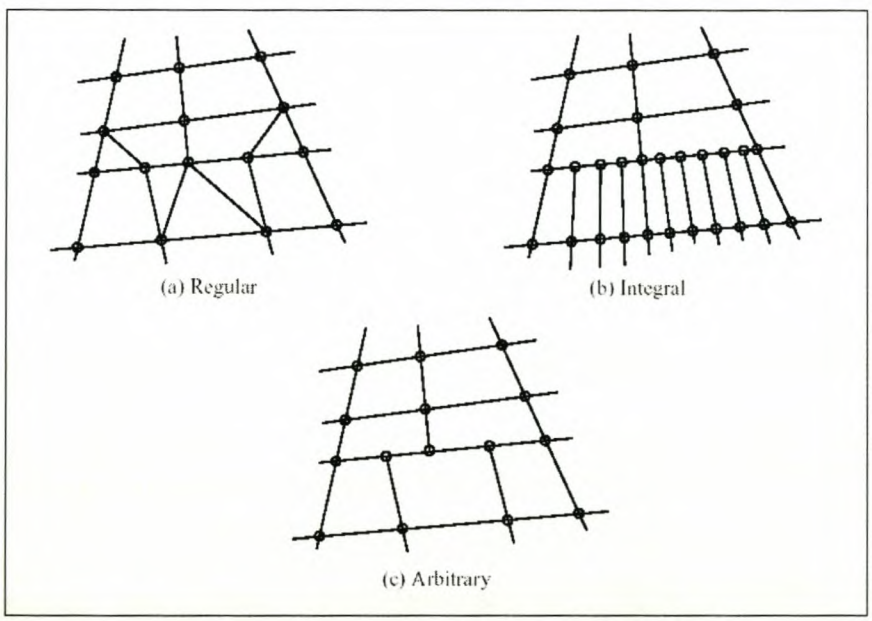

Figure 5-5: Mesh connectivity in StarCD (StarCD user guide, 2002)

The complex geometry of the combustion chamber was meshed with Patran (2001), a commercial code used for finite element modelling (FEM). Patran can perform tetrahedral meshing on any solid automatically as long as it can import the geometry. A mesh created for the combustion chamber is shown in Figure 5-6.

Stellenbosch University http://scholar.sun.ac.za

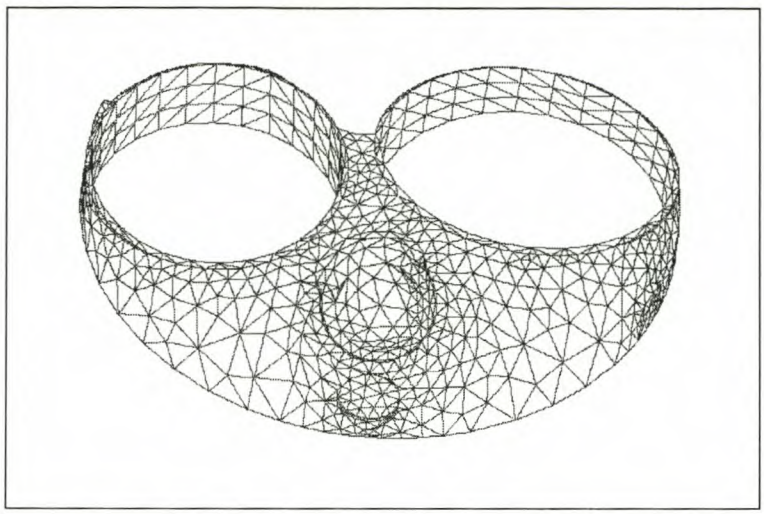

Figure 5-6: Tetrahedral mesh created in Patran

5.2 Fluid Property Function Definition

Thermodynamic fluid properties such as density, viscosity, specific heat and conductivity are functions of the state of the fluid such as the pressure, temperature and composition of the fluid. As a fluid stream can consist of more than one substance, such as a fuel-air mixture, the properties of the individual substances are first determined and then combined to form the mass averaged property of the fluid. The equation that relates the pressure and temperature and density of a substance is called an equation of state (Çengel and Boles, 1994). The most frequently used equation is the ideal gas equation of state. This equation predicts the pressure, temperature and density behaviour of a gas quite accurately within a properly selected region of pressure and temperature. Some of the substance properties do not vary considerably within a selected range of pressure and temperature variation and can be considered constant in that range. For most substances, the relationships among thermodynamic properties are too complex to be expressed by simple equations. Therefore, properties are often presented in the form of tables. When possible, the values in these tables are fit to a polynomial curve enabling the code to easily calculate them from the "known" state of the fluid.

Stellenbosch University http://scholar.sun.ac.za

5.3 Flow Properties

Solving fluid flow problems entails the simultaneous solution of equations for the conservation of mass, momentum and energy. These equations were derived by C. Navier and G. Stokes and are known by fluid dynamicists as the Navier-Stokes equations.

The characteristics of the fluid flow problem must be understood well and the flow properties specified to the CFD code in order to achieve meaningful results. Fluid flow properties include amongst others steady vs. transient, laminar vs. turbulent and incompressible vs. compressible flow. It must also be clear if the energy conservation equation needs to be employed, i.e. if temperature calculations need to be included.

5.3.1 Turbulent flow solutions

No general solution of the Navier-Stokes equations yet exists, although there are several known particular solutions, digital computer solutions and large quantities of experimental data. The reason is the drastic change in fluid behaviour at moderate Reynolds numbers. Flow changes from smooth laminar with low Reynolds numbers to fluctuating and turbulent at high Reynolds numbers. Figure 5-7 shows the different regimes of viscous flow, with u the instantaneous velocity measured by a hot-wire anemometer and plotted versus time. Other factors that influence the transition from laminar to turbulent flow is wall roughness, fluctuation in the fluid stream, and many more. Little theory is available on transition and therefore empirical data is relied upon (White, 1994).

Stellenbosch University http://scholar.sun.ac.za

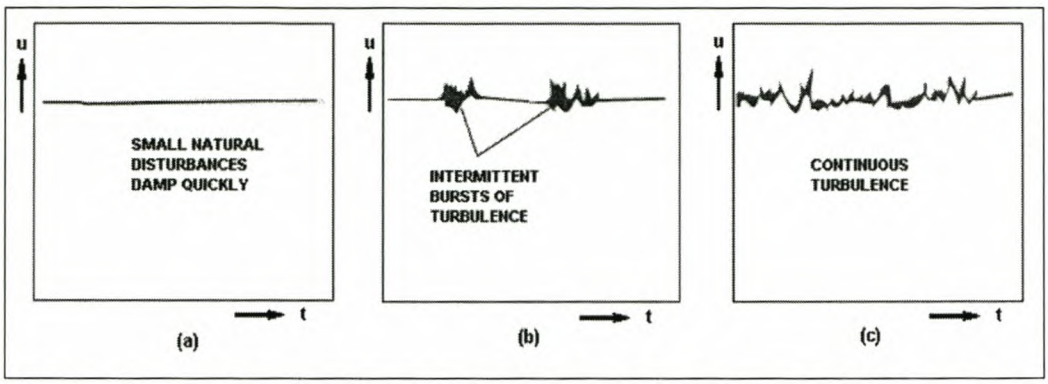

Figure 5-7: The three regimes of viscous flow namely a) laminar flow at low Reynolds number, b) transition at intermediate Re and c) turbulent flow at high Re (White, 1994)

Although digital supercomputers have been employed to solve the Navier-Stokes equations on a small enough physical and time scale to capture turbulence effects, this is not a viable option for large scale problems, and one has to resolve to semi-empirical turbulent flow models based upon dimensional analysis and physical reasoning (White, 1994).

For turbulent flow, every velocity and pressure term in the Navier-Stokes equations fluctuates randomly in time and space. As we are more interested in the average or mean values of velocity, pressure and shear stress, Osborne Reynolds (1895) time averaged turbulent variables as follows:

$$\overline{u_i} = \frac{1}{t} \cdot \int_0^t u_i \cdot dt \tag{5-1}$$

With u instantaneous and T some time scale larger than any significant period of fluctuations. The instantaneous velocity is defined as the average velocity $\overline{u}$ plus the velocity fluctuation u'.

Although the velocity fluctuations $u' = u - \overline{u}$ has zero mean value, its mean square is not zero and is a measure of its magnitude:

Stellenbosch University http://scholar.sun.ac.za

$$\overline{u_i'^2} = \frac{1}{t} \cdot \int_0^t u_i'^2 \cdot dt \neq 0 \tag{5-2}$$

The same is valid for products of fluctuating terms such as $\overline{u_i' \cdot u_j'}$.

This implies that the continuity equation is not influenced by turbulence i.e.

$$\frac{\partial}{\partial t}\rho + \frac{\partial}{\partial x_i}\left(\rho \cdot \overline{u_i}\right) = X \tag{5-3}$$

The momentum equation on the other hand presents products and squares of fluctuating terms, which are not zero and is illustrated below. Provided density fluctuations can be ignored, the momentum equation with turbulence, after time averaging is given by Kays and Crawford (1993) as:

$$\begin{aligned} &\frac{\partial}{\partial t}\left(\rho \cdot \overline{u_i}\right) + \frac{\partial}{\partial x_j}\left(\rho \cdot \overline{u_j} \cdot \overline{u_i}\right) \\ &\quad = -\frac{\partial \overline{P}}{\partial x_j} + \frac{\partial}{\partial x_j}\left(\overline{\tau_{ij}} - \rho \cdot \overline{u_j' \cdot u_i'}\right) + X_i \end{aligned} \tag{5-4}$$

This form of the momentum equation gives rise to an analogy between the viscous stress tensor and the term $-\rho \cdot \overline{u_j' \cdot u_i'}$, a turbulent stress tensor. This turbulent stress tensor is a set of nine terms with j = 1, 2, 3 for each of the i = 1, 2, 3, or x, y and z direction momentum equations. These terms are highly non-linear and reflect the inherently time-dependant character of turbulent flow.

StarCD employs mathematical models of turbulence to determine the Reynolds stresses and turbulent scalar fluxes. Additional differential or algebraic equations relate the Reynolds stresses and turbulent scalar fluxes to selected ensemble-averaged properties

Stellenbosch University http://scholar.sun.ac.za

of the turbulent flow field and thus provide a framework for calculating these properties.

Two terms appear in the turbulence momentum equation namely turbulent kinetic energy and turbulent dissipation rate. Turbulent kinetic energy is defined as follows:

$$k = \frac{1}{2} \cdot \overline{u_i' \cdot u_i'} \tag{5-5}$$

While turbulence dissipation rate is given by:

$$\varepsilon = \nu \cdot \overline{\frac{\partial u_i'}{\partial x_j} \cdot \frac{\partial u_i'}{\partial x_j}} \tag{5-6}$$

The k-ε turbulent flow model involves simultaneous solution to the momentum equation, continuity equation, k-equation and ε-equation. Since these equations all have the same general structure, their simultaneous solution by numerical methods does not add greatly to the complexity and time required for solution (Kays and Crawford, 1993).

Turbulent kinetic energy is calculated via the following transport equation (StarCD methodology, 2002):

$$\begin{aligned} &\frac{\partial}{\partial t}(\rho \cdot k) + \frac{\partial}{\partial x_j}\left(\rho \cdot \tilde{u}_j \cdot k - \frac{\mu_{eff}}{\sigma_k} \cdot \frac{\partial k}{\partial x_j}\right) = \\ &\mu_t \cdot (P + P_B) - \rho \cdot \varepsilon - \frac{2}{3} \cdot \left(\mu_t \cdot \frac{\partial u_i}{\partial x_i} + \rho \cdot k\right) \cdot \frac{\partial u_i}{\partial x_i} + P_{NL} \end{aligned} \tag{5-7}$$

Where

Stellenbosch University http://scholar.sun.ac.za

$$\mu_{eff} = \mu + \mu_t$$

$$\mu_t = f_\mu \cdot \frac{C_\mu \cdot \rho \cdot k^2}{\varepsilon}$$

$$P \equiv 2 \cdot s_{ij} \cdot \frac{\partial u_i}{\partial x_j}$$

$$P_B \equiv -\frac{g_i}{\sigma_{h,t}} \cdot \frac{1}{\rho} \cdot \frac{\partial \rho}{\partial x_i}$$

$$P_{NL} = \left(-u_i \cdot u_j - 2 \cdot s_{ij}\right) \cdot \frac{\partial u_i}{\partial x_j}$$

The first term on the left of equation 5.7 represents the transient changes in turbulence with the second term the convective and diffusive transport of turbulent kinetic energy. The first term on the right of equation 5.7 represents turbulent generation by shear and normal stresses and buoyancy forces. The second term on the right represents viscous dissipation and the third amplification due to compressibility effects. The last term accounts for non-linear contributions to turbulence generation.

The turbulence dissipation rate transport equation is as follows (StarCD methodology, 2002):

$$\begin{aligned} &\frac{\partial}{\partial t}(\rho \cdot \varepsilon) + \frac{\partial}{\partial x_j}\left(\rho \cdot \tilde{u}_j \cdot \varepsilon - \frac{\mu_{eff}}{\sigma_k} \cdot \frac{\partial \varepsilon}{\partial x_j}\right) = \\ &\quad \frac{\varepsilon}{k} \cdot \left[\left(C_{\varepsilon 1} \cdot P + C_{\varepsilon 3} \cdot P_B\right) - \frac{2}{3} \cdot \left(\mu_t \cdot \frac{\partial u_i}{\partial x_i} + \rho \cdot k\right) \cdot \frac{\partial u_i}{\partial x_i} \right] \\ &\quad -C_{\varepsilon 2} \cdot \rho \cdot \frac{\varepsilon^2}{k} + C_{\varepsilon 4} \cdot \rho \cdot \varepsilon \cdot \frac{\partial u_i}{\partial x_i} + C_{\varepsilon 1} \cdot \frac{\varepsilon}{k} \cdot P_{NL} \end{aligned} \qquad (5\text{-}8)$$

Where σ_ε, $C_{\varepsilon 1}, C_{\varepsilon 2}, C_{\varepsilon 3}$ and $C_{\varepsilon 4}$ are empirical coefficients.

The first term on the left of equation 5.8 represent transient changes and the second convective and diffusive transport of turbulent dissipation rate. The first term on the right of equation 5.8 describes turbulence dissipation rate generation by shear and normal stresses and buoyancy forces, the second viscous dissipation of turbulence

Stellenbosch University http://scholar.sun.ac.za

dissipation rate and the third accounts for non-linear effects. All the empirically determined constants for this turbulent flow model are available in the StarCD methodology guide.

The k-ε turbulent flow model was not developed to handle separated flows, buoyancy, streamline curvature, swirl, rotation, compressibility, adverse pressure gradients and axisymmetric jets. Flow in the combustion chamber and intake port presents a number of challenges to turbulent flow models. These include curved streamlines, separating flow, re-circulating flow, flow around curved surfaces and adverse pressure gradients. The subjection of the turbulent flow model to these conditions is very crude and inaccuracy in the results is therefore expected.

5.3.2 Transient flow calculations

The general Navier-Stokes equations contain transient terms. Many flow problems are solved for steady state i.e. not time dependant whereas transient solution imply that the solution changes with time. Performing transient calculations add another dimension to a fluid flow problem. The time dimension must, analogous to geometry, also be discretised into finite time steps. The extra terms in the differential equations are $\frac{\partial \rho}{\partial t}$, $\frac{\partial}{\partial t}(\rho \cdot \mathbf{U})$ and $\frac{\partial}{\partial t}(\rho \cdot \mathbf{H})$ in the continuity, momentum and energy equations respectively. Here ρ is the fluid density, **U** the fluid velocity and **H** the total enthalpy.

Initial conditions of the flow field must be specified when transient fluid flow problems are solved. Boundary conditions are the interface between the cells on the boundary of a solution domain and the environment of the solution domain (more details are given in the following section). Transient fluid flow problems often employ boundary conditions that vary with time. Poor initial conditions specification or abrupt changes in boundary conditions may put severe demands on the numerical algorithm when substituted into the finite-volume equations. It may be necessary to make use of unusually small time steps for the initial calculations of a transient solution to ensure numerical stability (StarCD user guide, 2002).

Stellenbosch University http://scholar.sun.ac.za

5.4 Boundary Conditions

The outermost cell face of the fluid flow domain defines the topography of boundaries. Finite volume cells inside the flow domain communicate flow properties to each other through their interfaces i.e. their surface. Cells that lie on the outer surfaces do not have neighbours to exchange information with and therefore need boundary conditions to be specified, thereby supplying enough information to enable solution of the simultaneous flow equations. Boundary conditions can mathematically be classified into two groups namely Neumann and Dirichlet conditions. Neumann boundary conditions imply that the gradient of the transported variable is given. Dirichlet boundary conditions specify the value of the transported variable (CFX, 2000). Combinations of Neumann and Dirichlet boundary conditions for different transported variables are used by commercial CFD codes for convenience. These include prescribed flow, outlet, prescribed pressure, stagnation conditions, cyclic, symmetry, etc. As this list can be as long as there are available combinations of Neumann and Dirichlet boundary conditions for each transported flow variable, only the ones relevant to this project are discussed here. These include prescribed pressure boundaries and impermeable wall boundaries.

5.4.1 Prescribed pressure boundaries

As their name imply, prescribed pressure boundaries allow the user to specify the pressure distribution on the boundary i.e. Dirichlet conditions are implied on pressure. The corresponding velocity magnitude and direction can then be either be Neumann or Dirichlet types. When velocity is specified as a Neumann condition a zero flow velocity gradient normal to the boundary face is assumed. Another available option is to specify the velocity parallel to the boundary as a Dirichlet condition and the component normal to the boundary face as a Neumann condition. Flow at a prescribed pressure boundary may be either into or out of the solution domain. When flow is into the flow domain, the distributions of relevant scalar variables such as temperature, species concentrations and turbulence parameters should be specified i.e. Dirichlet conditions are implied. When outflow occurs, these values are calculated as Neumann boundaries with zero gradients (StarCD methodology, 2002).

5.4.2 Impermeable wall boundaries

For impermeable wall boundaries no-slip prescriptions for velocity apply. This is a

Stellenbosch University http://scholar.sun.ac.za

Dirichlet condition i.e. velocity at the wall is specified as zero. Some turbulent flow calculations require the use of special mathematical representation of the velocity profile near the walls. Pressure and mass concentrations are handled as a Neumann condition with zero gradients.

Due to the spatial constraint that walls impose on fluctuating terms in turbulent flow, there are three regions of turbulent flow near a wall namely:

- Wall layer where viscous shear dominates
- Outer layer where turbulent shear dominates
- Overlap layer where both viscous and turbulent shear play significant roles.

Special mathematical models based on empirical data are employed to characterise the flow in wall boundary layers. For the high Reynolds number k-ε turbulent flow model employed in this project due to its simplicity, wall functions are used to determine boundary layer behaviour. These wall functions assume that:

- Variation in velocity is mainly normal to the wall
- Pressure gradient effects and body forces are neglected, leading to uniform shear stress
- Turbulence energy is produced and dissipated in the same quantities
- Turbulence length scale varies linearly

A non-dimensional distance from the wall is used in boundary layer flow namely y^+ and is defined as:

$$y^+ = \frac{y \cdot \sqrt{\tau_0 / \rho}}{\nu} \qquad (5\text{-}9)$$

Stellenbosch University http://scholar.sun.ac.za

With y the normal distance from the wall, τ_0 the wall shear stress, ρ the fluid density and ν the kinematic viscosity of the fluid. The cross stream profiles in terms of y^+ from the wall is given as follows:

$$u^+ = \begin{cases} y^+ & , \quad y^+ \le y_m{}^+ \\ \frac{1}{\kappa} \cdot \ln\left(E \cdot y^+\right) & , \quad y^+ > y_m{}^+ \end{cases} \qquad (5\text{-}10)$$

Further details, definitions and empirically determined constants are available in the StarCD methodology guide (2002).

Another way to calculate turbulent wall boundary layer flow is by two-layer turbulent flow models or low-Reynolds number turbulent flow model. The two-layer model requires a fine mesh near walls. The two methods for determining boundary layer flows are illustrated in Figure 5-8 (StarCD user guide, 2002).

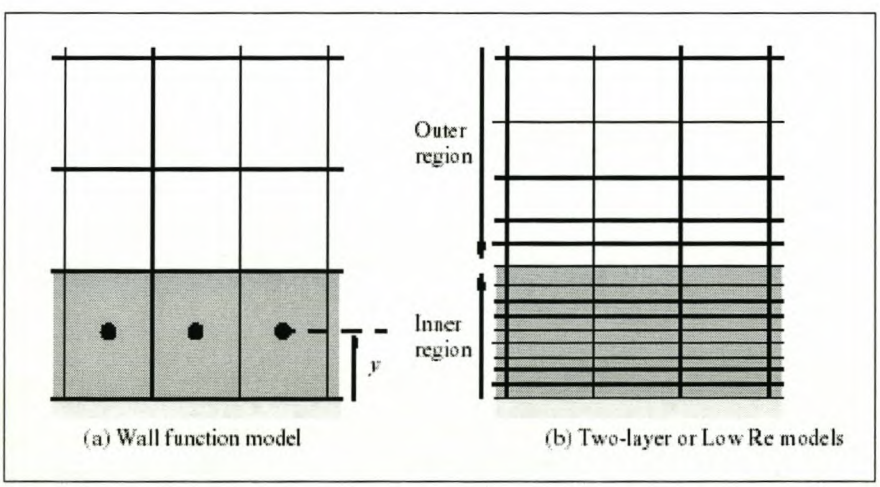

Figure 5-8: Near wall cell arrangement for a) wall functions and b) two-layer turbulent boundary layer methods (StarCD user guide, 2002)

StarCD can accommodate moving boundaries such as the moving of valves or the piston crown through its moving mesh features including general mesh motion, sliding meshes

Stellenbosch University http://scholar.sun.ac.za

and cell deletion and insertion. These boundaries are handled as impermeable wall boundaries with the exception that the velocity of the moving boundary specifies the velocity at the wall as a Dirichlet condition.

Stellenbosch University http://scholar.sun.ac.za

6 CFD IN COMBUSTION CHAMBERS

Although CFD is already playing a major role in combustion chamber modelling and design, it is very complex and research in the development of CFD techniques is still very active. In the following section, previous work done in CFD on combustion chambers is discussed. Flow in the combustion chamber is subjected to high levels of adverse pressure gradients, high turbulence levels, complex three-dimensional geometry with moving boundaries, heat transfer and chemical reaction. A thorough understanding of all these aspects is beyond the scope of this project and they are only briefly introduced here.

Mattarelli (2000) compared two different motorcycle engine combustion chamber shapes both experimentally and numerically. He focussed on cold flow and its properties in the engine. These properties include tumble and valve discharge coefficients. Tumble is a macroscopic flow property that is imposed when fluid flows into the combustion chamber and circulate around an axis perpendicular to the axis of piston movement. The discharge coefficient of a valve is a measure of the pressure drop across the valve at different valve openings with a prescribed fluid flow. The simulations were performed with a commercially available three-dimensional CFD package named Ricardo Vectis (2000), making use of the k-ε turbulence model to solve for turbulent flow. He found that discharge coefficients were over predicted by the CFD code, especially at low valve lifts, but comparative results between the two combustion chamber fluid flow simulations were in good agreement with experimental results. Mattarelli (2000) also did transient modelling of the intake stroke with assumptions of uniform, no-flow initial conditions. The motivation is that any flow properties derived by this simulation would be super-imposed on the effect of the initial conditions, i.e. although the simulation will be inaccurate, it will best relay the effect of changes in geometry. A result of the intake flow fields obtained by Mattarelli (2000) is shown in Figure 6-1.

Stellenbosch University http://scholar.sun.ac.za

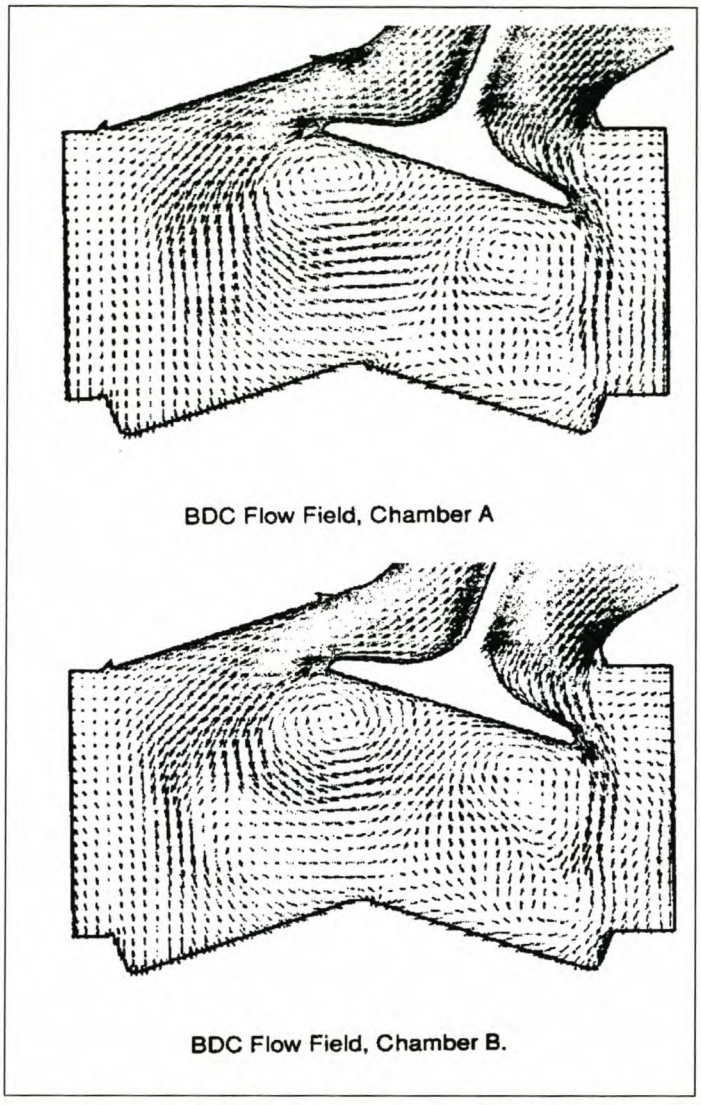

Figure 6-1: Velocity flow fields determined by Mattarelli (2000) for different combustion chamber geometries

Sinha et al. (1998) developed CFD techniques for modelling in cylinder flow on tetrahedral meshes. They developed a mesh motion scheme with automated cell layering which adds/deletes layers of tetrahedral cells as the piston moves. In addition the mesh motion is developed with the use of the spring analogy where the computational mesh is modelled as a spring network with spring stiffness inversely proportional to its length. Another method used is the solid body elasticity formulation where the domain is modelled as a linearly elastic solid. Cell layering was used to prevent large mesh distortion.

Stellenbosch University http://scholar.sun.ac.za

Sinha et al. (1998) modelled turbulence with a two-equation k-ε model. The cost and numerical errors generated by skewed tetrahedral meshes necessitated the use of a wall function. Another method of turbulence modelling employed during their testing is the large eddy simulation method. This fluid flow simulation started the calculations with constant initial flow conditions at the time when the intake valve opens with a 1 atm pressure and temperature of 300 K.

Jasak et al. (1999) produced a paper on the rapid CFD simulation of IC engines. This project entailed producing a mesh by use of a template-based mesh generator. The mesh-generator is supplied with a library of templates with each template providing the best mesh structure for a certain set-up. The templates are also supplied with their parameterised mesh movement routines. After the appropriate template is selected, the mesh is mapped onto the real geometry making use of feature edges and the real surfaces in between. Jasak et al. (1999) used the standard k-ε turbulence model with wall functions. Combustion was modelled using a two equation Weller (1993) model with stoichiometric air-fuel ratio. The solution was obtained by parallel flow solving, reducing the turn around time significantly. Advanced post-processing techniques have also been developed.

6.1 Geometrical Considerations

The nature of the reciprocating engine necessitates the use of moving boundaries for the flow domain. StarCD allows for the mesh to move by translating, rotating or distortion. This is done by specifying time-varying positions for some of the cell vertices. This type of mesh movement, which is sometimes referred to as 'Arbitrary Lagrangian-Eulerian', can accommodate a wide range of moving-boundary problems. Moving meshes are handled by solving of an additional equation called the space conservation law. This law relates the change in cell volume to the coordinate frame velocity. Demirdzić and Perić (1988) describe the space conservation law in detail. In order to prevent large distortion of the cells, StarCD also allows for cell deletion and addition or, more accurately, cell deactivation and activation. When cells are deactivated their mass is "squeezed out" into that the neighbouring cells in order to ensure continuity (StarCD user guide, 2002).

Stellenbosch University http://scholar.sun.ac.za

The complex geometry of the chamber necessitates the use of more advanced geometry definition capabilities such as that of a CAD package. Manufacturers drawings are imported into CAD, the necessary information extracted and errors in the geometry repaired. Advanced meshing software can then be used to perform meshing. Especially useful here is the use of automated meshing tools.

6.2 Weller Flame Area Model

The Weller flame area model makes use of a flame wrinkling factor Ξ to describe the flame surface. The flame area per unit volume is decomposed into the flame wrinkling factor, the flame surface area per unit-projected area, and a simple function of the normalised fuel mass fraction b. Here b is the ensemble-averaged regress variable or the so-called mixture fraction variable in CFD, which has the value 1 in the unburned gas and 0 in the burned gas.

Using conditional averaging techniques Weller (1993) describes in detail the development of a transport equation for the wrinkling factor. This equation contains a wrinkling generation coefficient, a wrinkling removal coefficient, flame stretch by the mean flow and a term for wrinkling removal by cusp formation.

According to Weller (1993), for cases involving small geometries such as the internal combustion engine, the effect of neglecting cusp formation and dissipation processes may be applicable. The lack of transient response could be remedied by obtaining an equilibrium wrinkling factor, Ξ_{eq} from analytical expressions for burning speed. Weller (1993) proposes the following linear expression.

$$\Xi_{eq} = \frac{S_t}{S_u} = 1 + A \cdot \frac{u'}{S_u} \qquad (6\text{-}1)$$

With S_t and S_u the turbulent and laminar flame speeds respectively and A, a model coefficient. Since this equilibrium wrinkling factor will not prevail during the initial stages of flame propagation, the evolution of Ξ is modelled by a time delay function.

Stellenbosch University http://scholar.sun.ac.za

$$\Xi = 1 + \left(\Xi_{eq} - 1\right) \cdot \left(1 - \exp\left(\frac{-\left(t - t_{sp}\right)}{\tau_d \cdot \tau_\eta}\right)\right) \tag{6-2}$$

With t_{sp} the time of spark ignition, τ_d is a time delay coefficient in the order of 15-20 and $\tau_\eta = \sqrt{\nu / \varepsilon}$ is the Kolmogorov time scale.

The transport equation for the mean regress variable is as follows:

$$\frac{\partial \bar{\rho} \cdot b}{\partial t} + \nabla \cdot \left(\bar{\rho} \cdot \hat{\mathbf{u}} \cdot b\right) - \nabla \cdot \left(\Gamma_b \cdot \nabla b\right) = S_{ig} + S_{err} + S_{WE} \tag{6-3}$$

With S_{ig} the fuel consumption due to ignition, S_{err} a discretisation error term and S_{WE} is the mean reaction rate given as follows:

$$S_{WE} = -\rho_u \cdot Y_u \cdot S_u \cdot \Xi \cdot |\nabla b| \tag{6-4}$$

This model only requires the solution of the equation for the regress variable and is therefore very computationally efficient, thus has been used for this project as computational power is limited.

6.3 Heat Transfer

The main form of heat transfer from gasses to the adjacent walls in the combustion chamber is by convective heat transfer. According to Ferguson (1986) radiation heat loss is less than 10% of convective heat loss, especially in spark ignition engines. The particles produced in diesel engine combustion tend to radiate more heat and then radiation plays a more significant role in heat transfer. The effect of radiation heat transfer will therefore be neglected for the purpose of this project.

Convective heat transfer coefficient in the turbulent boundary layer is calculated by

Stellenbosch University http://scholar.sun.ac.za

StarCD making use of special algebraic formulae called wall functions, to represent the distribution of velocity, temperature, turbulence, energy, etc. within the boundary layers that form at the walls (StarCD methodology, 2002). These wall functions have been utilised by Jayatilleka (1969) to obtain heat flux through the wall as function of shear velocity u^+, turbulent shear stress, Prandtl number, turbulent Prandtl number and free stream and wall temperature.

$$q = \frac{\overline{c}_p \cdot \rho \cdot u_\tau \cdot (t - t_w)}{\mathrm{Pr}_t \cdot (u^+ + P)} \tag{6-5}$$

With P named the sublayer resistance factor as a function of Prandtl number and turbulent Prandtl number.

$$P = 9.24 \cdot \left[\left(\frac{\mathrm{Pr}}{\mathrm{Pr}_t} \right)^{3/4} - 1 \right] \cdot \left[1 + 0.28 \cdot \exp\left(\frac{-0.007 \cdot \mathrm{Pr}}{\mathrm{Pr}_t} \right) \right] \tag{6-6}$$

With the heat flux at the wall, calculated as above, the energy equation can now be solved for the boundary nodes.

6.4 Boundary and Initial Conditions

The nature of the IC engine to induce and exhaust flow inherently makes the treatment of boundary conditions relatively simple in this case. The boundaries are chosen sufficiently far away from the area of interest so as to allow velocity profiles to fully develop. The intake and exhaust port boundary conditions are pressure, temperature and scalar concentrations specified. The turbulence intensities are zero gradient across the inflow boundaries.

The flow velocities, which may be inward or outward at pressure boundaries are calculated in this case from local pressure gradients with coefficients for the momentum

Stellenbosch University http://scholar.sun.ac.za

equations, calculated at cell centres (StarCD methodology, 2002). The pressure at the boundaries is specified in a table as a function of time. The transient pressure is obtained from the commercially available one-dimensional engine simulation software, Ricardo Wave (2000).

A preliminary transient simulation is performed in order to provide initial conditions for the flow field. For the preliminary transient simulation, the initial conditions are set to ambient conditions for pressure and temperature. Turbulence parameters and velocities are set to zero for this simulation. Scalar concentrations can be determined chemically and are specified as constants for the various fluids, with intake and combustion chamber conditions as unburned air-fuel and the exhaust port gas specified as complete combustion products.

Stellenbosch University http://scholar.sun.ac.za

7 EXPERIMENTAL PROCEDURE

7.1 Introduction

In this project two combustion chamber geometries are compared namely that of the Ford Rocam 1.3L and the Rocam 1.6L engines. By comparing the two engines at equivalent engine speed and load points, the effect of geometry can be isolated and thereby a comparison between the two engines can be made. The only substantial differences between the two engines are the difference in compression ratio and cylinder bore or diameter. Compression ratio is the ratio between volume when the piston is at the lowest point or bottom dead centre (BDC) and the highest point or top dead centre (TDC). The higher compression ratio of the 1.3L engine will increase pre-combustion temperatures resulting in increased initial burning velocity and thereby reduction of burn angles. This effect needs to be taken into consideration when comparing burn rates of the two engines.

Heat release analysis is performed at different speeds, throttle settings, air-fuel ratios and ignition timing settings. This allows one to evaluate the effect of the combustion chamber shape on combustion at different operating conditions. The two engines are compared at engine speeds of 2000, 2500, 3000, 3500 and 4000rpm.

The first experiment is a five-point power curve with a five point timing swing at each point. The lambda value is kept at 0.9 i.e. 10% rich throughout this experiment, as this is believed to be the optimum value for most wide open throttle load points. This experiment produces data at twenty five test points for each engine.

The second round of experiments consist of a five point timing swing and five point fuel loop at part throttle with a constant manifold absolute pressure (MAP) of 60kPa. This point was chosen, as it is the 100km/h in 5th gear equivalent load point for the 1.6L. The same test speeds will be used as in the previously mentioned experiment. Each speed point will consist of 10 test points, namely 5 different timing settings and 5 different fuel settings. The total number of points are therefore 50 per engine for this experiment.

Stellenbosch University http://scholar.sun.ac.za

The third experiment involves testing at one speed, but with varying loads. The chosen speed is the 3000rpm point with loads corresponding to full load, 80, 60, and 50kPa MAP. This experiment is done with a full timing swing and fuel loop at each throttled test point, resulting in 20 test points per engine as the WOT and 60kPa points have already been covered in the previous tests.

The total number of test points mentioned above is 95 per engine, implying a total number of 190 test points for both engines, although some tests using higher octane fuel were also done. Figure 7-1 shows a test matrix of the test points.

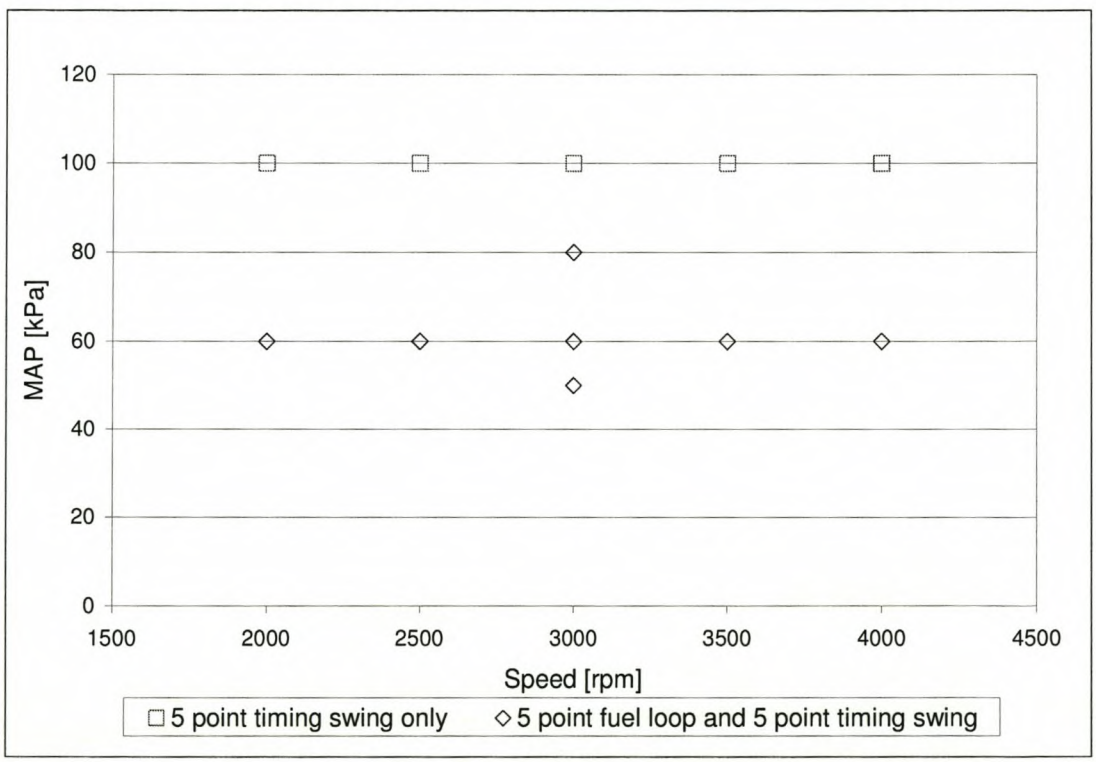

Figure 7-1: Experimental test matix.

Stellenbosch University http://scholar.sun.ac.za

7.2 Test Engines

The Ford Rocam 1.3L and 1.6L engines are compared in this study. Both engines are 8-valve, fuel injected and naturally aspirated. The engines have very similar valve lift profiles and their strokes and connecting rod lengths are equal, resulting in equal piston speed at equivalent rpm.

Figure 7-2 and Figure 7-3 illustrate the combustion chamber shapes of the 1.3L and 1.6L engines respectively. The Rocam 1.3L combustion chamber has a large 'nose' between the intake and exhaust ports where the 1.6L have a more open design. This nose assists in inducing swirl during the intake stroke as it directs the flow in a circumferential direction. The nose also increases the squish area and will therefore influence generation of turbulence. Increased turbulence at the time of ignition will reduce the induction period. The 1.3L intake port is quite heavily masked whereas that of the 1.6L is more open. Masking refers to material placed around the port opening in the cylinder head, thereby increasing flow resistance. The Rocam 1.3L combustion chamber seem to have been optimised for combustion efficiency and emissions while the Rocam 1.6L combustion chamber seems more beneficial to increased volumetric efficiency and therefore better performance.

The smaller bore of the Rocam 1.3L means that the maximum distance between the spark plug and the cylinder wall i.e. the distance of flame travel before all fuel is ignited is smaller than that of the 1.6L. This will reduce the burn angle for the Rocam 1.3L. The effect of this is expected to be almost linear to the maximum distance of flame travel. The higher compression ratio of the 1.3L causes un-burned mixture temperature to increase. The laminar flame speed will be increased by this and cause a reduction in induction period.

The effect of the smaller bore size of the 1.3L engine is correlated for in the data processing and presented in conjunction with the un-corrected data.

Stellenbosch University http://scholar.sun.ac.za

	Ford Rocam 1.3L	Ford Rocam 1.6L
Bore	73.96mm	82.0mm
Stroke	75.48mm	75.48mm
Connecting rod length	128.84mm	128.84mm
Compression ratio	10.2	9.5
Maximum distance between spark plug and cylinder wall	59.2mm	62.6mm
Intake port diameter	30mm	36mm
Exhaust port diameter	30mm	30mm
Fuel Type	RON 95 Unleaded	RON 95 Unleaded
Peak Power	56kW @ 5500rpm	70kW @ 5500rpm

Table 7-1: Specifications of 1.3L and 1.6L Ford Rocam engines

Stellenbosch University http://scholar.sun.ac.za

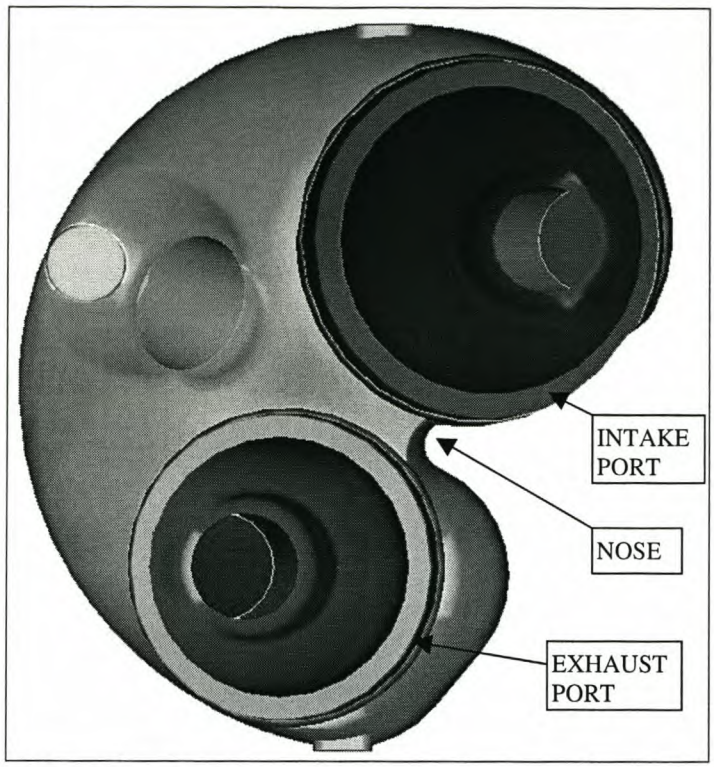

Figure 7-2: 1.3L Ford Rocam combustion chamber geometry defined in ProEngineer

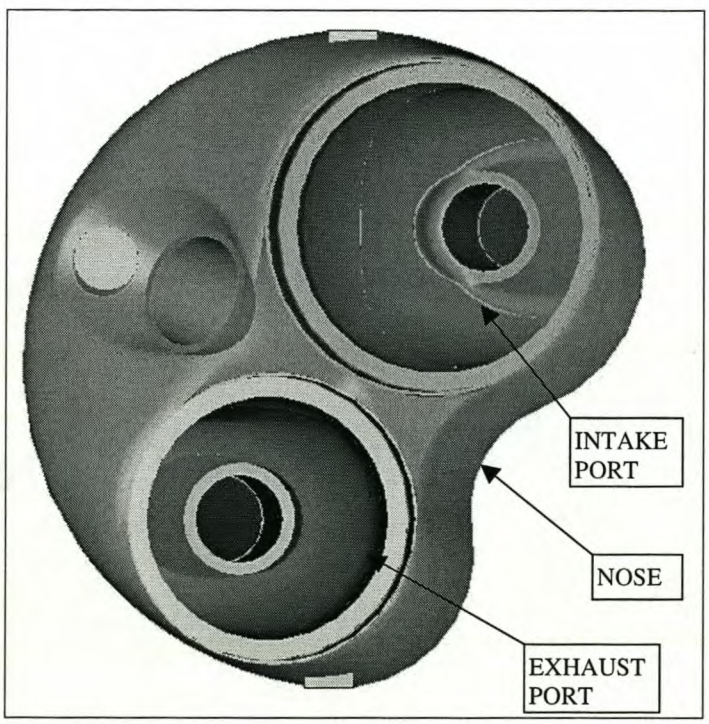

Figure 7-3: 1.6L Ford Rocam combustion chamber geometry defined in ProEngineer

Stellenbosch University http://scholar.sun.ac.za

7.3 Apparatus

The engines were set up on engine dynamometers and instrumented with thermocouples for measurement of all the important temperatures including, especially for the purpose of this project, intake air and exhaust gas temperatures. The dynamometer is fitted with a load cell providing the torque measurement used for determination of bmep. Pressure transducers are fitted to monitor manifold absolute pressure, ambient pressure and exhaust backpressure. A lambda sensor is fitted in the exhaust of the system, indicating the percentage excess air and thereby the equivalence ratio or lambda of the mixture that enters the combustion chamber. A spark advance meter is connected to monitor the ignition timing of the engine. Three speed pickup sensors are fitted onto the test bed, one on the dynamometer to monitor average engine speed. The second pickup is placed at a 60-tooth disk on the engine crank pulley. This pickup is used to determine the "exact" crank angle of number 1 cylinder in time. The third pickup is placed at a single tooth disk mounted on the engine crank pulley with the aim of detecting a reference point to the engine TDC. An AVL fuel flow meter is used to monitor mass flow rate of fuel into the engine, enabling the measurement of specific fuel consumption.

A spark plug mounted pressure transducer is installed in cylinder number 1, measuring cylinder pressure vs. time. This transducer produces an electric charge that is related to the piezometric pressure it is subjected to. This charge is converted by a charge amplifier to an electrical voltage that is related to pressure. The voltage is recorded along with the outputs from the speed pickups on the engine crank by Waveview via a PC30 data capture card. The information is streamed online into the PC memory and is thereafter saved to a text file. The sampling frequency can be anything between 0 and 100 kHz. As the PC30 card can only handle one channel at a time, there is a 10 microsecond delay between the recorded times of the measured channels.

A Kistler spark plug pressure transducer (model no: 611BCD25) is used with a Kistler charge amplifier (model no: 5011A). Data is recorded via a PC30GA data acquisition card with Waveview software. The ECU is controlled with ETAS ETK 3.1 with INCA VS100 software.

While the cylinder pressure and crank angle position is being measured, the engine

Stellenbosch University http://scholar.sun.ac.za

parameters are monitored online by the ETA (Engine Test Automation) software via PLC's connected to the engine sensors. This data is stored onto disk whenever requested by the user, usually at the same time that pressure readings are being recorded.

The spark plug transducer is used for convenience, as the need for machining of cylinder heads is eliminated. It is noted that this type of transducer is not as accurate as water-cooled transducers. Figure 7-4 illustrate the set-up used for experimental data collection for this project.

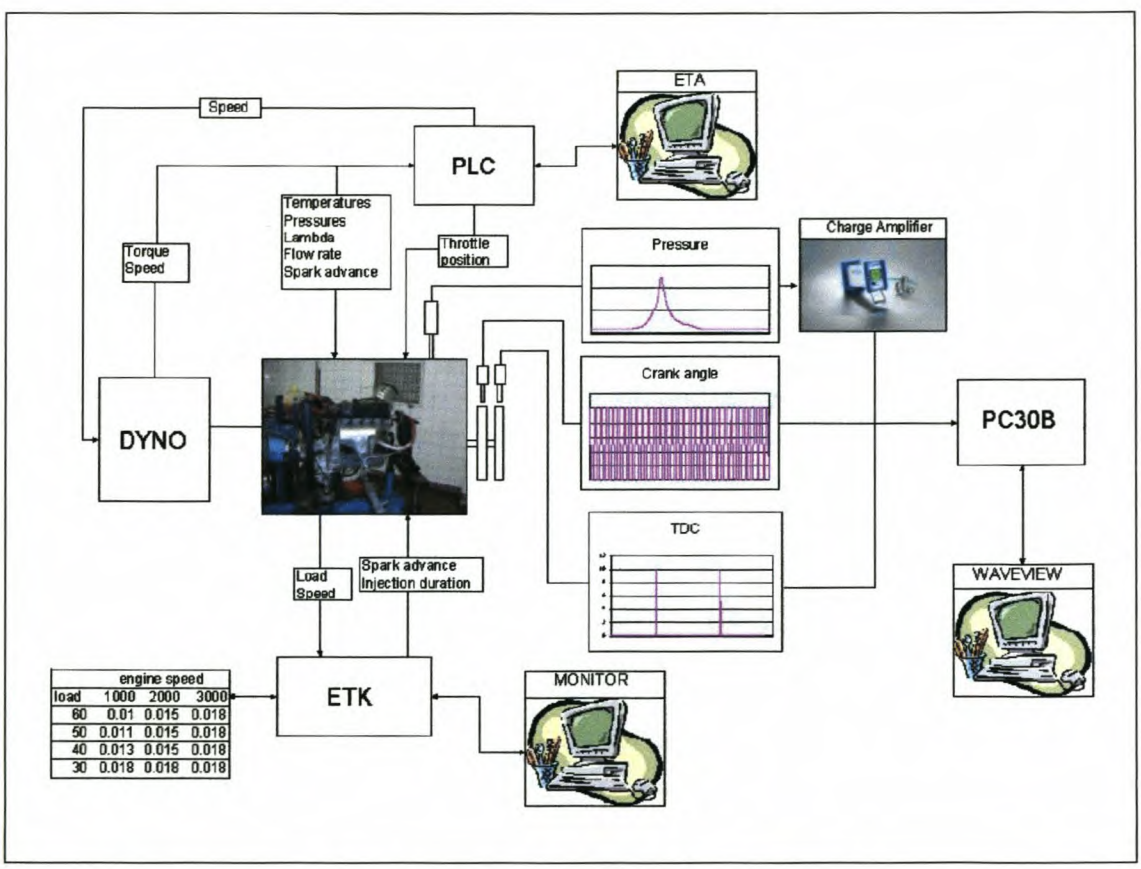

Figure 7-4: Experimental set-up including in-cylinder pressure data collection

7.4 Test Procedures

The first step is to test all the systems, ensuring that a pressure signal is obtained. The charge amplifier must be set to the correct sensitivity of the pressure transducer. This value is obtainable from the pressure transducer calibration certificate. The output scale of the charge amplifier must be set to the desired value, ensuring that the maximum

Stellenbosch University http://scholar.sun.ac.za

output will not exceed the limit of the recording system. The settings applicable to the equipment used in this experiment was:

- Transducer sensitivity: 16.7pC/bar
- Output gain: 20bar/volt
- The output gain was set to 10bar/volt for lower pressure testing.

A sample set of data is recorded and processed to ensure that all the settings of the recording software were correct. The settings in the Waveview recording software was as follows:

- Sampling frequency: $rpm \times 6 \times 1.1$
- Number of samples: 237 600 for 300 engine cycles
- Record mode: burst
- Channels: 1.) TDC, 2.) Crank and 3.) Pressure
- Input range: -10 to +10Volt

In the engine monitoring software the desired name for storing the test data is set. Finally the engine control unit (ECU) is set up and the standard engine calibration loaded. The appropriate options for changing of fuel and spark setting are selected.

7.4.1 Top dead centre offset determination

In order to determine the position of the reference pulse relative to the true top dead centre of the engine (tdc offset), motoring pressure was measured and analysed.

After warming the engine up to an oil temperature of at least 80°C or a point where engine conditions are relatively stable, the fuel injector plug is removed on the cylinder where pressure is monitored. A 300-cycle pressure measurement is performed while the engine runs in this state i.e. while the measured cylinder is motored. A thermodynamic

Stellenbosch University http://scholar.sun.ac.za

combustion analysis is done on the measured pressure data. The tdc offset is a function of the position of the tdc tooth on the tdc measurement disk and the engine tdc. This fixed value is determined by trial and error in the combustion analysis software, and must be determined every time a change is made to the position of the speed pickups and/or the toothed disks.

Cylinder pressure data along with the referenced tdc signal and crank angle signal was recorded for 300 cycles at 2000, 3000, 4000rpm, WOT for both engines:

7.4.2 In-cylinder pressure data collection

Cylinder pressure data is collected in the same fashion as is the motored data, but with the injector connected. For each test point the required spark, lambda and load value is set by the operator. The engine is allowed to stabilise before measurement is commenced and the cylinder pressure monitored by an oscilloscope to detect the occurrence of knock.

The ignition timing was advanced until torque starts to drop and then 5° further if knock does not limit it. The timing was then retarded 5° between each recording step. The fuel loops consist of five points namely 0.90, 0.95, 1.00, 1.05 and 1.10 lambda settings. For the timing swings, the lambda was set to the ECU default, and for the fuel loops the standard ignition timing was used.

7.5 Data Processing

A script (Postwave) was written in Delphi to handle the large amount of data that was recorded during testing. Postwave was developed specifically for the use of this project and performs data averaging. The output is in a .prs file for each test point, containing the averaged, smoothed pressure for each crank angle as well as the standard deviation of pressure at each crank angle.

The .prs file is then processed by another script named Burnrate. This script uses the combustion analysis methods described in chapter 4. Burnrate was also written for the specific use in this project, but makes use of some subroutines from Racer (Moran,

Stellenbosch University http://scholar.sun.ac.za

1997), which is software developed in previous research and masters projects at Stellenbosch University.

Stellenbosch University http://scholar.sun.ac.za

8 DATA INTEGRITY CHECKING

The heat release model can be verified by ensuring that no chemical heat is released except during combustion. Another way of checking results is by ensuring that the mass of fuel burned and the total heat released correlates to within an acceptable tolerance. If engine friction is known then the imep calculated from the dynamometer (bmep + fmep) should correlate with that of the pressure measurements. Possible causes of deviation from the above mentioned could be:

- The heat transfer model is inaccurate
- The angular reference of pressure data is incorrect
- Pressure measurement was inaccurate
- Pressure referencing was incorrect

Log P vs. log V plots can be used to check cylinder pressure data quality. Log P vs. log V plots for motored data are used for checking if the heat transfer model is correct, if angular reference is correct and if the correct reference pressure is being used (Heywood, 1988). Any flaw in the above-mentioned would result in curvature and/or crossover of the compression and expansion curves of the motored log P vs. log V graph. Thermal cycling effects on pressure data are evident from excessive curvature on the expansion stroke of the log P vs. log V plot (Heywood, 1988).

8.1 Crank Angle Phasing

If the tdc offset is not correct, cylinder pressure data is referenced to the wrong crank angle. As the crank angle is used to determine cylinder volume, the P versus V graph will be distorted. These distortions are amplified by viewing this graph as a log P vs. log V. The motored data is recorded by running the engine with the fuel injector for the measured cylinder deactivated by disconnecting it from the engine control unit (ECU). This implies that no fuel is injected into the cylinder in question and that the gas inside

Stellenbosch University http://scholar.sun.ac.za

the cylinder is pure air. Since both the compression of air and the expansion of air approach isentropic processes, log P should vary linearly with log V or in mathematical terms:

$$\begin{aligned} P \cdot V^k &= \text{const} \\ \log P + k \cdot \log V &= \text{const} \\ \log P &= -k \cdot \log V + \text{const} \end{aligned} \tag{8-1}$$

This implies that the log P vs. log V curves should be straight lines for both compression and expansion. Figure 8-1 and *Fi*gure 8-2 illustrate the log P vs. log V curves for both engines in the motored state. Evident from the log PV plots is that the 1.6L engine shows less curvature during the final stages of the expansion stroke. Both curves are very linear through the compression and early and mid-expansion stages.

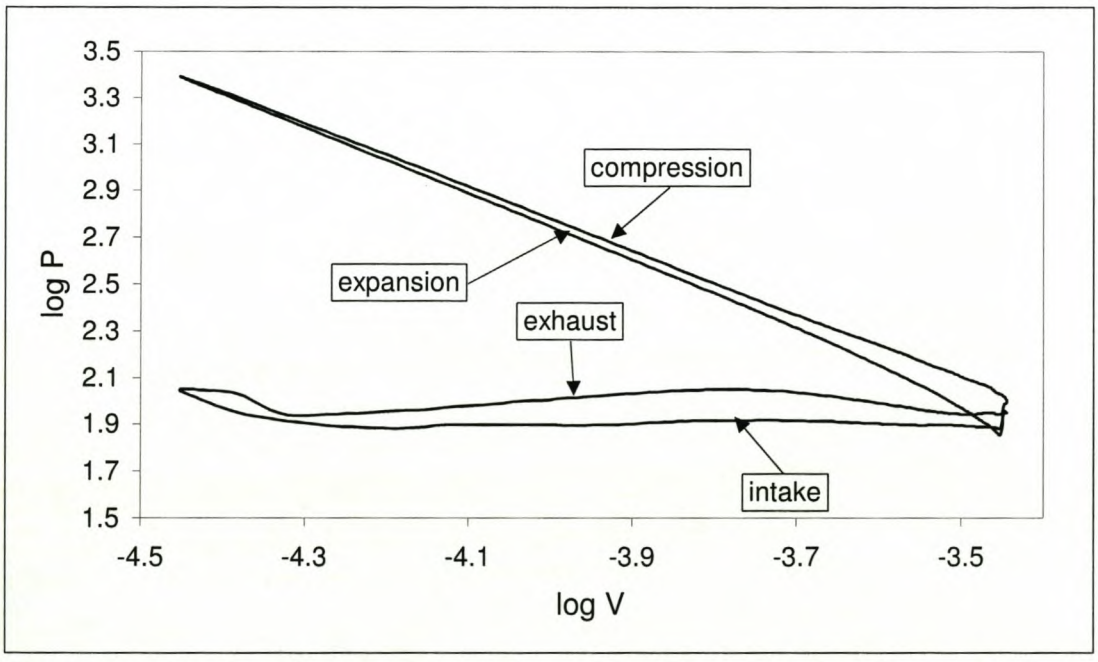

Figure 8-1: Rocam 1.3L log P vs. log V diagram for motored pressure data at 3000rpm WOT

Stellenbosch University http://scholar.sun.ac.za

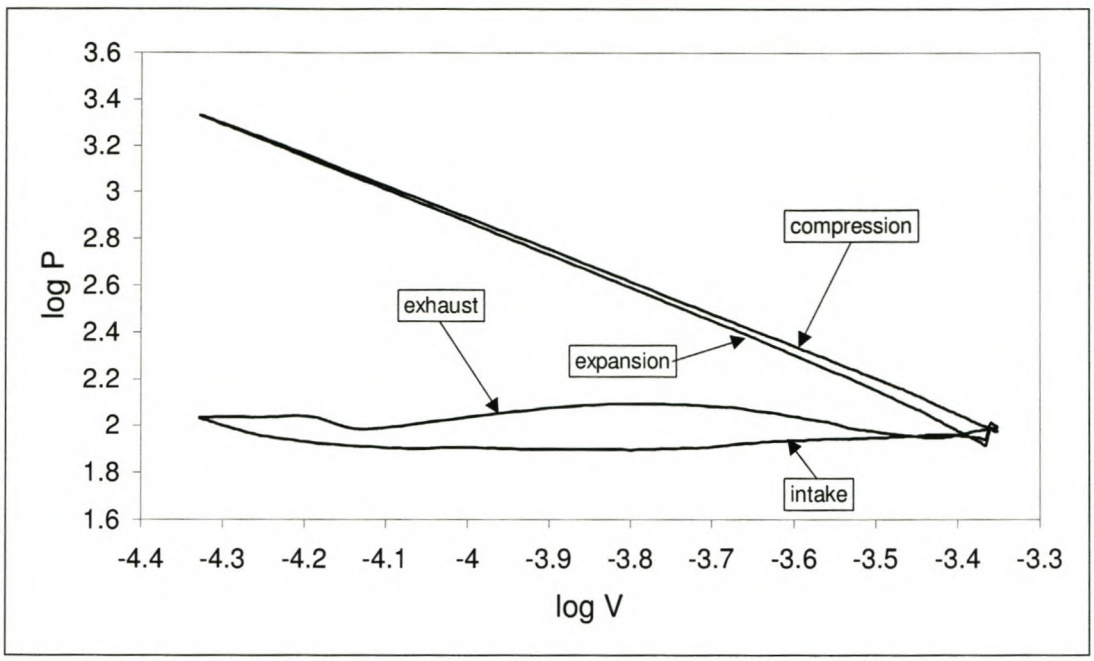

Figure 8-2: *Rocam 1.6L log P vs. log V diagram for motored pressure data at 3000rpm WOT*

Figure 8-3 illustrates the gas temperature variation in both engines estimated from the cylinder pressure data and the ideal gas relation:

$$\frac{T_2}{T_1} = \frac{P_2 \cdot V_2}{P_1 \cdot V_1} \tag{8-2}$$

The gas temperature variation of the 1.3L is higher than that of the 1.6L due to its higher compression ratio. The increased heat transfer in the 1.3L could be responsible for the crossover of the 1.3L and 1.6L temperatures during the expansion phase. The higher temperature variation could be responsible for more severe thermal strain effects of the transducer evident from Figure 8-1.

Stellenbosch University http://scholar.sun.ac.za

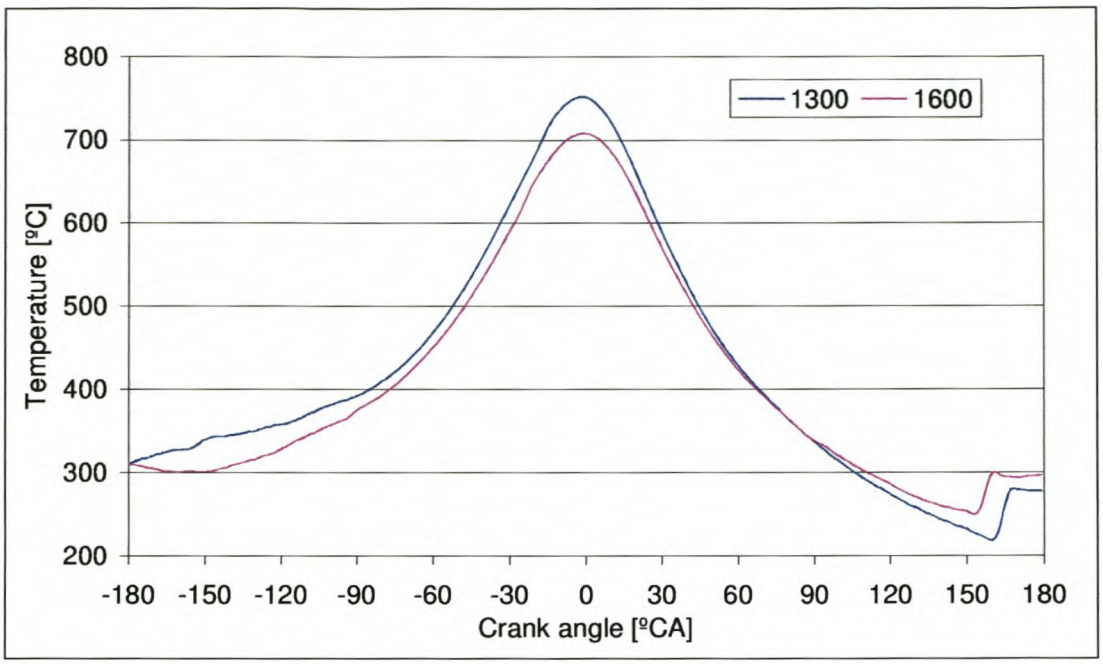

Figure 8-3: Gas temperature variation in 1.3L and 1.6L Rocam combustion chambers. Engines were motored at 3000rpm WOT. Data obtained from experimental pressure measurements and the ideal gas law

Incorrect volume referencing would cause crossing of the compression and expansion curves, which is not the case in Figure 8-1 and *Fi*gure 8-2. Incorrect tdc volume specification would result in curvature of the compression and expansion curves at the tdc point. The figures illustrate that the heat release analysis is well configured for both engines.

8.2 Energy Balance

The cumulative heat released calculated by combustion analysis is compared here with the fuel energy content as calculated from fuel consumption and lambda data. The latter is calculated by determining the fuel consumption per cylinder per cycle as follows:

$$m_{fuel} = \dot{m}_{fuel,engine} \times \frac{1}{4} \times \frac{120}{N} \qquad (8\text{-}3)$$

The energy release is then determined by calculating the mass of fuel burned times the

Stellenbosch University http://scholar.sun.ac.za

lower heat of combustion. For petrol the lower heat of combustion is given by (Ferguson, 1986) as 44MJ/kg, although this value is highly fuel specific.

$$Q_{ch} = m_{fuel} \cdot 44 \cdot 10^3 \quad [\text{kJ}] \tag{8-4}$$

Thus, in compact form:

$$Q_{ch} = \left(\dot{m}_{fuel,engine} \times \frac{1}{4} \times \frac{120}{N} \right) \cdot 44 \cdot 10^3 \left[kJ \right] \tag{8-5}$$

Figure 8-4 compares the cumulative heat release determined by combustion analysis and the product of mass times lower heating value calculated above for different engine conditions for the Rocam 1.3L and 1.6L engines. It is clear that all values lie beneath the 45° straight line, indicating a difference between the fuel energy in and the measured heat release. There are various factors that would cause such a difference including:

- Poor combustion efficiency
- Inaccurate heat transfer model
- Pressure measurement errors
- Inaccurate fuel flow measurement

Combustion efficiency is defined as the fraction of the fuel energy released divided by the fuel energy supplied to the combustion process (Heywood, 1988). Heywood (1988) mentions that combustion efficiency for stoichiometric air-fuel mixtures range from 95 to 98% for spark ignition engines. For rich mixtures the combustion efficiency decrease even further due to oxygen starvation. Unburned fuel, CO, and other incomplete combustion products therefore leave the combustion chamber.

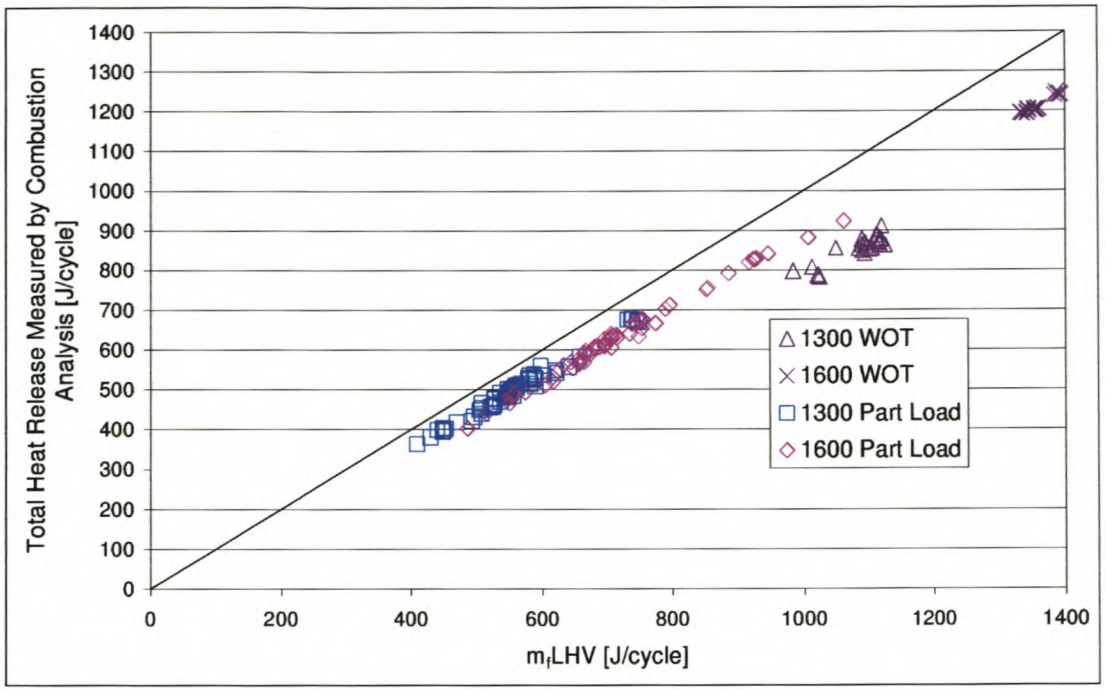

Figure 8-4: Comparison between heat release determined by combustion analysis and heat release determined from fuel flow measurement for all test data

The heat transfer model is verified by looking at heat-released data for a motored engine. As no fuel is burned during the motoring cycle, the model should predict a zero burn rate and no heat release due to combustion. Figure 8-5 illustrate the results of heat release analysis for motored pressure data. The burn rate is nearly zero during the whole cycle except for the end of the expansion cycle where the exhaust valve opens. This is due to the fact that the heat transfer model does not take mass transfer past the valves into account. This does not affect combustion parameters, as they do not take that part of the cycle into account.

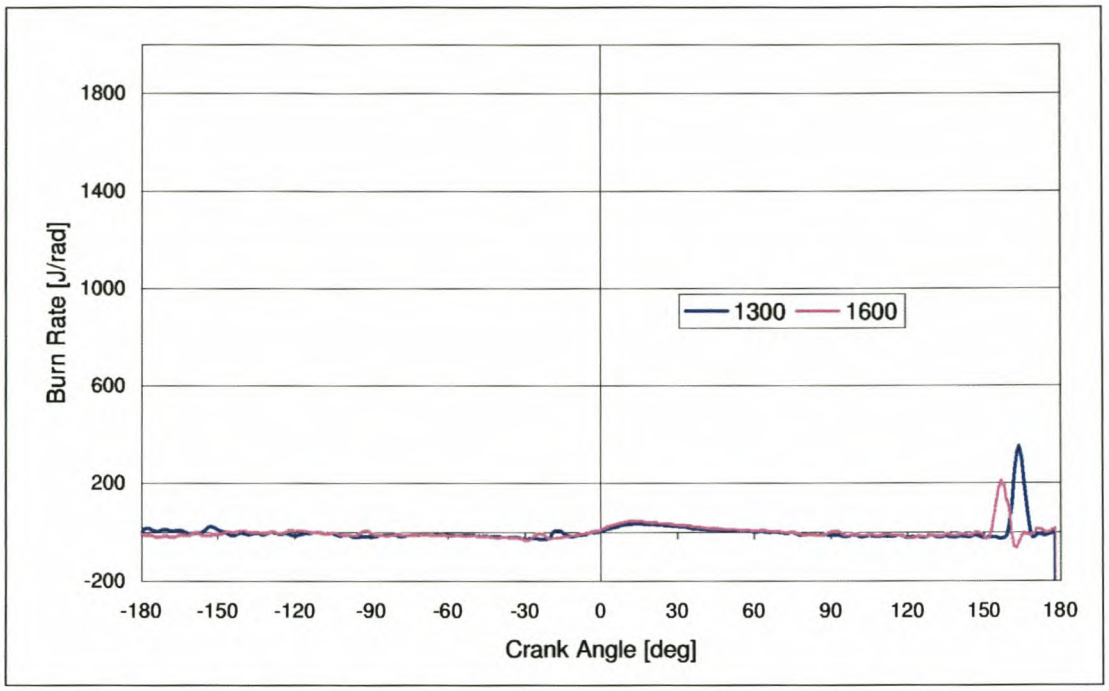

Figure 8-5: Burn rate graph for 1.3L and 1.6L motored engines at 3000rpm WOT determined from heat release analysis of in-cylinder pressure data

8.3 Thermal Strain

The effect of thermal strain of the pressure transducer can be detected by looking at the latter part of the expansion stroke and the exhaust stroke in the P vs. V diagram. During these phases the diaphragm suffering thermal strain would relax from the distorted position as it cools. The rate of cooling is relatively low during expansion and exhaust due to the hot gasses in contact with the diaphragm. As the fresh air enters the combustion chamber during intake, the relaxation occurs faster and the error is finally reduced. As the highest source of thermal strain is the energy released by combustion, thermal strain during motored operation is much lower than when the engine is fired and thermal effects are not present in the same order of magnitude when the engine is motored. Comparison between the fired and motored P vs. V diagrams would therefore reveal the effects of thermal strain quite clearly. A possible indication of thermal strain was evident from Figure 8-1 displaying curvature at the bottom end of the expansion stroke of the 1.3L motored engine. Comparing the P vs. V diagrams of motored and fired engine data in Figure 8-6 and Figure 8-7 for the 1.3L and 1.6L engines respectively with Figure 4-7 from Stein et al. (1987), it is found that thermal strain may not be as

prominent as was expected. The pressure at the beginning of the exhaust stroke does not seem to undershoot as is clear in Figure 4-7b, which is an indication of the effect of thermal strain.

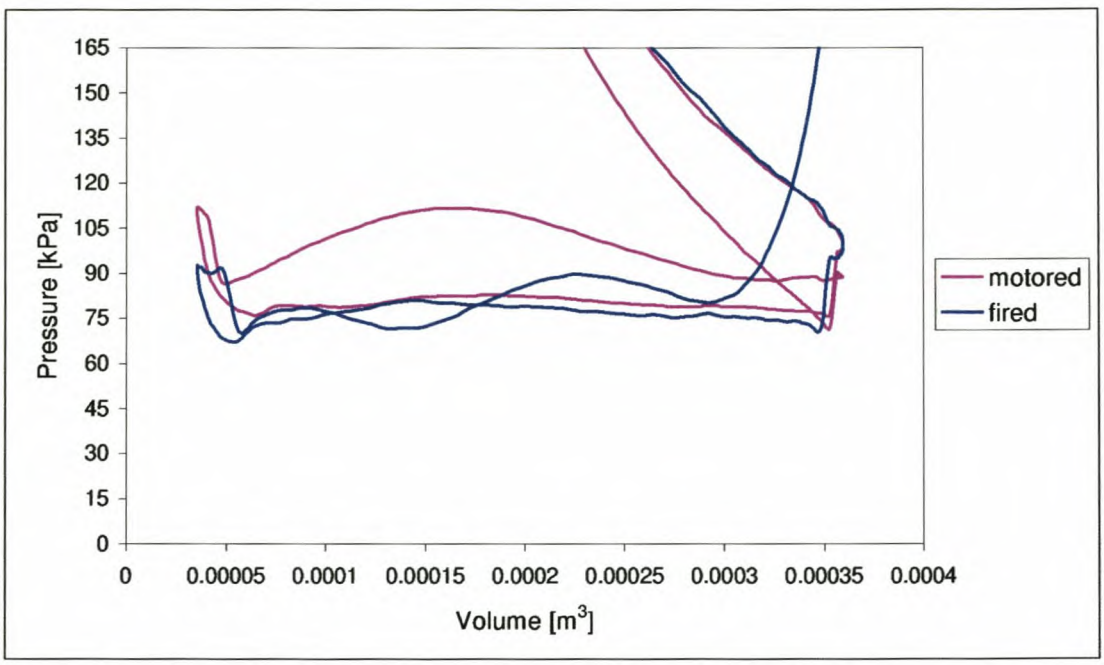

Figure 8-6: 1.3L Fired and motored P vs. V graphs measured at 3000rpm WOT

It is clear from both Figure 8-6 and Figure 8-7 that the intake and compression strokes are very similar for the fired and motored data. Comparing the fired exhaust strokes of both engines with their respective motored exhaust strokes it is evident that the pressures are only slightly reduced due to dynamic effects in the exhaust system. These figures compare well to Figure 4-7a, which was measured by a coated transducer. The effect of thermal strain does therefore not seem to be as prominent as was initially expected. A possible explanation for this is the fact that the diaphragm of the spark plug transducer is not flush with the combustion chamber surface, but rather slightly removed from the latter by a short passage. If no fuel burning occurs in this passage as may well be expected, then the gas in the passage would insulate the diaphragm and thereby reduce thermal effects. The previously determined correction factors for thermal strain are therefore not applied to the data from experimental testing by this pressure transducer.

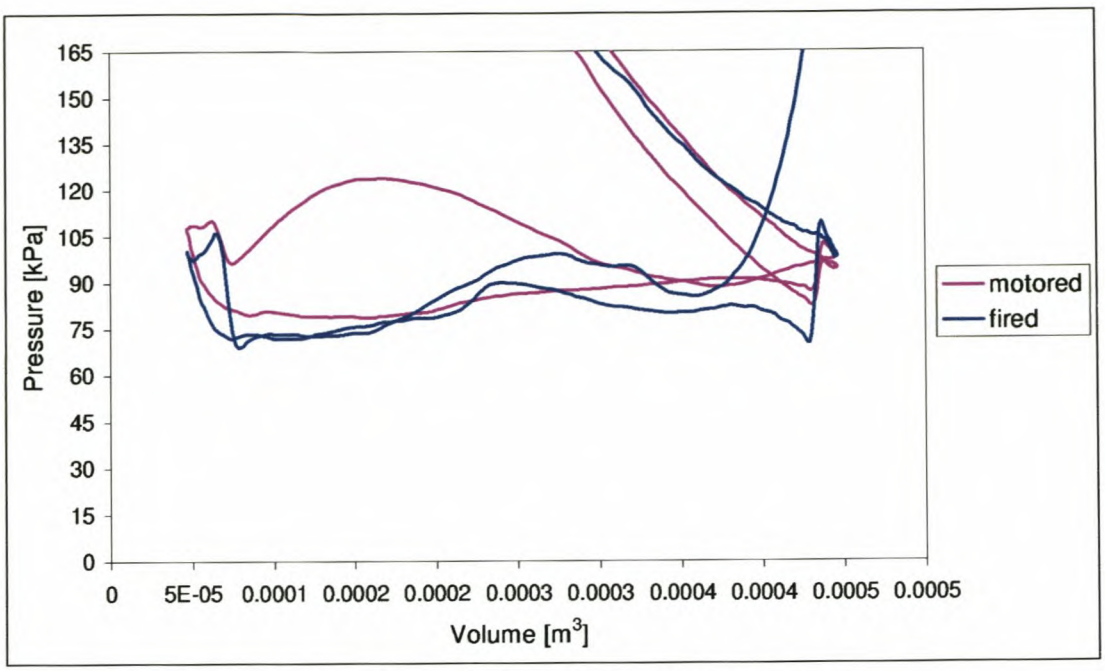

Figure 8-7: 1.6L Fired and motored P vs. V graphs measured at 3000rpm WOT

8.4 Mean Effective Pressures

Mean effective pressure (mep) is a very effective manner to compare engines of different sizes. This section looks at the mep results and their credibility. The aim is to compare the measured mep results with generally known trends and thereby validate the measured data.

Figure 8-8 from Ferguson (1986) illustrate typical mep data for a spark ignition engine. It is evident that friction increases with increasing load due to the increased forces in the piston/crank assembly of the engine at higher loads. However, pumping work decrease due to lower pumping losses when the throttle opens at higher loads.

The mean effective pressures determined from in-cylinder pressure data is shown in Figure 8-9. The pumping mean effective pressure (pmep) follows the same trend and is in the same order of magnitude as that shown by Ferguson (1986).

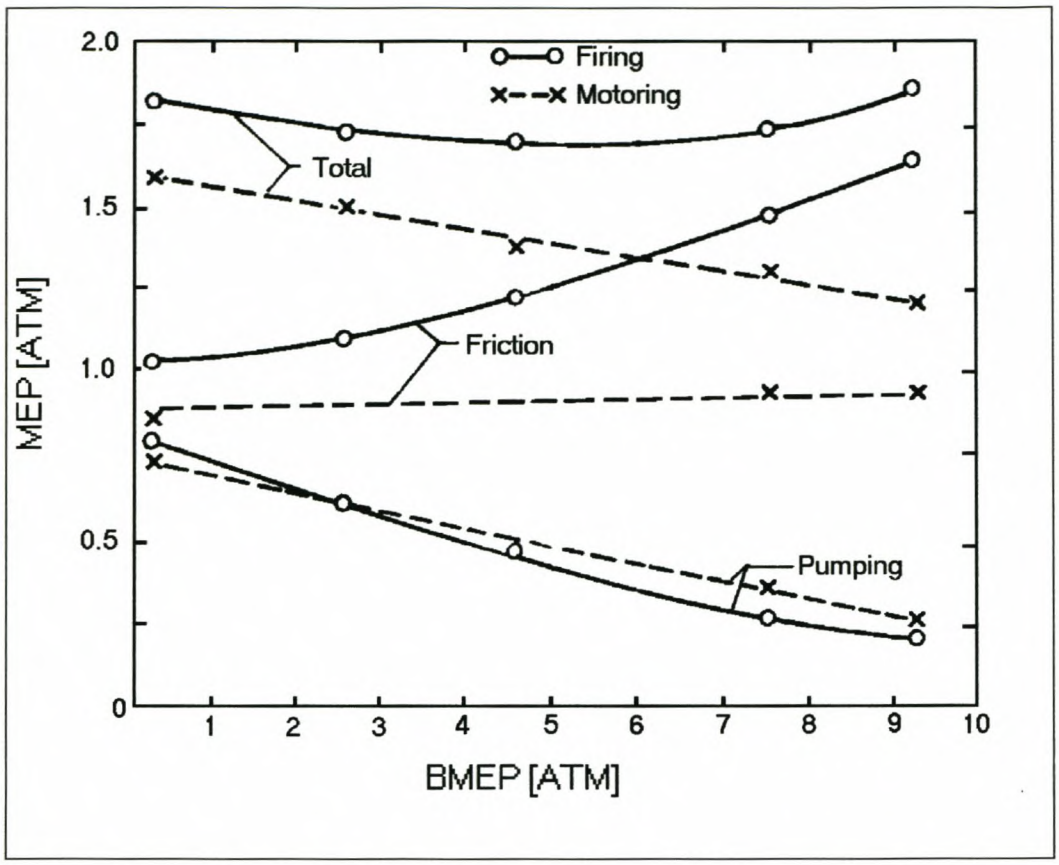

Figure 8-8: Typical motored and fired mean effective pressure data (Ferguson, 1986)

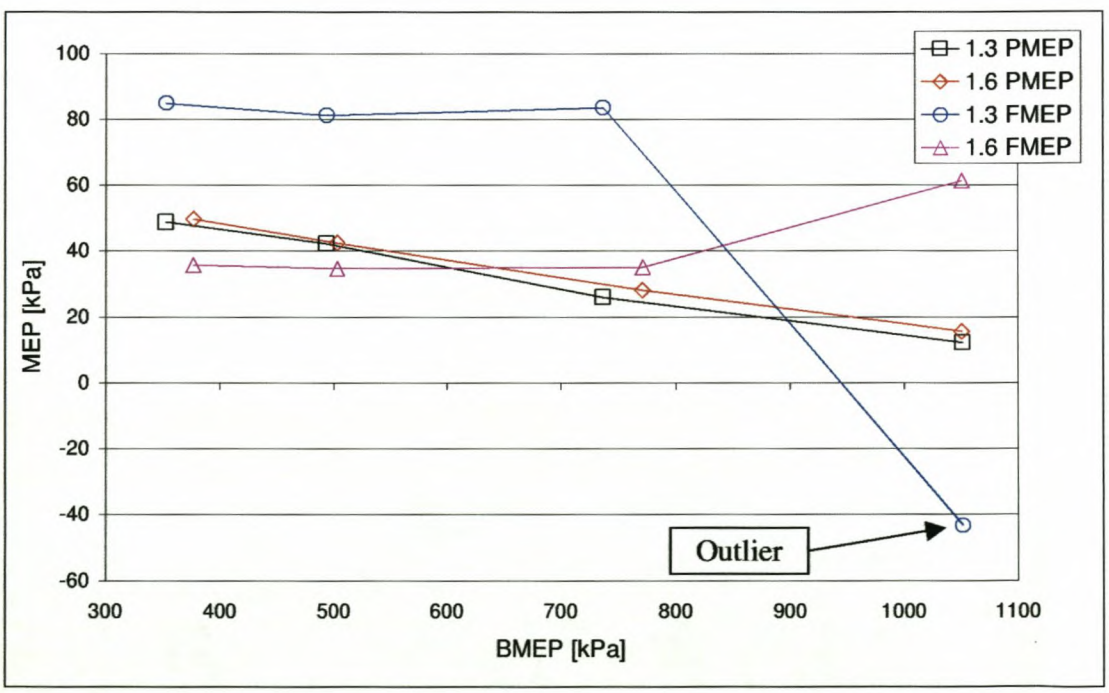

Figure 8-9: Pumping and friction mean effective pressures for 1.3L and 1.6L Rocam engines at 3000rpm. Data from heat release analysis

Friction mean effective pressure (fmep) of the 1.3L and 1.6L data follows a similar trend as Ferguson's graph, although the WOT data point for the 1.3L is suspect. The higher fmep of the 1.3L can be explained by the fact that the 1.3L engine is subjected to the same friction as is the 1.6L i.e. the friction to power ratio is higher for the 1.3L engine. Friction is calculated by subtracting brake work from indicated work as follows:

$$\text{fmep} = \text{imep}_{\text{net}} - \text{bmep} \tag{8-6}$$

The method for calculating brake work is straightforward and depends on the accuracy of torque measurement, which is assumed to be within 1% for the equipment used in this facility. The bmep is calculated as follows:

$$\text{bmep} = \frac{2 \cdot \pi \cdot T}{1000 \cdot V_d} \cdot [kPa] \tag{8-7}$$

The accuracy of fmep therefore depends on the accuracy of the calculated imep (net). Net imep is determined by subtracting the pmep from the gross imep which is the area under the pressure vs. volume graph during expansion minus the area during compression i.e. expansion work minus compression work. This value is therefore directly dependant on the accuracy of the in-cylinder pressure data. It is evident from Figure 8-9 that the fmep, and therefore the imep (net) at 3000rpm, wide open throttle (WOT) for the 1.3L is unexpectedly low. As the pmep at this load point for the 1.3L seems correct, it seems that the gross imep has been influenced by another factor, or was determined incorrectly due to faulty pressure measurements. This unexplained error recurred repeatedly in different tests at 3000rpm, WOT for the 1.3L engine, and is therefore not excluded from graphs.

8.5 Discussion of Data Integrity Check

The crank angle phasing of the pressure data has been proved to be correct as a log P vs. log V diagram has straight lines during compression and expansion phases. A possible effect of thermal strain effect is detected in this diagram, as curvature at the end of the expansion phase of the 1.3L data. Heat release analysis on the motored pressure data revealed that the heat transfer is accurate to within acceptable tolerance. Comparison of the motored (less thermal strain) and fired (more thermal strain effects) P vs. V graphs does not reveal extreme occurrence of thermal strain effects. Mean effective pressure data follow expected trends reasonably well except for the sudden drop in fmep of the 1.3L engine at 3000rpm, WOT. Data are thus considered to be valid with the exception of the 3000rpm at WOT for the 1.3L engine.

It should however be emphasised that an error in fmep does not mean that heat release is wrong. It is important to note that fmep calculation is far more sensitive to pressure data quality than is burn rate calculations.

9 EXPERIMENTAL RESULTS

The objective of the experimental testing is to determine the effect of the combustion chamber geometry on combustion chamber processes. Combustion chamber processes are characterised by the combustion analysis results as described in section 4. The main parameters are:

1. Cyclic variability
2. Induction period
3. Maximum heat release rate
4. Burn angle
5. Total heat released
6. Peak pressure and temperature

These parameters were determined from the in-cylinder pressure data by the heat release analysis software, Burnrate, developed for this project, using subroutines from the Racer, the combustion analysis code developed previously at the University of Stellenbosch.

Before analysing the combustion parameters of the engines, it is worth taking a look at the parameters measured directly from engine tests as opposed to combustion analysis results. The parameters investigated are mean effective pressures, volumetric efficiency, specific fuel consumption and thermal efficiency.

9.1 Indicated and Brake Mean Effective Pressures

Figure 9-1 is a comparison between the 1.3L and 1.6L brake mean effective pressures determined by torque measurement at different indicated manifold absolute pressures and 3000rpm. The effectiveness of mean effective pressure to compare engines of

different sizes is clear by noting the similarity in bmep's between the 1.3L and 1.6L data. It is very interesting to note the similarity in bmep at WOT. At WOT bmep for the 1.3L is 1051.7kPa and that of the 1.6L is 1051.2kPa.

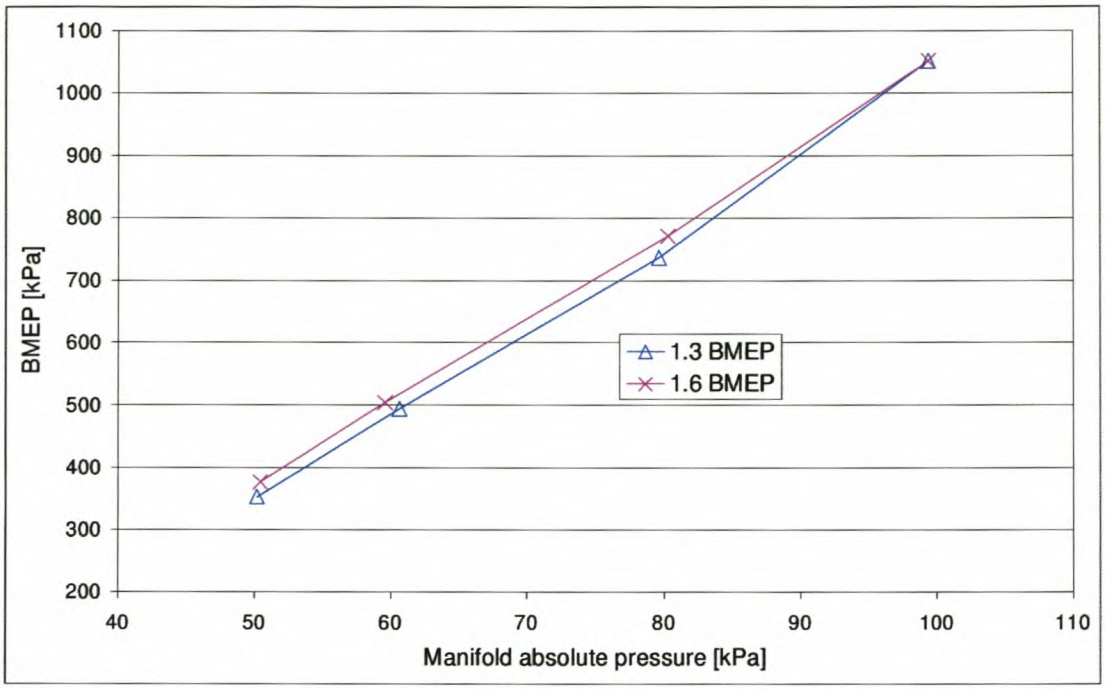

Figure 9-1: Comparison between 1.3L and 1.6L brake mean effective pressures at 3000rpm for different load settings

Figure 9-2 illustrate the difference in indicated work between the two engines. This highlights that more work is done by the working gas in the 1.3L engine to achieve the same output as the 1.6L engine. Higher specific friction losses in the 1.3L than in the 1.6L could be the cause of the bmep to be the same despite the higher imep. This mainly occurs due to the fact that the 1.3L is subjected to the same camshaft torque, water pump and oil pump work as the 1.6L, although it is a smaller engine.

It is noted from Figure 9-2 that the unexpectedly low imep at WOT is the source of the low friction found at this data point in Figure 8-9.

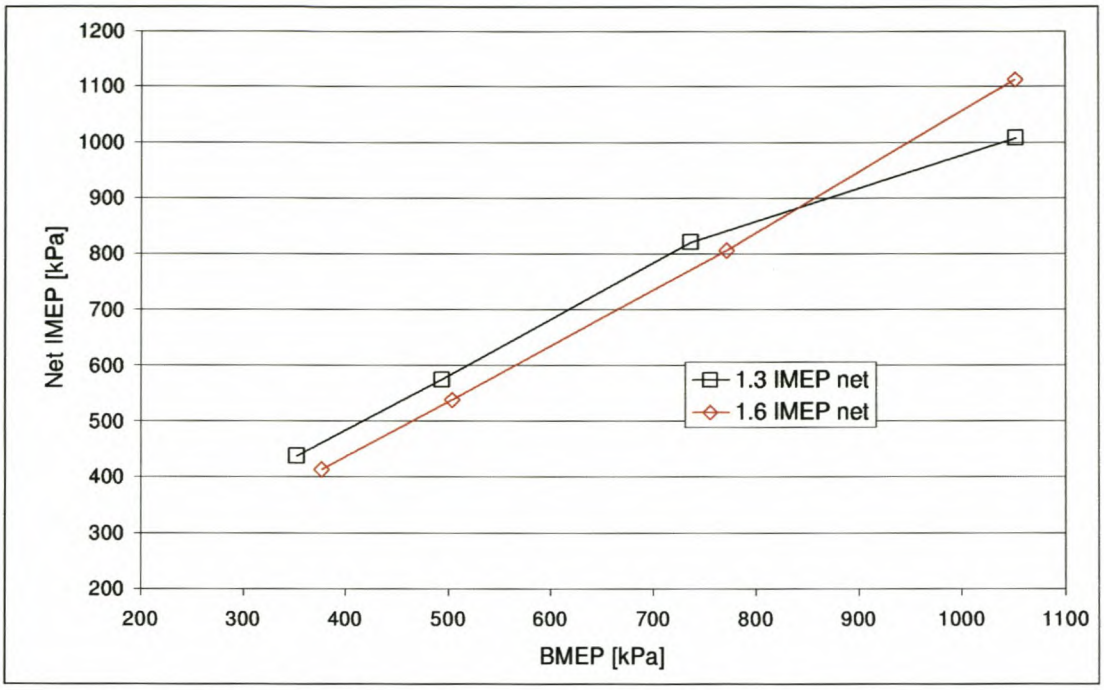

Figure 9-2: Net imep vs. bmep comparison between 1.3L and 1.6L engines at 3000rpm

9.2 Pumping Mean Effective Pressure

Pumping work is that work required to draw air into the cylinder through the intake port during the intake stroke and to expel air through the exhaust port during the exhaust stroke. On the intake side flow is mostly restricted by the air filter, throttle, intake manifold, the intake port and valve and on the exhaust side by the exhaust valve, port, manifold and the exhaust system.

Figure 9-3 illustrate the pumping work for both engines vs. bmep. Although the intake port to cylinder diameter of the 1.3L is lower than that of the 1.6L, the 1.6L engine has a higher volume throughput with the same exhaust port diameter and exhaust system as the 1.3L engine, causing increased pumping work. This indicates that the 1.6L exhaust system may not be optimal for this engine.

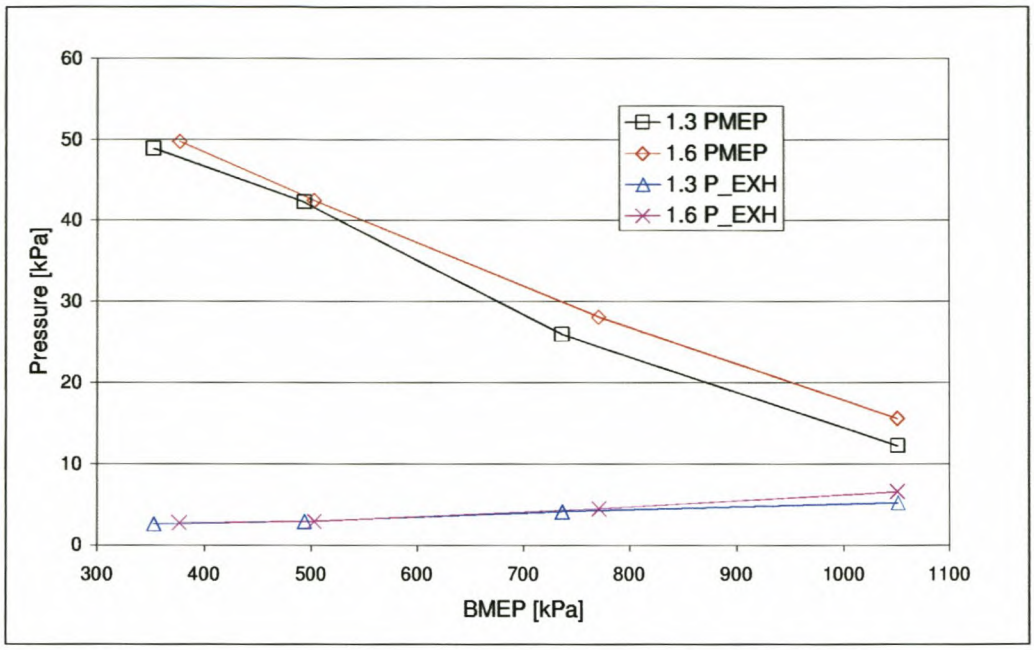

Figure 9-3: Comparison between pumping work done vs. bmep by the 1.3L and 1.6L engines

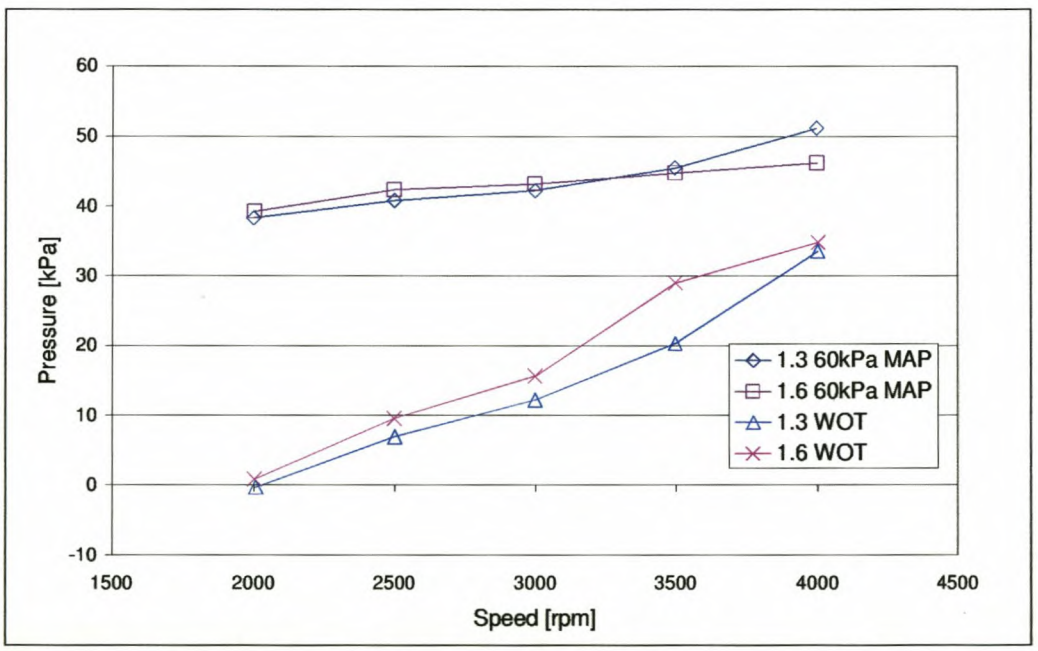

Figure 9-4: Comparison between pmep for the 1.3L and 1.6L engines vs. speed at 60kPa manifold absolute pressure and WOT

Figure 9-4 illustrate how pmep increase with increasing engine speed for the 1.3L and 1.6L, especially at WOT. At 4000rpm there is a reduction in the 1.6L pmep with respect to the 1.3L. This is the speed where the maximum torque is achieved, i.e. the engine

manifold and exhaust pipe lengths and diameters were tuned to achieve this as illustrated in chapter 2. This effect is illustrated further in Figure 9-6 comparing the in-cylinder pressure data of the 1.3L and 1.6L at 4000rpm WOT as pressure vs. direct angle between tdc and the crank. The reduced pressure at the end of the exhaust stroke of the 1.6L is a result of tuning the 1.6L exhaust pipe length for optimum torque at this speed.

The effect of speed on exhaust backpressure is illustrated in Figure 9-5. Volumetric flow rate of air increase almost linearly with speed, causing an exponential increase in flow resistance or in this case exhaust backpressure in obedience to the Bernoulli equation. The increased fluid flow through the 1.6L with exhaust diameter the same as the 1.3L is responsible for the increased exhaust backpressure of the 1.6L engine.

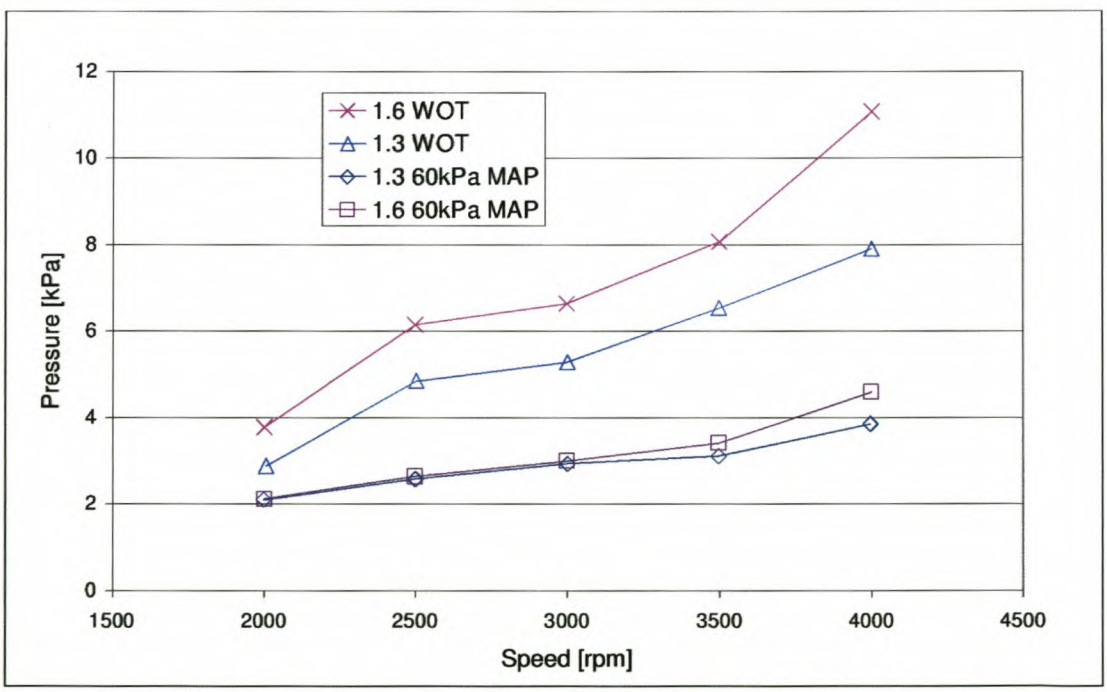

Figure 9-5: Exhaust backpressure vs. speed at part load and WOT for the Rocam 1.3L and 1.6L engines

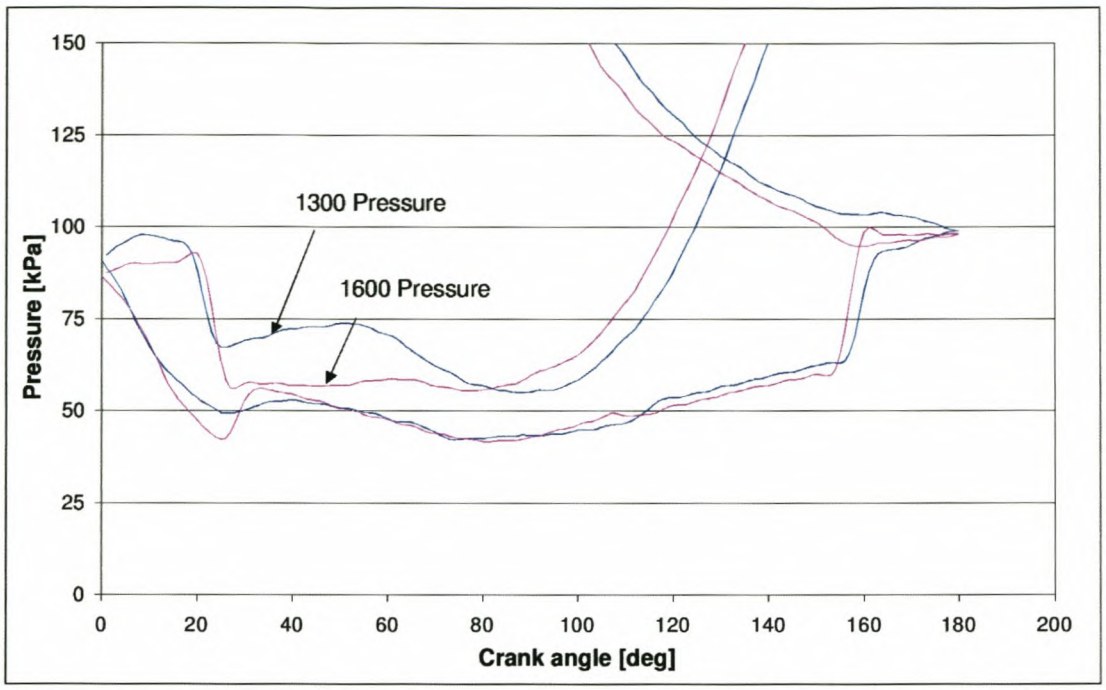

Figure 9-6: Comparison between in-cylinder pressure data at 4000rpm WOT of 1.3L and 1.6L Rocam engines

9.3 Volumetric Efficiency

Volumetric efficiency is a measure of the amount of air that the engine pumps through it versus the capacity of the engine. It is measured here by determining the mass flow rate of fuel and, from the air-fuel ratio, deducing the air flow rate. Ferguson (1986) deduced the stoichiometric fuel-air ratio for iso-octane as 0.0665 and this value is used for these exercises.

$$\eta_{vol} = 100 \cdot \frac{120 \cdot \left(\dot{m}_a + \dot{m}_f \right)}{\rho \cdot V_d \cdot N} \tag{9-1}$$

With density determined from manifold conditions and air flow determined from:

$$\dot{m}_a = \lambda \cdot \frac{\dot{m}_f}{0.0665} \tag{9-2}$$

Figure 9-7 indicates increased volumetric efficiency for the 1.3L over the 1.6L at 3000rpm part load, but at high load the 1.6L volumetric efficiency is higher than that of the 1.3L.

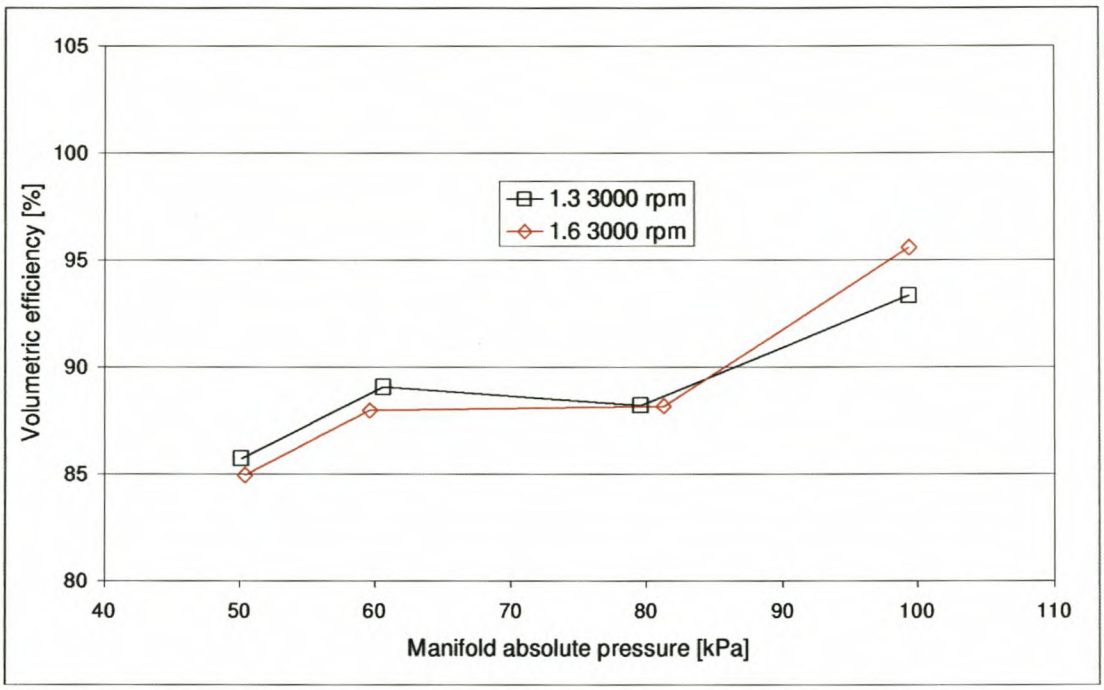

Figure 9-7: Volumetric efficiency vs. MAP at 3000rpm comparison between 1.3L and 1.6

The effect of speed on volumetric efficiency at part load and WOT is illustrated by Figure 9-8. The 1.3L volumetric efficiency increases steadily with speed at part load, whereas the 1.6L volumetric efficiency fluctuates. The increased volumetric efficiency of the 1.6L at 4000rpm is achieved by dynamic effects in the piping i.e. more air is pumped into the combustion chamber by making use of pressure pulses timed by the lengths of pipes in the intake and exhaust systems. At WOT the 1.6L volumetric efficiency is higher than that of the 1.3L engine from 2000 to 4000rpm. The more open design of the 1.6L combustion chamber could be responsible for this gain.

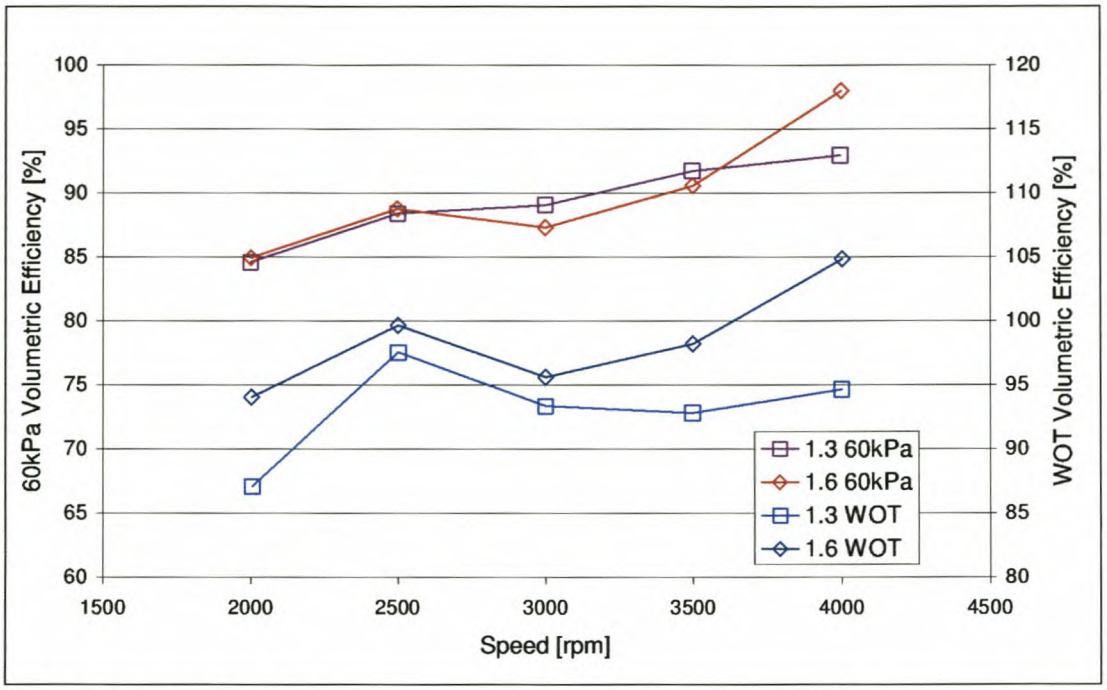

Figure 9-8: Volumetric efficiency vs. speed at 60kPa manifold pressure and WOT comparison between 1.3L and 1.6

These results are as expected as it is assumed that the 1.6L was optimised for better performance while the 1.3L was optimised for better combustion i.e. lower emissions levels. The 1.3L engine therefore induces more turbulence on the incoming air stream, which is done by restrictions on the airflow, thereby causing poor volumetric efficiency, especially at wide open throttle.

9.4 Specific Fuel Consumption and Thermal Efficiency

Measures of an engines ability to make use of chemical energy are the specific fuel consumption and the thermal efficiency. The gross indicated work produced by an engine approach a maximum as the cycle approach the Otto cycle and to achieve this as much as possible heat must be released close to tdc, which can be achieved by as short as possible burn angle at optimum ignition timing. The output power of the engine is however also influenced by heat transfer, friction and pumping work, and therefore the SFC and thermal efficiency is the net effect of mainly imep, pmep and fmep.

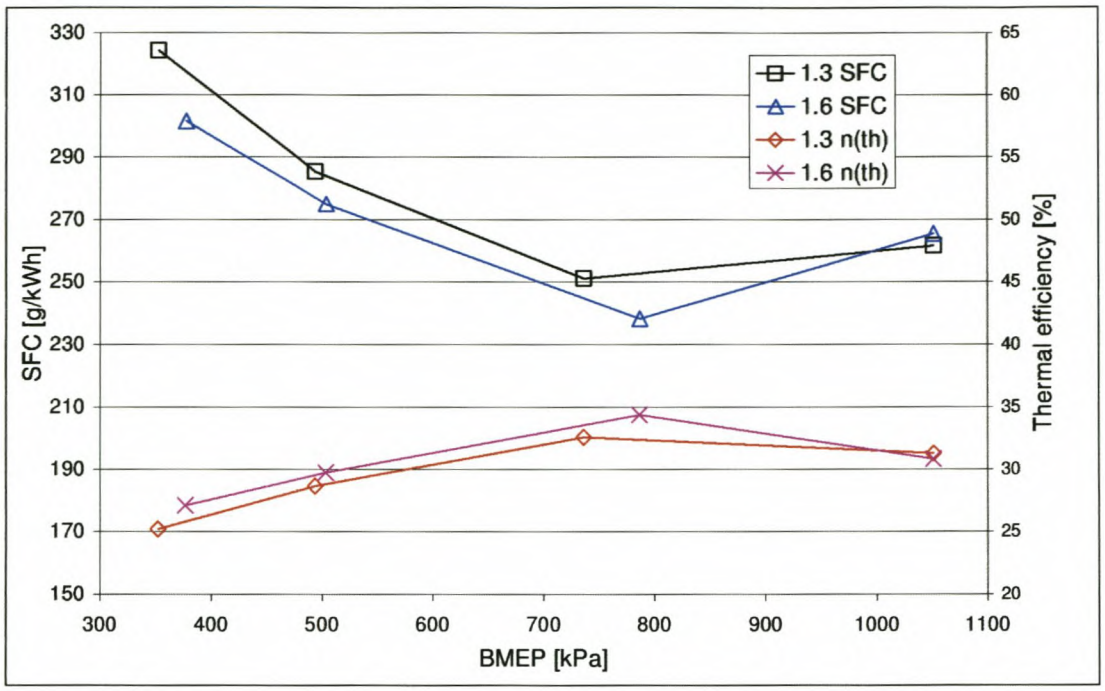

Figure 9-9: Comparison between 1.3L and 1.6L specific fuel consumption and thermal efficiencies vs. bmep at 3000rpm

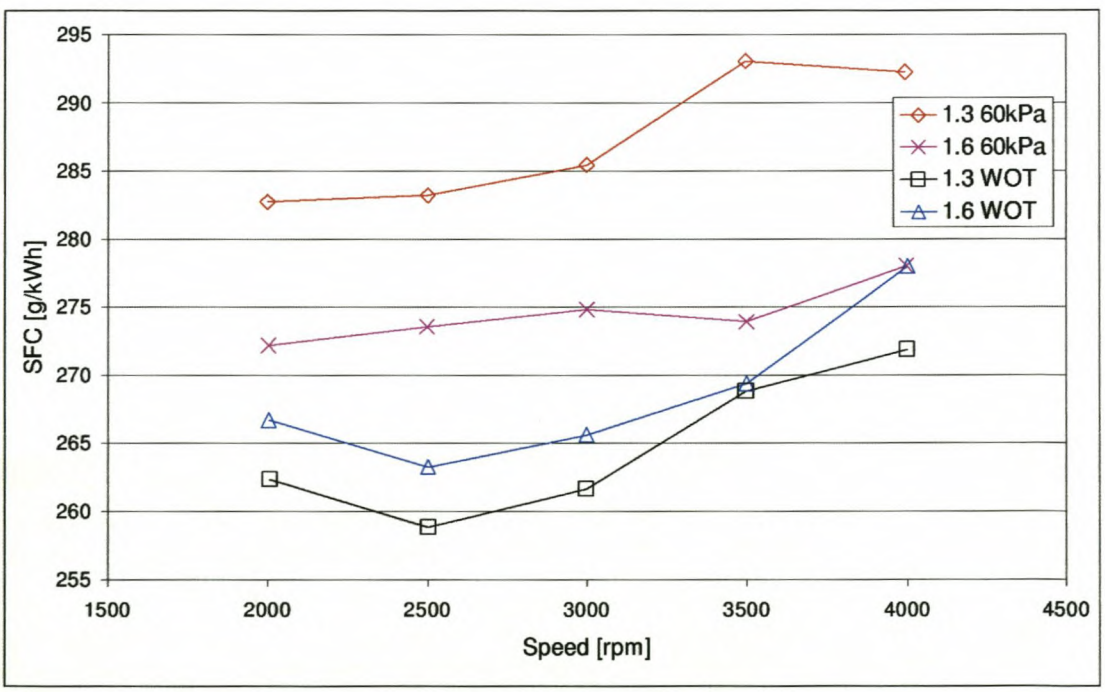

Figure 9-10: Comparison between 1.3L and 1.6L SFC vs. speed at 60kPa MAP and WOT

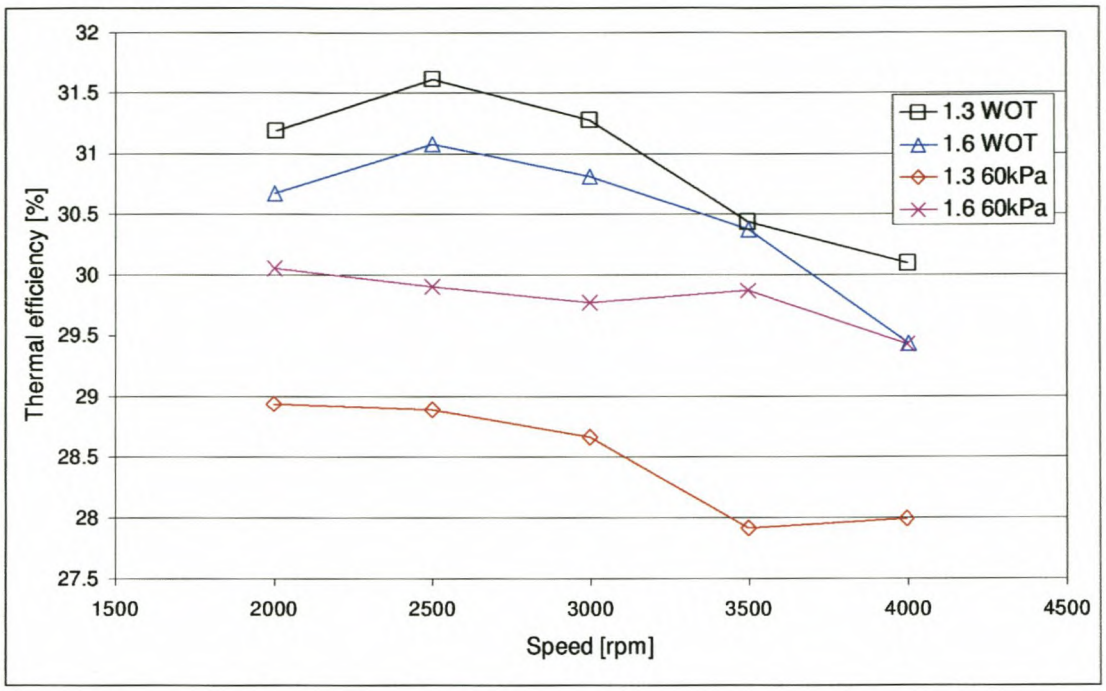

Figure 9-11: Comparison between 1.3L and 1.6L thermal efficiency vs. speed at 60kPa MAP and WOT

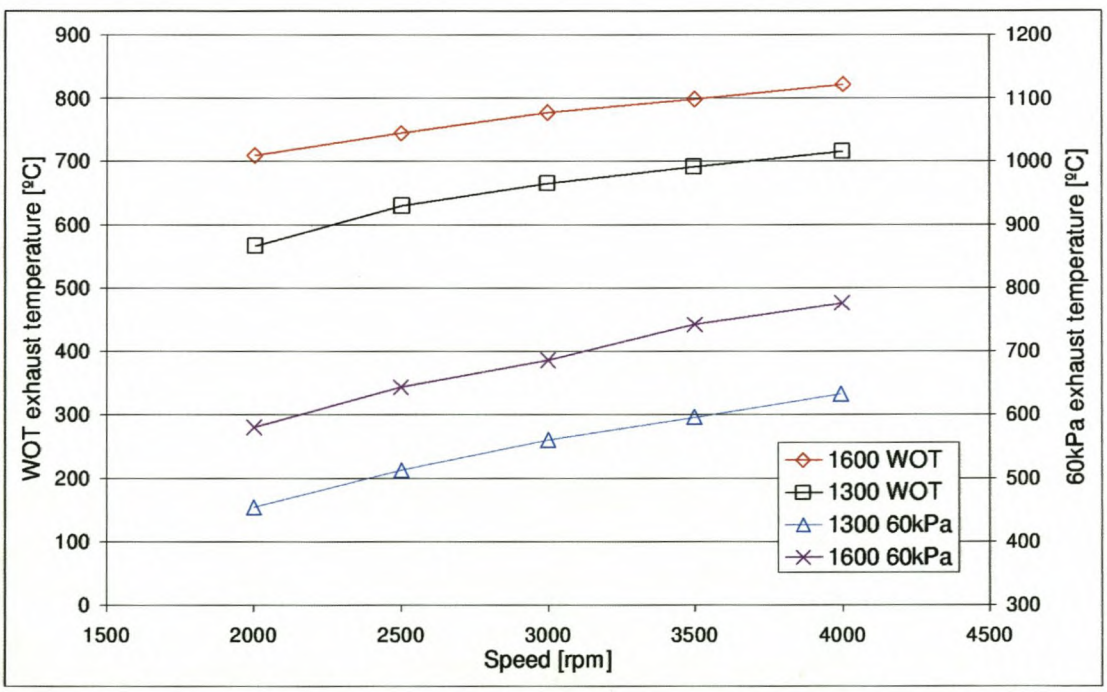

Figure 9-12: Exhaust gas temperature comparison between 1.3L and 1.6L at WOT and 60kPa MAP for different speeds

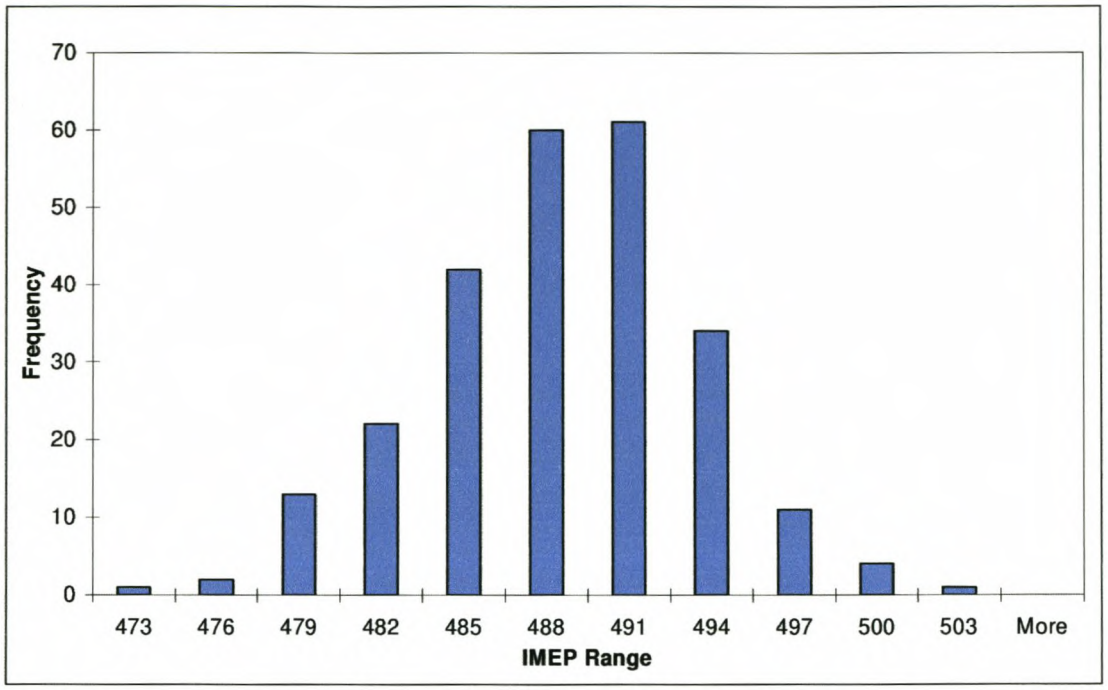

Figure 9-13: Histogram of cyclic variability of imep for 1.3L at 50kPa MAP 3000rpm

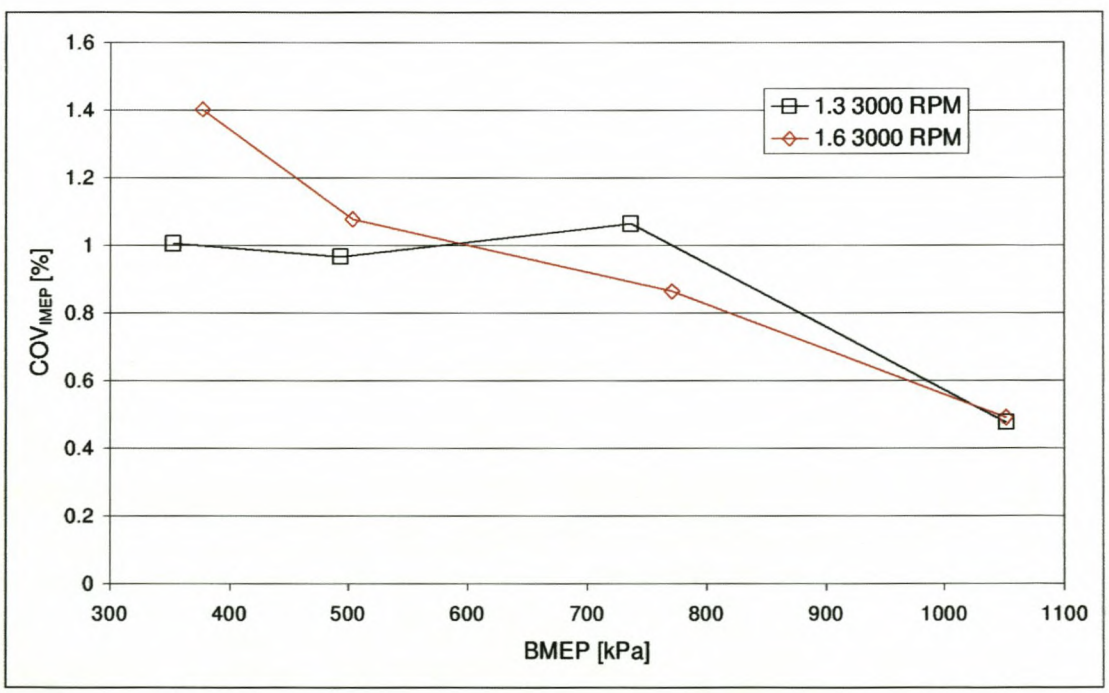

Figure 9-14: Coefficient of variation vs. bmep: 1.3L vs. 1.6

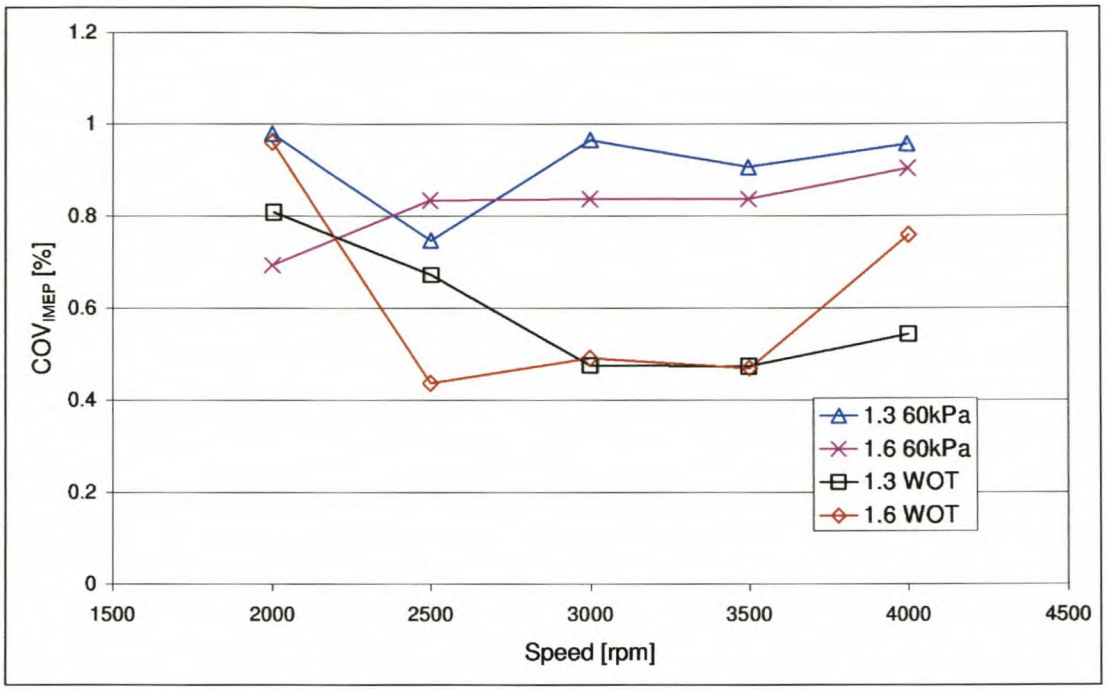

Figure 9-15: Coefficient of variation vs. speed at different loads: 1.3L vs. 1.6L engines

As is evident from Figure 9-15 cyclic variability of the 1.3L seems worse on average than that of the 1.6L at part throttle. Through most of the speed range, the 1.3L has equal or lower cyclic variability at WOT than the 1.6L. This may be a result of better fuel mixing due to the increased motion of air in the 1.3L combustion chamber, especially at WOT and increased speed.

9.6 Burn Angle and Induction Period

A major parameter that is optimised when optimising combustion and especially emissions of an engine is the burn angle. The ideal cycle in the spark ignition combustion engines is the Otto cycle where all the energy is released at tdc. In order to approach this cycle and therefore the ideal efficiency, the burn angle should be as short as possible and timed to occur close to tdc. Burn angle is influenced by the speed at which combustion occurs and parameters that influence it are discussed in more detail in section 4 of this literature. For the purpose of this exercise, the 5 to 95% burn angle and the 0 to 5% induction period is chosen for comparing combustion between engines. Due to the difference in bore size of the two engines a normalisation is applied to the burn

angles of the 1.3L in order to compare the two as follows:

$$\theta_{BURN(1300\_NORMALISED)} = \theta_{BURN(1300)} \cdot \frac{D_{(1600)}}{D_{(1300)}} \qquad (9\text{-}4)$$

With $D_{(1.3L)}$ and $D_{(1.6L)}$ the maximum distance of flame travel from the spark plug to the opposite side of the combustion chamber for the 1.3L and 1.6L engines respectively. As this is not a verified normalisation technique, the normalised data will be presented with the measured data when results are considered for informative purposes only.

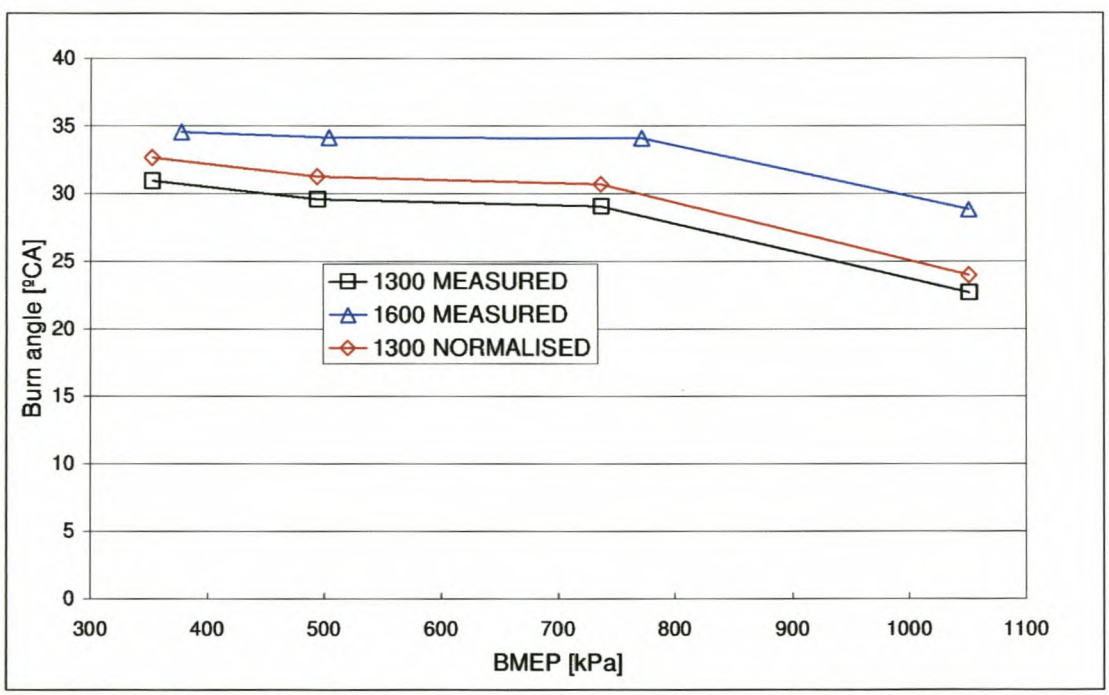

Figure 9-16: Burn angle and induction period vs. bmep at 3000rpm. 1.3L and 1.6L engine data

Figure 9-16 illustrate the measured and normalised burn angle vs. bmep for the 1.3L and 1.6L engines at 3000rpm. It is clear that the 1.3L burn angles are shorter than that of the 1.6L, even when normalised. The difference between the 1.3L and 1.6L burn angles increase with increasing load. The higher compression ratio of the 1.3L plays a significant role in the shorter burn angle. Another effect that would reduce the burn angle at increasing load is increased fluid motion during the intake and compression

strokes causing swirl and increased turbulence that assist in flame propagation. This effect is thought to increase with increasing load as a result of higher mass flow. It is also clear that burn angles for both engines decrease with increasing load. This is due to the increasing pressure and temperature in the combustion chamber at high load.

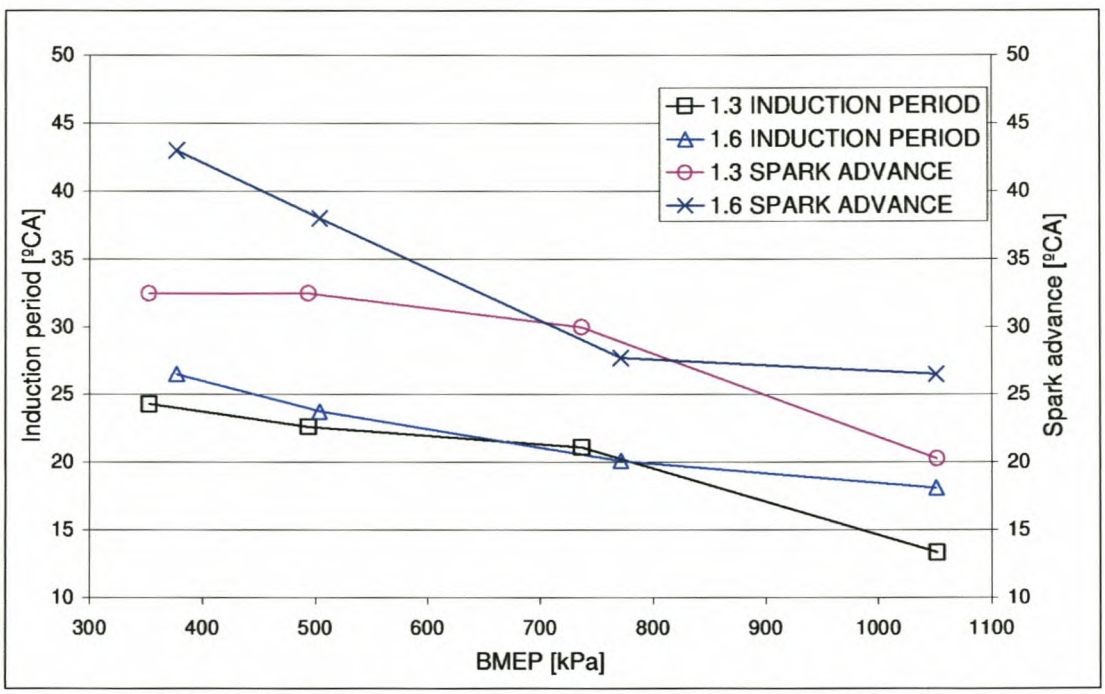

Figure 9-17: Induction period and spark advance vs. bmep at 3000rpm for 1.3L and 1.6L engines

Figure 9-17 indicates the induction periods and spark advance settings for the 1.3L and 1.6L vs. bmep at 3000rpm. Through most of the load range the 1.3L has a shorter induction period than the 1.6L. The WOT induction period of the 1.3L is extremely low. This may be the effect of increased turbulence generation at the ignition region by the 1.3L combustion chamber. Note that the spark advance at this point is 6° more retarded for the 1.3L than that of the 1.6L.

Figure 9-18 and Figure 9-19 illustrate burn angles vs. speed for the 1.3L and 1.6L at part load and WOT respectively. The 1.3L measured and normalised burn angles are shorter than the 1.6L burn angles throughout the testing range.

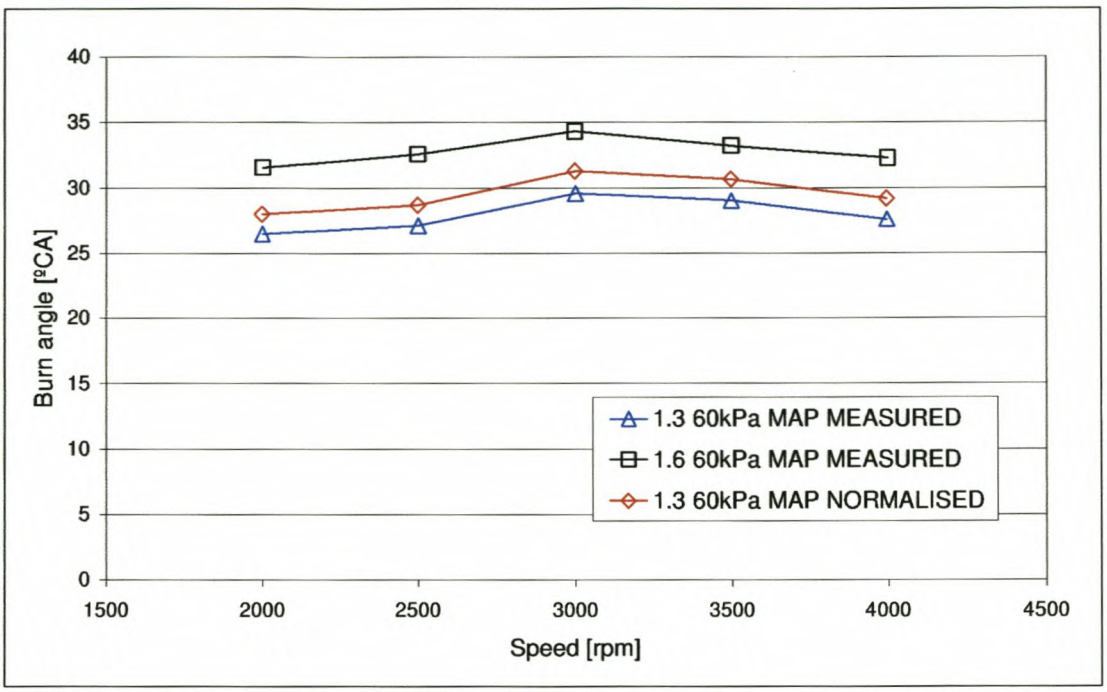

Figure 9-18: Measured and normalised burn angle vs. speed comparison between 1.3L and 1.6L at 60kPa manifold pressure

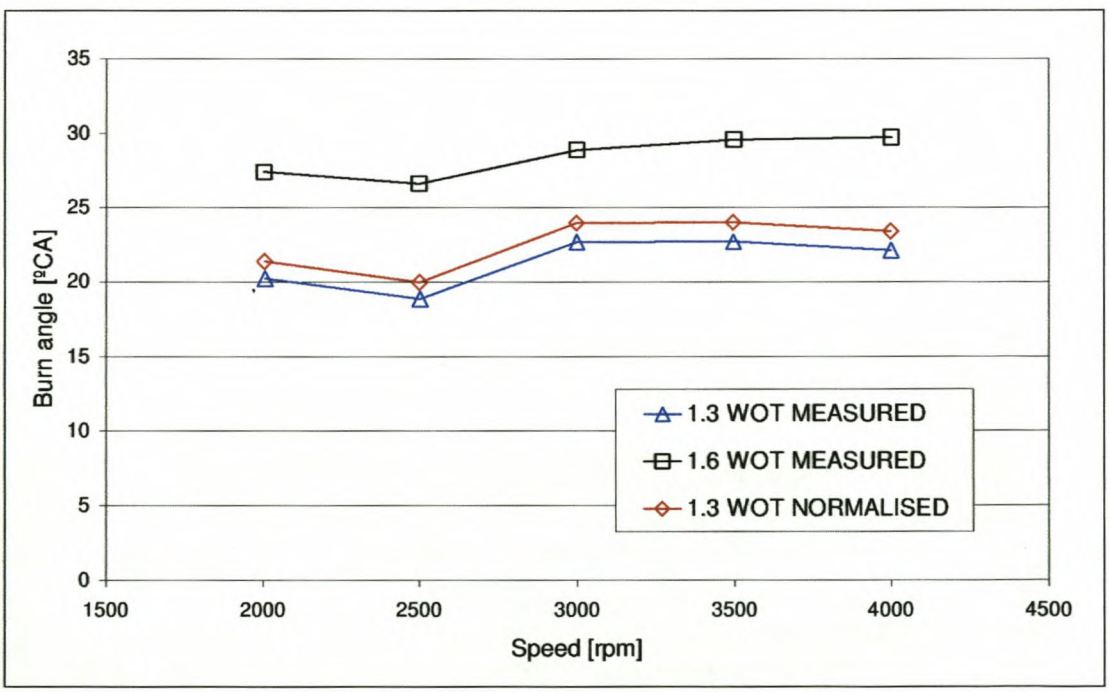

Figure 9-19: Measured and normalised burn angle vs. speed comparison between 1.3L and 1.6L at WOT

At WOT the effect of speed and therefore more turbulence in the combustion chamber is to reduce the 1.3L burn angle whereas that of the 1.6L increase with increasing speed at WOT.

Figure 9-20 illustrate the 1.3L and 1.6L induction periods vs. speed at 60kPa MAP and WOT. At 60kPa MAP the 1.3L and 1.6L induction periods do not differ significantly. The slopes of the 1.3L induction period curves with speed are more negative than that of the 1.6L indicating that the effect of speed is to generate more turbulence in the 1.3L whereas this effect is reduced for the 1.6L. At WOT the 1.3L induction periods are shorter throughout the entire range of speeds tested. The major cause of this would be the result of the increased compression ratio of the 1.3L engine.

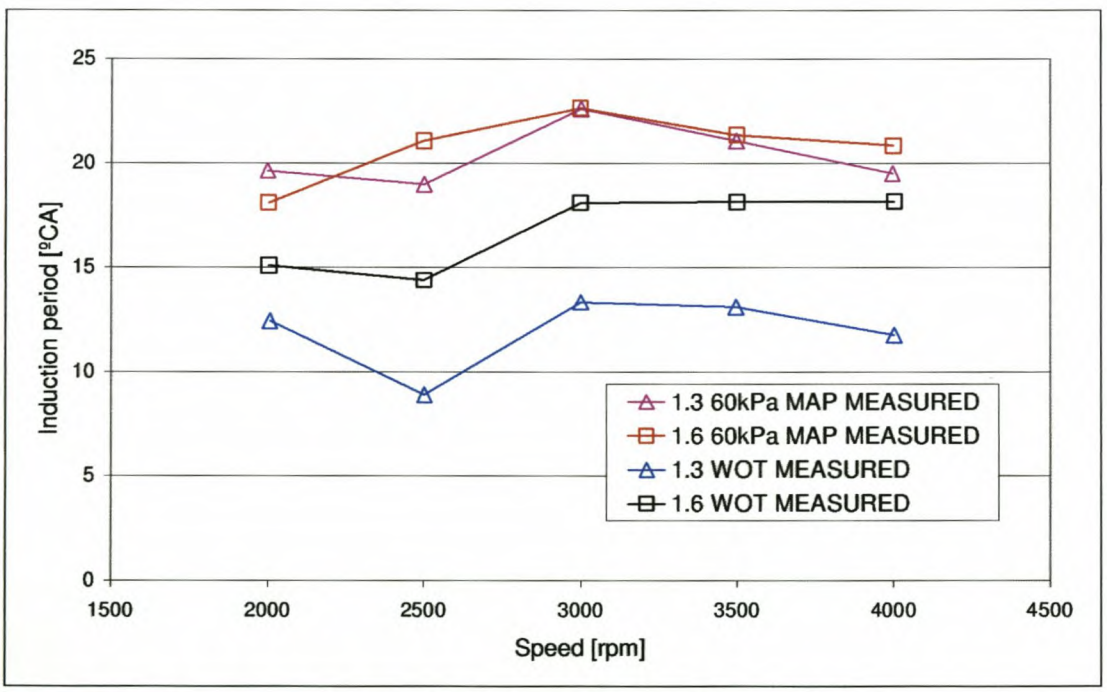

Figure 9-20: Induction periods vs. speed for 1.3L and 1.6L at part load and WOT

9.7 Maximum Gas Pressure and Temperature

The maximum in-cylinder pressure is dependant on both the compression ratio of the engine and the rate of heat release. If heat is released faster, then cylinder pressure rises more rapidly close to tdc and therefore cause higher maximum pressures. The effect of increasing volumetric efficiency will be to increase the mass of fuel and air in the combustion chamber and subsequently cause an increase in the maximum pressure.

Figure 9-21 illustrates the higher maximum pressure in the 1.3, which is attributable to both compression ratio and faster burning. The higher volumetric efficiency of the 1.6L at WOT causes an increase in the maximum pressure as is evident by the rise in the slope of the maximum pressure curve in Figure 9-21. The WOT maximum temperatures of the 1.6L are higher than that of the higher compression ratio 1.3L engine, which is most likely caused by slow burning, i.e. fuel burning at the later stage of expansion. This effect is well illustrated by Figure 9-22 showing the angle where the maximum pressures and temperatures for both engines occur.

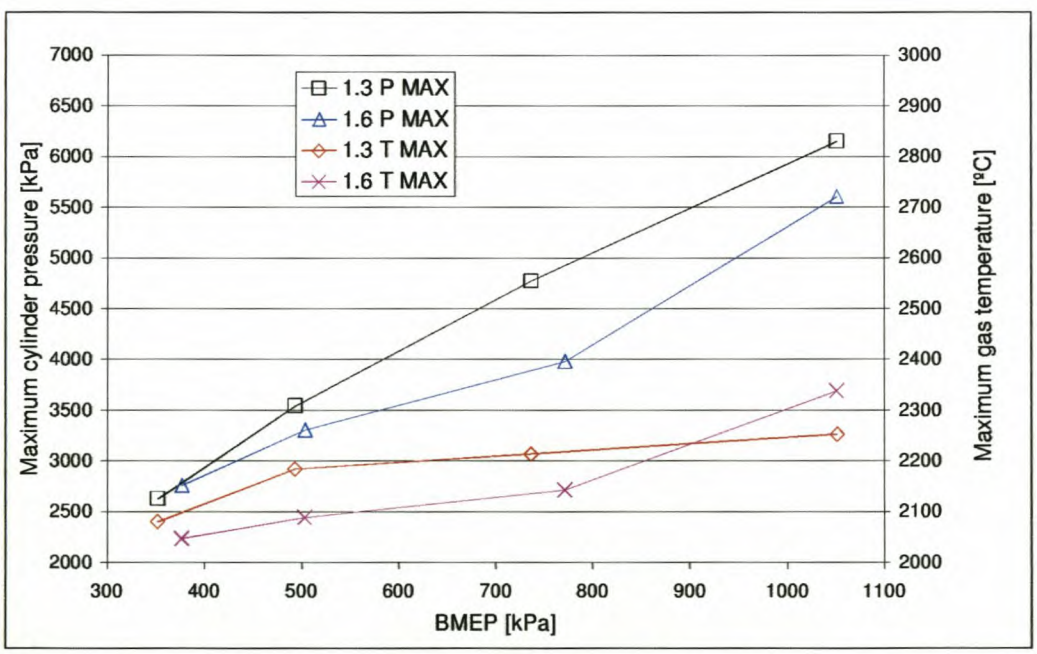

Figure 9-21: Maximum in-cylinder pressure and temperature vs. load at 3000rpm: comparison between 1.3L and 1.6L engines

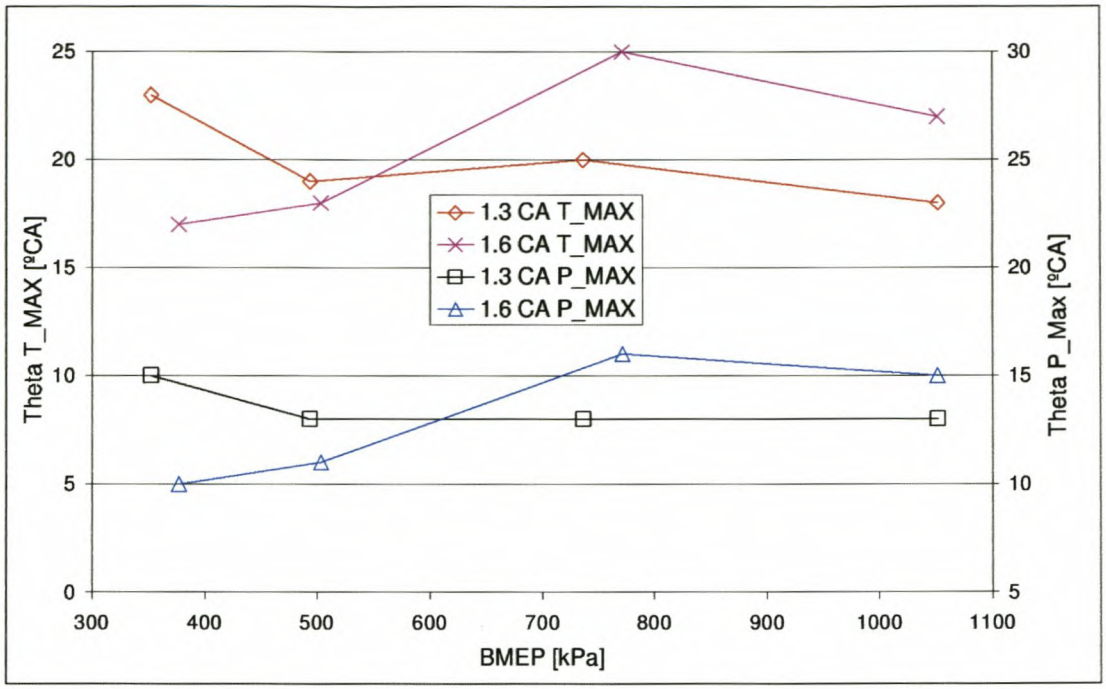

Figure 9-22: Crank angle where maximum pressure and temperature occur vs. bmep at 3000rpm for 1.3L and 1.6L engines

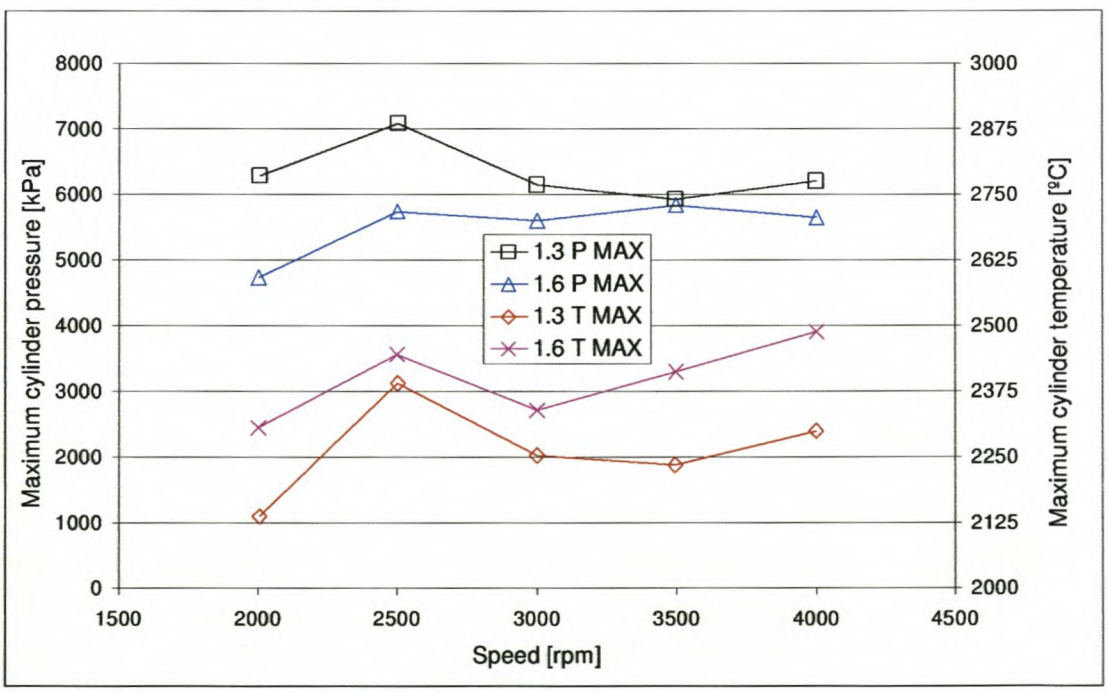

Figure 9-23: Maximum gas pressures and temperatures vs. speed at WOT in the 1.3L and 1.6L engines

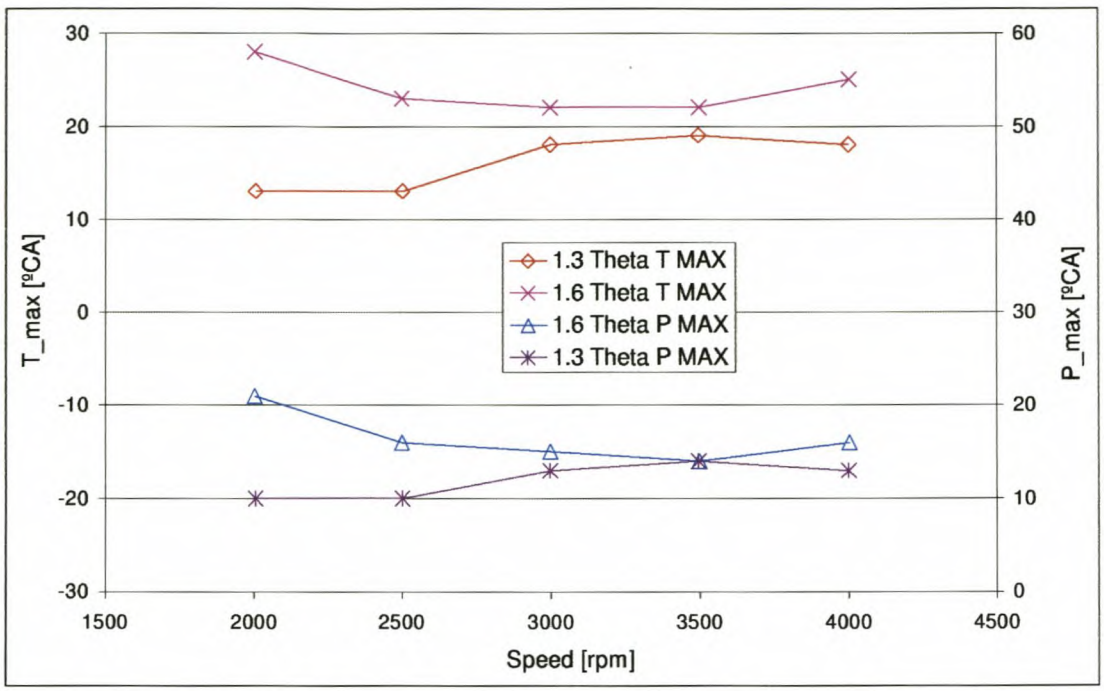

Figure 9-24: Crank angle where maximum pressures and temperatures occur vs. speed at WOT

Figure 9-23 indicates that the peak pressure of the 1.6L decrease at 4000rpm while the maximum temperature increases. This is an effect that is most likely caused by slower burning with increasing speed in the 1.6L, which is evident from Figure 9-24 illustrating the angle where maximum pressure and temperatures occur. The 1.3L engine, generating more turbulence in the combustion chamber at increased speed, does not show the trend of the decreasing maximum pressure at 4000rpm.

Figure 9-25 and Figure 9-26 illustrate the maximum gas pressures and temperatures and their respective angles of occurrence at 60kPa MAP vs. increasing speed. It is clear that for both engines the maximum temperatures and pressures increase with increasing speed. Maximum pressure in the 1.3L chamber is constantly higher than that in the 1.6L. A likely cause is the faster burning in the 1.3L, also evident from the higher maximum temperature in the 1.3L chamber.

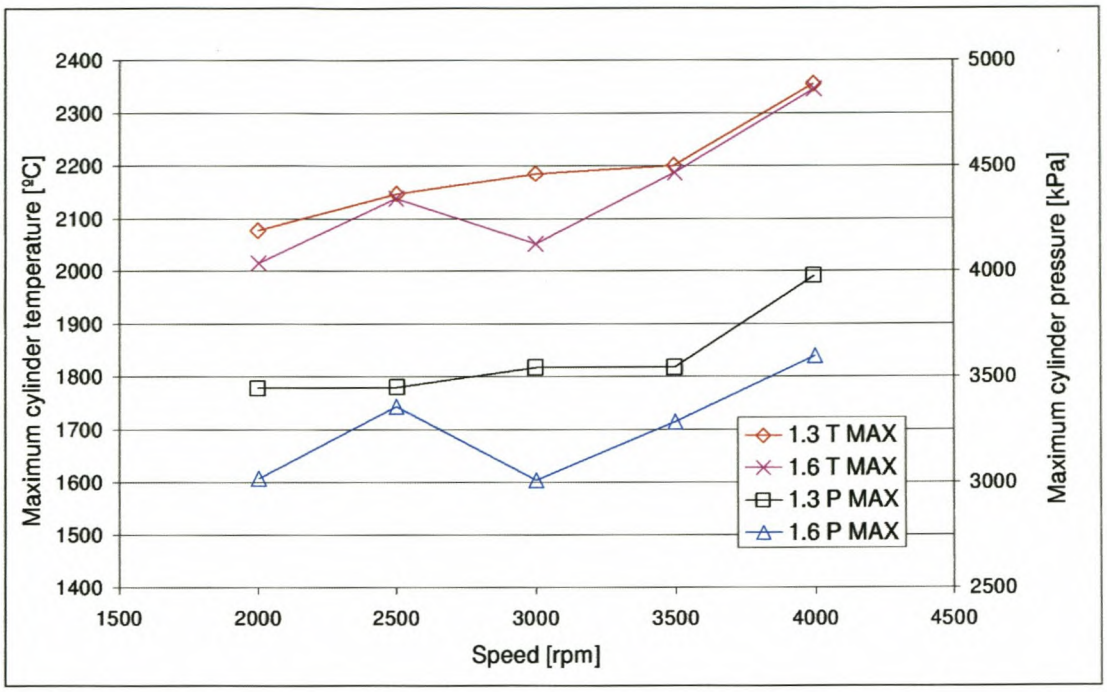

Figure 9-25: Maximum gas pressures and temperatures vs. speed at 60kPa MAP in the 1.3L and 1.6L engines

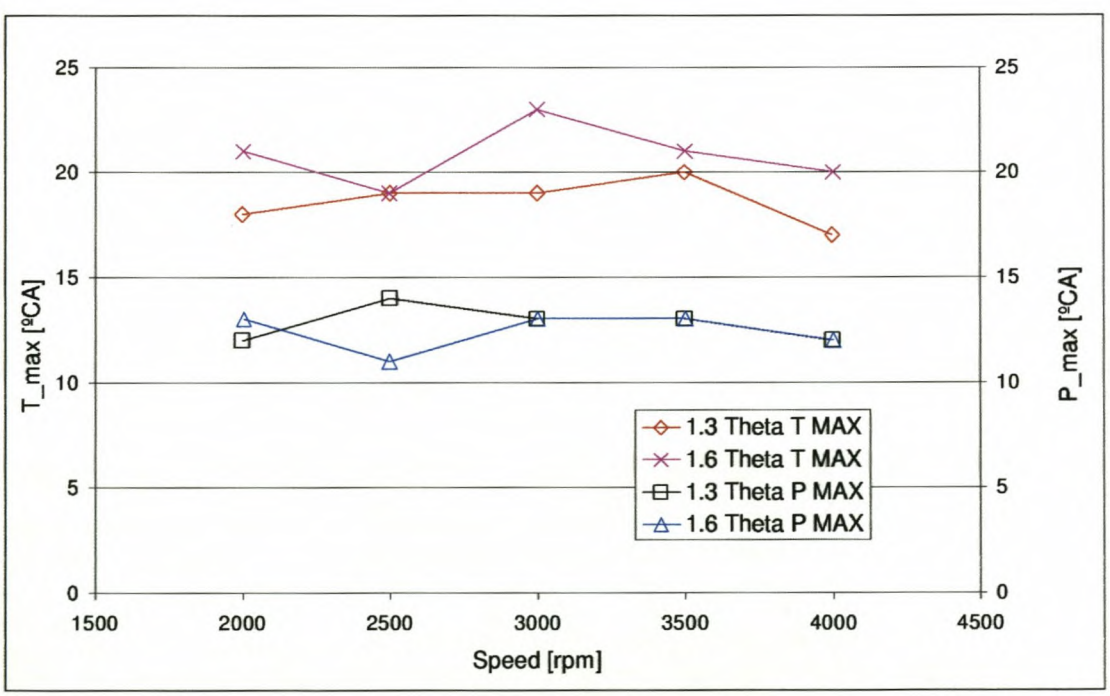

Figure 9-26: Crank angle were maximum pressures and temperatures occur vs. speed at 60kPa MAP

Maximum gas temperature and pressure is influenced by spark timing and fuel mixture. Advancing the spark timing physically moves the pressure increase due to combustion into phase with the pressure increase due to compression and therefore the peak pressure increases. Accordingly the temperature will also increase (see Figure 9-27).

When fuelling is decreased, the amount of oxygen that is burned, decrease accordingly and this causes a reduction in maximum pressure and temperature as the mixture is leaned out as seen in Figure 9-28. This is in contrast to the exhaust temperature that reaches a maximum for a stoichiometric mixture and decrease with both increasing or decreasing lambda as seen in Figure 9-28. The decrease in exhaust temperature due to richening of the mixture is the effect of evaporative cooling by the excess fuel as it is clear from Figure 9-28 that the cumulative heat released increases when lambda decreases.

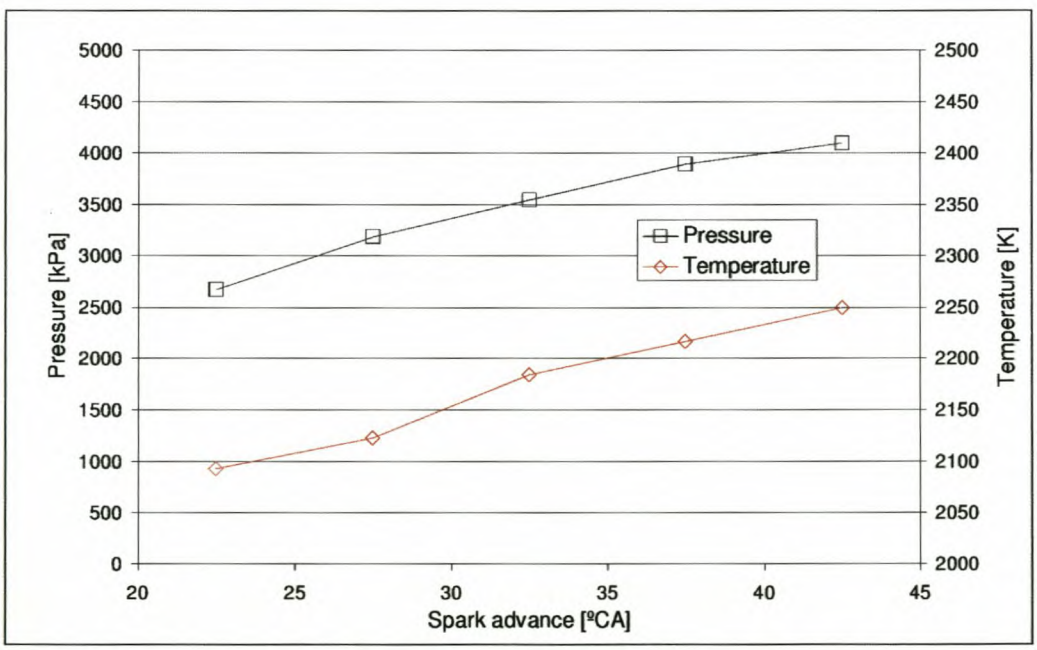

Figure 9-27: Peak gas pressure and temperature as influenced by spark advance for the 1.3L engine at 3000rpm part load

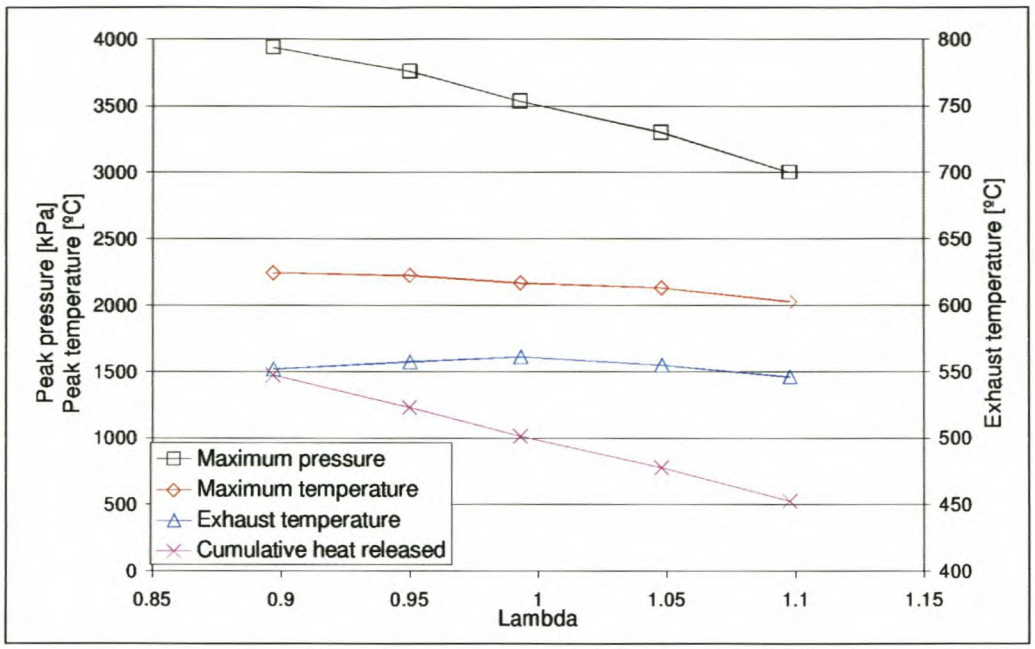

Figure 9-28: Peak cylinder pressure and temperature vs. lambda at 3000rpm part load for the 1.3L engine

9.8 Discussion of Experimental Results

The mean effective pressure data implied that friction in the 1.3L is slightly more than that of the 1.6L, mainly caused by a higher friction to power ratio i.e. the proportional crankshaft, piston, camshaft and auxiliary friction is higher for the 1.3L than for the 1.6L engine. The pumping work for the 1.6L engine seems higher than that of the 1.3L as a result of the more restrictive exhaust port and system. The 1.6L exhaust system seems to be well tuned for 4000rpm.

Volumetric efficiency for the 1.3L is slightly higher than that of the 1.6L at part load whereas the 1.6L engine has superior volumetric efficiency at WOT, especially at high speed. This is the effect of the more open geometry of the 1.6L combustion chamber.

The 1.6L engine is the more efficient of the two at part load, mainly due to the reduced friction playing a substantial role at part load. The 1.3L engine is more efficient than the 1.6L at full load, indicating that the effect of more efficient combustion overcomes the effect of increased friction at WOT, especially at low speed where the shrouding generates more turbulence in the 1.3L.

The 1.3L engine proved to be more stable at part load than the 1.6L, possibly due to better fuel-air mixing in the 1.3L than in the 1.6L at part load, but at high load the cyclic variation of both engines is similar, indicating that both induce enough turbulence.

The 1.3L engine has shown shorter burn angles than the 1.6L throughout the testing range, even when corrected for difference in cylinder bore. The effect of the compression ratio will be partly responsible for this. It was seen though that increasing speed has the effect of shortening the 1.3L burn angle and increasing the 1.6L burn angle, indicating that the increased fluid motion and turbulence generated in the 1.3L chamber reduce burn angles for this engine. Induction periods for both engines are similar at part throttle, mainly because compression ratio and cylinder bore does not play a major role in these conditions, and the effect of the 1.3L combustion chamber to increase fluid motion and turbulence only shows visible differences at WOT and increased engine speed. At WOT the induction period for the 1.3L is reduced due to these effects, and the compression ratio effect to increase the un-burned fluid temperature. As speed increases the 1.3L induction period decreases significantly more than that of the 1.6L at both part and full load, indicating the effect of the 1.3L geometry of increasing turbulence and thereby induction period decrease with increasing speed.

The 1.3L maximum cylinder pressures are higher than that of the 1.6L at all of the tested points, although the same does not apply to maximum temperatures. The 1.6L has increased maximum temperatures at WOT and at 60kPa the maximum temperatures of the two engines are similar throughout the speed range tested. The maximum temperature of the 1.6L also occurs later in the cycle for most of the data. This is an indication of slower burning of the 1.6L and will have the effect of decreasing efficiency and increasing the emissions of nitrogen oxides.

10 FLOW PROCESS SIMULATION

This section describes the majority of the steps taken in order to perform a numerical simulation of the flow processes in the combustion chamber. A brief overview is given of the software tools used and developed. The process of defining the mathematical model is then described starting with the strategic planning, geometry definition and mesh generation. Details on the thermodynamic and physical fluid and flow properties, solution parameters and boundary and initial conditions are then supplied. The numerical simulation results are processed, graphical and numerical results are extracted and presented. These results are firstly discussed in isolation from the experimental results and then compared to the latter.

10.1 Numerical Simulation Tools

10.1.1 Software

StarCD v 3.10B (1999)

The three-dimensional CFD code StarCD was used in conjunction with the pre- and post processing software ProStar to build the combustion chamber mesh, perform flow calculations and post process the results. ProStar is used to set up the mesh and define the fluid properties, flow properties and boundary conditions. As this computation involves a moving mesh, ProStar is run in conjunction with Star solver when performing a simulation.

Ricardo Wave v 3.6 (2000)

Due to the simplicity of the pipe network around the combustion chamber, flow calculations in these regions were done with a one-dimensional flow simulation tool developed by Ricardo software namely Ricardo Wave (2000). This simulation provides boundary conditions for the three-dimensional StarCD flow simulation.

ProEngineer 2001 Educational (2001)

The computer aided design (CAD) package ProEngineer was used for the purpose of fixing geometrical errors in the imported files from the engine manufacturer. The flow

domain is also broken down into the relevant sub regions described later in this section with this package and solid geometry of each region is produced. The educational software includes the surface and mould modules used in this project.

Patran 2001 (2001)

Patran has a very well developed tetrahedral auto-meshing capability that proved very useful for meshing the complex geometries of the intake and exhaust ports as well as the cylinder head portion of the combustion chamber. Patran 2001 can directly import ProEngineer 2001 solid geometry. The Patran created mesh is then exported to a neutral file that can be read by ProStar.

Engine script

A script file was developed to feed a series of commands to ProStar. This script automates the generation of the mesh for the engine combustion chamber geometry. It sets up all the user defined variables, imports the mesh created by Patran, sets up the moving mesh and defines all flow conditions for a certain problem. This is very useful when more than one geometry is analysed and to ensure consistency between simulations. Modification of user-defined variables also easily implements changes in the problem definition.

PostStar

An application was developed to extract data from a StarCD output file. This application creates an output that is similar to the in-cylinder measured results and can be read in directly by the heat release analysis application Burnrate. This allows for direct comparison between experimental and computational results. PostStar also reads in the in-cylinder data integrated over volume and mass and produce results that can be compared to the combustion analysis results from Burnrate. This is used to check the comparison between the combustion analysis and the CFD results.

10.1.2 Hardware

Simulations were performed on a Pentium AMD Duron 800 MHz single processor workstation with 756MB RAM. Although this workstation is insufficient for performing efficient simulations of this nature, it is used to illustrate the capability of the numerical simulation and results between the 1.3L and 1.6L were analysed comparatively.

10.2 Strategy for Defining the Mathematical Model

The flow domain consist of three main regions namely the intake, combustion chamber and exhaust. CAD drawings of these regions are acquired and manipulated in order to subdivide them into smaller sub-regions or parts, each part defined in such a way as to achieve the ability to be meshed in a functional manner. The term functional mesh is used here to describe the ability of the mesh to perform a certain function, whether it is to define complex geometry, adapt to moving boundaries or perform a connectivity function. These parts are then meshed individually with the required mesh structure for each part designed to perform a function. Table 10-1 contains a functional breakdown of the flow domain from a main function level to a parts level. More detail of each part is given in the following section.

Mesh design in regions with moving mesh and changing cell connectivity is dominated by the need to keep the mesh simple so it can be changed easily during the transient run. The initial mesh contains all the cells that will be used in the analysis, resulting in overlapping cells in the vicinity of the valves.

Table 10-1: Functional breakdown of flow domain

MAIN FUNCTION	SUB-FUNCTION	PROPERTY	PART
Intake	Connect intake boundary to intake port	Layered mesh	Intake port boundary
	Transport fluid from intake manifold to combustion chamber	Complex geometry	Intake port
	Open and close connection to combustion chamber	Moving mesh	Intake valve top
Exhaust	Open and close connection to combustion chamber	Moving mesh	Exhaust valve top
	Transport fluid from combustion chamber to exhaust manifold	Complex geometry	Exhaust port
	Connect exhaust port to exhaust boundary	Layered mesh	Exhaust port boundary

MAIN FUNCTION	SUB-FUNCTION	PROPERTY	PART
Combustion chamber	Accommodate valves, spark plug and combustion region	Complex geometry	Combustion Chamber
	Initiate combustion	Ignition	Ignition region
	Allow intake valve movement	Moving mesh	Intake valve bottom moving mesh
	Connect intake valve flow to port and chamber	Connect	Intake valve connect
	Allow exhaust valve movement	Moving mesh	Exhaust valve bottom moving mesh
	Connect exhaust valve flow to port and chamber	Connect	Exhaust valve connect
	Allow piston movement	Moving mesh	Cylinder moving mesh

10.3 Geometry Definition

CAD geometry of the surfaces involved in the flow domain, in this case the cylinder head, and piston crown is used as a starting block. The manufacturer provided the cylinder head geometry in a STEP file format. The goal of the CAD part of the project is to import the geometry into ProEngineer, then extract only the necessary data from the initial geometry, i.e. copy surfaces of one intake port, exhaust port and combustion chamber from the cylinder head geometry. These surfaces are then used to construct the solid geometry of the entire flow domain in the form of an assembly. Figure 10-1 illustrates the geometry of a cylinder head. As this geometry is of the entire cylinder head, and contains more information than is required, only the necessary surfaces are copied in ProEngineer to acquire geometry of the combustion chamber as in Figure 10-2.

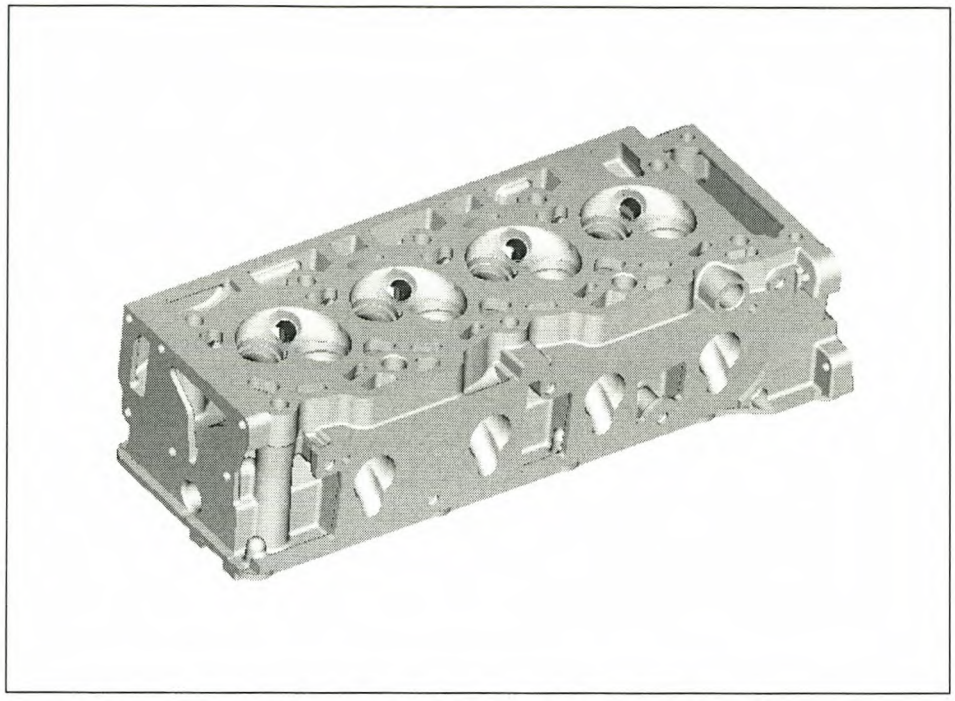

Figure 10-1: ProEngineer geometry of 1.3L Rocam cylinder head

The different coloured parts in the assembly of Figure 10-2 illustrate how the geometry was broken down. Some of the parts in the assembly are then further disassembled to achieve the ground level functionality in the functional breakdown described in Table 10-1. The assembly in Figure 10-2 does not contain the cylinder, as only the top and bottom surfaces are necessary to create the mesh. All the parts in the assembly and how they were handled geometrically are explained in the following paragraphs.

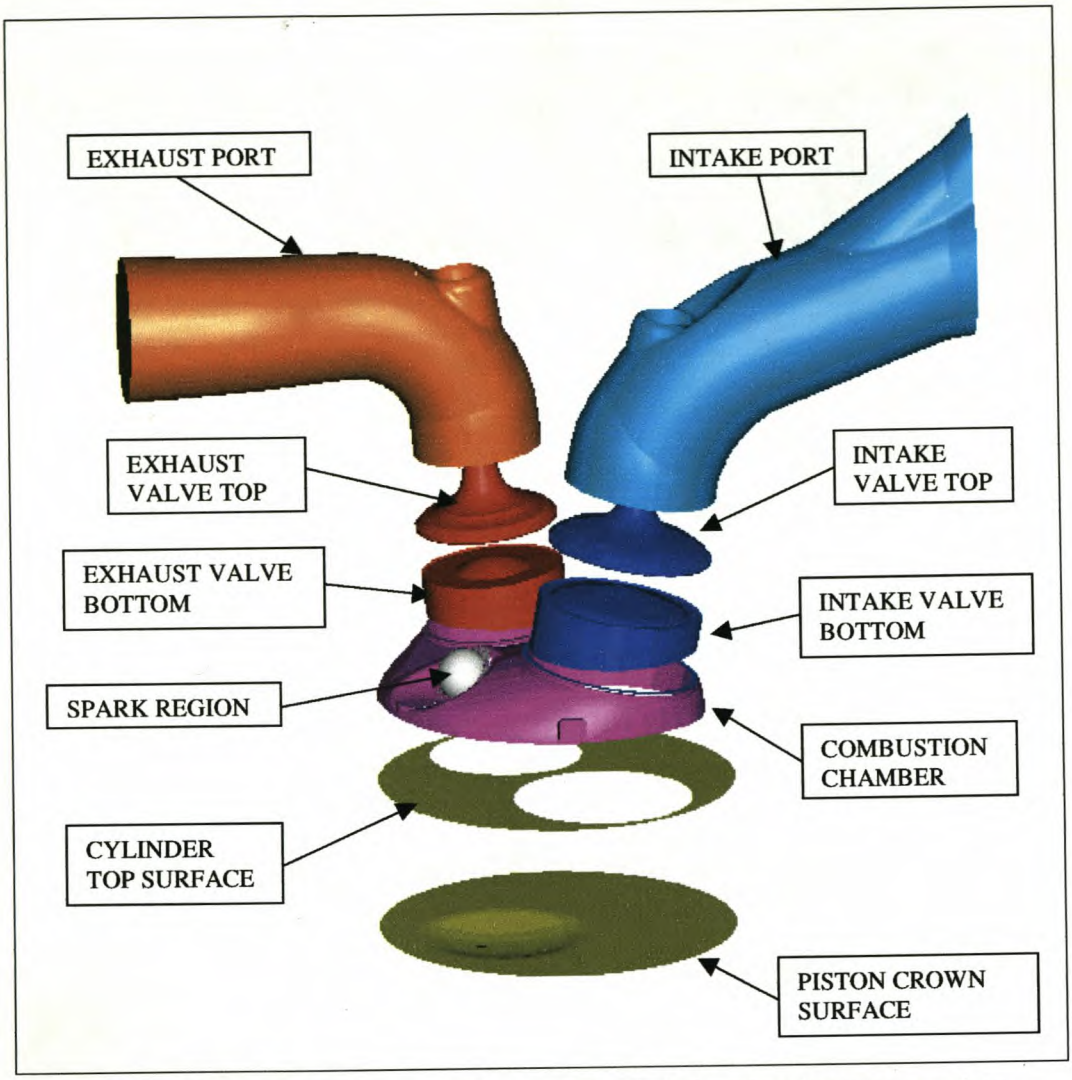

Figure 10-2: 1.3L ProEngineer geometry of the flow domain broken down into various regions

10.3.1 Intake port geometry

The port geometry is the complex geometry that connects flow from the intake manifold to the valve top. This region is defined separately as the complexity of the geometry is handled by automatic tetrahedral meshing techniques resulting in an unstructured mesh. The geometry of the intake port is created by copying the boundaries from the cylinder head drawing, and then closing the open ends with flat surfaces. The enclosed space is then transformed to a solid. The intake valve, intake valve guide and intake valve seat are intake port accessories that are not included in the cylinder head drawing.

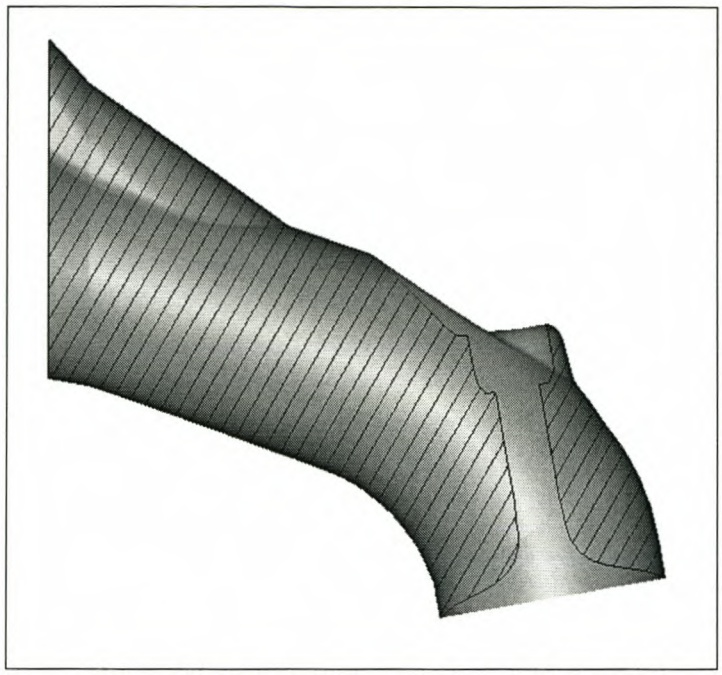

Figure 10-3: Intake port geometry with the section showing the final result after subtraction of the accessories in the assembly

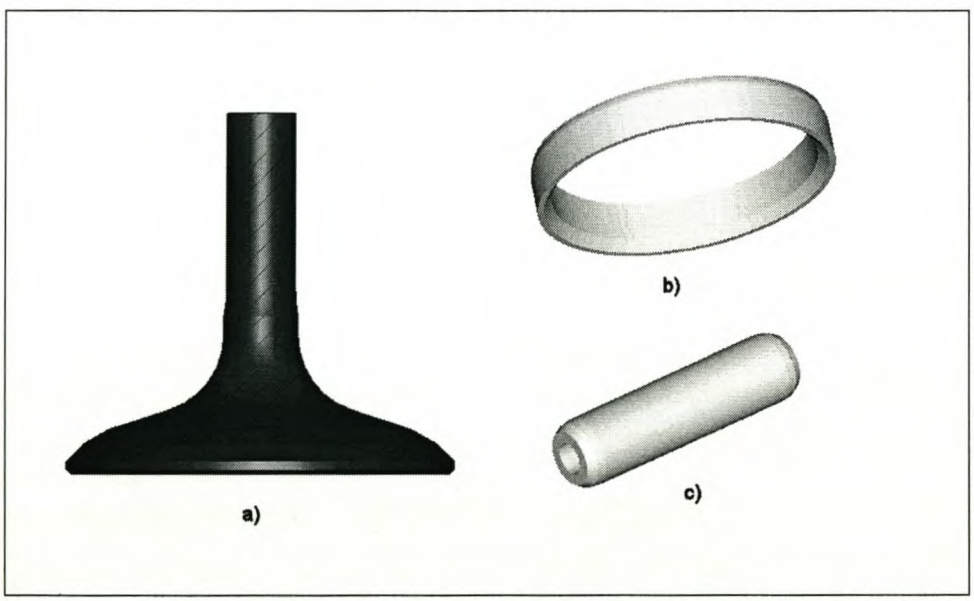

Figure 10-4: Accessories to the intake port namely (a) intake valve (b) intake valve seat (c) intake valve guide

Geometry of the accessories is constructed in ProEngineer from the manufacturers drawings and is illustrated in Figure 10-4. These parts are all assembled in a ProEngineer assembly and then, using the mould layout application of ProEngineer,

accessories that overlap with the port are subtracted from the original port. The final port geometry (after subtraction of the accessories) is shown in Figure 10-3.

10.3.2 Exhaust port geometry

The exhaust port geometry is created in exactly the same manner as the intake port. The exhaust port geometry and accessories are illustrated in Figure 10-5 and Figure 10-6.

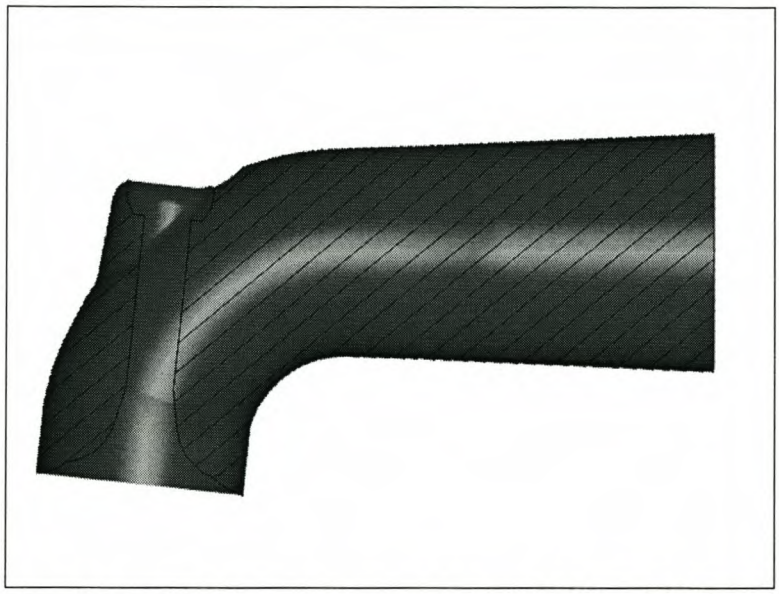

Figure 10-5: Exhaust port geometry with section showing remaining material after accessories are removed

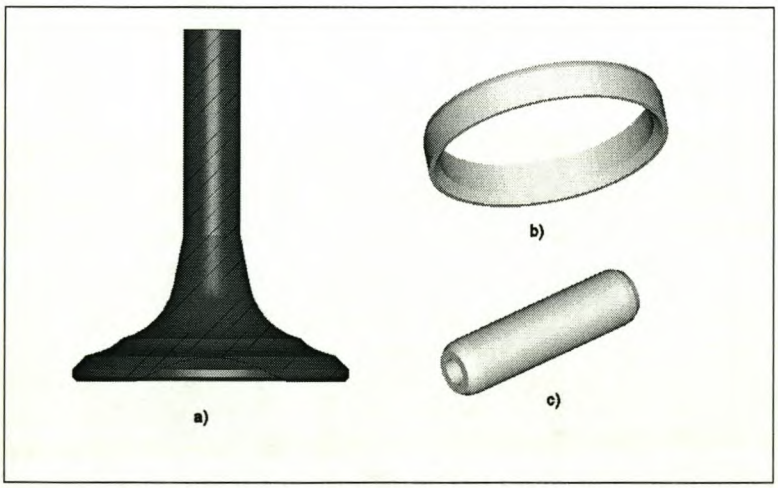

Figure 10-6: Exhaust port accessories (a) exhaust valve (b) exhaust valve seat (c) exhaust valve guide

10.3.3 Combustion chamber geometry

As is evident from Table 10-1, the combustion chamber and cylinder region contains 7 different sub regions. The combustion chamber geometry is firstly created as a single solid by copying all the appropriate surfaces from the original geometry of the cylinder head and closing the holes with flat surfaces. The original solid geometry created from the cylinder head geometry is shown in Figure 10-7.

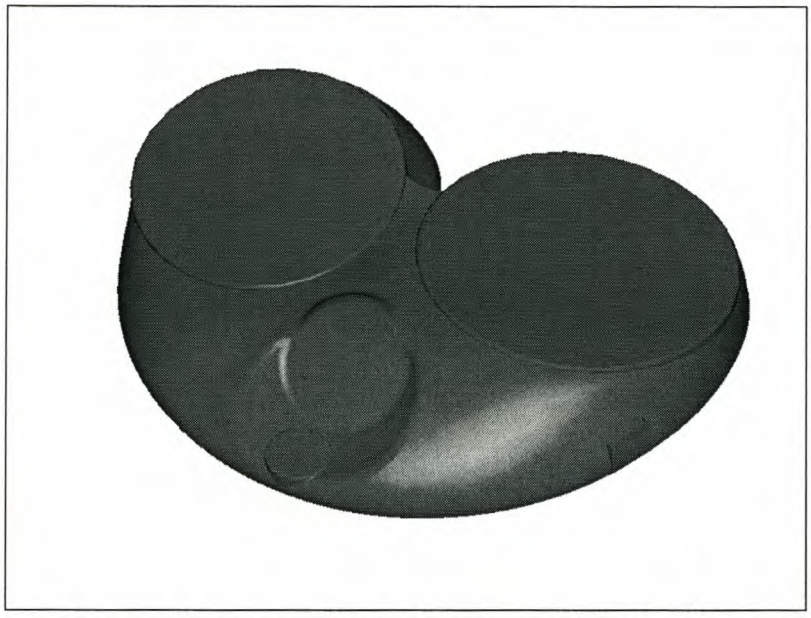

Figure 10-7: Combustion chamber geometry created from the cylinder head geometry

The solid geometry is then divided into the seven sub regions or parts that possess the properties required in that sub-region. The chamber boundaries describe the complex geometry of the surface and are therefore separated from any moving mesh regions.

Moving meshes will be used where the valves move, i.e. the region below the intake and exhaust valves. Two rings of cells named valve-connecting cells surround these moving mesh regions. The connecting cells are used to connect the structured mesh in the moving mesh region with the unstructured tetrahedral mesh in the combustion chamber as the vertices of moving meshes should line up with its surrounding mesh in order to qualify for cell attachment during simulation. The coupling between the connecting

cells and combustion chamber can be optimised by ensuring that the faces are flat on top of each other. One way to accomplish this is by faceting the holes in the chamber geometry before creating the mesh. A manually discretised circle i.e. a polygon is extruded and deleted from the chamber geometry to accomplish the faceted hole as illustrated in Figure 10-8. This operation is performed for both the intake and exhaust valve holes.

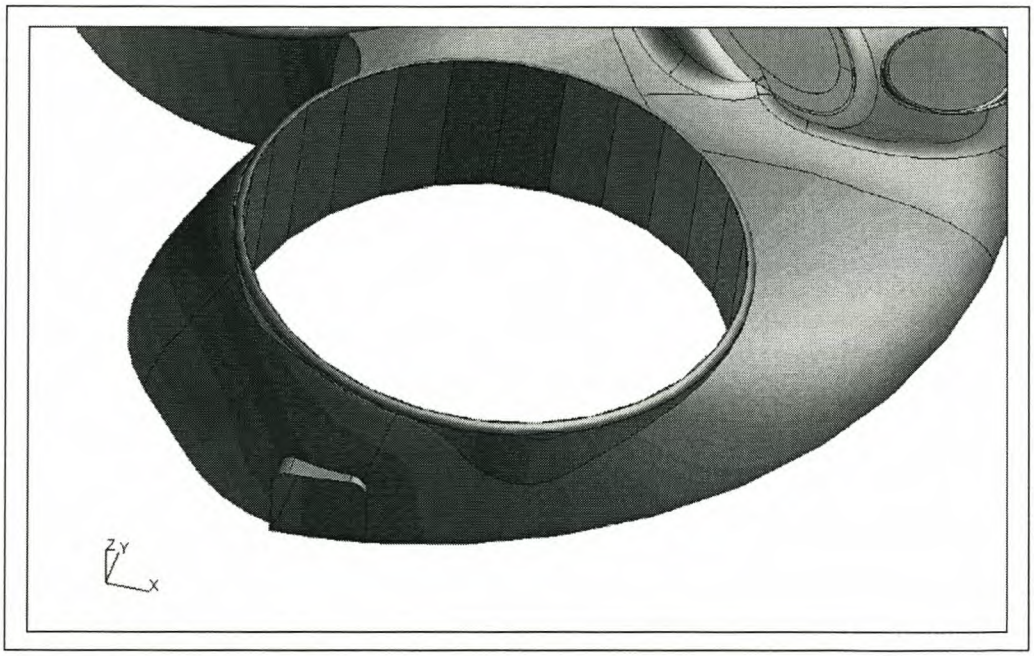

Figure 10-8: Illustration of faceted hole in chamber geometry

The valve bottom cells fill the open space surrounded by the connecting cells. The valve bottom and valve connecting meshes are extruded from surface cells defining these regions. These surfaces are the bottom surfaces of the valves and surfaces created from the edges of the ports and holes in the cylinder head geometry.

A separate region namely the spark region is defined where combustion is initiated. The combustion model employed by the code is initiated by specifying that this region of cells have completely burned the mixture within at a give time step. Due to the lack of information of the flow in this region prior to simulations, the flame is considered to propagate in all directions, causing a spherical flame front. The sphere is cut out of the

chamber by deleting it from the assembly (see Figure 10-2). The removed material is replaced by a half-sphere built in Patran. Building this solid in Patran ensures that the vertices of the meshes of the chamber and spark region coincide with each other which is necessary for good mesh connectivity.

10.3.4 Cylinder

The perimeter of the bottom surface of the cylinder head does not define the perimeter of the top of the cylinder, as the chamber has a nose between the intake and exhaust ports. The cylinder geometry is created in ProEngineer by an extruded cylinder with the manufacturer's specified bore. This cylinder is added to the chamber assembly, thereby ensuring that the chamber perimeter is correct (see Figure 10-9). In this case a small amount of material was removed from the chamber by deleting the cylinder from the chamber geometry, as the chamber geometry did not tie up exactly with the perimeter of the cylinder due to reference markings in the cylinder head geometry. The piston crown surface is added to the assembly and fitted into the same cylinder as above, thereby ensuring that the crown and cylinder surfaces have identical perimeters.

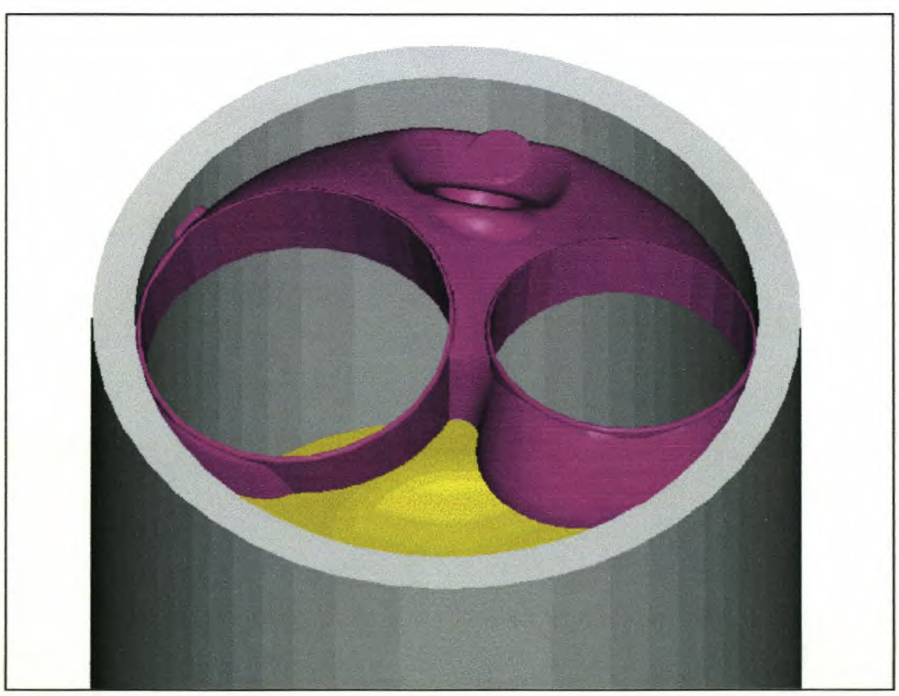

Figure 10-9: Cylinder wall used to ensure boundaries of chamber and piston crown have identical perimeters

10.3.5 Intake and exhaust valve lift

A spline is fitted in ProStar through the valve lift versus crank angle data. The spline is referenced to the tdc position of the crank and used during the moving mesh operations to calculate the position of the valve as a function of crank angle.

10.3.6 Summary

Information supplied by the manufacturers include:

- Cylinder head geometry (three-dimensional geometry)
- Intake valve drawing
- Intake valve guide drawing
- Intake valve seat drawing
- Exhaust valve drawing
- Exhaust valve guide drawing
- Exhaust valve seat drawing
- Piston crown drawing
- Camshaft drawing

The above information was utilized and manipulated to produce the following output:

- Intake port geometry (three-dimensional geometry)
- Intake valve (three-dimensional geometry)
- Exhaust port geometry (three-dimensional geometry)
- Exhaust valve (three-dimensional geometry)

- Combustion chamber geometry with spark region deleted (three-dimensional geometry)
- Cylinder top surface (two-dimensional geometry)
- Piston crown surface (two-dimensional geometry)
- Valve lift profile (spline)

The above information is now used as an input to the mesh generation process.

10.4 Mesh Generation

The ProEngineer files are imported into Patran with the import to parasolid and Patran sew options enabled. Patran sew is a feature that closes small gaps between surfaces that cause problems in defining a solid. Parasolid is defined in Patran as a parametric solid i.e. a solid geometry with eight edges that are definable by mathematical equations. Different meshing techniques are applied to mesh the flow domain. Tetrahedral cells define complex geometries while more simple geometries are discretised into hexahedral cells. Patran has a built in tetrahedral meshing capability that is used in this case to perform meshing. The regions are meshed individually according to the function of a specific mesh. The number of vertices and cells and the structure of the mesh in each region are documented in Table 10-2 and will be used during mesh creation when the computational space is created in ProStar. The numbering system contains enough space between the numbers of vertices and cells in different regions in order to allow for cell refinement when necessary.

Table 10-2: Mesh parameters for the Rocam 1.3L and Rocam 1.6L combustion chamber meshes.

Region	Number of Cells	
	Rocam 1.3L	Rocam 1.6L
Intake port boundary	245	500
Intake port	11775	15625
Intake valve top	2688	3072
Intake valve bottom	4212	4914
Intake valve connect	812	928
Exhaust port boundary	240	720
Exhaust port	12586	14765
Exhaust valve top	2688	3072
Exhaust valve bottom	3564	4860
Exhaust valve connect	812	928
Combustion chamber	15107	12615
Ignition region	170	339
Cylinder	5664	7872

10.4.1 Intake and exhaust boundary cells

The intake and exhaust boundary cells are extruded in Patran to form a layered mesh at the boundaries. The mesh in this region is not refined as it is a region where no interest exists in the exact velocity profile. No specific numbering scheme is required in this region.

10.4.2 Intake port top end

The intake port geometry is divided into two different regions. The solid port geometry

is split at a surface created in Patran. This surface is parallel to the valve bottom and intersects a point where the valve stem starts when the valve is closed, i.e. where the valve stem has the same diameter as at its top. This is done to avoid the occurrence of moving vertices in the tetrahedral mesh of the intake port cells.

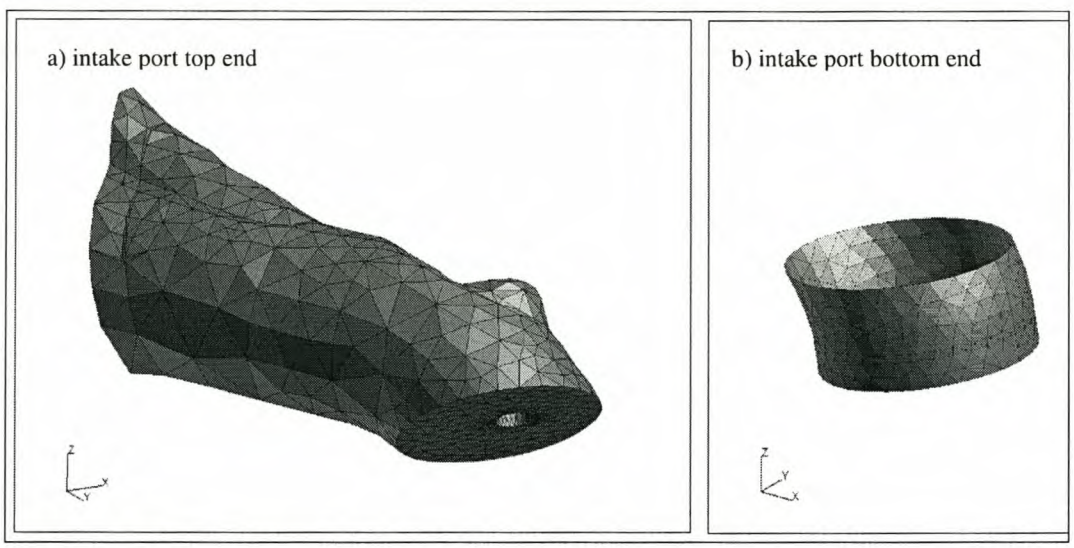

Figure 10-10: Tetrahedral mesh created by Patran for intake port

An example of the mesh created for the intake port region is shown in Figure 10-10a. Note that the tetrahedral mesh does not contain any moving vertices. The bottom surface is flat, thereby preventing any cracks when connecting to a hexahedral mesh.

10.4.3 Intake port bottom end

The bottom end of the intake port is discretised into a hexahedral mesh in ProStar thereby enabling the mesh to be programmed for the movement above the valve. The surface of this region is meshed in Patran with triangular elements (Figure 10-10b) and used for the boundary in ProStar when creating the hexahedral cells. The valve top surface mesh is extruded up to the mesh of the port top ends. The surfaces are created in Patran as follows. The ProEngineer solid geometry of the valve is imported into Patran and the surface created by revolving the spline that defines the valve edge around the valve axis. This parametric surface can then be easily meshed as seen in Figure 10-11. The numbering of the valve top surface vertices is very important, as it will play a role in

the extrusion process described later. The vertices are numbered from the outer perimeter starting with 1 at the rightmost vertex and increasing in the anti-clockwise direction and towards the inside as shown in Figure 10-12.

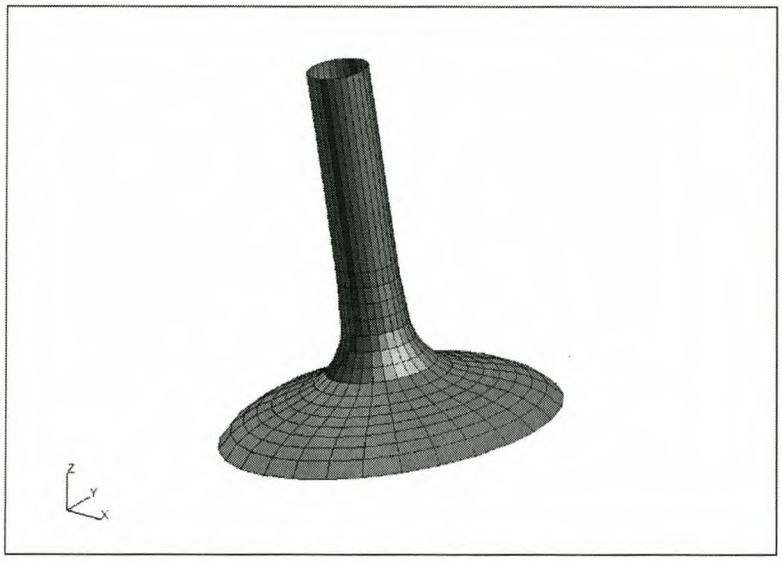

Figure 10-11: Intake valve top surface mesh from Patran

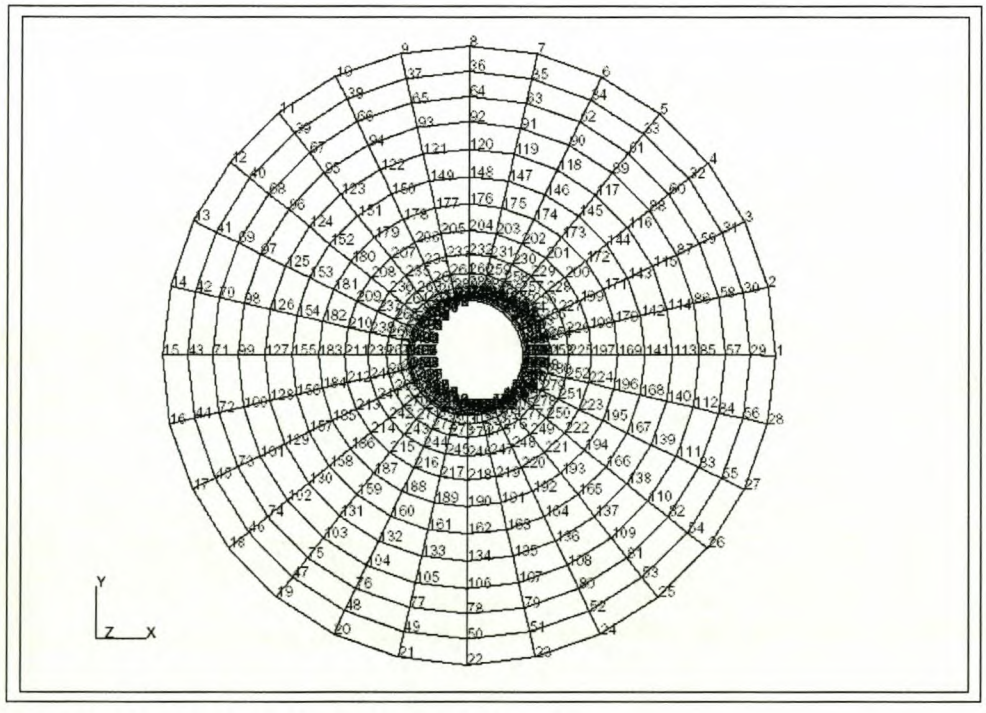

Figure 10-12: Intake valve top surface numbering scheme

The intake valve top mesh contains all cells used in the simulation, including those above the valve that will be deleted when the valve is closed. The valve surface mesh is moved down 15mm along the valve axis before the data is exported to the neutral file, allowing space for the addition/deletion cells above the valve surface.

The valve top surface shell cells are imported into ProStar and then the cells that form the bottom surface of valve top mesh (highlighted in Figure 10-11) are extruded in the z-direction of its local coordinate system.

10.4.4 Exhaust port

The exhaust port is handled exactly the same as the intake port. Figure 10-13 displays the exhaust port mesh.

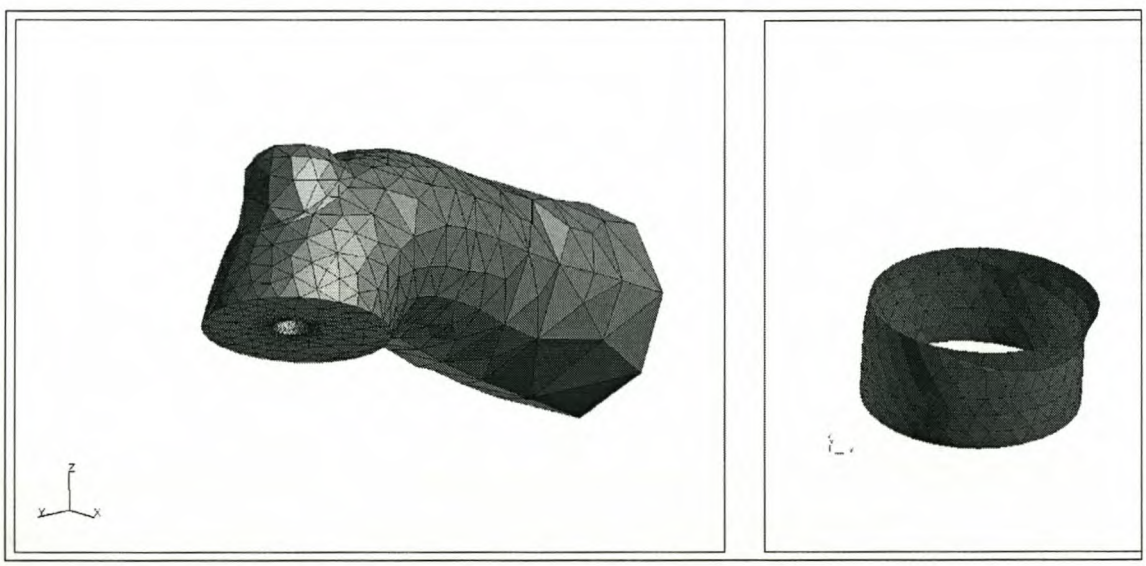

Figure 10-13: Tetrahedral mesh created for exhaust port

10.4.5 Combustion chamber and ignition cells

The combustion chamber geometry with the manually discretised holes for the valve movement regions is imported and meshed into tetrahedral cells by Patran. The spherical hole that was cut out for the ignition region is filled with a solid half sphere in Patran and its mesh created together with the chamber mesh to ensure alignment of the vertices. The combustion chamber mesh is illustrated in Figure 10-14.

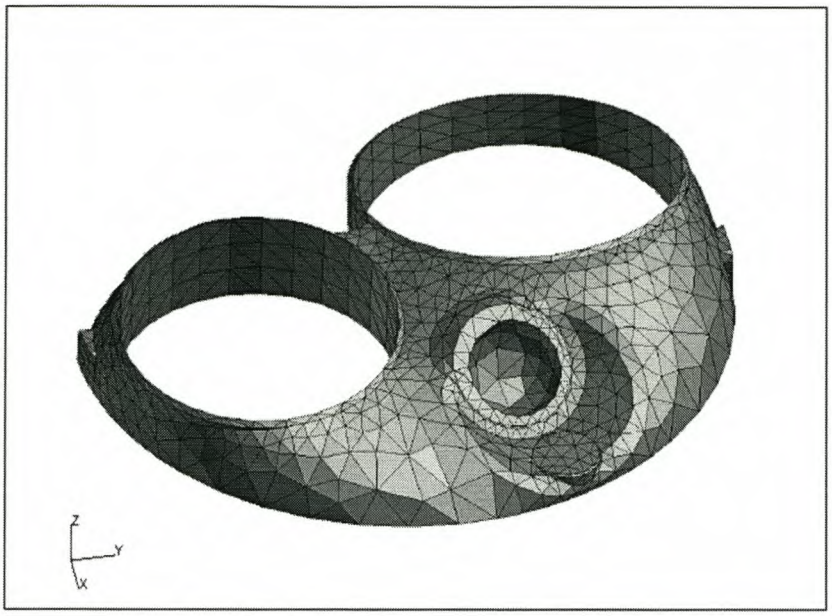

Figure 10-14: Combustion chamber mesh with ignition cells removed

10.4.6 Valve connecting mesh

The geometries of the valves and the combustion chamber have already been imported into Patran at this stage. The valve connecting regions connect the domains of the port flow, the combustion chamber flow and flow in the regions where valves move. The top surface of the connecting region is bounded by the top valve edges and the edge of the combustion chamber port holes. The numbering system employed is important as mesh movement operations at later stages will rely on the numbering starting with 1 on the inside perimeter rightmost vertex, increasing in the anti-clockwise direction and outward (see Figure 10-15a). The exhaust valve numbering system is handled exactly as the intake valve but starts with 501 instead of 1 (see Figure 10-15b).

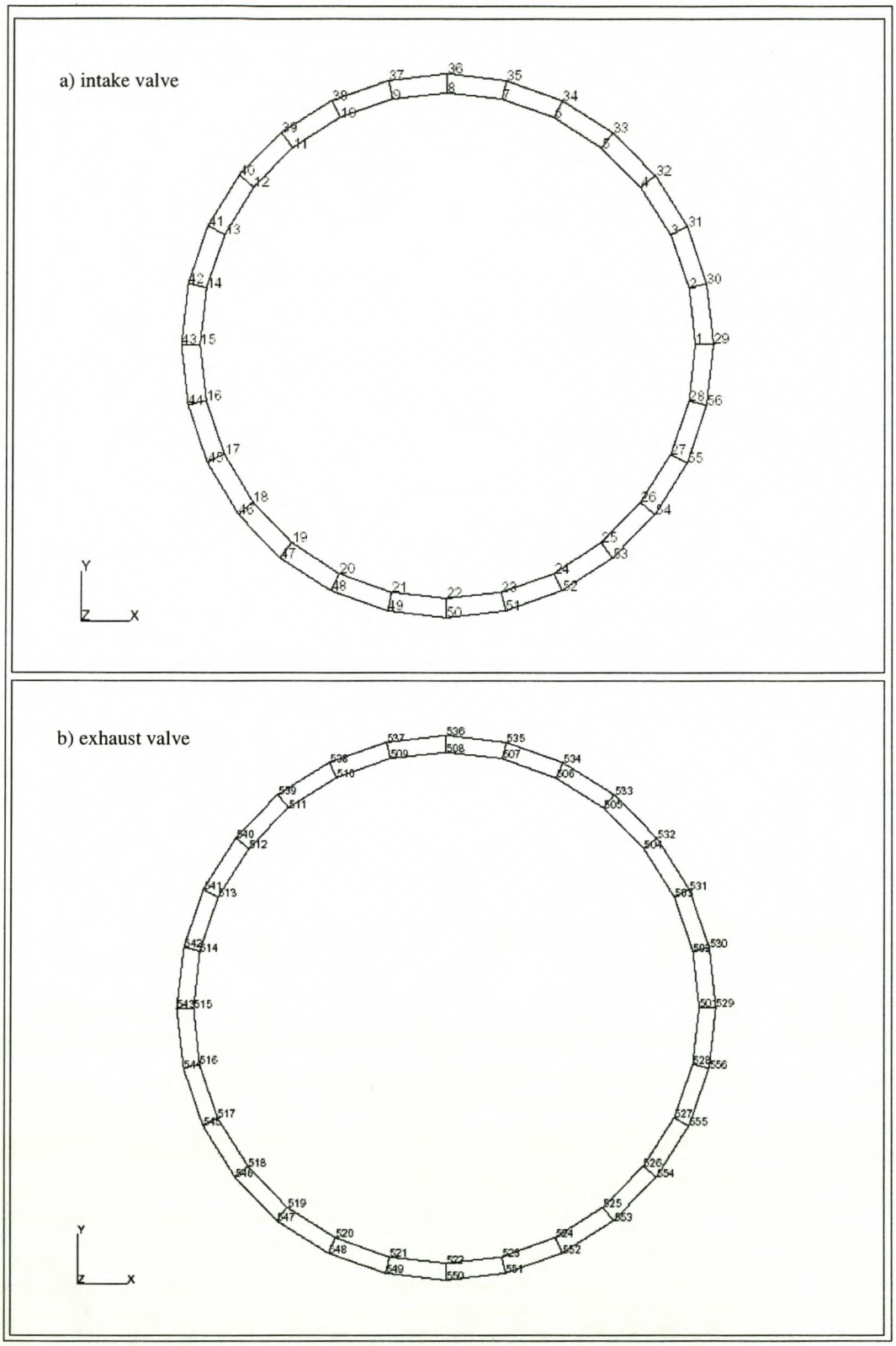

Figure 10-15: Numbering system for the valve connecting mesh (top view)

10.4.7 Valve bottom mesh

The mesh below the valve is generated in ProStar from shell cells that are created in Patran. The imported valve surface is meshed in Patran.

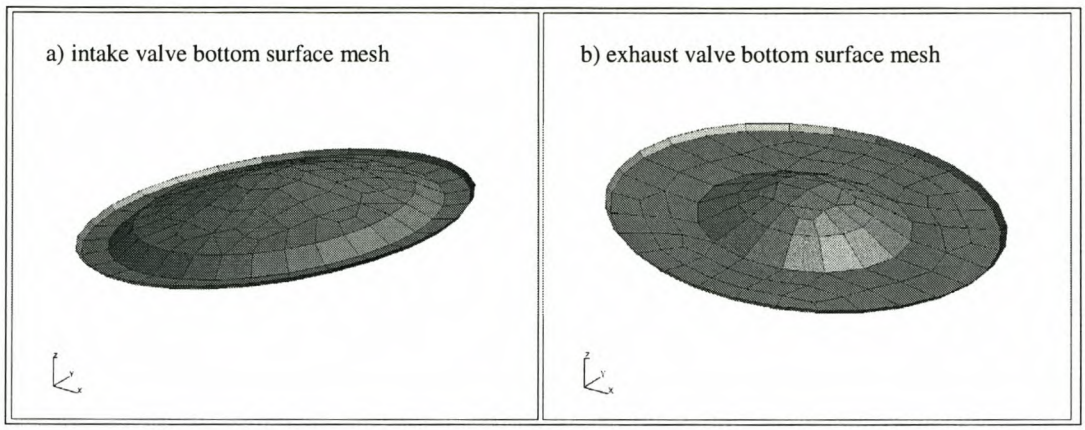

Figure 10-16: Surface mesh of the valve bottom surface. a) Intake valve b) Exhaust valve

For the mesh of the intake valve bottom surface (Figure 10-16a) vertex numbers on the perimeter are according to the convention used in the previous sections, starting with 151 on the right most vertex. Vertices of the exhaust valve bottom surface (Figure 10-16b) are numbered according to the same structure as the intake starting with 651.

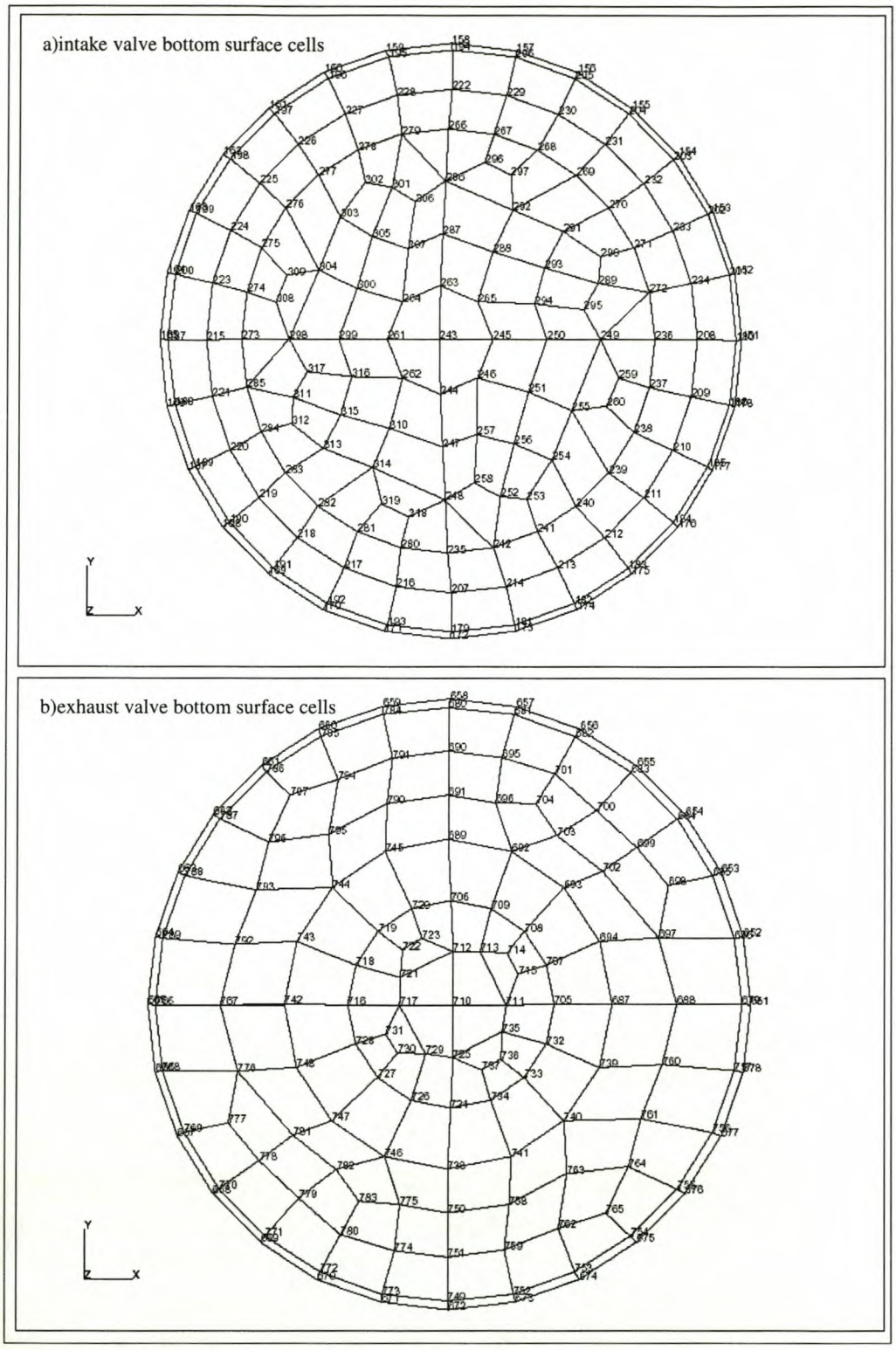

Figure 10-17: Numbering system of the valve bottom surface cells

10.4.8 Cylinder mesh

The surface that defines the area inside the cylinder between the valves is imported from ProEngineer to Patran. This surface is meshed by Patran. Care is taken to ensure that the mesh ties up with the edges on the holes. The only important part of this numbering system is that vertex 1 lies on the outer perimeter. Figure 10-18 shows the shell cells defining the cylinder top surface.

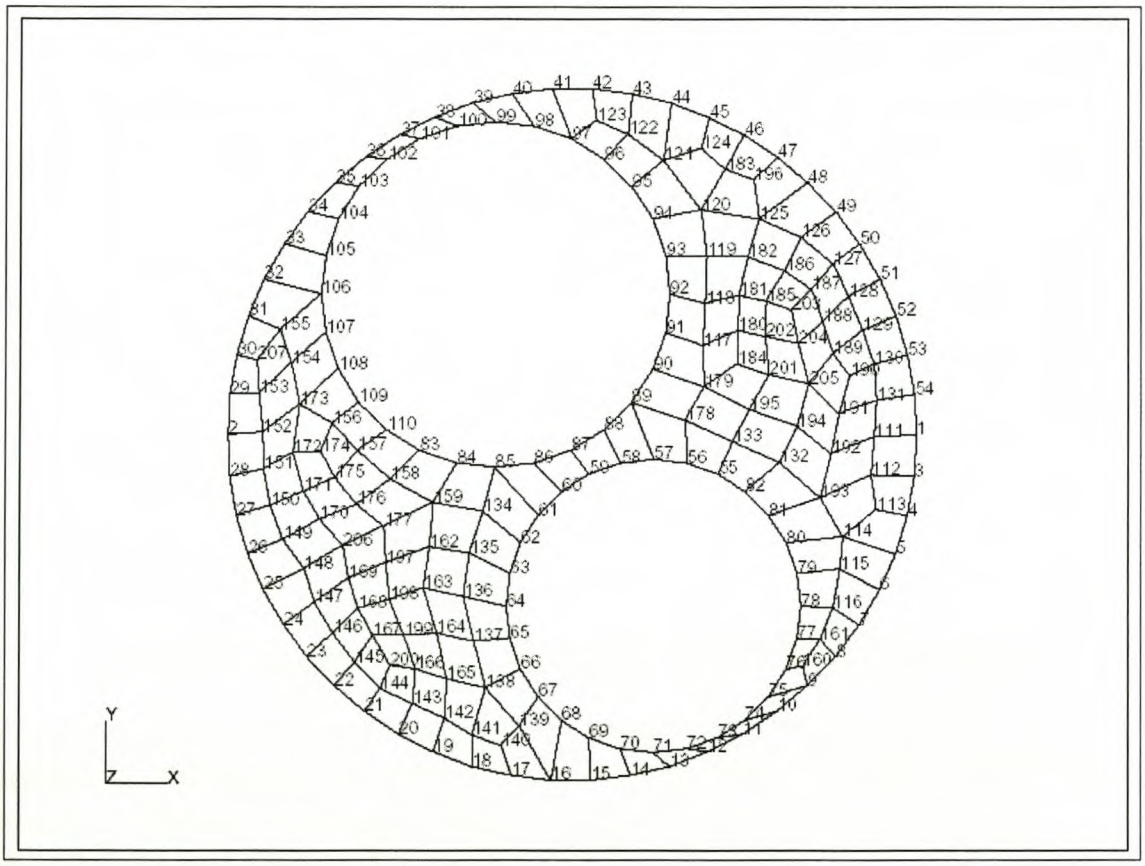

Figure 10-18: Mesh defining cylinder region top surface

10.4.9 Piston crown

Finally the piston crown surface is imported into Patran and meshed. This surface is only used to project the cylinder mesh onto during the moving mesh operations, therefore number of cells and numbering system is not important, as long as enough cells are used to ensure that the meshed surface represent the real surface with sufficient accuracy.

10.4.10 Moving mesh

ProStar commands are executed during the transient analysis, redefining the mesh at every time step. These mesh-changing operations are called events and are defined in an events file, each event with a unique time of occurrence. Events that move the mesh occur at every time step, while cell addition or removal events are defined to occur at certain predetermined time steps. StarCD initiates a temporary ProStar session before each time step is solved, setting up the mesh for that time step. StarCD provides a number of built in variables that are updated at every time step for the purpose of mesh generation. Additional user variables are also defined.

The strategy used here is to start with the piston at tdc at time = 0 and the valves in their appropriate positions, i.e. the intake and exhaust valves are slightly open. The piston starts moving down as time increase with the crank angle determined from the time and speed as:

$$\theta = 6 \cdot N \cdot t \tag{10-1}$$

With N the engine speed in revolutions per minute and t the time in seconds.

The position of the piston at any time is found from a graph consisting of a spline fit through a number of points defining the position of the piston vs. crank angle. This spline is defined by the slider crank mechanism. A vertex is placed on the x-axis at the appropriate crank angle and is then projected onto the spline. The piston position is then set equal to the y-coordinate of the projected vertex. This is easily performed by the StarCD code. The same methodology is followed in order to determine the intake and exhaust valve lifts vs. crank angle position. When piston and valve positions are known, vertices are placed at their surfaces and the mesh in-between filled with vertices that define the cells. By moving the vertices the cell positions and shapes are automatically updated by ProStar and the necessary space conservation laws applied. As the piston and valves move, events are defined at finite positions where cells are added or removed from the flow domain in order to prevent large cell distortions.

10.5 Thermodynamic and Physical Fluid and Flow Properties

Flow through the internal combustion engine is turbulent, with heat transfer taking place between fluid and walls. High temperature variations occur in the flow field due to the effects of compression and combustion. Chemical species are present in the flow field with chemical reaction taking place in the form of combustion. Compression of the fluid occurs causing density variation. For the purpose of this simulation radiation effects are ignored. According to Ferguson (1986) radiation effects in spark ignition engines contribute to less than 10% of the heat loss to the combustion chamber walls. Density is determined by the ideal gas law as a function of pressure and temperature. The molecular viscosity is assumed constant. Specific heat is determined from a polynomial with coefficients given by Kee et al. (1990). Conductivity is constant. Turbulence is modelled with the high Reynolds number k-ε turbulence model with standard coefficients as prescribed by StarCD with near-wall turbulence determined by the law of the wall. Temperature calculations are carried out with the static thermal energy conservation equation. The Weller flame area model is used to simulate chemical reaction. The Weller coefficient was set iteratively to achieve better correlation with experimental results. Most of the parameters were set to the default StarCD settings unless otherwise mentioned.

10.6 Solution Parameters

Internal combustion flow is transient due to the moving boundaries. Currently StarCD only employs the PISO solution algorithm to solve transient flow problems.

The following parameters are prescribed to the solution algorithm and were chosen by starting off with the default values, and then modifying when necessary to prevent divergence of the solution:

- Maximum number of corrector stages: 100
- Reduction in residual for corrector stages: 0.25

- Under-relaxation factor for pressure correction: 0.2

- Scalar solver type with implicit temporal discretisation

- Upwind differencing scheme used for solution of u, v, w, turbulence, temperature and scalar concentrations with central differencing used for density calculation

- Time step of 10 steps per degree crank angle with a simulation of 720 degrees i.e. 7200 time steps. At 3000rpm this corresponds to 5.55556E-06 seconds per time step.

10.7 Boundary and Initial Conditions

The boundaries between the solution domain and the environment are through the intake and exhaust ports. The pressure at these boundaries is determined through the one-dimensional fluid flow simulation code Ricardo Wave. A sample of the pressure data acquired by Ricardo Wave is illustrated in Figure 10-19. This data is written to a table file that is read in by ProStar and used as a reference when the problem set-up file is written.

The temperature at the intake port is specified as constant at 330K. Intake port temperature variation was found to be negligible according to the Ricardo Wave simulation as is illustrated in Figure 10-20. It is not worth the extra computational set-up to use a table for such a low temperature variation.

Exhaust port temperature is considered as constant at 905K. Although the exhaust port temperature varies significantly during the exhaust phase as illustrated in Figure 10-20, flow is out of the domain and the temperatures are calculated from the upstream (combustion chamber side) conditions. The specified temperature will therefore have little influence on the results. Turbulence parameters are specified as zero-gradient and are therefore calculated by the code.

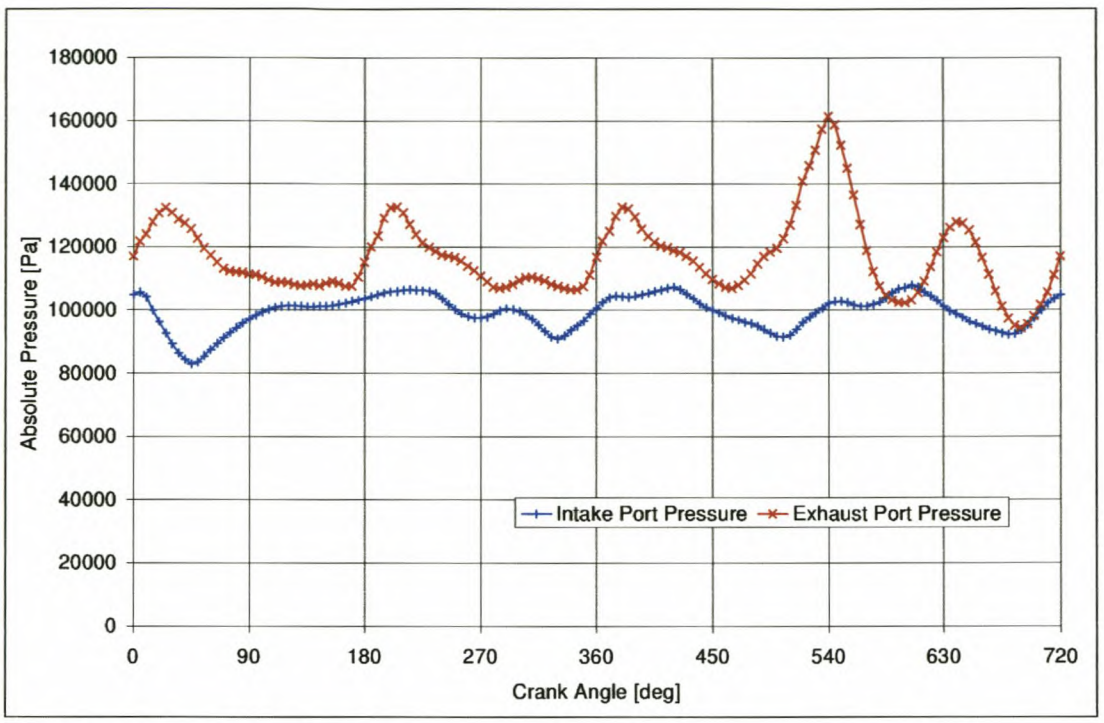

Figure 10-19: Intake and exhaust port pressure data for 1.6L Rocam engine at 3000rpm, WOT. Simulation performed in Ricardo Wave

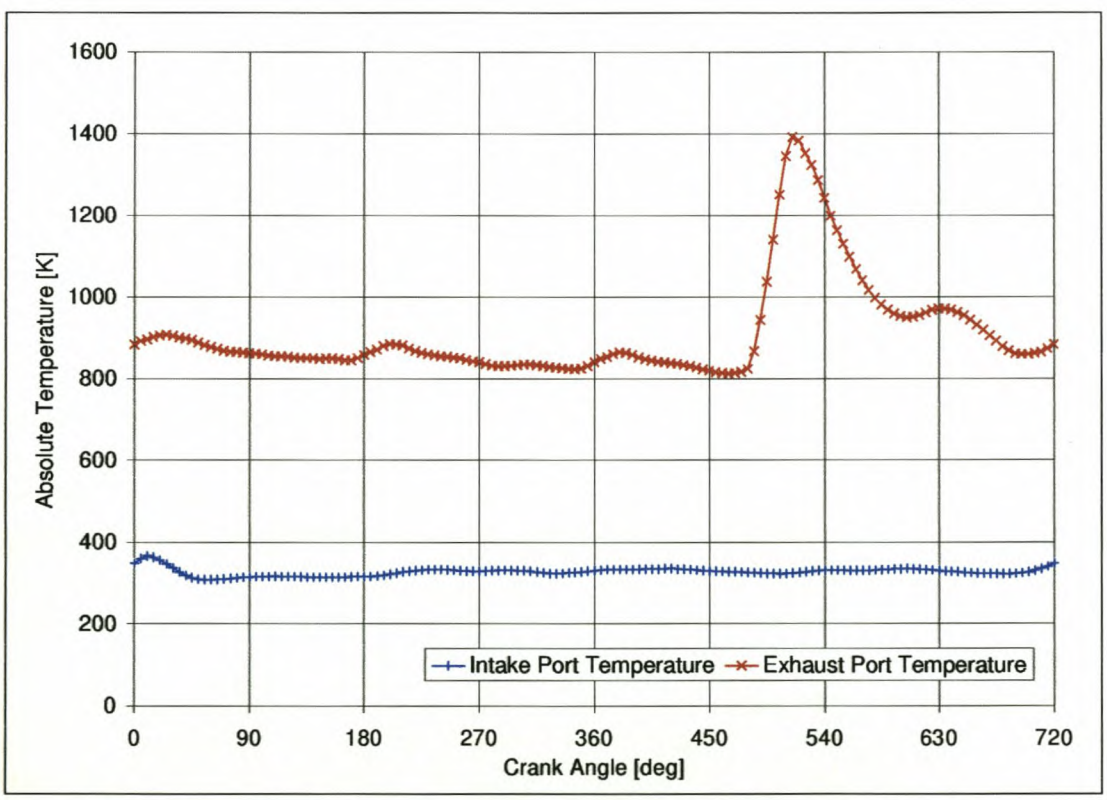

Figure 10-20: Intake and exhaust port temperatures of the Rocam 1.6L engine at 3000rpm, WOT. Simulation performed in Ricardo Wave

A first simulation is performed with the initial conditions at atmospheric pressure and temperature and the velocity field at zero. The volume integrated pressure and temperature at the end of this simulation is then used as initial conditions to the next simulation. Zero velocities are specified for the initial conditions of the second simulation. A summary of the boundary and initial conditions are listed in Table 10-3 and Table 10-4.

Table 10-3: Engine simulation boundary conditions

	T[K]	P
Intake port	330	TABLE
Exhaust port	905	TABLE
Intake port wall (Bell, 2003)	310	N.A
Combustion chamber wall (Bell, 2003)	420	N.A
Cylinder wall (Bell, 2003)	445	N.A
Piston crown (Bell, 2003)	520	N.A

Table 10-4: Initial conditions for engine simulation

	T[K]	P[Pa rel]	C_8H_{18}	O_2	CO_2	H_2O	N_2	RVB
Intake port	330	2643	0.067	0.201	0	0	0.732	1
Combustion chamber	1250	23700	0.067	0.201	0	0	0.732	1
Exhaust port	905	26575	0	0	0.178	0.817	0.732	0

All the above values are easily adjustable in the main program of the problem set-up code.

10.8 Flow Analysis

The analysis is started from the initial conditions specified in Table 10-4. These conditions are applied to specific fluid streams. While the analysis is running StarCD runs ProStar in the background to perform the mesh changing operations defined in the moving mesh and events files.

The analysis continues without combustion until the specified ignition time is reached. The chemical reaction scheme is initialised at the user specified time step and combustion commences. When the concentrations of either oxygen or fuel reach zero combustion will end, although the model is still active. The combustion model is therefore deactivated before the intake valve opens, as failing to do so would result in combustion during the period at the end of the exhaust stroke when the intake valve is open. The analysis is stopped anywhere in between the time when combustion is complete and the time when the intake valve opens to deactivate the combustion model.

During the analysis the code integrates selected properties over the mass and volume of the in-cylinder cells of the flow domain. These quantities are:

- Velocity
- Pressure
- Temperature
- Turbulent kinetic energy
- Turbulence dissipation rate
- Turbulent length
- Turbulent time scale
- Mass
- Volume
- Fuel concentration

The integration is performed and information written to disk at every time step and provides a bulk of information that is accessible during the simulation.

StarCD writes cell data to a post-processing file at every 50 time steps or 5 degrees crank angle. This data is useful for looking at the flow field in physical space and to

create a visual understanding of the solution. A restart file is written to disk every 50 time steps and is useful for restarting the analysis whenever it has stopped prematurely. Backup restart files can also be created in order to restart from previous points in time. Other quantities such as angular momentum about an axis are calculated after the analysis from the transient post data using ProStar in conjunction with Microsoft Excel.

A full analysis for this model with 50 000 cells take about 125 hours to complete, and therefore time limitation prohibited further mesh refinement to be performed. This type of computation could be performed more effectively on large processors.

11 NUMERICAL SIMULATION RESULTS

The results produced by the simulations are divided into two categories namely graphic output and text output. The graphic output is created from cell data and produces visual representation of the flow field in terms of vectors and scalar contours. These results prove very informative of the flow inside the cylinder. The text output contains engineering type data that can be directly linked to experimental data such as in-cylinder pressure, temperature and combustion analysis results. Although experimental methods are also available to confirm visual results, it is outside the scope of this project.

11.1 Flow Into the Combustion Chamber

Figure 11-1 and Figure 11-2 illustrate the simulation results at 90 degrees crank angle for the 1.3L and 1.6L Rocam engines respectively. This is the point with the maximum piston speed. The maximum air velocity is 137.5 m/s for the 1.3L engine and 96.08 m/s for the 1.6L. The higher maximum fluid velocity of the 1.3L is partly caused by the smaller intake port to cylinder bore diameter. The 1.3L has a diameter ratio of 0.405 while the 1.6L has a ratio of 0.44. The red vectors all around the intake valve of the 1.6L indicate that the velocity of airflow around the valve is more evenly distributed than the 1.3L with red arrows only around the right hand side of the valve. A probable cause for this could be the more severe masking of the intake port as well as the "nose" between the intake and exhaust ports of the 1.3L. Masking is defined as the material placed around the valve, thereby increasing flow restriction from the port to the combustion chamber. The higher velocity of air flow into the 1.3L indicates a higher pressure gradient i.e. more pumping work will be required to draw air into the cylinder, although this is also a function of the pressure at the intake port.

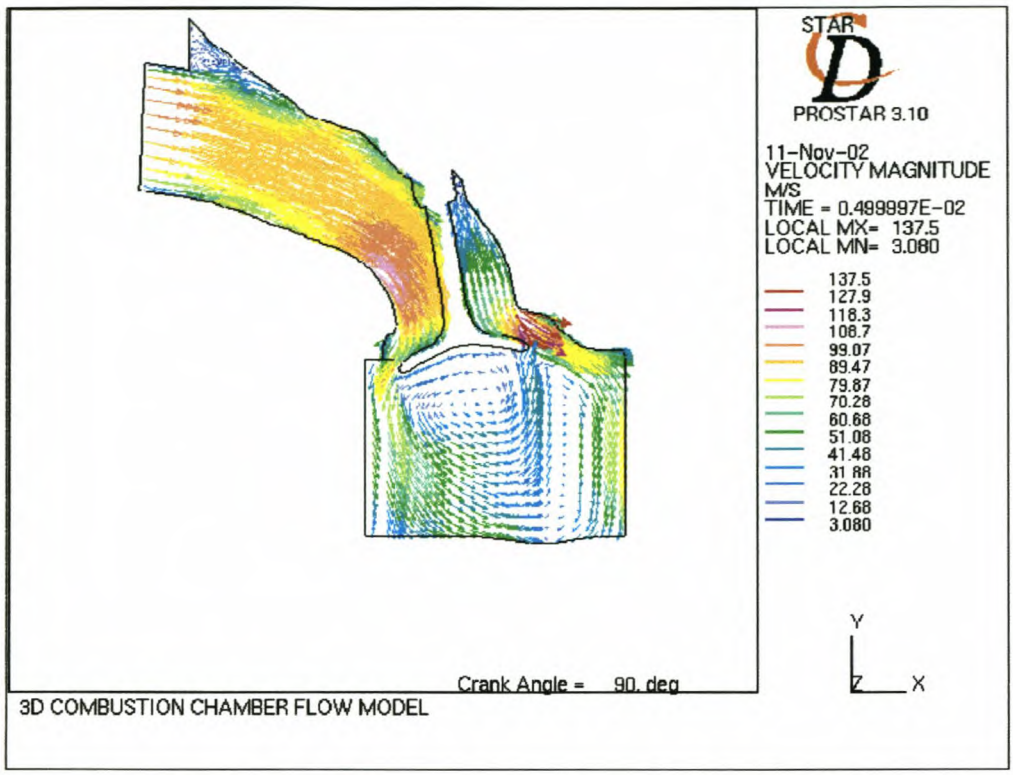

Figure 11-1: Flow into the 1.3L Rocam combustion chamber at 90° crank angle, 3000rpm WOT. Simulation performed by StarCD

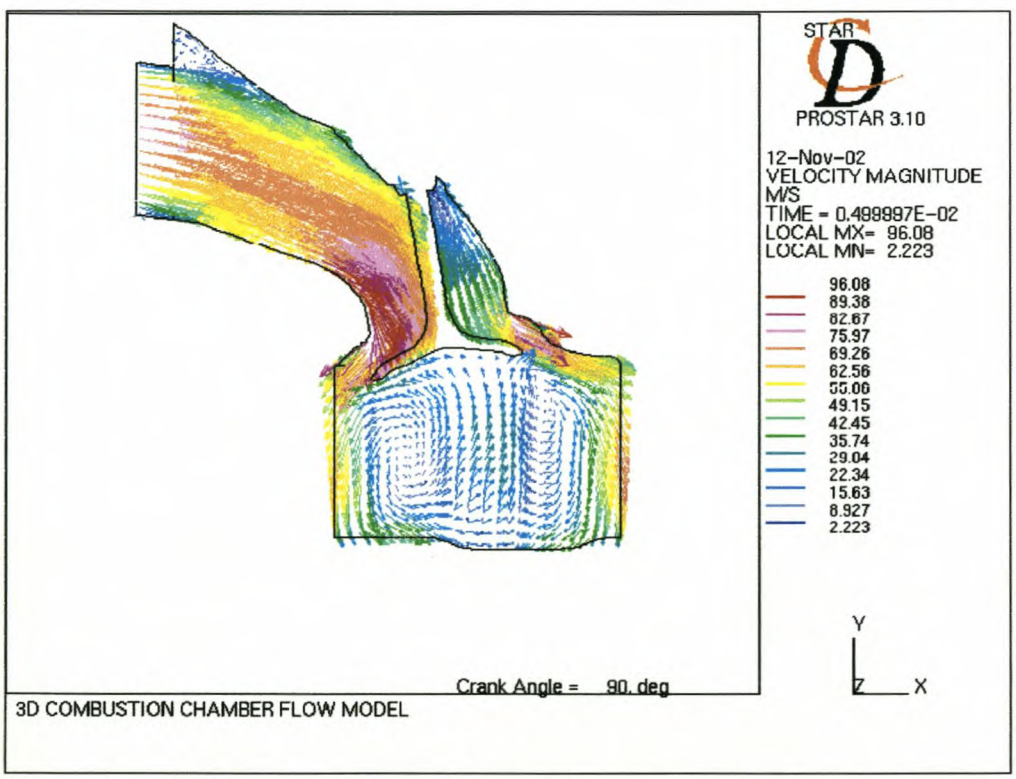

Figure 11-2: Flow into the 1.6L Rocam combustion chamber at 90 degrees crank angle, 3000rpm WOT. Simulation performed by StarCD

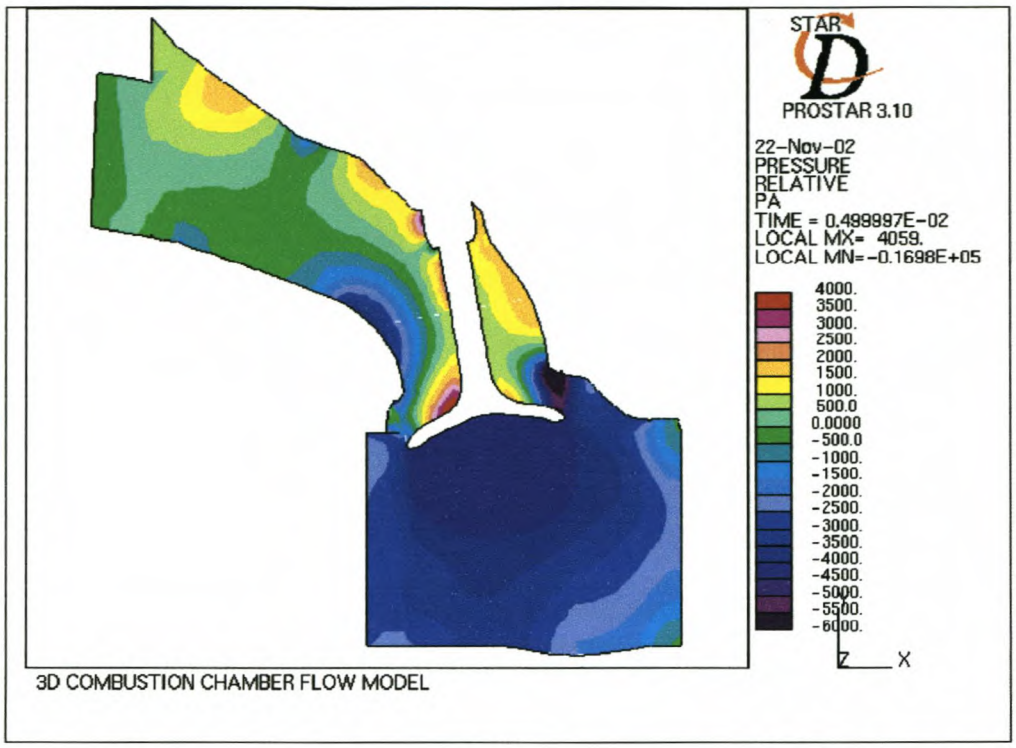

Figure 11-3: Pressure distribution in the 1.3L combustion chamber at 90° crank angle. StarCD simulation of flow at 3000rpm WOT

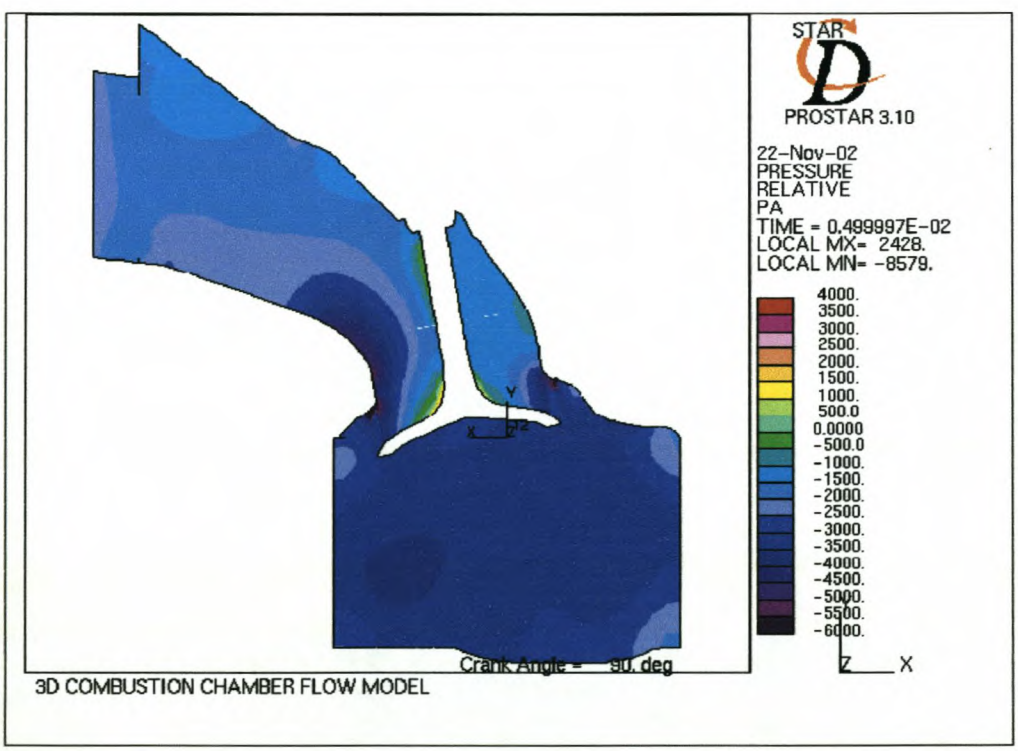

Figure 11-4: Pressure distribution in the 1.6L combustion chamber at 90° crank angle. StarCD simulation of flow at 3000rpm WOT

Figure 11-3 and Figure 11-4 illustrate the pressure distributions in the 1.3L and 1.6L engines at 90° crank angle i.e. during the intake stroke. The figures illustrate that the pressure change across the 1.3L port far exceeds that over the 1.6L port. This is the direct influence of the lower port-to-cylinder diameter ratios of the 1.3L geometry.

11.2 Tumble

Tumble can be defined as the momentum of fluid flow over an axis parallel to the piston surface. Quantification of tumble is challenging when comparing two different engine sizes, as the characteristic distance is a mixture between bore and stroke. For comparison, tumble is broken down into two components. One component is the velocity in the x-direction (see Figure 11-5 for coordinate system), u, mass integrated over the y-direction and the other component is v, the velocity in the y-direction mass integrated over the x-direction. The first component is integrated over the cylinder bore of the engine and is normalised by diving by the bore and fluid mass. The second component is integrated over the vertical distance and a typical dimension to use for normalisation is stroke times mass. The resulting dimension for the tumble number H_T defined above is m/s.

$$H_T = \frac{1}{M} \cdot \left(- \int_{mass} \frac{u \cdot y}{S} \cdot dm + \int_{mass} \frac{v \cdot x}{B} \cdot dm \right) \qquad (11\text{-}1)$$

With M the total in-cylinder mass, S the stroke and B the bore.

The flow fields at the time of intake valve closure for the 1.3L and 1.6L are illustrated in Figure 11-5 and Figure 11-6. The induced tumble is clear in the 1.3L flow field with $H_T = -2.23 m/s$, with a vortex in the middle of the chamber, while the 1.6L shows less tumble with $H_T = -2.00 m/s$. As the piston moves up the tumbling flow is broken down into smaller turbulent eddies that add in the flame development during the induction period. Figure 11-5 illustrates the effect of the squish region of accelerating flow away from itself.

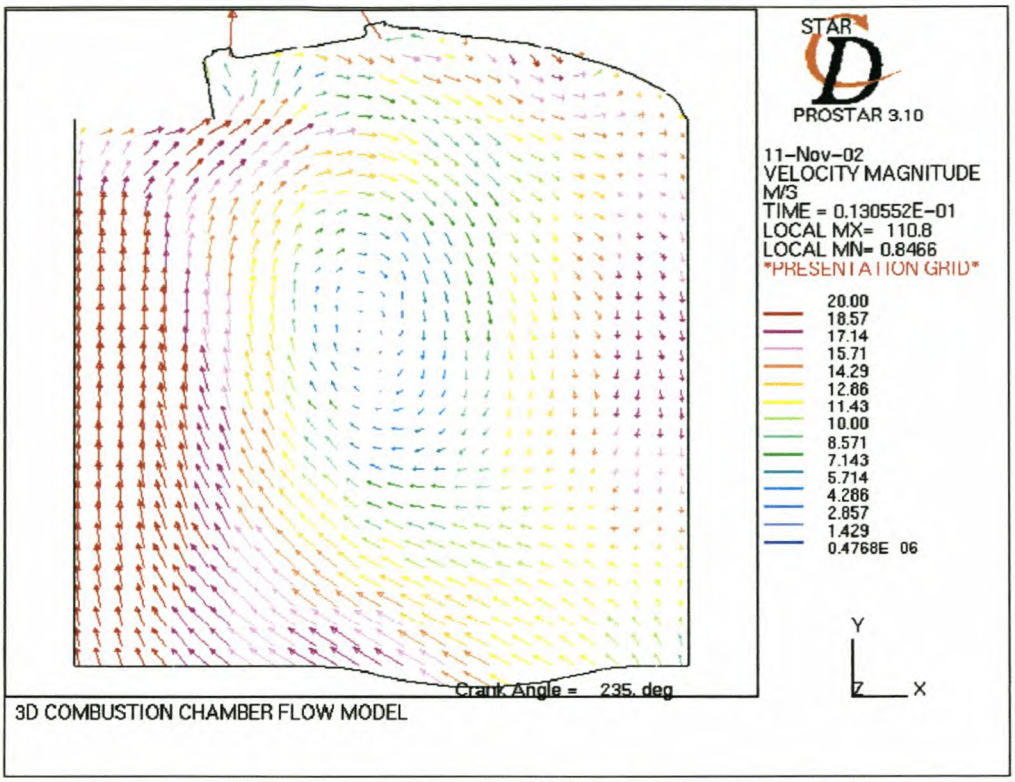

Figure 11-5: Flow in the 1.3L Rocam combustion chamber at intake valve closure, 3000rpm WOT. Simulation performed by StarCD

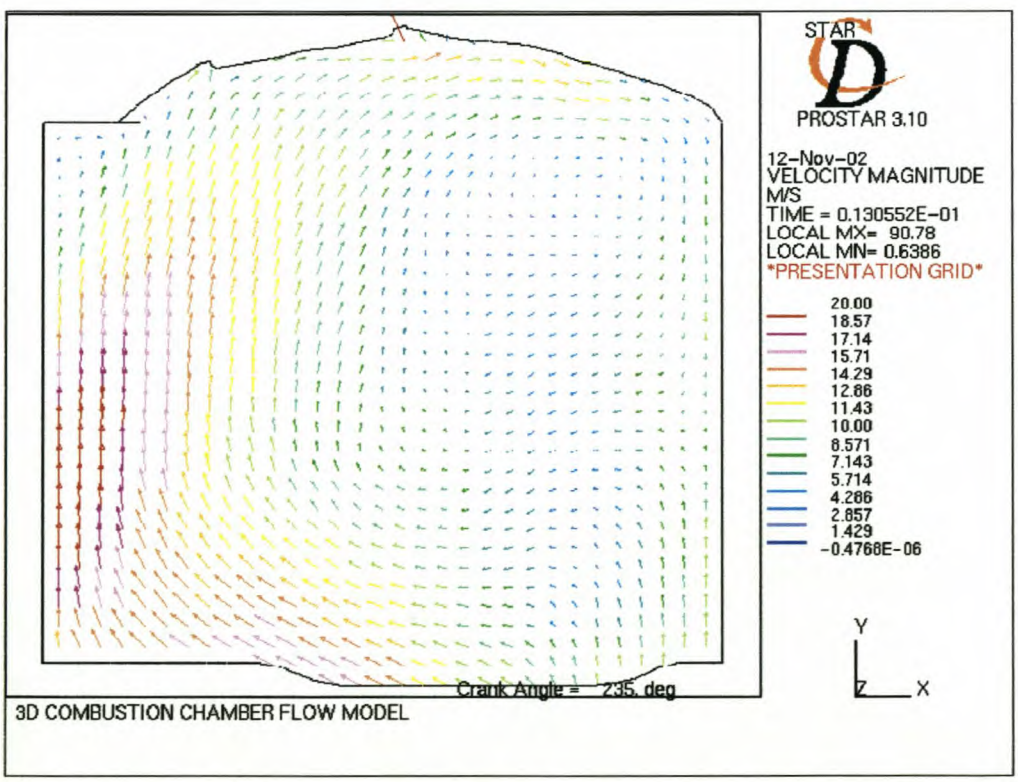

Figure 11-6: Flow in the 1.6L Rocam combustion chamber at intake valve closure, 3000rpm WOT. Simulation performed by StarCD

Figure 11-7 and Figure 11-8 illustrate the flow fields of the 1.3L and 1.6L at the time of ignition. Tumble numbers in the 1.3L and 1.6L are $-0.2m/s$ and $-0.3m/s$ respectively. Although circulating flow is still visible in the combustion chamber at this stage, the maximum velocity of the tumbling motion is considerably less than at the time of intake valve closure.

Although the 1.6L tumble number at intake valve closure is less than the 1.3L tumble number at the same instant, the 1.6L has higher tumble at the time of ignition. The bigger squish area of the 1.3L combustion chamber may be the cause of the increased decay of tumble in the 1.3L chamber, translating tumble energy into turbulence.

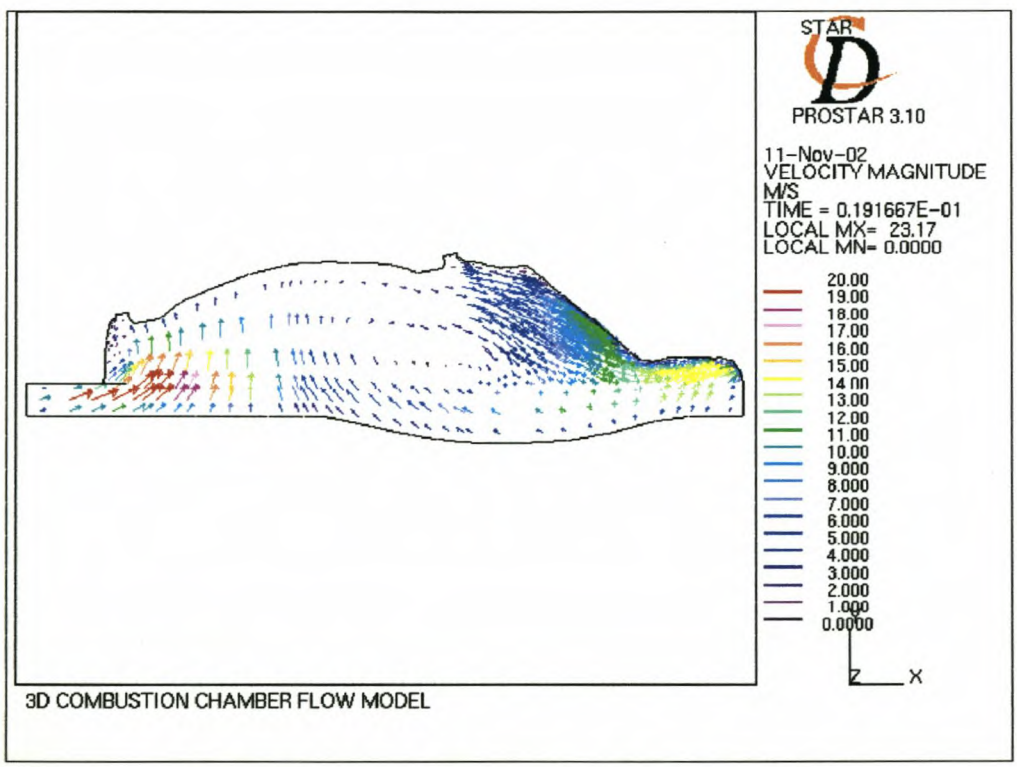

Figure 11-7: Flow in the 1.3L Rocam combustion chamber at the time of ignition, 3000rpm WOT. Simulation performed by StarCD

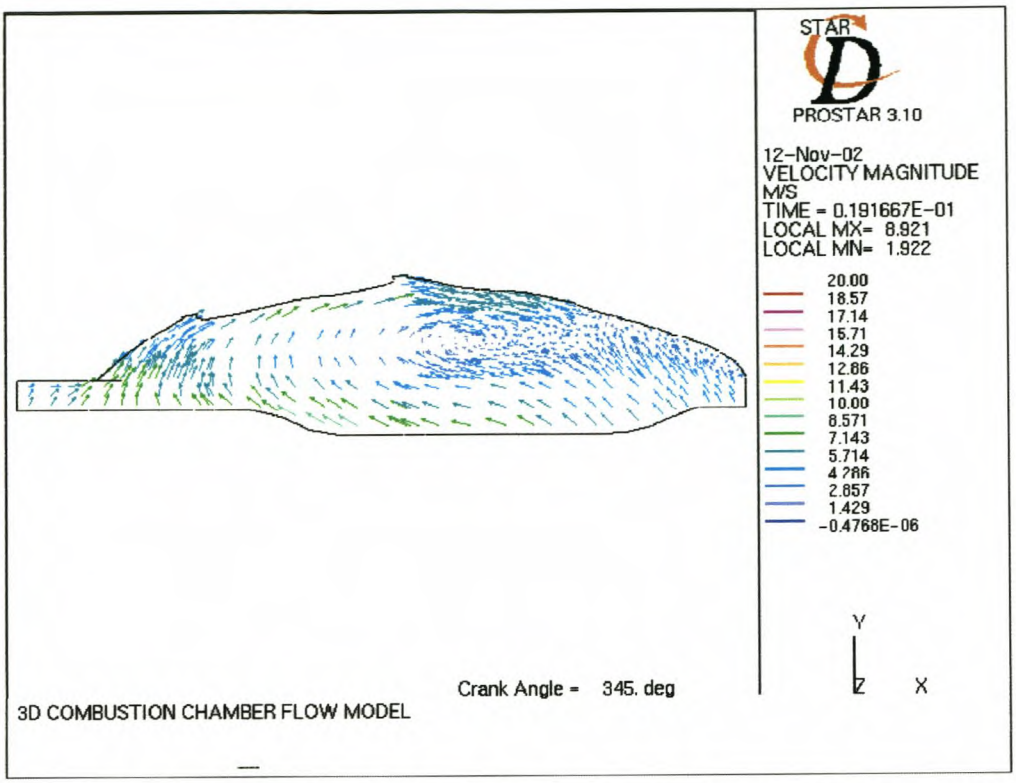

Figure 11-8: Flow in the 1.6L Rocam combustion chamber at the time of ignition, 3000rpm WOT. Simulation performed by StarCD

11.3 Swirl

Another form of in-cylinder fluid motion namely swirl is characterised by the fluid velocity in a circumpherential direction about the cylinder axis. Swirl is normalised by dividing by the bore times cylinder mass and quantified by the swirl coefficient H_S as follows:

$$H_S = \frac{1}{M} \cdot \left(\int_{mass} \frac{u \cdot z}{B} \cdot dm - \int_{mass} \frac{w \cdot x}{B} \cdot dm \right) \qquad (11\text{-}2)$$

With M the total in-cylinder mass, x, z, u and w in the coordinate system indicated in Figure 11-9. B is the cylinder bore.

The swirling motion of flow just after intake valve closure is illustrated in Figure 11-9 and Figure 11-10 for the 1.3L and 1.6L engines respectively. Swirl numbers for the

1.3L and 1.6L engines are –4.46m/s and –0.55m/s respectively at the time of intake valve closure. This indicates the effect of the nose and masking of the 1.3L intake port. Although swirl is slowed down by shear and obstructions in the combustion chamber, the movement of the piston does not break down swirl to the same effect as tumble. As the cylinder charge is squeezed into the cylinder head region of the combustion chamber, the cross sectional flow area is decreased and flow is further accelerated as illustrated in Figure 11-11. At this point in time, a spark is introduced to the flow field and combustion occurs. The swirl numbers at the time of ignition are –2.75m/s and -0.65m/s for the 1.3L and 1.6L engines respectively. The swirl number in the 1.6L combustion chamber have increased slightly due to the decreasing area, whereas the 1.3L swirl decreased significantly (although it is still much higher than that of the 1.6L) due to the restriction caused by the nose. Figure 11-12 illustrate the squish in the 1.6L, which is directed straight to the centre of the chamber as opposed to the 1.3L where squish forces flow in a circumferential direction.

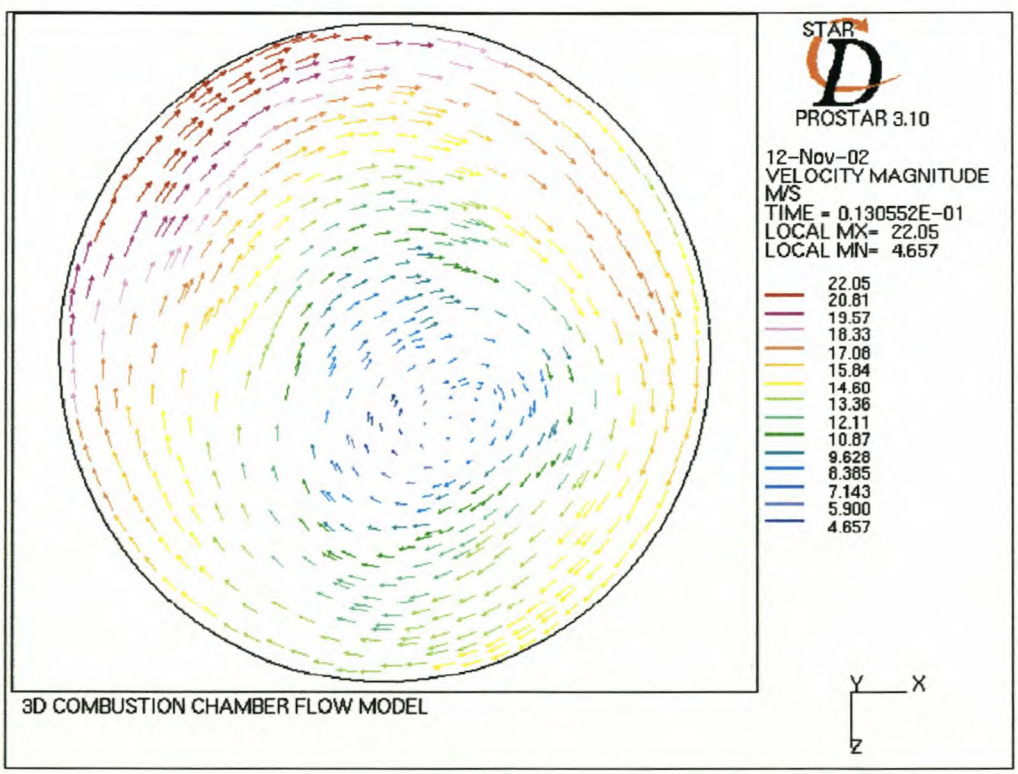

Figure 11-9: Flow in the 1.3L Rocam combustion chamber at intake valve closure, 3000rpm WOT. Simulation performed by StarCD

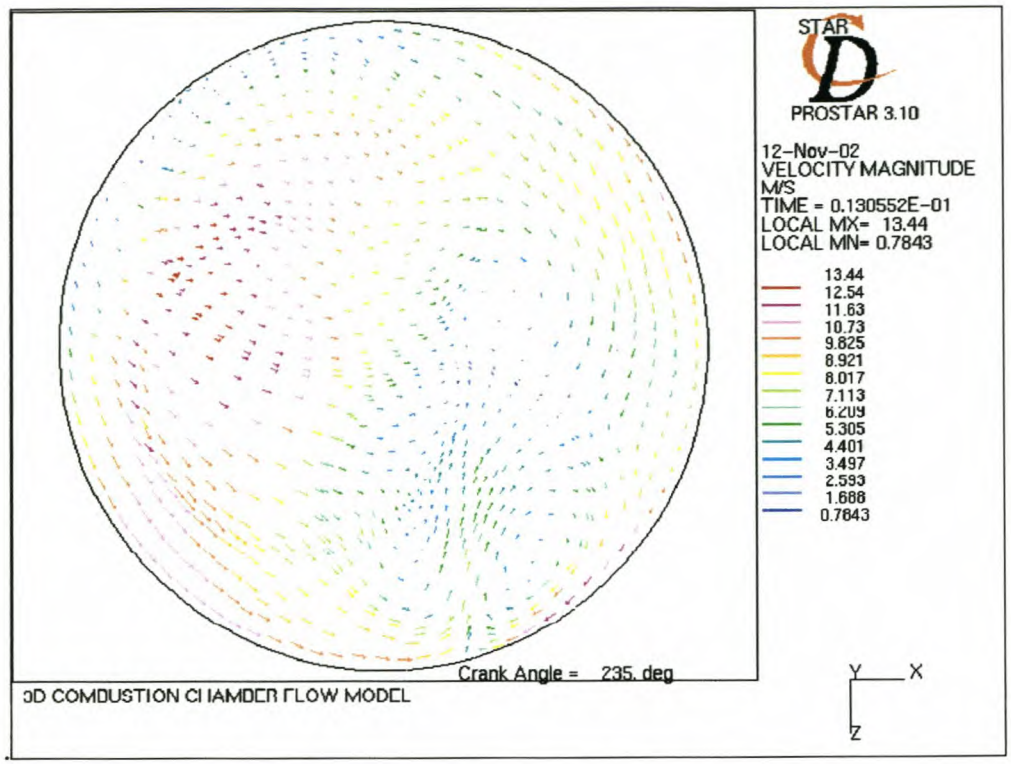

Figure 11-10: Flow in the 1.6L Rocam combustion chamber at intake valve closure, 3000rpm WOT. Simulation performed by StarCD

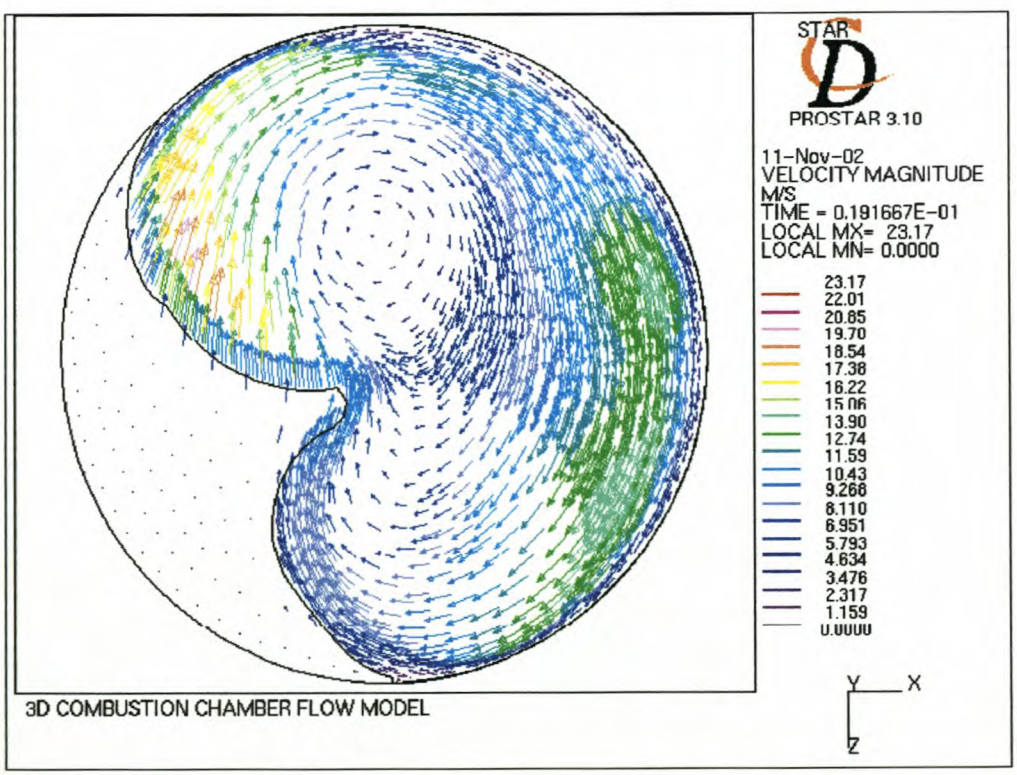

Figure 11-11: Flow in the 1.3L Rocam combustion chamber at the time of ignition, 3000rpm WOT. Simulation performed by StarCD

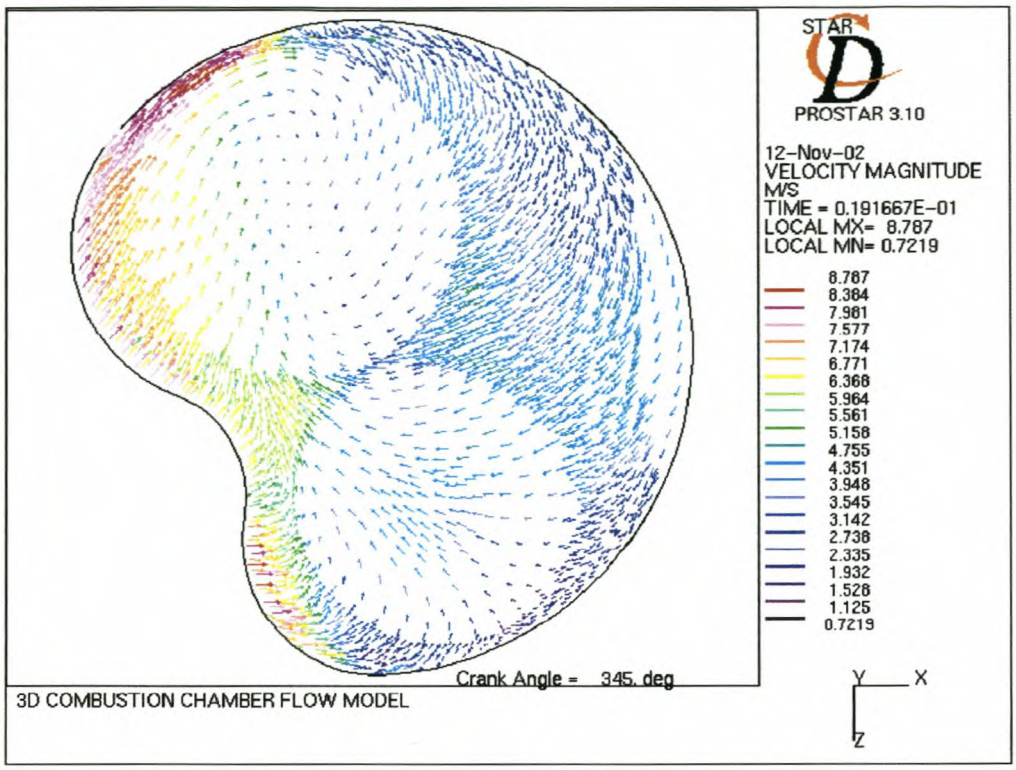

Figure 11-12: Flow in the 1.6L Rocam combustion chamber at the time of ignition, 3000rpm WOT. Simulation performed by StarCD

11.4 Turbulent Kinetic Energy

Figure 11-13 illustrate the turbulent kinetic energy for the 1.3L and the 1.6L engines from 25° before top dead centre (BTDC) until 15°BTDC. The section is parallel to the piston surface and halfway between the piston surface and the topmost surface of the combustion chamber.

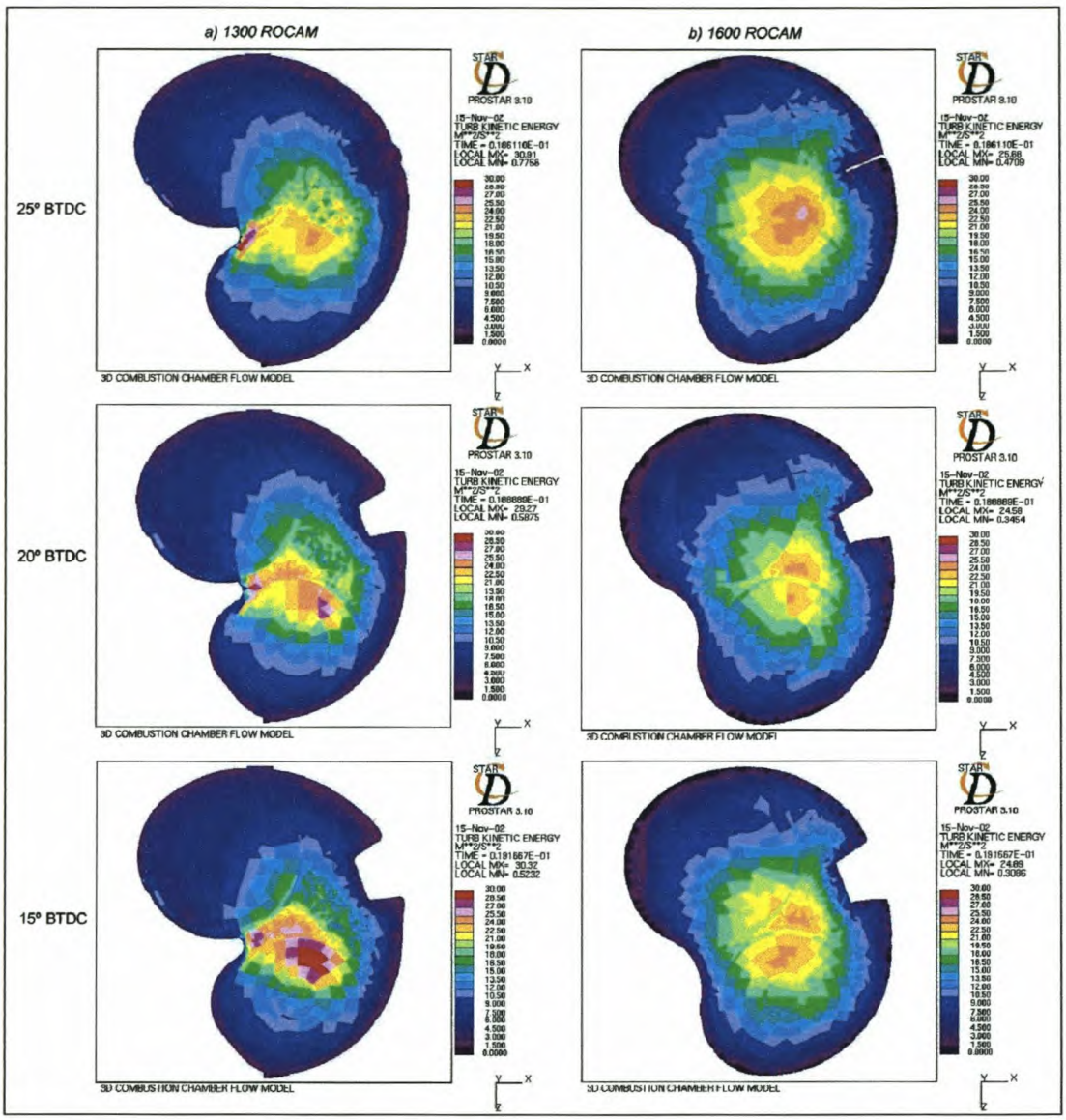

Figure 11-13: Cross section of Rocam 1.3L and 1.6L combustion chambers illustrating turbulent kinetic energy around the time of ignition, 3000rpm WOT. Simulation performed by StarCD

As the piston approach TDC, turbulent kinetic energy is created through the occurrence of squish, i.e. the acceleration of flow from the volume between the nose of the piston surface into the rest of the combustion chamber. Tumbling flow is also broken down into smaller turbulent eddies by the decreasing distance between the cylinder head and the piston crown. As the distance between the cylinder head and piston becomes very small turbulence starts to decay, and therefore the ignition should be timed to occur when turbulent kinetic energy is at its maximum around the spark region in order to achieve the maximum flame propagation rate at spark i.e. shorter induction period.

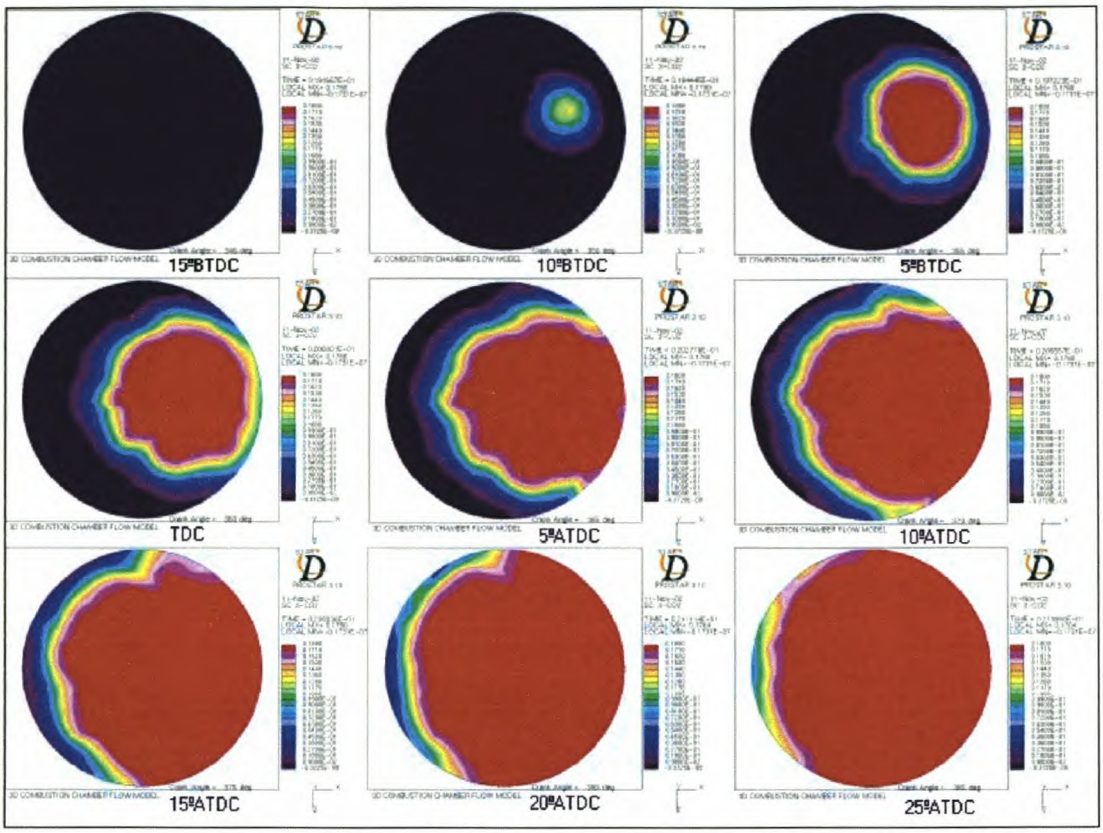

Figure 11-14: Combustion in the 1.3L Rocam engine simulated by the Weller flame area model in StarCD, 3000rpm WOT. The section is through a plane halfway between the cylinder head and the piston surface. The graphs show the CO_2 mass fractions in the combustion chamber.
(For easy comparison these graphs were scaled, making the scales and titles unreadable. Red shows the CO2 concentration in the fully burned mixture. Black shows the CO2 concentration in the unburned mixture.)

From comparison of combustion in the 1.3L and combustion in the 1.6L as illustrated by Figure 11-15, the effect of lower swirl in the 1.6L is clear. The flame propagates almost symmetrically from the ignition zone towards the opposite wall for the 1.6L. Comparing the 10 deg BTDC frames, it seems that the initial stage of combustion for the 1.6L developed quicker than the 1.3L, but the 1.3L flame spread slightly faster towards the later stages of combustion, possibly due to increased swirl and turbulence.

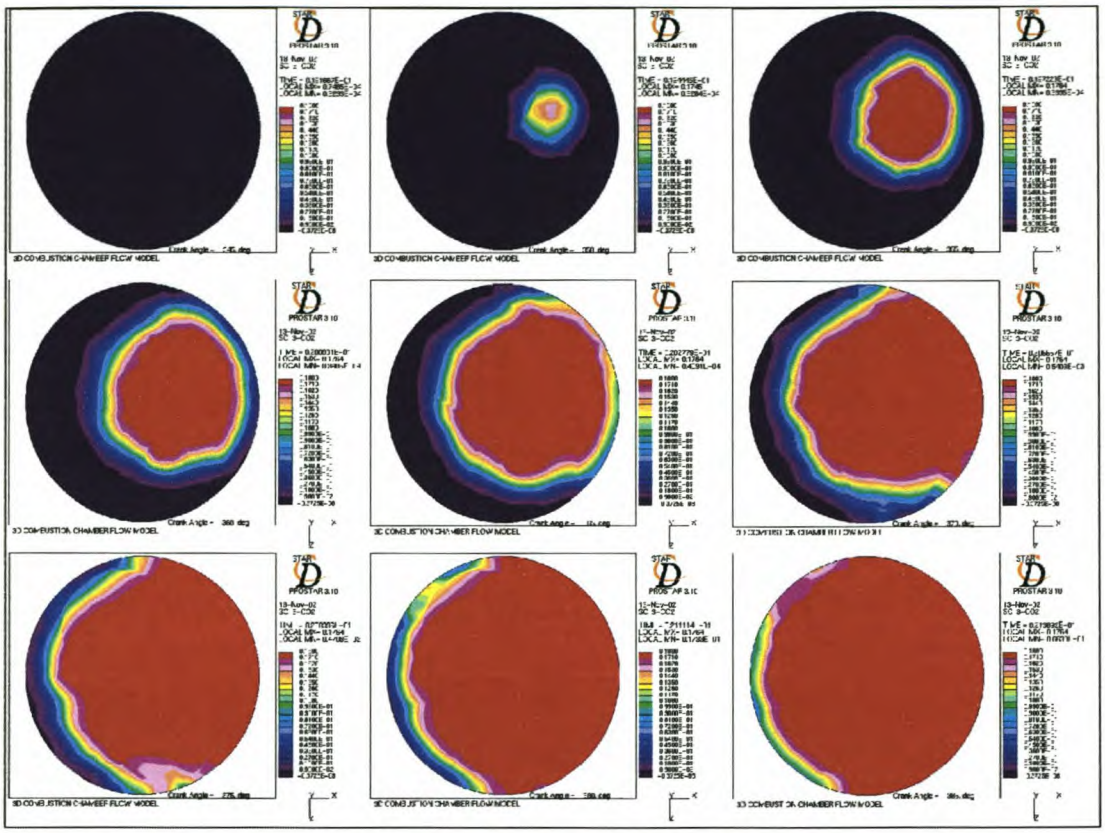

Figure 11-15: Combustion in the 1.6L Rocam engine simulated by the Weller flame area model in StarCD, 3000rpm WOT. The section is through a plane halfway between the cylinder head and the piston surface.
(For easy comparison these graphs were scaled, making the scales and titles unreadable. Red shows the CO_2 concentration in the fully burned mixture. Black shows the CO_2 concentration in the unburned mixture.)

The cumulative heat released in the combustion chamber is calculated at every crank angle degree from the mass concentration of fuel integrated over the entire volume subtracted from the initial mass of fuel in the chamber times the lower heating value of the fuel. Heat release rate is then determined from differentiation of the cumulative heat release data.

The heat release analysis results are illustrated in Figure 11-16. The normalised 1.3l burn rate is faster than that of the 1.6l from ignition up to 4°ATDC. At 4°ATDC the 1.6l burn rate has overtaken that of the 1.3l as 50% of the fuel has been burnt in the 1.3l at this point. The higher compression ratio and turbulent kinetic energy of the 1.3l could be the cause of the increased burn rate for this combustion chamber. Because of the quicker burn rate, the flame front of the 1.3l reach the walls sooner than that of the 1.6l,

causing the burn rate curve to flatten out earlier than the 1.6l burn rate curve.

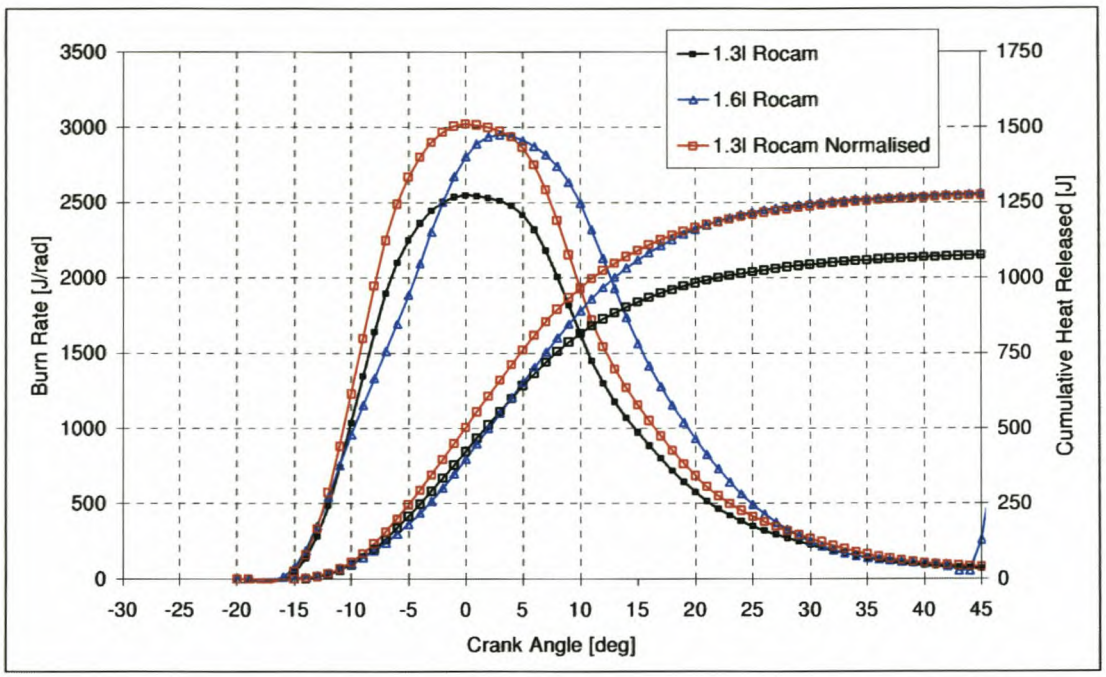

Figure 11-16: Cumulative heat released and burn rate comparison between 1.3L and 1.6L engines at 3000rpm, WOT. Data from StarCD simulation

Other parameters of the heat release data are determined from the in-cylinder heat release, pressure and temperature data. The results indicate that the 1.3L has a higher imep than the 1.6L. The pmep of the 1.3L is less than for the 1.6L due to lower exhaust backpressure. The 1.3L reached a higher peak pressure than the 1.6L as a result of higher compression ratio, and possibly faster initial burning. The higher maximum temperature of the 1.6L is a result of slower burning in the initial stage of combustion, leaving more fuel to burn toward the end of combustion. In-cylinder fluid pressures and temperatures for both engines are plotted vs. crank angle in Figure 11-17.

Table 11-1: Combustion simulation results for the 1.3L and 1.6L Rocam engines at 3000, WOT. Simulation performed by StarCD

	1.3L	1.6L
Displacement volume [m^3]	0.000324	0.000399
IMEP [kPa]	1194.104	1180.824
PMEP [kPa]	-22.9102	-26.8971
IMEP(net) [kPa]	1171.193	1153.927
Pressure max [kPa]	6034.55	5567.74
Pressure max - crank angle [deg]	13	13
Cumulative heat released max [kJ]	877	1085
Cumulative heat released max - crank angle [deg]	41	42
Heat release rate max [kJ/rad]	2102	2688
Heat release rate max - crank angle [deg]	1	3
Ignition timing [deg]	-15	-15
Temperature maximum [K]	2717	2729
Temperature maximum - crank angle [deg]	22	22
Induction period 0 to 5% [deg]	6	6
Burn angle 5 to 95% [deg]	30	30
Crank angle of 50% fuel burned [deg]	3	4

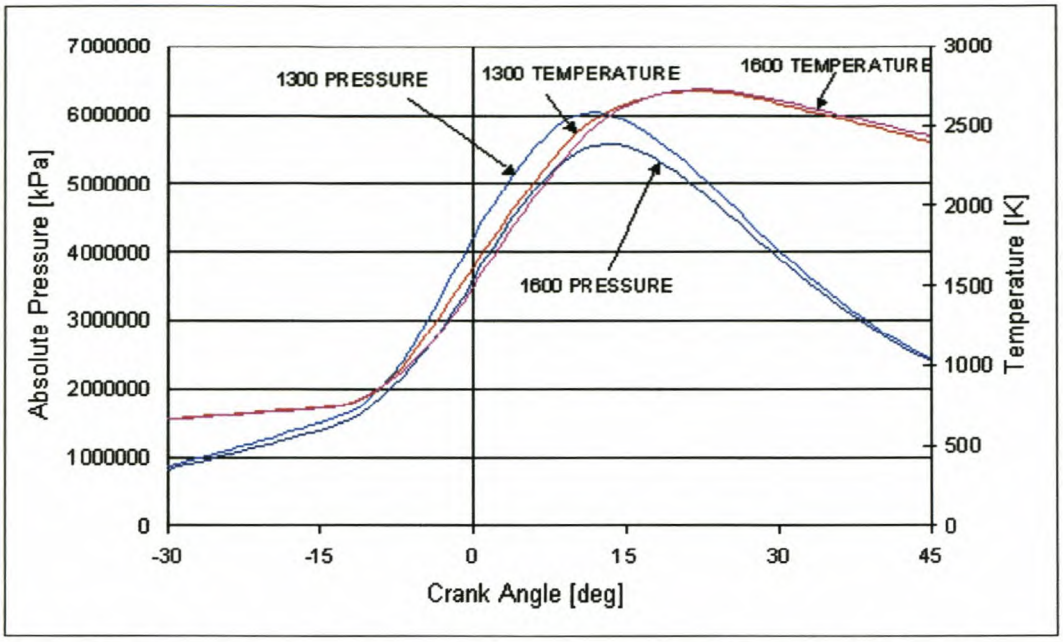

Figure 11-17: Average in-cylinder pressure and temperature vs. crank angle for the 1.3L and 1.6L engines. Data from numerical simulation in StarCD

11.6 Discussion of Numerical Simulation Results

Numerical simulation results were processed and the results presented in the form of vector and scalar plots, with some volume-integrated numerical values determined for quantifiable properties such as swirl, tumble and burn angle. Maximum pressures and temperatures were also determined.

It is important to note that a mesh refinement study was not performed due to the constraints on time and processing power. The results could, therefore change with mesh refinement meaning that this is not a converged solution. Results will therefore serve only as a guideline and experimental results will take preference to numerical simulation results.

From the given results, it is deduced that flow into the 1.3L chamber directed in the circumpherential direction, inducing almost an order of magnitude more swirl than for the 1.6L chamber. Tumble is induced by both engines with only slight difference in magnitude, indicating that the difference in the 1.3L and 1.6L geometry does not play a major role with respect to induced tumble. The generation of turbulent kinetic energy from the breaking down of tumbling motion is however different for the two engines.

The 1.3L combustion chamber generated more turbulence due to the sharp nose in the combustion chamber, but in the region of the spark plug the 1.6L achieved higher turbulent intensity, causing quicker initial flame propagation and burn rate. The higher in-cylinder turbulent kinetic energy and swirl of the 1.3L caused the burn rate of the 1.3L to rapidly overtake that of the 1.6L and achieve quicker fuel burning during the first half of combustion.

12 DISCUSSION OF EXPERIMENTAL RESULTS VS. NUMERICAL SIMULATION RESULTS

The numerical simulation data and the experimental results are correlated by comparison of in-cylinder pressure data. Experimental methods are available to verify the flow field visually but this is beyond the scope of this project. The engine developer is most interested in the pressure data as this could be directly related to engine performance in the form of mean effective pressure.

The imep results obtained from CFD were found to correlate well with experimental measurement results. Figure 12-1 and Figure 12-2 gives a first order indication of the difference between simulation results and experimental results in the form of pressure vs. crank angle data for the 1.3L and 1.6L engines respectively. A more informative comparison is that shown in Figure 12-3 and Figure 12-4 illustrating the log P vs. log V results for the two engines.

It was noted from Figure 9-2 that, unfortunately, the experimentally measured imep for the 1.3L engine at 3000rpm WOT does not comply with the trend in the rest of the data. According to the trend of the 1.3L engine imep data in Figure 9-2, the imep for the 1.3L should be 40kPa above that of the 1.6L engine, which amounts to 1150kPa, whereas the measured value is 1020kPa. The value of 1150kPa deduced from the trend was found to correlate well with the imep of 1151kPa of the 1.3L engine determined by numerical simulation. The experimentally determined imep for the 1.6L engine is 1128kPa while the numerical simulation yielded an imep of 1140kPa for this engine, which is a reasonable correlation. It was found from simulation results that the best time for ignition, i.e. the time when turbulence is optimum for increased flame spreading, was around 15° and 21°BTDC for the 1.3L and 1.6L engines respectively. The lag between numerical and experimental data could be contributed to the fact that in practise, a finite time is required for ignition to take effect, hence the earlier spark.

A few differences are highlighted by the comparisons between experimental results and simulation results in Figure 12-3 and Figure 12-4 of log P vs. log V for the 1.3L and 1.6L engines. Firstly, it is clear that the measured pressure during the exhaust stroke is substantially lower than the simulation results for both the 1.3L and the 1.6L engines.

Possible causes for this difference are incorrect pressure measurement, a difference in the average cylinder pressure and the pressure at the point where pressure is measured or inability to capture dynamic effects in the exhaust system through numerical simulation. If the pressure transducer in use in this experiment suffers from thermal strain, the effect would be to lower exhaust pressure as in Figure 4-6 as determined by Stein et al. (1987). The point of pressure measurement is close to the exhaust valve. This implies that when the exhaust valve opens, flow accelerates into the exhaust port past the cavity of the pressure transducer causing a reduction in the static pressure at the cavity and a subsequent reduced pressure measurement. The third possible cause for the difference between experimentally measured pressure and numerical simulation results is the inability to simulate the dynamic effects in the exhaust system. The boundary conditions specified to the flow simulation do not transmit pressure pulses as is present in the exhaust system of an engine. The effect of the pressure pulses is, if timed correctly, to reduce the pressure when the exhaust valve opens. If this effect is present at the speed under consideration then the experimental pressure measurement would reflect on the reduced pressure whereas the numerical simulation would not.

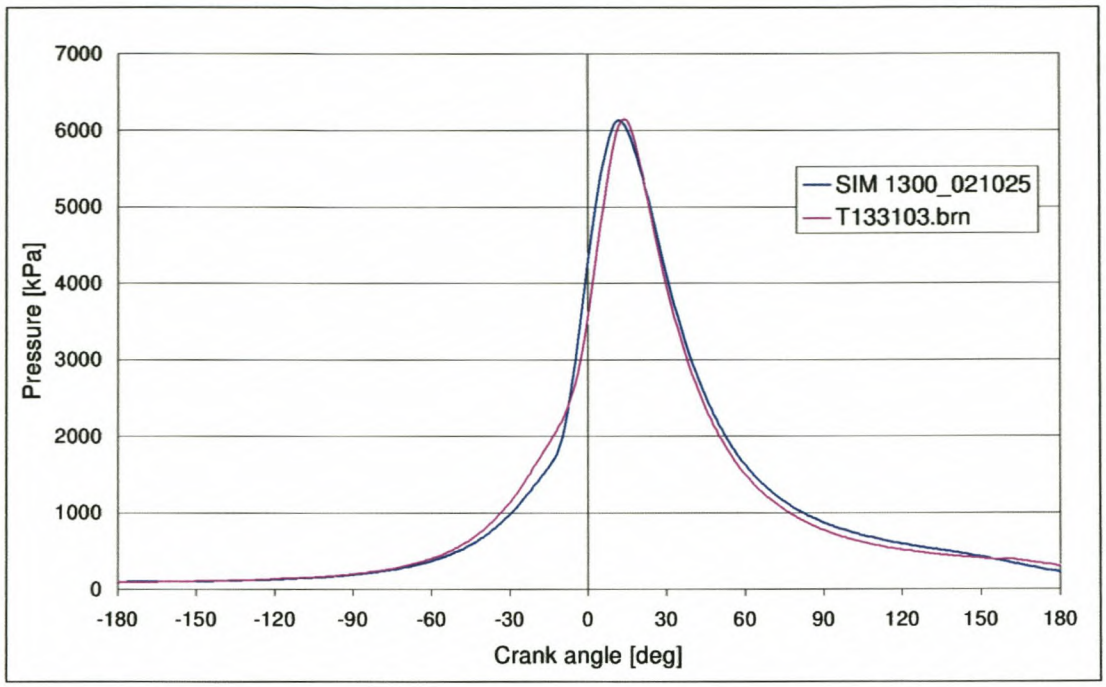

Figure 12-1: Comparison between in-cylinder pressures in the 1.3L obtained from experimental testing and by numerical flow simulation (3000rpm WOT)

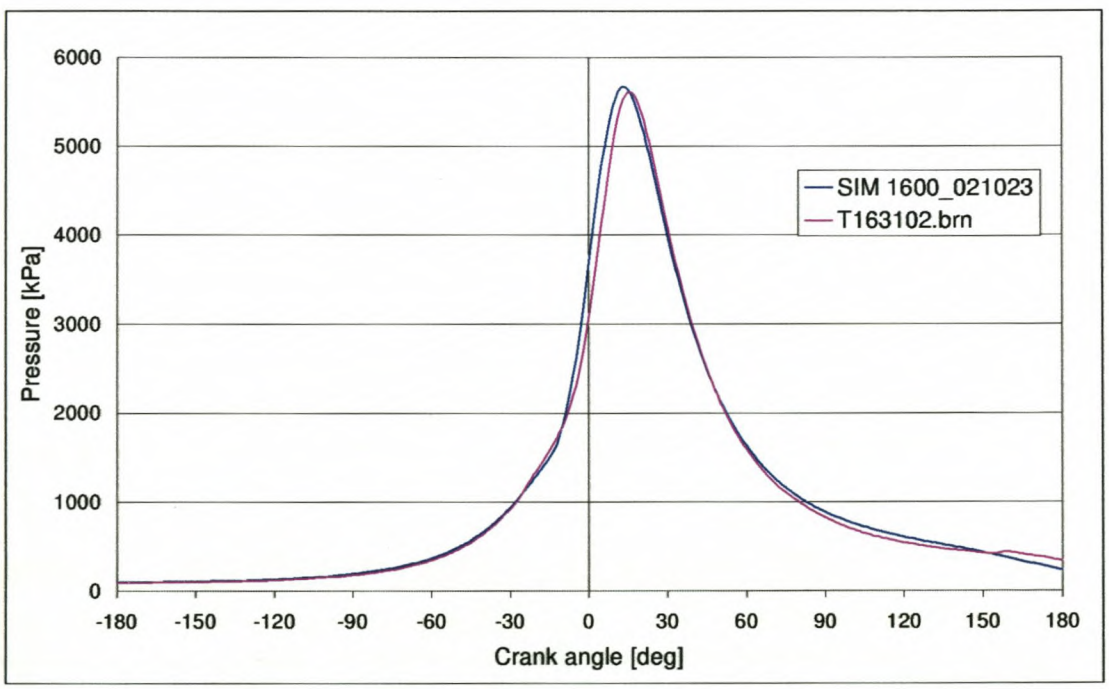

Figure 12-2: Comparison between in-cylinder pressures in the 1.6L obtained from experimental testing and by numerical flow simulation (3000rpm WOT)

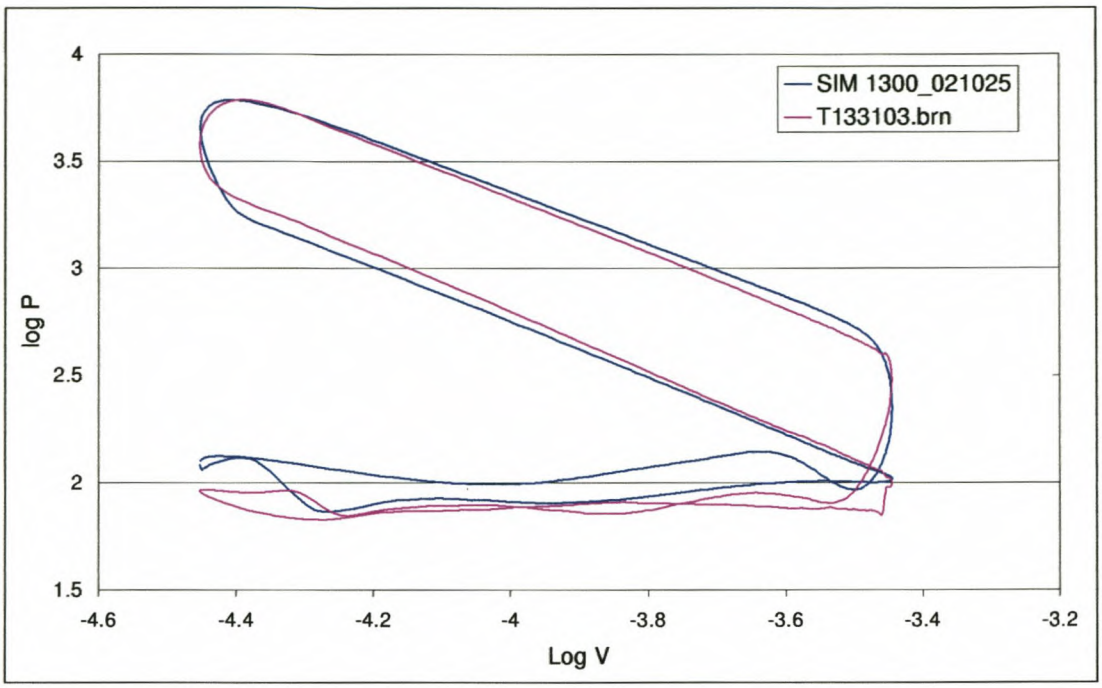

Figure 12-3: Comparison between log P vs. log V in the 1.3L obtained from experimental testing and by numerical flow simulation (3000rpm WOT)

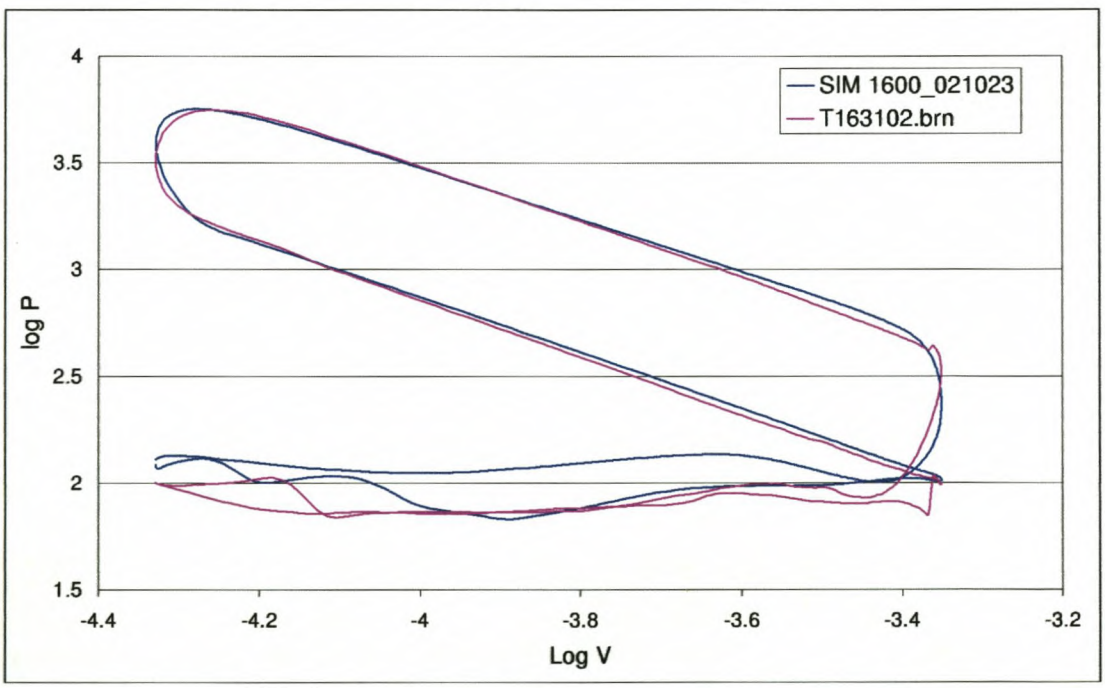

Figure 12-4: Comparison between log P vs. log V in the 1.6L obtained from experimental testing and by numerical flow simulation (3000rpm WOT)

13 CONCLUSION

The experimental results proved that the 1.3L Rocam engine achieve shorter burn angles than the 1.6L. This is proven by burn angle results from combustion analysis as well as from the fact that maximum in-cylinder temperatures for the 1.3L are located earlier in the cycle even though ignition is initiated later. The burn angles for the 1.3L are shorter than that of the 1.6L as a result of the increased compression ratio and the increased motion that is induced by masking of the intake valve. The main benefit of the shorter burn angles is reduced exhaust gas emissions due to more complete combustion at the time the exhaust valve opens. The effect of the combustion chamber and port configuration is well envisaged from the computational fluid dynamics results. Numerical simulation results indicated that 8 times more swirl is present in the combustion chamber of the 1.3L engine, assisting in air-fuel mixing and in turbulent flame spreading. It was also found that the 1.3L induces more turbulent kinetic energy than the 1.6L, but that this turbulence might be slightly misdirected, as swirl transports the turbulence away from the spark region. The smaller than expected difference in measured induction periods for the two engines also hints that this might be the case.

The second assumption was that the 1.6L was optimised for increased volumetric efficiency and therefore increased power by designing an open combustion chamber. It was experimentally determined that the 1.6L volumetric efficiency is superior to that of the 1.3L at WOT. It was found that the geometry the 1.3L intake port imposes an increased pressure gradient on flow into the combustion chamber as a direct result of a smaller port to diameter ratio than the 1.6L. The increased masking of the 1.3L port also influences the inflow pressure drop. The increased volumetric efficiency of the 1.6L was therefore both experimentally and numerically proven.

In conclusion, the geometry of the 1.3L combustion chamber with its smaller intake port, masking around the intake port and the sharp nose between the intake and exhaust ports are features that direct the flow into a swirling motion and enhance turbulence generation that contributes quicker flame spreading. These features should be incorporated into the combustion chamber of an engine that requires low exhaust gas emissions. When emissions goal are secondary to performance the combustion chamber should be more open such as that of the 1.6L engine, enhancing volumetric efficiency.

The scope of this project did not include modelling of emissions. This is a subject for further evaluation in future projects.

As a secondary objective, a three-dimensional fluid flow simulation capability was developed at Stellenbosch University. The imep results of the simulations were well correlated by experimental results although the model was not refined for mesh convergence. In the case of the 1.3L engine the imep determined from numerical simulation results seems more realistic than that determined experimentally. The simulation results also predicted optimum ignition angles quite accurately. The effect of difference in geometry of the combustion chambers under consideration on combustion chamber flow and processes was well predicted by the numerical simulation tool. The numerical model can be utilised in the future when developing new combustion systems for a similar engine especially with the aid of more powerful processing capability.

14 SUGGESTIONS FOR FURTHER RESEARCH

During completion of this project some areas have been identified that could be the topics of small to large-scale studies. Further research into any one of these topics would compliment this study. Multi-processor flow simulations would overcome the time constraint that is currently experienced for simulations of this nature. This is a method that is widely used by large CFD companies and is seen as the way of the future. Implementation of multi-processor simulations should be considered for future use in CAE. Automatic mesh generation could also assist in achieving shorter turn around times for simulations. Although some effort was made during completion of this project to automate mesh generation, this was done in a very specialised manner for the configuration of the engines under consideration here. The need exists for more generalised meshing methods. Auto-ignition simulation is already incorporated into StarCD and use of this tool may enhance the capabilities of this numerical simulation significantly. The use of the simulation to assist in programming of the engine control unit in order to optimise for emissions and performance would benefit greatly from the ability to simulate auto-ignition. Cold flow simulation and experimental verification of port flow provides a simple method to verify some of the numerical simulation results. The capability to perform this work will be invaluable to the designer of combustion chamber and port configurations. The accuracy of the pressure measurement equipment used in this study is not well understood and needs to be investigated in the interest of future testing. The final topic is a study on the effect of compression ratio on combustion. Knowledge of this effect will provide an improved understanding of the effect of compression ratio and geometry on the combustion and flow process. The topics that are suggested for future research are listed below for clarity.

- Multi-Processor Computer Simulations
- Development of Rapid Mesh Generation Techniques
- Simulation of Auto-Ignition
- Cold Flow Simulation of Port Flow with Experimental Verification

- Investigation Into the Accuracy of the Spark Plug Pressure Transducer

- Numerical and Experimental Study on the Effect of Compression Ratio on Combustion

15 REFERENCES

Alkidas, A.C., and Meyers, J.P. (1982): "Transient Heat-Flux Measurements in the Combustion Chamber of a Spark Ignition Engine," Journal of Heat Transfer, ASME Transactions, Volume 104, pp. 62-67.

Bell, A.J. (2003): "The Effect of Fuel Formulation on the Exhaust Emissions of Spark Ignition Engines," PhD Thesis, Department of Mechanical Engineering, Stellenbosch University, to be published.

Caris, D.F., and Nelson, E.E. (1959): "A New Look at High Compression Engines," SAE Transactions, Volume 67, p. 112.

Çengel, Y.A., and Boles, M.A. (1994): "Thermodynamics: An Engineering Approach," McGraw-Hill Book Company.

Chun, K.M., and Heywood, J.B. (1987): "Estimating Heat-Release and Mass-of-Mixture Burned from Spark-Ignition Engine Pressure Data," Combustion Science and Technology, Volume 54, pp. 133-144.

Computational Dynamics Limited. (2002): "StarCD Version 3.15: Methodology Volume."

Computational Dynamics Limited. (1999): "StarCD Version 3.10B: User Guide."

Computational Dynamics Limited. (2002): "StarCD Version 3.15: User Guide."

Demirdzić, I., and Perić, M. (1988): "Space Conservation Law in Finite Volume Calculations of Fluid Flow", International Journal on Numerical Methods in Fluids, Volume 8, pp. 1037-1050.

Ferguson, C.R. (1986): "Internal Combustion Engines, Applied Thermosciences," Wiley.

Gatowski, J.A., Balles, E.N., Chun, K.M., Nelson, F.E., Ekchian, J.A., and Heywood, J.B. (1984): "Heat Release Analysis of Pressure Data," SAE Paper 841359.

Heywood, J.B. (1988): "Internal Combustion Engine Fundamentals," McGraw-Hill.

Jasak, H., Luo, J.Y., Kaluderčić, B., Gosman, A.D., Echtle, H., Liang, Z., Wirbeleit, F., Wierse, M., Rips, S., Werner, A., Fernström, G., and Karlsson, A. (1999): "Rapid CFD Simulation of Internal Combustion Engines," SAE Paper 1999011185.

Jayatilleka, C.L. (1969): "The Influence of Prandtl Number and Surface Roughness on the Resistance of the Laminar Sub-Layer to Momentum and Heat Transfer," Progress in Heat and Mass Transfer, 1, pp. 193-330.

Kays, W.M., and Crawford, M.E. (1993): "Convective Heat and Mass Transfer 3rd edition," McGraw-Hill.

Kee, R.J., Rupley, F.M., and Miller, J.D. (1990): "The Chemkin Thermodynamic Database," Sandia Report, SAND 87-8215B.UC-4.

Lancaster, D.R., Krieger, R.B., and Lienesch, J.H. (1975): "Measurement and Analysis of Engine Pressure Data," SAE Paper 750026, SAE Trans., vol. 84, 1975.

Mattarelli, E. (2000): "Comparison Between Two Combustion Chambers for a Motorcycle Racing Engine," SAE Paper 2000011894.

Metghalchi, M., and Keck, J.C. (1982): "Burning Velocities of Mixtures of Air with Methanol, Isooctane and Indolene at High Pressure and Temperature," Combustion and Flame, Volume 48(2), pp. 191-210.

Moran, D.P. (1997): "Racer for Windows: - Version 2 Manual," Stellenbosch Automotive Engineering.

MSC Software. (2000): "CFX-4 Solver Manual."

MSC Software. (2001): "Patran 2001 Manual."

Peck, E. (2001): "Internal Combustion Chambers," http://www-personal.wccnet.org /~eileen/ FourStroke.html, World Wide Web.

Phoenix (2001): "PHOENIX Turbulence Guide," http://www.cham.co.uk/phoenics/ dpolis/denc/turmod/enctu.htm#contents, World Wide Web.

Poulos, S.G. and Heywood, J.D. (1983): "The Effect of Chamber Geometry on Spark-Ignition Engine Combustion," SAE Paper 830334.

PTC Software. (2001): "ProEngineer 2001 Manual."

Rai, H.S., Brunt, F.J., and Loader, C.P. (1999): "Quantification and Reduction of IMEP Errors Resulting from Pressure Transducer Thermal Shock in an S.I. Engine," Sae Paper 1999011329.

Rassweiler, G.M. and Withrow, L. (1980): "Motion pictures of Engine Flames Correlated with Pressure Cards," SAE Paper 800131.

Ricardo Software. (2000): "Vectis Computational Fluid Dynamics Release 3.4.4: Vectis theory manual," Burr Ridge, IL, USA.

Ricardo Software. (2000): "Wave Documentation: User's Manual," Burr Ridge, IL, USA.

Roensch, M. (1949): "Thermal efficiency and mechanical losses of automotive engines," SAE Journal, Volume 51, pp. 17-30.

Rosseel, E., Sierens, R., and Baert, R.S.G. (1999): "Evaluating Piezoelectric Response to Thermal Shock from In-Cylinder Pressure Data," SAE Paper 1999010935.

Ruckenbauer, F. (1999): "The Precision Measurement of Pressures in Internal Combustion Engines for the Purpose of Thermodynamic Cycle Analysis," AVL.

Sinha, N., Cavallo, P.A., Lee, R.A., Hosangadi, A., Kenzakowski, D.C., Dash, S.M., Affes, H., and Chu, D. (1998): "Novel CFD Techniques for In-Cylinder Flows on Tetrahedral Grids," SAE Paper 980138.

Stein, R.A., Mencik, D.Z., and Warren, C.C. (1987): "Effect of Thermal Strain on Measurement of Cylinder Pressure," SAE Paper 870455.

Weller, H.G. (1993): "The Development of a New Flame Area Combustion Model Using Conditional Averaging," Thermo-Fluids Section Report TF/9307, Department of Mechanical Engineering, Imperial College of Science Technology and Medicine.

Westbrook, C.K., and Dryer, F.L. (1980): "Prediction of Laminar Flame Properties of Methanol-Air Mixtures," Combustion and Flame, Volume 37(2), pp. 171-192.

White, F.M. (1991): "Viscous Fluid Flow 2nd edition," McGraw-Hill.

White, F.M. (1994): "Fluid Mechanics 3rd edition," McGraw-Hill.

Witze, P.O. (1982): "The effect of Spark Location on Combustion in Variable-Swirl Engine," SAE Paper 820044, Volume 91, pp. 165-175.

Wölfle, M., Köss, A., Gasper, W., Utech, K., Rechs, M., and Kune, O. (1999): "Ford's New Small Engine Family for New and Emerging Markets," Motortechnische Zeitschrift 60 Nr. 12, pp. 854-865.

Woschni, G. (1967): "A Universally Applicable Equation for the Instantaneous Heat Transfer Coefficient in the Internal Combustion Engine," SAE Paper 670931.